X-ray photoelectron spectroscopy investigations of resistive switching in Te-based CBRAMs

Munique Kazar Mendes

NNT : 2018SACLS285

Thèse de doctorat

X-ray photoelectron spectroscopy investigations of resistive switching in Te-based CBRAMs

Thèse de doctorat de l'Université Paris-Saclay
préparée à l'Université Paris-Sud

École doctorale n°564 Physique en Île-de-France (EDPIF)
Spécialité de doctorat: Physique

Thèse présentée et soutenue à Grenoble, le 04 octobre 2018, par

Munique KAZAR MENDES

Composition du Jury :

M. Marc Simon Directeur de recherche, Université Pierre et Marie Curie	Président
M. Christophe Vallée Professeur, Université Grenoble Alpes	Rapporteur
M. Thierry Conard Team leader, IMEC	Rapporteur
M. Arnaud Etcheberry Directeur de recherche, Université de Versailles St-Quentin-en-Yvelines	Examinateur
Mme. Marie-Paule Besland Directeur de recherche, Université de Nantes	Examinateur
M. Nicholas Barrett Directeur de recherche, Université Paris-Sud – CEA Saclay	Directeur de thèse
Mme. Eugénie Martinez Docteur, Université Grenoble Alpes – CEA Grenoble	Co-Directeur de thèse

Acknowledgements

Firstly, I would like to express my sincere gratitude to my advisors Nick Barrett and Eugénie Martinez for the continuous support and guidance, for their patience, motivation, and immense knowledge. Thanks to Remy Gassilloud, Aurélie Marty, Mathieu Bernard, Philippe Blaise and Gabriel Molas for fruitful discussions and for sharing your knowledge about resistive memories. I would also like to thank Anass Benayad who introduced me to XPS knowledge during my master internship and for accepting to be part of my thesis committee together with Stéphane Fusil.

I would like to acknowledge the NanoCharacterisation PlatForm (PFNC) of CEA Grenoble and the *Institut Rayonnement-Matière of CEA Saclay (IRAMIS)*. A big thanks to all the members of staff at CEA Grenoble, EDPIF and Paris Sud/ Paris-Saclay University for the support during this thesis work.

I would also like to acknowledge, Thierry Conard and Christophe Vallée, who have kindly accepted to evaluate this thesis work and Arnaud Etcheberry, Marie-Paule Besland and Marc Simon, who have accepted to be members of the jury.

Afterwards, I would like to thank my colleagues from the PFNC group that I had the opportunity to meet during this experience for the very friendly atmosphere which has always made me enjoying going at work.

I will finish by expressing my deepest gratitude to my parents Eliete and Silvestre and my boyfriend Rodrigo for the help, support and patience they have given me throughout my studies. Obrigada!

Acknowledgements

Abstract

Conducting bridging resistive random access memories (CBRAMs) are one option currently investigated for the next generation of non-volatile memories. Data storage is based on switching the resistivity between high (HRS) and low (LRS) resistance states. Under electrical bias, a conductive path is assumed to be created by ions diffusion from the active electrode into the solid electrolyte. Recently, special attention has been drawn to devices containing an elemental semiconductor such as tellurium, operating with reduced currents and less retention failures. In these subquantum CBRAM cells, the filament is thought to contain tellurium, yielding a 1-atom conductance (G_{1atom}) significantly reduced compared to standard CBRAMs and thus allowing low power operation. In this thesis, we use X-ray photoelectron spectroscopy (XPS) to learn about electrochemical reactions involved in the switching mechanism of Al_2O_3 based CBRAMs with ZrTe and TiTe alloys as active electrode. Two methods are used: i) non-destructive Hard X-ray photoelectron spectroscopy (HAXPES) to investigate the critical interfaces between the electrolyte (Al_2O_3) and the top and bottom electrodes and ii) Gas Cluster Ion Beams (GCIB), a sputtering technique that leads to lower structure degradation, combined with XPS depth profiling to evaluate chemical depth distributions. ToF-SIMS measurements are also performed to get complementary in-depth chemical information. The aim of this thesis is to clarify the driving mechanism and understand the chemical changes at both interfaces involved in the forming process under positive and negative polarization as well as the mechanism of the reset operation. For that, we performed a comparison between as-grown state, i.e. the pristine device with a formed state, i.e. the sample after the first transition between HRS and LRS, and reset state, i.e. the sample after the first transition between LRS and HRS.
Conducting bridging resistive random access memories (CBRAMs) are one option currently investigated for the next generation of non-volatile memories. Data storage is based on switching the resistivity between high (HRS) and low (LRS) resistance states. Under electrical bias, a conductive path is assumed to be created by ions diffusion from the active electrode into the solid electrolyte. Recently, special attention has been drawn to devices containing an elemental semiconductor such as tellurium, operating with reduced currents and less retention failures. In these subquantum CBRAM cells, the filament is thought to contain tellurium, yielding a 1-atom conductance (G1atom) significantly reduced compared to standard CBRAMs and thus allowing low power operation. In this thesis, we use X-ray photoelectron spectroscopy (XPS) to learn about electrochemical reactions involved in the switching mechanism of Al_2O_3 based CBRAMs with ZrTe and TiTe alloys as active electrode. Two methods are used: i) non-destructive Hard X-ray photoelectron spectroscopy (HAXPES) to investigate the critical interfaces between the electrolyte (Al_2O_3) and the top and bottom electrodes and ii) Gas Cluster Ion Beams (GCIB), a sputtering technique that leads to lower structure degradation, combined with XPS depth profiling to evaluate chemical depth distributions. ToF-SIMS measurements are also performed to get complementary in-depth chemical information. The aim of this thesis is to clarify the driving mechanism and understand the chemical changes at both interfaces involved in the forming process under positive and negative polarization as well as the mechanism of the reset operation. For that, we performed a comparison between as-grown state, i.e. the pristine device with a formed state, i.e. the sample after the first transition between HRS and LRS, and reset state, i.e. the sample after the first transition between LRS and HRS.

Abstract

Contents

Introduction

Resistive Random Access Memories (RRAMs) are interesting candidates for the next generation of non-volatile memories (NVMs) due to their scalability, simple structure and potential high storage density [1–3]. Data storage principle is based on switching the resistivity between high (HRS) and, low (LRS) resistance states by applying voltage or current pulses. Among them, conductive-bridge resistive random access memories (CBRAMs) are a promising option as shown by some preliminary industrial demonstrators [4–6]. These cells are composed by an active electrode, a solid electrolyte (insulating layer) and a bottom electrode. Their resistive switching mechanism is based on the electrochemical formation/dissolution of conducting filaments in the solid electrolyte layer, forming a bridge between the two electrodes. The formation of these filaments occurs by the dissolution of the metal present in the active electrode according to $M \rightarrow M^{z+} + ze^-$, subsequent metal cation migration inside the electrolyte layer and the reduction of the M^{z+} at the bottom electrode surface according to : $M^{z+} + ze^- \rightarrow M$. This model is adopted to explain the resistive switching, however, the physical mechanisms driving these phenomena have not been fully understood.

CBRAMs improve the cycling endurance while maintaining good scaling and high operation speed. However, this technology still presents several issues including, high switching voltage, the complexe chemistry of the forming process and high power consumption. Therefore, a better knowledge of the resistive switching mechanism as well as the exploration of new materials is essential for the future device development.

Recently, special attention has been drawn to the use of devices containing an elemental semiconductor such as tellurium, operating with reduced currents while keeping good retention properties [4]. In these subquantum CBRAMs, the filament is thought to contain tellurium. The current required to program a standard CBRAM cell is directly related to the conductance of a 1-atom filament (G_{1atom}). For metals, G_{1atom} is comparable to the quantum $G_0=2e^2/h$ [7], whereas for a semiconductor such as Te, it is sub-quantum (0.03 G_0) enabling operation at low currents. Subquantum CBRAMs based on an Al_2O_3 electrolyte and an active top electrode of a Te binary alloy such as ZrTe, TiTe and HfTe, are the most promising systems reported in the literature, with cell operating current and power as low as 10 µA and 0.01 mW [8].

The aim of this thesis is the investigation of the electrochemistry of the forming and reset processes for ZrTe (TiTe)/Al_2O_3-based CBRAMs. The filament creation, known as forming, is an irreversible process required to enable the write/erase (SET/RESET) cycles of the memory cell. It is a key step to be

controlled for the optimization of CBRAMs cells[4,6]. More information about filament formation would facilitate the control and manufacturing of such memory cells. It is also necessary to better understand the cycling of the cell. Thus, not only the electroforming step must be investigated [9], but also the switching between the LRS to the HRS, known as the reset step.

To investigate the resistive state-dependent chemistry in such Te-based CBRAMs, we have used Hard X-ray photoelectron spectroscopy (HAXPES) which enables non-destructive analysis of the buried interfaces between realistic electrodes and insulating layer thanks to the much greater probing depth [10]. The high sensitivity of this technique is also crucial due to the small changes expected in signal during resistive switching relative to that from the surrounding matrix. XPS depth profiling using Gas Cluster Ion Beams (GCIB) as sputtering technique was also used to study the elemental distribution through the sample. In addition Time-of-flight secondary ion mass spectrometry (ToF-SIMS) depth profiling was used as a complementary technique to provide in-depth profiles with a high depth resolution (< 1nm) and with a better sensitivity (< 10 ppm)[11]. To investigate the possible impact of the environment on the resistive switching of these cells, X-ray photoelectron spectroscopy with in-situ electrical polarization (under-ultra-vacuum) was used to highlight the role of the surface and interface oxidation in the forming process[12–14]. For that an assembly was developed using a specific sample holder allowing the bias application directly in the XPS analysis chamber.

The thesis work has been carried out in the framework of a collaboration between the NanoCharacterization Platform (PFNC) of CEA Grenoble and the *Institut Rayonnement-Matière of CEA Saclay (IRAMIS).* All of the samples were fabricated and optimized by the Department of Deposits (SDEP). The Hard X-ray photoelectron spectroscopy (HAXPES) analyses were performed at the GALAXIES beamline of the synchrotron SOLEIL and at the BL15XU beam line of the Japan Synchrotron Radiation Research Institute (SPring-8).

Preface

- Chapter 1 introduces the key concepts related to the resistive random access memories (RRAM): the advantages and characteristics, the physical processes involved in the resistive switching, the filamentary theory and the influence of the input parameters on the device performances characterization. A description of CBRAM and OxRRAM mechanisms and characteristics is presented. The last part shows a description of the subquantum CBRAMs cells based on Te which are the subject of this manuscript and the problematic of this thesis.
- Chapter 2 provides a description of the characterization techniques, experimental methods, as well as the sample preparation: growth method, lithography and circuitry for the *ex-situ* and *in-situ* studies of the cells. The principles of the photoemission spectroscopy are presented together with the specifics of Hard X-ray photoemission spectroscopy. In addition, this chapter outines the principles of ToF-SIMS.

  The experimental results are presented and discussed in the following three chapters.
- Chapter 3 shows the investigation of the electrochemistry of the resistivity change during the direct forming of ZrTe/Al_2O_3 based CBRAMs. The direct forming occurs when a positive bias is applied on the top electrode to form the filament. HAXPES probes the buried interface between the ZrTe active electrode and the Al_2O_3 layer. XPS and ToF-SIMS depth profiling investigate the oxygen, tellurium and zirconium migration. The last part correlates the electrical characterization of the TiTe/Al_2O_3-based devices under positive polarization with the physical chemistry response of the system.
- Chapter 4 is the investigation of the negative forming of Te-based CBRAMs, also called reverse forming, in which a negative voltage is applied on the top electrode and the first reset step i.e. the first transition from LRS to HRS. Compared to positive forming, the device operation is modified and the bottom electrode may also play a role in addition to the active electrode. To test the validity of this scenario in the case of Te-based CBRAMs, we study the redox phenomena observed in the different layers. We compare results obtained for three samples: as-, formed and reset. The aim is to clarify the switching mechanisms and understand the chemical changes at both electrode/electrolyte interfaces for devices with TiTe and ZrTe as active electrodes.
- Finally, chapter 5 shows the investigation of the forming process performed in-situ, i. e. under ultra-high vacuum, to get closer to real operating conditions. X-ray photoelectron spectroscopy is performed to analyse the surface and bulk chemical composition, by combining standard and depth profiling measurements. Results are compared with ex-situ forming under air.

Chapter 1

1. Resistive Random Access memory - RRAM

In the first part of this chapter will be introduced the key concepts related to the resistive random access memories (RRAM): the advantages and characteristics, the physical processes involved in the resistive switching, the filamentary theory and the influence of the input parameters on the device performances characterization. The second part describes the specific CBRAM and OxRRAM mechanisms and characteristics. Finally, we present the subquantum CBRAMs cells based on Te which are the subject of this thesis.

1.1. Non-volatile memories – NVM

Semiconductor memories are essential components of electronic systems [15,16] and can be classified as shown in Figure 1.1. There are two basic categories of memories: Volatile Memories and Non-Volatile Memories (NVM). The volatile memories are devices that lose stored information when switched off. Their application is mainly in systems with a relatively high speed of writing or requiring a short access time. Two examples are the DRAM (Dynamic Random Access Memory) used as cache in computer systems and SRAM (Static Random Access Memory) used as main memory in computer RAMs [6]. On the contrary, the NVM keep the information when switched off. Examples of NVM include read-only memory, flash memory, magnetic storage devices (e.g. hard disks and magnetic tapes), and optical discs. Among these types of memory, flash memory stands out, as it provides higher density, lower cost and much improved portability than traditional hard disk drives (HDD).

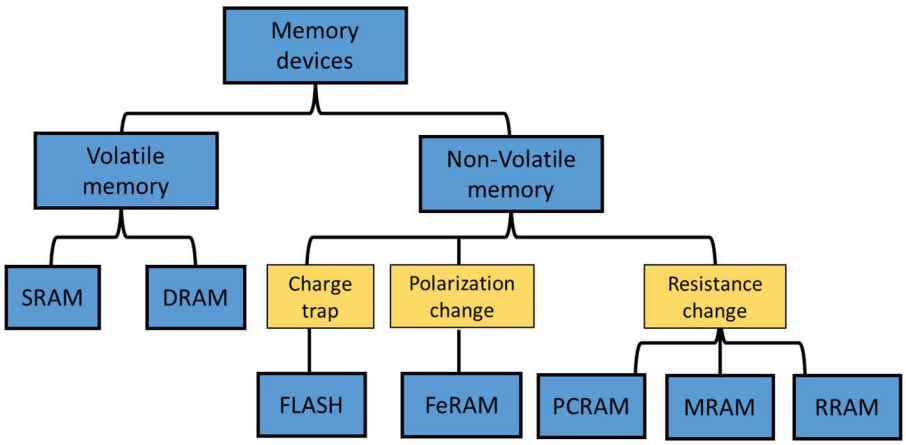

Figure 1.1. Classification of solid-state semiconductor memories.

With the advent of the Internet of Things (IoT), there is an increase of the number of devices that contain non-volatile memories being used in everyday situations. This increase has generated a great demand for memories of low power consumption, reliable data storage and fast access to stored data. However, the conventional memory cells don't seem to converge to these operating standards. The flash memories are approaching the integration limit. One of the major problems to be faced in the future of flash memories is their miniaturization. The decrease of the chips size, consequently leads to a decrease of their tunnel dielectric thickness. This decrease induces a discharge of the electrons present in the floating gate which can lead to a considerable reduction of the retention time of the data recorded in the memory[5,17].

Several novel nonvolatile memories (generally referred as emerging memories) have been proposed to find a replacement for flash, such as: Magnetoresistive RAM (MRAM), Phase Change RAM (PCRAM) and Resistive RAM (RRAM). Their interest is based mainly on low-power and high reading speed. However, their price and scalability are a barrier to compete with DRAM and NAND flash technologies (found mainly in small electronic devices as USB flash drives and memory cards). These new memories contain different materials and exhibit different mechanisms of data storage in comparison to established memories [5,6,18]. The development of these memories aims to optimize the main characteristics that a memory should have such as: high write/ read speed (ns), low-power (<1 V), endurance (>10 years) and good scalability (<10 nm) [18].

Among the emerging memories the RRAMs is very promising in the near future to replace flash memories and is under development by several companies such as: Panasonic, HP, Adesto Technologies, and Crossbar, among others. According to Yole's Development report in 2017[19], the first target to RRAM application will be the embedded memories i.e. a memory that is integrated into a logic chip circuit. These memories are adapted to devices that needs a memory with a high-temperature retention [20] i.g. automotive devices and also for low power applications [21] as for example smart cards, IoT, etc. After that, the target of RRAM applications will be to replace 3D NAND in microcontrollers and consequently enable their integration into a systems-on-a-chip (SoC).

1.2. Resistive random access memory (RRAM)

The RRAM is a metal–insulator–metal (MIM) resistance-changing device as shown in Figure 1.2. The change of the insulator layer resistance is induced by the application of an electric field. The two resistive states of the device are called: high resistance state (HRS) or low resistance state (LRS). The transition HRS → LRS is defined by "set" and the inverse by "reset". It is generally assumed by the researchers that the resistive switching is based on conducting filaments formation through the insulating oxide [1,2,4,22–24]. However, the physical mechanisms driving these phenomena have not been fully understood. Therefore, studies about

the electrochemical mechanisms involved in the resistive switching are essential for the future development of this type of memory.

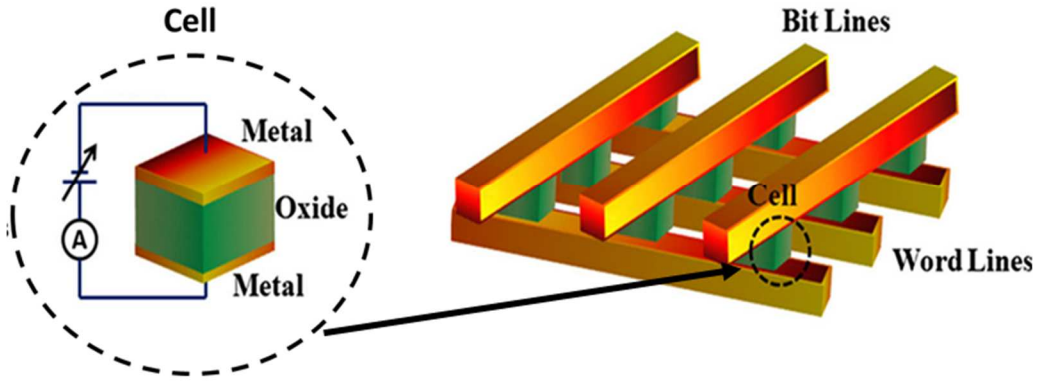

Figure 1.2. MIM structure of a RRAM cell. Adapted from Meena et al. [5].

1.2.1. RRAM technology

The RRAM is one of the most promising emerging memory technologies and present the following advantages [6,25,26]:

- Simple cell structure: 2-terminal MIM structure allowing 3D integration;
- fast speed for read and write-erase process (ns) and for flash (µs-ms);
- low power consumption;
- low cost to fabricate;
- possibility to achieve a high-density by the formation of a cross-point structure without using access devices [25].

Table 1.1 shows a comparison of some characteristics of RRAMs and flash memories. Among the critical issues for the future development of RRAMs we can highlight the forming operation, endurance, reliable and data retention. Another key challenge is fully understand the resistive switching of this memories to better optimize the cells and with that improving its performances.

Table 1.1. Comparison between Flash and RRAM. Adapted from [3,4,6]

		Flash	RRAM
Cell size (F)	Demonstrated	4	4
	Projected		
Read time (ns)	Demonstrated	100	50
	Projected		< 10
Read voltage (V)	Demonstrated	4.5	0.2
	Projected		0.1
Endurance (cycle)	Demonstrated	105	10^{12}
	Projected		$>10^{12}$
Write Voltages (V)	Demonstrated	15-20	0.6
	Projected	15	<0.5
Write /Erase time (ns)	Demonstrated	1000/100	< 1
	Projected		

1.2.2. Resistive switching mechanisms

Several studies proposed a model based on the formation/rupture of a conducting filaments connecting the two conducting electrodes i.e. inside the insulating layer to explain the resistive switching mechanism of the RRAMs. However, the exact formation mechanism and the chemistry of the filaments is still unclear. Figure 1.3 illustrates this mechanism and shows each step of the switching process: forming, reset and set.

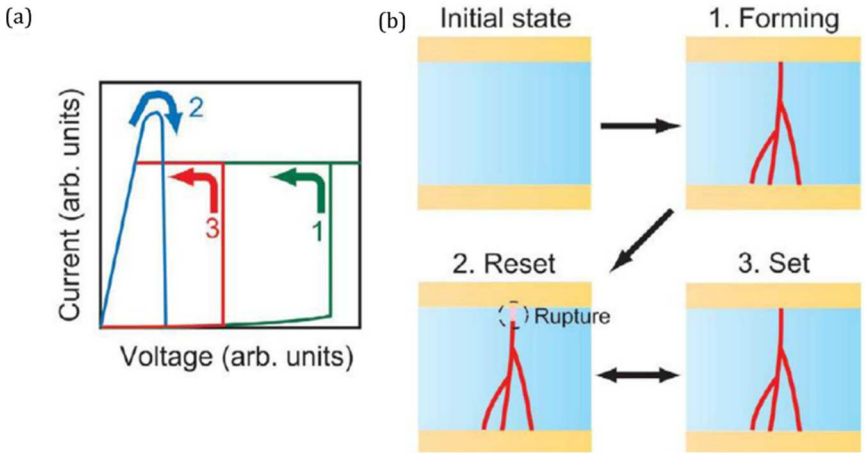

Figure 1.3. (a) Current-Voltage curve for a unipolar RRAM (b) Schematic of the forming, reset and set processes. Adapted from Sawa et al. [23].

The creation of conducting filaments through the insulating dielectric layer, known as forming, is an irreversible process required to activate the write/erase (set/reset) cycles of the memory cell. The forming process (1) is the first switching between the initial virgin state (VS) and the low resistance state (LRS). It is triggered by the forming voltage (V_F) and controlled by a compliance current (I_{cc}), which avoids the breakdown of the insulator layer. This forming process induces defects in the insulator; the formation of conductive paths across the dielectric is assumed after the bias application, following the filamentary theory. During the reset (2), which is the transition from the LRS to the High Resistance State (HRS), we have a partial recovery of these defects yielding to partial rupture of the conducive filaments. During this process, the current decreases abruptly at V_{Reset}. The subsequent process, called set (3), is the re-forming of the filament i.e. the switching from HRS to LRS. The set voltage (V_{set}) is smaller than V_F since the conducting filament is not entirely dissolved during the reset. Note that a non-filamentary resistive switching caused by a change at the interface and/or volume of the oxide is also possible. In this case, the LRS of the memory is inversely proportional to the device area[27]. Whereas for a memory with a resistive switching based on conductive filaments, the LRS is independent of the cell-area as demonstrated in the next section (Figure 1.7).

The RRAM may present a bipolar or unipolar resistive switching mechanism. Figure 1.4 shows the different hysteretic curves for each electrical behavior. In the unipolar behavior (Figure 1.4 (a)), the switching process does not depend on the polarity of the applied voltage, i.e. V_{Reset} has the same polarity as V_{set}. For a bipolar behavior, it is necessary to reverse the polarity, that is, V_{set} occurs in a polarity and V_{Reset} in the opposite polarity [2,22,28] as shown in Figure 1.4 (b).

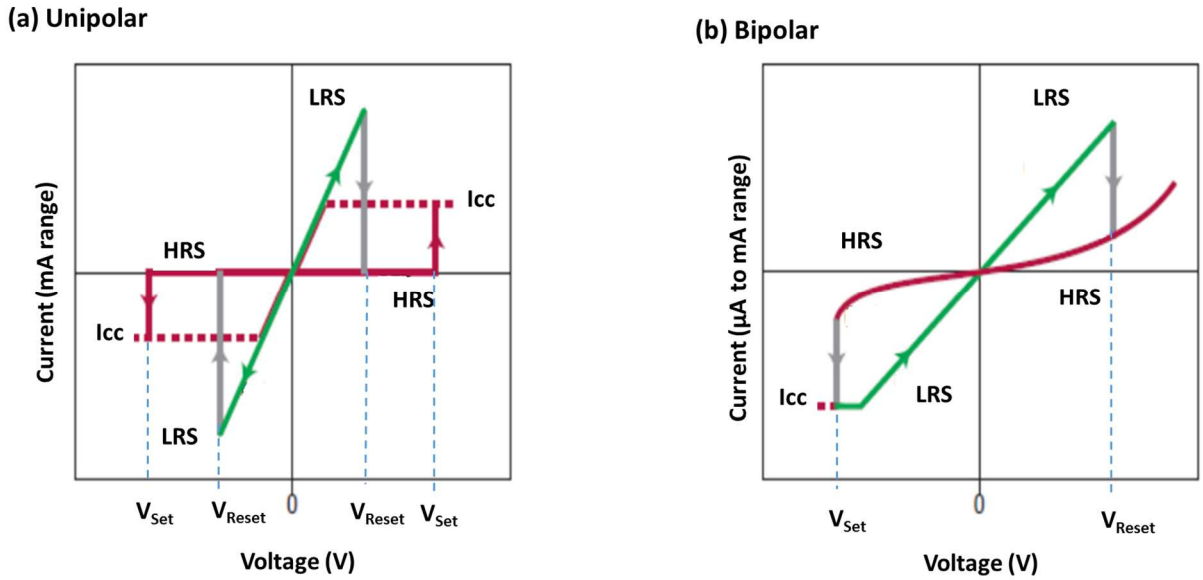

Figure 1.4. (a) Unipolar and (b) bipolar behavior of resistive switching. The red lines represent the system in the high resistance state (HRS) and the green line the low resistance state (LRS). I_{cc} represents the compliance current used to protect the device. Adapted from Waser et al. [28].

The mechanisms of resistive switching can be thermally, chemically or electronically activated. The resistive switching of a RRAM that presents an unipolar behavior is related mainly to thermal effects (joule heating) [29].The reset process in this case occurs by a thermal dissolution of the conducting filaments due to the very high power density (around 10^{12} W/cm^3) in the filament zone[28]. In most of the devices with noble metal electrodes (e.g. Pt) the unipolar behavior is obtained. On the other hand, the resistive switching mechanism for bipolar devices is mainly related to redox reactions and ions migrations [1,30]. This behavior mainly occurs in MIM devices that exhibit asymmetry, i.e. electrodes with different compositions and oxidizable materials. It is important to note that an oxide (insulator layer) may exhibit both unipolar and bipolar behavior. In this case, the change in the resistive switching mode is determined by the top/bottom electrode materials and/or by the compliance current and polarization used during the forming process.

1.2.2.1. Filamentary RRAM- Experimental evidences

Resistive switching via a conducting filament was observed in different RRAM devices using conductive atomic force microscopy (C-AFM) [31,32]. Figure 1.5 shows the electrical measurements done by C-AFM on a Pt/TiO_2 stack[31]. This technique allows the identification of the active regions in the device. The conducting filaments are created locally by applying a potential difference between the conductive tip and the bottom electrode (Figure 1.5 (a)). The I-V curves of the forming, reset and set processes are shown in Figure 1.5 (b). After the forming process, as shown in Figure 1.5 (c), the conductive regions are localized by an increasing current flowing though the structure (bright intensity). In turn, Figure 1.5 (d) shows a decrease of these conductive regions after the reset process. Whereas this study confirms the filamentary nature of

the resistive switching and the nanoscale of the conducting filaments diameter, the chemistry and the formation mechanism of the filaments was not demonstrated.

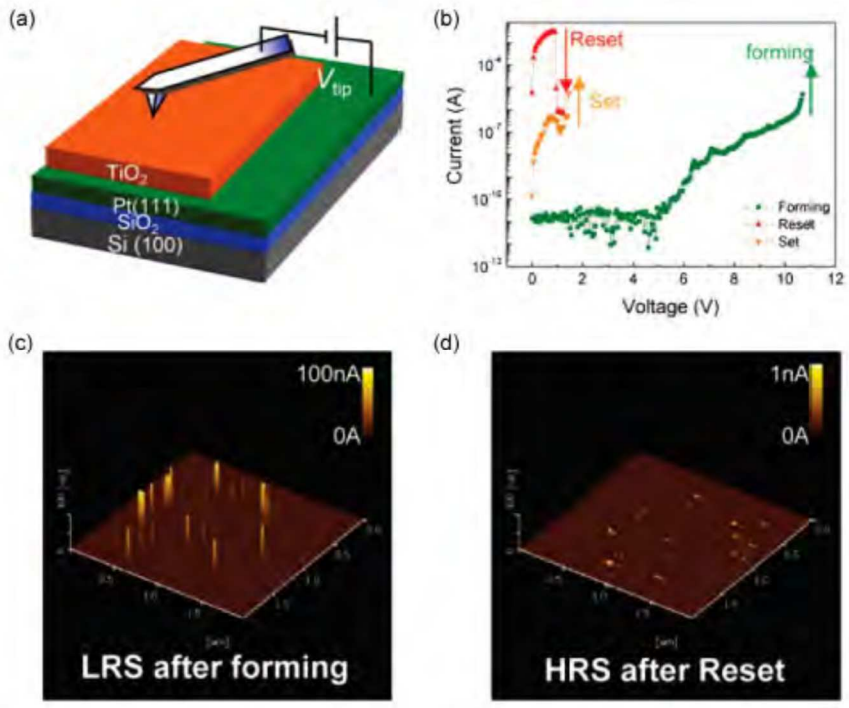

Figure 1.5. (a) Schematic diagram of the C-AFM experimental system, (b) I-V curve of the resistive switching using a AFM tip as top electrode, (c) Mapping of the current flow through the surface after the forming operation shows locally conducting regions, d) after the reset operation these regions disappears. Adapted from Chae et al. [31].

In addition Kwon et al. [33] showed by high resolution transmission electron microscopy (HR-TEM) that a filament for a memory based on TiO_2 has a dimension around 10 nm in diameter as shown in Figure 1.6 . This information is very important to improve the scalability of the memories for future applications. However, it is important to note that the study of the nanofilament using TEM or STEM-EELS is still a challenge as the preparation of a TEM lamella can causes artifacts (mechanical stress, amorphization, Ga implantation) and thereby modify the filament region. In addition, due to the nanometric size of the regions of interest, the localization of the conductive areas is a challenge to prepare the TEM-section.

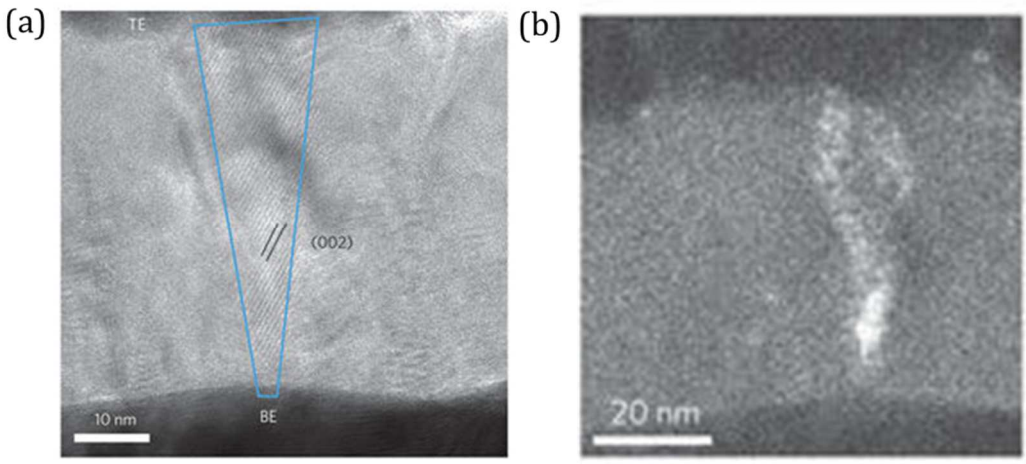

Figure 1.6. (a) HR-TEM image of a Ti_4O_7 nanofilament and (b) a fast Fourier transformed micrograph of the HR-TEM image. Adapted from Kwon et al. [33].

Another evidence of the formation and rupture of conducting filaments during the resistive switching is that the RRAM exhibits LRS resistance independent of the cell-area [28]. This fact was demonstrated by Xu et al.[34] for TiN/ZnO/Pt devices. This study showed the area dependence of the resistance measured in the HRS and LRS as shown in Figure 1.7. R_{LRS} does not vary significantly with an increasing cell area. More variability is observed for R_{HRS}. Nevertheless, these measurements suggest that this device presents a filamentary conducting mechanism.

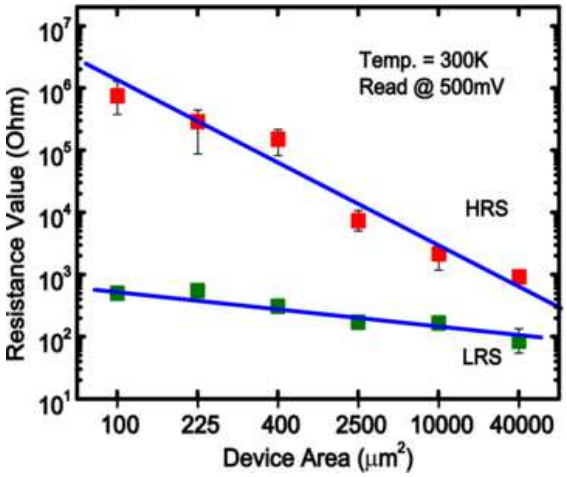

Figure 1.7 Area dependence of the resistance values in HRS and LRS for TiN/ZnO/Pt devices, from Xu et al. [34].

The resistive memory cells can be categorized into two groups, namely Oxide-based Resistive Random Access Memories (OxRRAM) and the Conductive Bridge Random Access memories (CBRAM). A description for both is presented in the next sections.

1.2.3. Oxide- based resistive random access memory (OxRRAM)

In this type of memory, the resistive switching is based on the formation of oxygen vacancies ($V_O^{\bullet\bullet}$) inside the electrolyte layer, as a result of oxygen-ion migration. The electrochemical process is shown schematically in Figure 1.8. During the forming process (soft dielectric breakdown), oxygen ions migrate toward the top electrode/electrolyte interface, driven by the electric field. This migration causes the formation of an interfacial oxide layer and the creation of conducting filaments formed by a collection of oxygen vacancies ($V_O^{\bullet\bullet}$) in the insulator layer, leading the memory to a LRS[1,35].

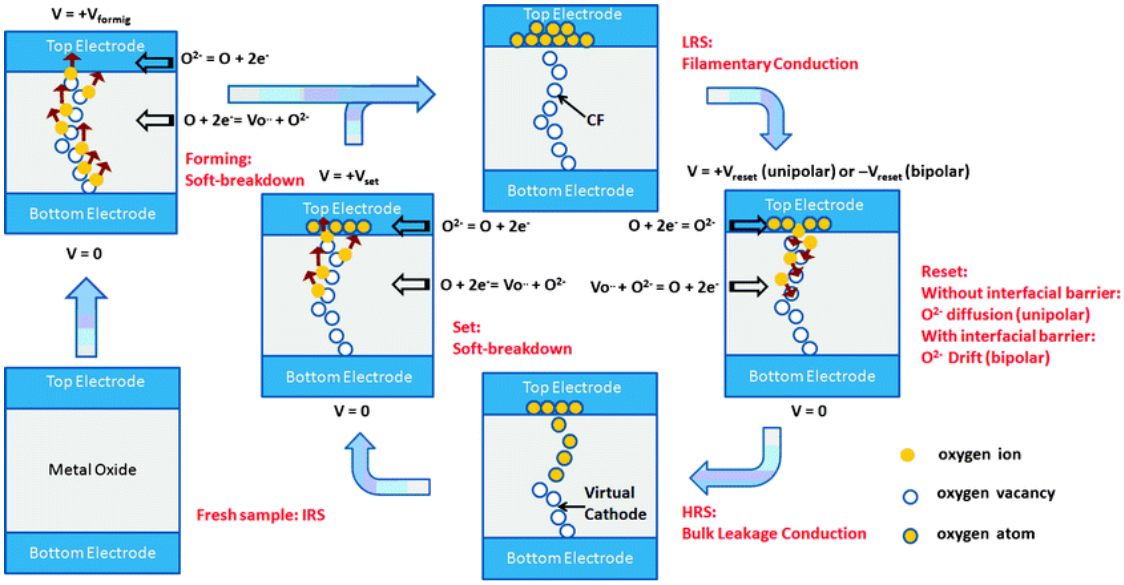

Figure 1.8 Schematic of the resistive switching mechanism for an OxRRAM cell. Adapted from Yu et al. [35].

On the contrary, the reset is characterized by the migration of O^{2-} ions towards the electrolyte. During this process, there is a partial recombination of oxygen ions with $V_O^{\bullet\bullet}$. The reset causes only a partial rupture of the conducting filaments. Therefore, the set process is similar to the forming but the migration of O^{2-} (creation of $V_O^{\bullet\bullet}$) occurs only near the top electrode/electrolyte interface. For a unipolar switching, the Joule heating is responsible for thermally activating the O^{2-} diffusion. In the bipolar switching, the diffusion barrier is the interface between the top electrode and the electrolyte and the ion drift back is driven by the electric field. The OxRRAM presents a M-O-M structure (Metal-Oxide-Metal) based on a transition metal oxide that exhibits resistive switching, a large band gap, CMOS compatibility and good switching performances. High-k metal-oxides such as HfO_x [36], TaO_x [37] and AlO_x [38] have been widely studied due to their good retention , endurance properties and CMOS compatibility. In addition, amorphous materials are preferred in comparison to crystalline oxides. The materials used in top and bottom electrodes also influence the mechanism and performance of the resistive switching. Some examples of materials widely used are: W, Cu, Ti, Ni and Pt. The unipolar behavior is favored in OxRRAMs that use noble metals as electrodes (i.g. Pt). On

the other hand, the devices with oxidizable electrodes (i.g. Ti, TiN) exhibit mainly a bipolar behavior. For example, Zhou et al. [39] showed that a memory with a TaN/CuO_x/Cu structure exhibits a bipolar behavior caused by the formation of TaON at the TaN/CuO_x interface. However, the same structure with a Pt electrode instead of TaN showed an unipolar behavior without oxide formation at the interface. For the unipolar behavior, the reset mechanism is due to a thermal dissolution of the conducting filaments by local Joule heating. During the set there is an accumulation of O^{2-} near the anode. Thereafter, the Joule heating would activate the combination of O^{2-} with the oxygen vacancies causing the conducting filament dissolution i.e. reset process. Whereas for the bipolar behavior, the interfacial layer, in this case TaON act as a barrier to the oxygen diffusion therefore the thermal diffusion mentioned above is not sufficient to cause the conducting filament dissolution. Therefore, in this case, the application of a reversed electric field is necessary to promote the drift back of the oxygen ions and consequently the reset process. The interfacial oxide layer acts as an "oxygen reservoir". During the set this interfacial layer stores the oxygen ions and during the reset process, it drives them back to the oxide.

Figure 1.9 shows a study of the resistive switching of a Pt/TiO_2/Pt OxRRAM using optical microscopy [24]. In Figure 1.9 (a), the image shows the growth of bubbles on the top electrode during the polarization of the cell. After removing the polarization, the bubbles disappear as shown in Figure 1.9 (b). This study brought evidence of a possible oxygen migration from the oxide towards the top electrode during the resistive switching.

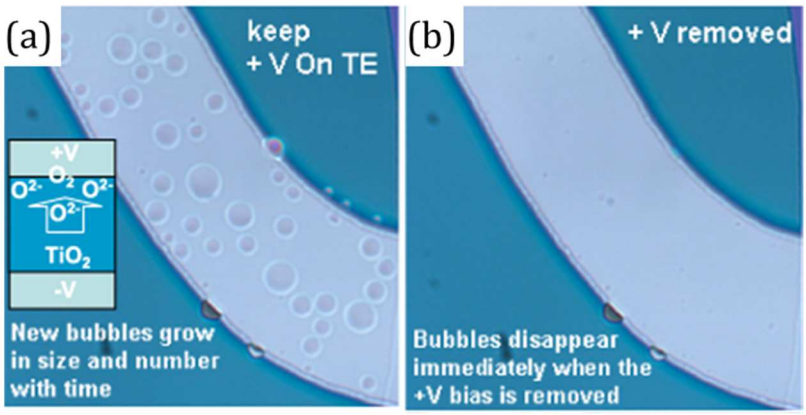

Figure 1.9 (a) Optical microscopy image of a Pt/TiO_2/Pt device during top electrode polarization and (b) after removing the polarization. Adapted from Yang et al. [24].

The creation of oxygen vacancies in the oxide layer changes its electronic structure. For example, the Figure 1.10 shows a computed electronic density of states (DOS) as a function of the valence band edge relative energy of HfO_2 and HfO_x for a TiN/HfO_2/TiN device. The formation of oxygen vacancies in the HfO_2 layer reduces the *effective* band gap by a factor of 6 resulting in a semiconducting-like material [40].

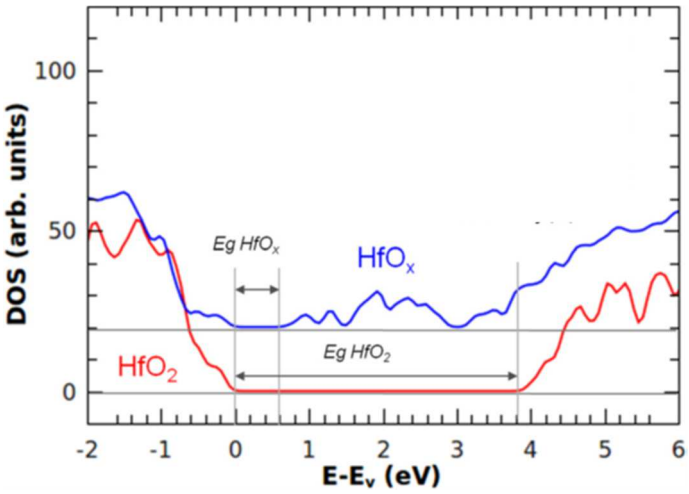

Figure 1.10 DOS of the HfO_x and HfO_2 structures as function of the energy relative to the valence band edge (E_V); Eg (HfO_x, HfO_2) indicates the energy bandgap of the two simulated atomic structures. Adapted from Stefano et al. [40].

The number of conducting filaments in the oxide can depend of the compliance current (I_{cc}) used during the forming process. The variation of the number of conducting filaments and the I_{cc} was studied using 2D kinetic Monte Carlo (KMC) simulation [41] and the results are shown in Figure 1.11.

Figure 1.11 (a) shows the set process using different compliances currents. The comparison between the defect maps for I_{cc} = 100 µA (Figure 1.11 (b)) and for 200 µA (Figure 1.11 (c)) showed that the number of parallel conducting filaments created in the electrolyte layer increases with the I_{cc}. This dependence can be used to increase the number of defects during the resistive switch thus making it easier to analyze the filament chemistry.

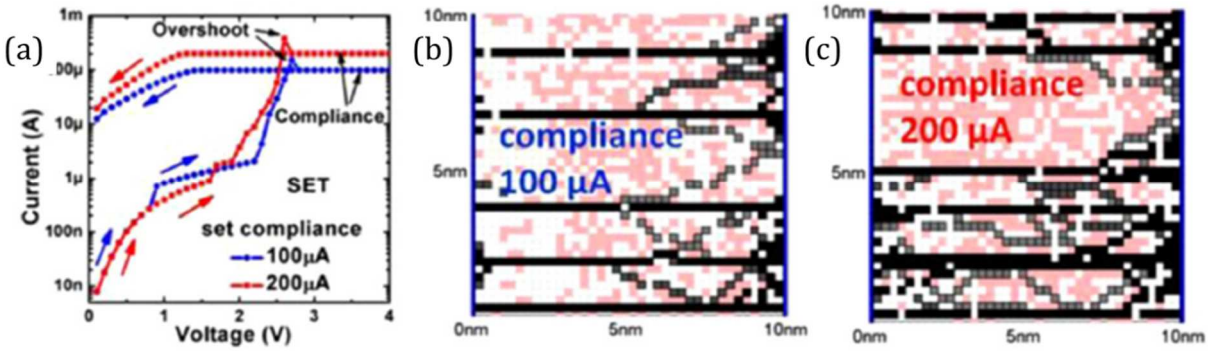

Figure 1.11. KMC modeling of resistive switching (a) I-V curves of the set process at different compliance currents (b), conducting filaments formation between two electrodes using (b) 100 µA and (c) 200 µA. Adapted from Guan et al. [41].

1.2.4. Conductive bridge random access memory (CBRAM)

Among the RRAMs the Conductive bridge random access memory (CBRAM) stands out for its low energy operation and higher resistance window, i.e. the ratio between the high (HRS) and low (LRS) resistance state [4]. CBRAM is a device whereby the changes in resistivity are explained by the metal cation migration inside the electrolyte layer to form a conducting bridge. The cell is a MIM structure based on an active electrode, a dielectric layer and an inert electrode. The active electrode is generally formed by Ag, Cu and Ni, the electrolyte is formed by sulphides, oxides and chalcogenides thin films and the inert bottom electrode is generally made of Pt, W, Ta or TiN [42–47].

The electrochemical process suggested for the resistive switching of this type of memory is shown schematically in Figure 1.12 for an Ag-based CBRAM.[4] By applying a positive voltage to the top active electrode of the device, (B and C) metal cations from the active electrode migrate into the electrolyte. (D) They are reduced when reaching the bottom electrode and the filament is formed by accumulation in the electrolyte. In the same way, (E) by reversing the polarity of the applied voltage, some of the cations return to the active electrode and the filament is partially destroyed. This resistive switching exhibits a bipolar behavior as shown in the I-V curve in Figure 1.12.

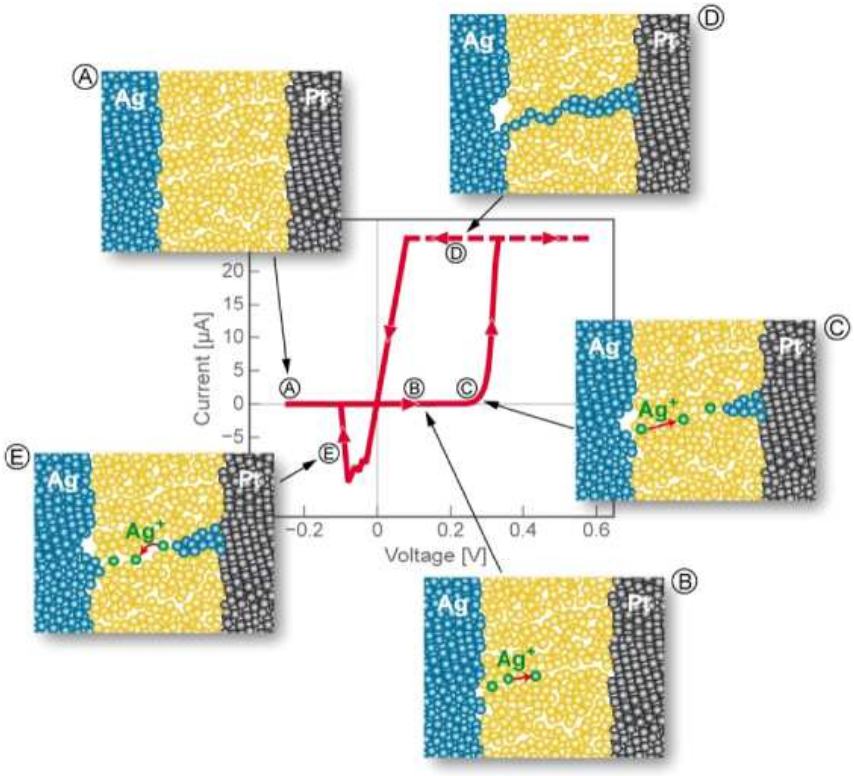

Figure 1.12. Schematic diagram of resistive switching mechanism of an Ag-based CBRAM and the current - voltage (I-V) curve for the forming and reset processes, from Valov et al. [4].

The resistive switching under a positive bias application on the top electrode involves the following chemical reactions [1]:

Anodic dissolution of M:

$$M \rightarrow M^{z+} + ze^{-} \quad 1.1$$

Reduction of the metal cation on the inert electrode surface:

$$M^{z+} + ze^{-} \rightarrow M \quad 1.2$$

In the forming/set process, i.e. during positive polarization of the top active electrode, the oxidation of the metal present in the active electrode occurs at the interface with the insulation layer (step B of the Figure 1.12). After that, as illustrated in the step C, the M^{z+} migrate across the insulator layer. The step D shows the reduction of the metal cations at the bottom electrode interface to form the conducting filament according to reaction 1.2. The low resistance state is attained when the metal filament has grown sufficiently to form a contact with the opposite active electrode.

The reset process, by the application of an opposite polarization, causes a partial rupture of the M filament as illustrated in the step E. By increasing the potential difference beyond a certain value (V_{Reset}), the metal filament will be oxidized again and field induced transport occurs. Note that current - induced Joule heating may also contribute to the filament rupture. Thus, during the reset process, the filament will retract from the active electrode[28,48–51].

1.2.4.1. CBRAM heterostructures

- **Active electrode**

The CBRAM active electrodes are often Ag or Cu alloys. The diffusing element and composition of the film can contribute to the thermal stability as well as the quality of the interface with the electrolyte. In addition, the composition of the Ag or Cu alloys can affects the resistive switching and the filament stability. For example, according to Goux et al. [21] the proportion between Cu and Te (Cu_xTe_{1-x}) has an influence on the formation of Cu filaments. For a CuTe/Al_2O_3-based device the optimal range is $0.5 < x < 0.7$ for improving the stability of the resistive switching and enabling the selflimited filament formation. However, for $x < 0.3$ the results showed an instable filament formation (memory behavior loss), for $0.3 < x < 0.5$ a filament with a low stability (reset at a low voltage) and for $x > 0.7$ a filament too stable with an $I_{Reset} > I_{cc}$. These results

demonstrated that the presence of tellurium in the alloy decreases the stability of the Cu filaments but is important to enable their dissolution i.e. the reset process.

Others adapted active electrode alloys are: CuAg, , CuGe, CuGeTe and AgGe [52]. The use of a semiconductor as diffusing element can improve, for example, the conducting filament stability and decrease the operation currents, as showed by Jameson et al. [8] for an active top electrode of a Te binary alloy such as ZrTe, TiTe and HfTe. The deposition methods used to fabricate the active electrodes are: sputtering, physical vapor deposition (PVD) or chemical vapor deposition (CVD) and thermal evaporation[49].

A protective layer is used to prevent the oxidation of the active electrode. This layer is very important since the oxidation level of the active electrode can affect the resistive switching and influence the endurance and retention time of the memory [14,53].

- **Solid electrolyte**

The solid electrolyte is an insulator with good thermal stability, ionic conductivity and should also be CMOS compatible. Some examples of solid electrolytes are: sulphides (Cu_2S, Cu-doped GeS_2), selenides (Cu-doped GeSe), chalcogenides (GeSbTe) and iodides (AgI, $RbAg_4I_5$). Moreover the oxides and nitrides (e.g. SiO_2, Al_2O_3, Ta_2O_5, WO_3, ZrO_2, $SrTiO_3$, TiO_2, Si_3N_4) stand out for their good CMOS compatibility, retention and endurance properties[52]. The deposition process leads to a significant difference in the electrolyte properties (i.e. ionic conductivity) for the same material. For example, sputtered SiO_2 exhibits a defect-rich structure favoring the resistive switching, whereas atomic layer deposited (ALD) SiO_2 shows higher density and less defects. Therefore, the solid electrolyte and also the deposition method can be used to optimize the resistive switching.

Amorphous Al_2O_3 is an attractive electrolyte for CBRAM cells. This oxide exhibits a high band gap (around 5.1–7.1 eV) [54,55], large breakdown electric field (5 – 10 MV/cm) and thermal stability up to 1273 K [56]. It has been studied as insulator layer in many CBRAM cells configurations[21,57,58] and has been used in this thesis.

- **Bottom (inert) electrode**

The material used for the bottom electrode must be stable and inert, i.e. must not electrochemically dissolve into the electrolyte. In addition, the material has to provide a good adhesion with the electrolyte layer and CMOS compatibility. For this purpose, W, Ru, TiW, Ta and TiN are viable and interesting options for CBRAM cells[52].

1.2.4.2. Experimental evidence of conducting filaments

Hirose and Hirose (1976) [59] first observed the creation and destruction of conducting filaments in the form of dendrites in a planar system where the electrolyte was an amorphous As_2S_3 film photo-doped with Ag. The application of an electric field caused the growth of Ag dendrites on the surface of the electrolyte as shown in Figure 1.13.

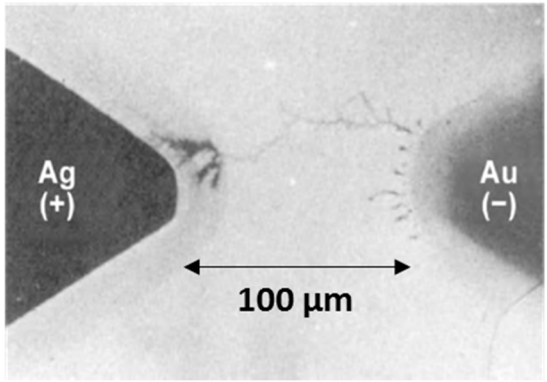

Figure 1.13. Optical microscopy image of the Ag dendrites growth inside of the amorphous As_2S_3 film (planar structure). Adapted from Hirose et al. [59].

It is important to note that the filament formation on planar structures, as shown above, cannot be generalized to bulk devices since the diffusivity of the ions as well as the redox activation energies involved in the filament formation can be very different. In addition, as we can observe in Figure 1.13, this experiment was based on a large planar structure (length of the Ag dendrite = 100µm) while for a real RRAM cell the filament has a nm-length scale. Considering that, recent studies analyze the nanostructure of the conducting filaments, using mainly transmission electron microscopy (TEM). Figure 1.14 (a) and (b) show respectively the scanning TEM (STEM) images of the conducting filaments formation/dissolution for Cu/CuGeTe/Pt [60] and for Ag/ZrO_2/Pt devices [61]. For both samples the conducting filaments exhibit a conical shape. However, the base of the cone is positioned in opposite electrodes, showing different growth directions for these two cases. In the device with CuGeTe as electrolyte, the filament starts to grow from the inert (Pt) toward the active electrode (Cu). This phenomenon occurs because this electrolyte presents a good ionic mobility and low reduction rate. On the opposite, ZrO_2 is an electrolyte that presents a low ionic conductivity and high reduction rate and consequently the filament grows in the opposite direction. Given the low migration speed of the metal cation (Ag^+) in ZrO_2 (low ionic conductivity), they will be reduced back to Ag by the electron flux after migrating a small distance and before reaching the Pt bottom electrode. This process causes an accumulation of Ag atoms at the Ag electrode/ZrO_2 interface as shown in Figure 1.14 (c). This comparison showed a good example of how the solid electrolyte can influence on the characteristics of the conducting filaments (shape, size and growth direction)[52].

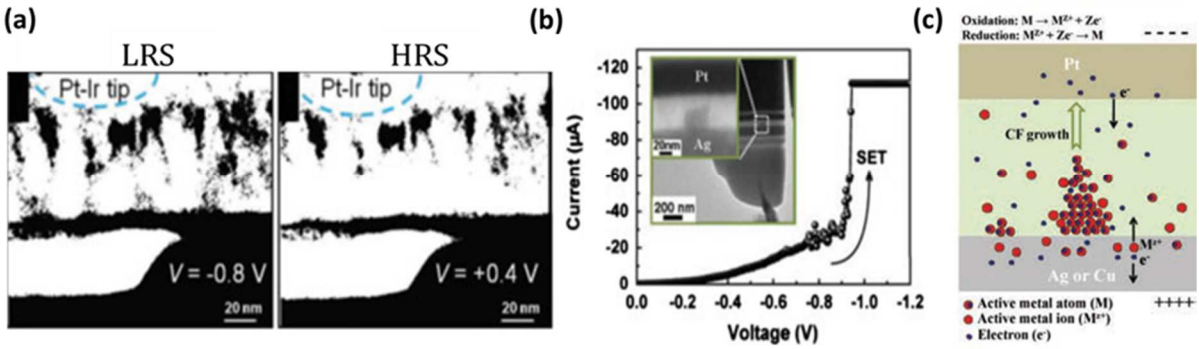

Figure 1.14. (a) STEM images of the conducting filaments formation in CuGeTe electrolyte for LRS and HRS. Adapted from Choi et al. [60] (b) Cross-section TEM image of the Ag/ZrO_2/Pt device after electrical stress application (c) Schematic of the conductive filament growth mechanism. Adapted from Liu et al. [61].

The filament composition, chemistry and morphology investigation can be made by several different techniques such as: tomographic atomic force microscopy (T-AFM) [62] , X-ray photoelectron spectroscopy (XPS) [63,64], scanning tunneling microscopy (STM)[65] etc. AFM and STM have high lateral resolution and enable morphological and electrical characterization of the CBRAMs while XPS depth profiling and Hard X-ray photoelectron spectroscopy (HAXPES) give depth sensitive chemical information about cation diffusion and oxidation-reduction (redox) reactions produced during the resistive switching.

1.2.4.3. Role of the oxygen vacancies

Cation migration inside an oxide layer might be helped oxygen vacancies, as suggested by several studies [61–65]. These works showed that the creation of oxygen vacancies decreases the energy cost to insert cations inside an oxide under bias application. According to Yamamoto et al. [66], cation migration can be enhanced by introducing cation vacancies. When the migrating cation is surrounded by others cations, it generates strong coulomb repulsive interactions hindering the diffusion. On the other hand, in the presence of cations vacancies, this cation can shift to the open space decreasing the repulsive interactions and consequently decreasing the cation energy migration. However, the diffusion mechanism of cations through cationic or interstitial sites is still unclear.

Several studies suggest a hybrid mechanism, i.e. a combination of both CBRAM (ions diffusion) and OxRRAM ($V_O^{\bullet\bullet}$ formation by O^{2-} transport) mechanisms to form the filament [51,67,68]. For example, according to Saadi et al.[51], the resistance transition can be divided in two stages. The first is the creation of oxygen vacancies and the second is the migration of the ions along $V_O^{\bullet\bullet}$ paths. The positive bias application causes migration of O^{2-} towards active electrode and an accumulation of oxygen vacancies next to the bottom electrode. However the creation of oxygen vacancies across the entire oxide layer cannot be exclude.

According to Jeon et al., in Cu/TaO_x/TiN devices, the resistive switching mechanism is based on the formation of $V_O^{\bullet\bullet}$ /Cu conducting filaments [69]. As shown in Figure 1.15 (a), the pristine cell has already Cu ions and $V_O^{\bullet\bullet}$ inside the TaO_x layer. During the positive polarization (Figure 1.15 (b)), the Cu ions migrate towards the bottom electrode and are reduced to Cu metal. The $V_O^{\bullet\bullet}$ conducting filaments are formed in the gap between the active electrode and the electrolyte. This resistive switching mechanism based on conducting filaments composed of not only metallic Cu but also $V_O^{\bullet\bullet}$ (created by the O^{2-} migration under bias application) may explain why this device has a gradual set in comparison to conventional CBRAMs presenting an abrupt set.

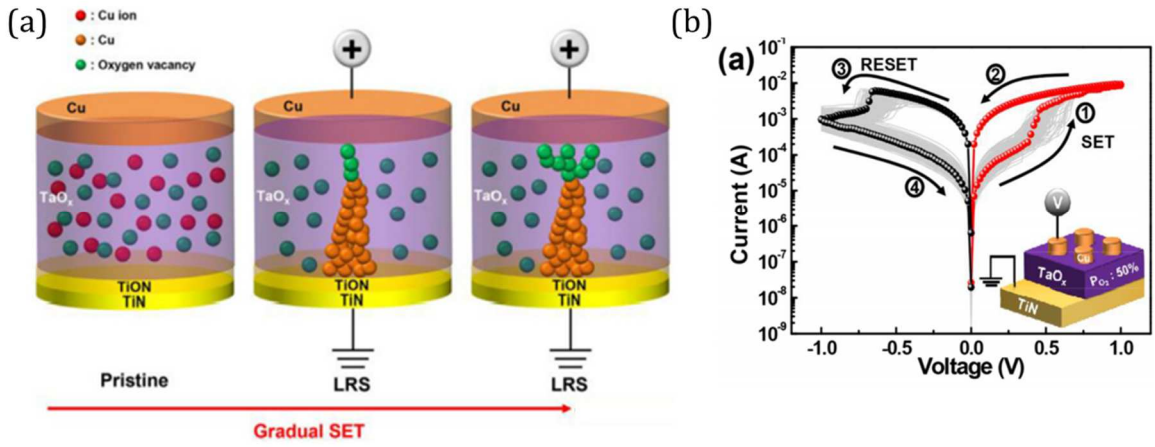

Figure 1.15. Proposed resistive switching mechanism with combined $V_O^{\bullet\bullet}$ /Cu conducting filaments formation in the Cu/TaO_x/TiN device. Adapted from Jeon et al. [69].

Chung et al. [68] showed for a Ag/TaO_x/Pt device that the resistive switching mechanism of a CBRAM depends on the temperature operation and on the defects in the insulating oxide electrolyte. For a resistive switching at 100K, the conducting filaments proved to be a combination of metal atoms and oxygen vacancies as shown in Figure 1.16 (b). However, the resistive switching at 300 K showed a standard CBRAM behavior i.e. a filament formed by Ag atoms as shown in Figure 1.16 (c). This variation of the resistive switching behavior can be explained by the larger activation energy of Ag diffusion (E_a = 1.19 eV) in TaO_x compared to O^{2-} (E_a = 0.91 eV). The diffusivity of O^{2-} may be equal or greater than Ag at 100K thus enabling the formation of a conducting filaments by a combination of Ag and $V_O^{\bullet\bullet}$.

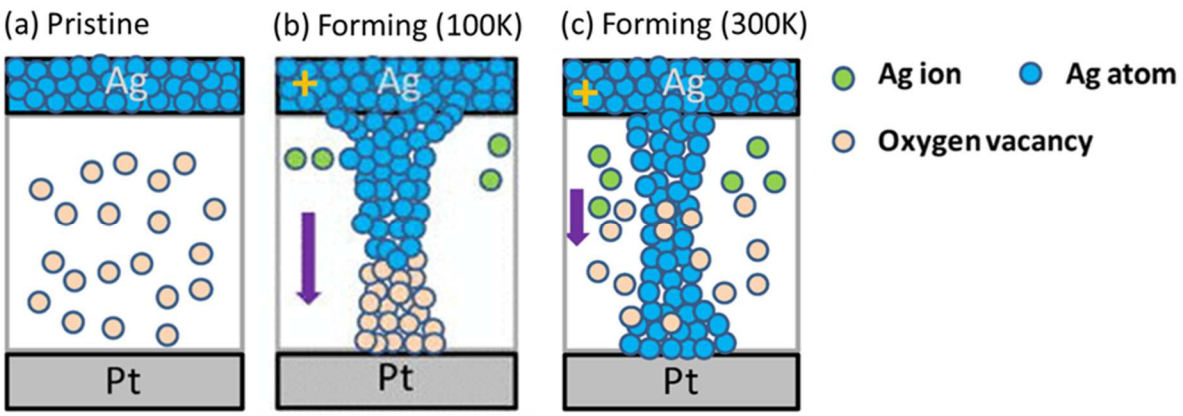

Figure 1.16 Schematic illustration of (a) Pristine device (b) forming operation at 100 K and (c) at 300 K. Adapted from Chung et al. [68].

Reverse forming ,i.e. a forming using negative polarization, was observed in several standard Cu-based CBRAMs structures [70,71] and also reported to be related to metal cations and/or oxygen vacancies ($V_O^{\bullet\bullet}$). Compared to positive forming, the bottom electrode may also play a role together with the active electrode.

Reverse forming can be used also to improve the resistive switching of the CBRAMs. According to Molas et al.[67], for a Cu-based cell a negative pre-forming induces oxygen vacancies in the oxide (OxRRAM behavior) as shown in Figure 1.17 (a). During the subsequent direct forming (i.e. at positive polarization), the presence of oxygen vacancies facilitate the injection of Cu ions and the formation of the conducting filaments inside the electrolyte. Figure 1.17 (b) shows that the pre-forming reduces the forming voltage of the direct forming, thus indicating that this step can optimize the resistive switching in CBRAMs. According to this work, the pre-forming leads to an intermediate HRS (with a lower resistance in comparison to the pristine cell) thus decreasing the energy cost to insert Cu cations during the subsequent positive forming. However, as discussed before, the reason why cationic sites improves the cation migration is still an open question.

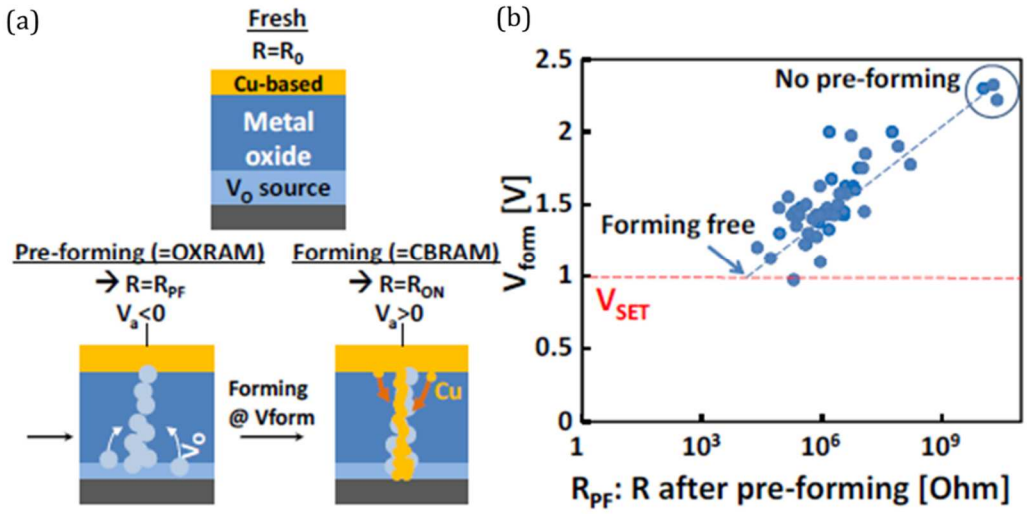

Figure 1.17 Schematic illustration of a reverse and direct forming (b) V_F as a function of the cell resistance after reverse forming operation. Adapted from Molas et al.[67].

Hybrid RRAMs are interesting because they combine the advantages of CBRAM and OxRRAM memories. The CBRAMs structures are characterized by higher resistance windows, i.e. higher resistance ratios between the high (HRS) and low (LRS) resistance state, compared to OxRRAM, and by lower programming currents [68]. In turn the OxRRAM has a high thermal stability and good cycling.

1.2.4.4. Impact of the oxygen from air on the CBRAM resistive switching

As showed before, the mechanism of a CBRAM can be a combination of cations and oxygen diffusion. Therefore, we cannot rule out a possible impact of the environment, typically ambient air, on the resistive switching mechanism of CBRAMs. Indeed, this environment provides an additional oxygen reservoir which might influence the internal oxygen scavenging processes and oxygen vacancies formation in the oxide layer. As a consequence, oxygen movements and corresponding oxidation/reduction processes might be modified. This has already been mentioned in the literature for standard OxRRAMs [12-14].

D. S. Jeon et al. [12] have reported that the external oxygen from air can be incorporated in the top electrode under positive bias application, causing chemical oxidation at the interface with the oxide layer and consequently retarding the accumulation of oxygen vacancies responsible of the resistive switching. This study was performed by the comparison between forming under ambient air and forming in a vacuum chamber, using C-AFM and ToF-SIMs to characterize the sample. L. Goux et al. [14] showed that the thickness of the top electrode and the operating environment have strong influence on the resistive switching and on the stability of the device. In addition, Ding et al.[13] showed that under positive polarization in vacuum

conditions, some oxygen outgases into the ambient air increasing the oxygen vacancies concentration in the oxide and also at the top electrode/ oxide interface, resulting in a V_{set} decrease. This analysis shows that, under vacuum, the oxygen scavenging at the top interface is enhanced, facilitating the forming process.

Knowing that a CBRAM can presents a hybrid mechanism, a similar study to that shown for the OXRRAMs may be interesting to understand the role of the oxygen on the resistive switching.

1.2.5. Subquantum CBRAM

This thesis addresses the study of subquantum CBRAMs. These cells contain an elemental semiconductor such as Te in the active electrode and operate with reduced currents and less retention failures of the LRS. Instead of using a filament containing a metal (Ag, Cu), these new memory cells are based on the diffusion of Te in the electrolyte. The current required to program a standard CBRAM cell is directly related to the conductance of a 1-atom filament (G_{1atom}). For metals, G_{1atom} is comparable to the quantum $G_0=2e^2/h$, whereas for a semiconductor such as Te, it is sub-quantum (0.03 G_0) enabling operation at low currents as showed in Figure 1.18 (a) [8] and therefore low power while avoiding breakdown, providing also higher endurance.

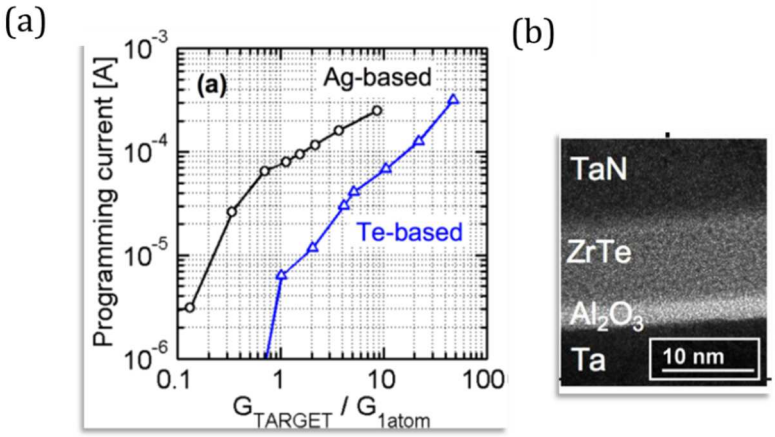

Figure 1.18. (a) Comparison between the median programming current of the subquantum Te-based CBRAM cells and of the Ag-based cells for target conductance ranging from 10 G_{1atom} to 1G_{1atom}. , (b) Cross sectional TEM of the subquantum cells. Adapted from Jameson et al. [8].

Jameson et al. [8] suggested that a possible resistive switching mechanism for a ZrTe/Al_2O_3-based device (Figure 1.18 (b) is the release of Te (semiconductor) induced by Zr oxidation as oxygen is scavenged from the Al_2O_3 under the electric field. The proposed mechanism for Zr oxidation and Te release at the interface is described by:

$$ZrTe_x + O_2 \rightarrow ZrO_2 + xTe \qquad 1.3$$

These cells must contain a Te-based alloy thermally stable as active electrode and an amorphous oxide as switching layer to provide the oxygen required for the replacement reaction 1.3.

The $TiTe_x$ alloy is an interesting alternative for the active electrode of subquantum CBRAMs as it features a retention behavior controlled by a similar critical conductance as that for ZrTe. Considering this fact, a comparison between a cell with ZrTe and a cell with TiTe as active electrode is important to understand the impact of the alloy composition on the resistive switching mechanism. The study of different active electrodes can help the optimization of these devices. It is important to note that not all binary alloys of Te favor the formation of a filament containing a semiconductor, i.e. exhibits a subquantum CBRAM behavior. For example in the case of the $CuTe_x$ based memory, the filament is formed preferably by Cu not by Te[48].

Table 1.2 shows a comparison of power and performance for flash, metal-based CBRAM (prototypal cell) and subquantum CBRAM. The features of subquantum CBRAM compared to flash are: voltage operation 3 V lower, program energy 100 times lower, read voltage 2 V lower and speed operation 10 times faster. Compared to metal-based CBRAM the subquantum CBRAMs present operating current and power as low as 10 µA/cell and 0.01 mW/cell (10 times lower compared to the metal-based CBRAM).

Table 1.2. Comparison of power and performance parameters for flash, standard metal-based CBRAM (Prototypal cell) and subquantum CBRAM cells. Adapted from [72]

	G_{1atom}	Read Voltage (V)	Program voltage (V)	Current (µA/cell)	Program Time (µs/cell)	Power (mW/cell)	Program Energy (pJ/cell)
Floating gate flash	…	3-5	6-9	100-300	1-10	0.5	1000
Metal-based CBRAM Prototypal (Ag/Cu-based)	$\sim 1G_0$	1	1-3	100-1000	0.01-0.1	0.1-1	1-100
Te-based subquantum CBRAM	$0.03\ G_0$	1	1-3	10-100	0.01-0.1	0.01-0.1	0.1-10

For low-power applications as Internet of Things (IoT) the ability of the subquantum CBRAM cells to work at low voltage (around 3 V) in comparison to flash (around 9 V) is particularly interesting. For embedded NVMs the program time 10 times lower than flash improves operating efficiency for these systems [72].

1.3. Conclusion and Challenges

Taking into account the promising advantages of this new type of Te-based CBRAM, the focus of this work is bringing answers about the resistive switching mechanism for $ZrTe/Al_2O_3$ and $TiTe/Al_2O_3$- based cells.

The assumptions of Jameson et al. showed electrical evidence of a Te filament formation during the resistive switching, but the Te migration to form the filament has never been directly demonstrated. Studying the resistive state-dependent chemistry in these Te-based CBRAMs requires advanced characterization techniques as characterizing RRAMs is challenging because of the small amount of net change due to the filament formation. Moreover, the changes most likely occur in a thin layer buried under a thicker top electrode. This requires non-destructive characterization methods able to probe through thick capping layers with high sensitivity. We have used hard X-ray photoelectron spectroscopy (HAXPES) to probe the buried interface between the active electrode and the Al_2O_3 layer. This technique enables non-destructive analysis of the buried interfaces between realistic electrodes and insulating layer thanks to the much greater probing depth [10]. The high sensitivity of this technique is also crucial to analyse the small changes that occur during resistive switching. This technique has already been successfully used to investigate the redox reactions that occurs during the resistive switching of oxide-based resistive memories and CBRAMs.

The CBRAM resistive switching mechanism is complex. A CBRAM cell can present a hybrid mechanism, i.e. a combination of both CBRAM (ions diffusion) and OxRRAM ($V_O^{\bullet\bullet}$ formation by oxygen transport) mechanisms to form the filament. It is therefore necessary to investigate the depth distribution of Te and O during the resistive switching. For that, depth profiling measurements (XPS and ToF-SIMS) have been carried out.

In addition, the ambient air may also influence the resistive switching behavior of the CBRAMs cells as shown in section 1.2.4.4. *In-situ* experiments (under vacuum) must therefore be compared to *ex-situ* (under air exposure) to analyse the impact of the oxygen from air on the resistive switching.

.

Chapter 2

2. Methods and techniques

The first part of this chapter describes the sample preparation: growth method, lithography and circuitry for the *ex-situ* and *in-situ* studies of the cells. The second part presents the main experimental techniques that have been implemented in this thesis work to characterize the samples.

2.1. Sample design and preparation

The sample development of this work was a collaboration. All of the samples described below were entirely fabricated and optimized by the Department of Deposits (SDEP).

2.1.1. Stack geometry

The CBRAM cells are a metal/insulator/metal (MIM) structure where an electrolyte is inserted between two metallic electrodes: the bottom electrode (BE) and the top electrode (TE). This active top electrode is covered by a protective layer to avoid oxidation under air exposure. As described in chapter 1 the active top electrode is the ion source to the conductive filament formation and must be protected since the oxidation level of this electrode can change the resistive switching mechanism. Two systems mentioned by Jameson et al. [8] as the most promising, were investigated: ZrTe/Al_2O_3 and TiTe/Al_2O_3-based devices.

Figure 2.1 shows an illustration of the stacks analyzed and Table 2.1 shows a description of each different sample composition used in this work. The round sample were used for *ex-situ* analyses and the squares samples were used to facilitate the electrical contact on the top electrode for *in-situ* analyses (see section 2.2.2.).

A sample with 2mm of diameter was used in this work to facilitate the XPS and ToF-SIMS measurements and to avoid a possible influence of the oxidation at the edges. The thicknesses of the top electrode and protective layer are also thinnest at the edges, due to the deposition process through a specific mask. A relatively large sample enables selecting the center of the sample as area of analysis thus discarding these edges effects.

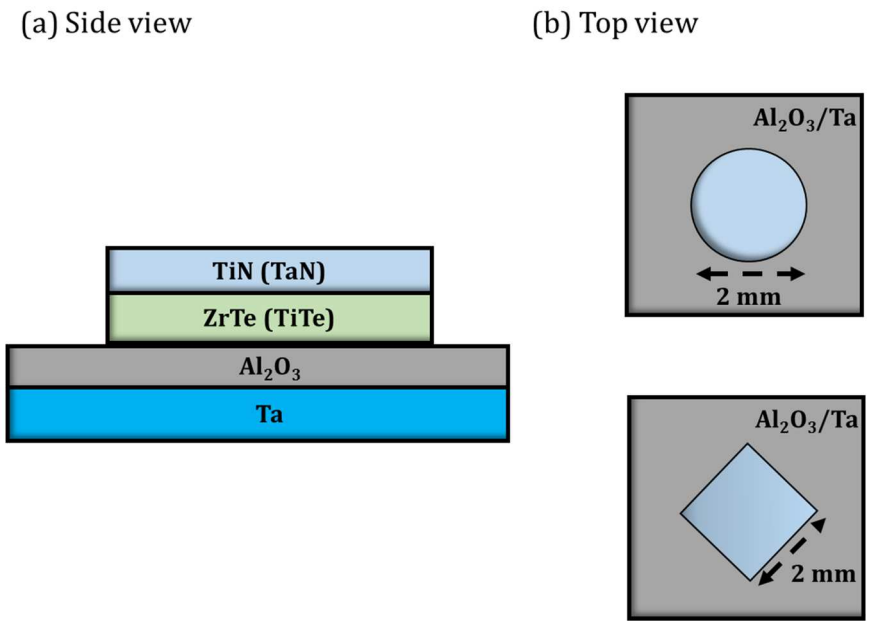

Figure 2.1. Illustration of the stacks analyzed in this work (a) side view and (b) top view (round and square samples).

Table 2.1. Sample composition for each sample analyzed in this work

Protective layer (5 nm)	Active electrode	Electrolyte (5 nm)	Bottom electrode (200 nm)
TaN	ZrTe (15 nm)	Al_2O_3	Ta
	ZrTe (5 nm)		
	TiTe (5 nm)		
TiN (15 nm)	ZrTe (10 nm)		

2.1.2. Deposition method – PVD

The technique used to grow the layers of the memory cells was the physical vapor deposition (PVD). Its principle is based on the formation of an atom vapor produced from a solid source (metal, metal oxide or even polymer) in a vacuum chamber. This vapor is transported to the surface of the substrate to be coated, where it condenses [73]. In this thesis two PVD processes were used: sputtering/co-sputtering and reactive sputtering.

2.1.2.1. Sputtering

This technique is widely used to deposit semiconductor materials as coatings on metallic, ceramic or polymeric substrates. Energetic plasma particles bombard the surface of a solid target with enough energy to eject one or more atoms. The ejected atoms are directed towards the substrate by an electric field, where

they reorganize. The process occurs within a chamber in controlled atmosphere, in order to ensure quality and reduce impurities. The energetic particles that induce the sputtering are inert gas ions (such as Ar^+) accelerated by the difference between the plasma potential and the cathode (target) potential as shown in Figure 2.2.

In this technique, it is possible to use both metals and insulators as targets. However, sputtering using a DC source is possible only for targets consisting of conductive materials. In the targets with low conductivity, there is an accumulation of positive charges on the surface (due to gas ions), increasing its potential and repelling further Ar^+ leading to the extinction of the discharge. For this reason, to induce plasma formation on an insulating target, an alternating voltage source with frequency of the order of MHz is used (RF sputtering)[73,74].

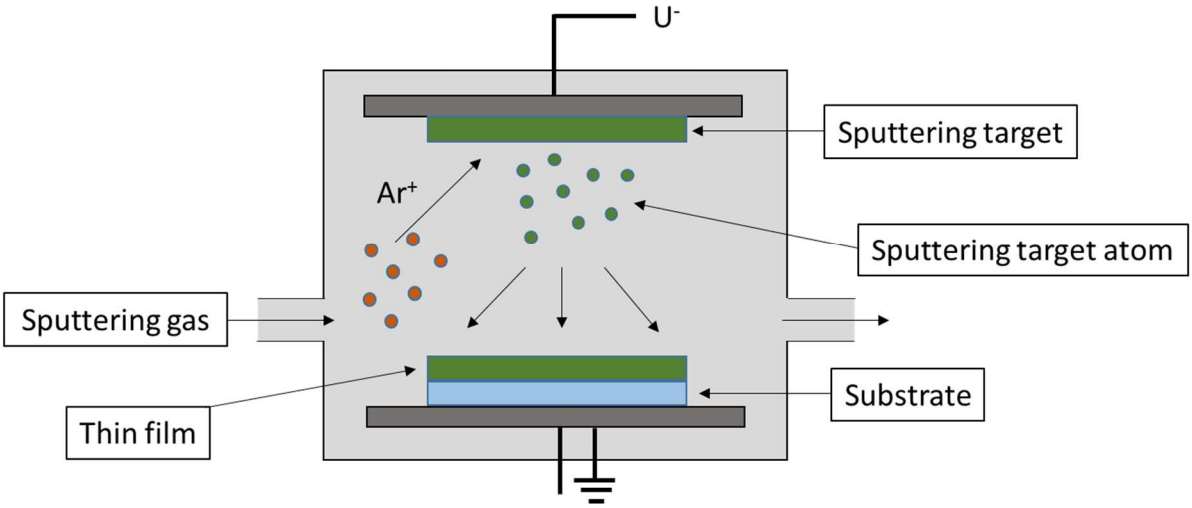

Figure 2.2. Illustration of a sputtering PVD process.

2.1.2.2. Reactive sputtering

The reactive sputtering process can be used to obtain thin films of simple elements, alloys or compounds. Thin films are deposited on the substrate by sputtering the atoms from the target in the presence of a reactive gas (e.g. N_2, O_2), usually mixed with the inert gas[74]. The stream of sputtered particles passes through and reacts with the reactive gas: the product formed by the chemical reaction is thus directed by the electrical field towards the substrate where it condenses. This process is usually used to deposit oxide films (e.g. Al_2O_3, SiO_2) among others. For this, in addition to argon, O_2 or N_2 is injected into the chamber with a certain flow. This gas becomes reactive in the presence of plasma discharges due to collisions with energetic particles and subsequently dissociates into neutral or charged atomic components. The stoichiometry of the sample is established as a function of the flow [73].

2.1.3. Sample fabrication

Figure 2.3 shows the fabrication process of the memory cells on a Si wafer using a shadow mask technique. After the step 1, illustrating the deposition of the electrolyte and bottom electrode, the step 2 shows the fixing of the mask. In the step 3, the active electrode ZrTe or TiTe and protective layer (TiN or TaN) are deposited. The step 4 exhibits the finished sample after the mask removal. The mask was a 100mm-silicon wafer, and the holes (round and square) are drilled by laser with diameters of 1 mm and 2mm. The equipment used for sputtering deposition is an EVATEC/OERLIKON Clusterline 200, which is an industrial equipment with five deposition chambers, thus enabling the deposition of several layers without air break. The methods and parameters used for the deposition of each layer are described in Table 2.2.

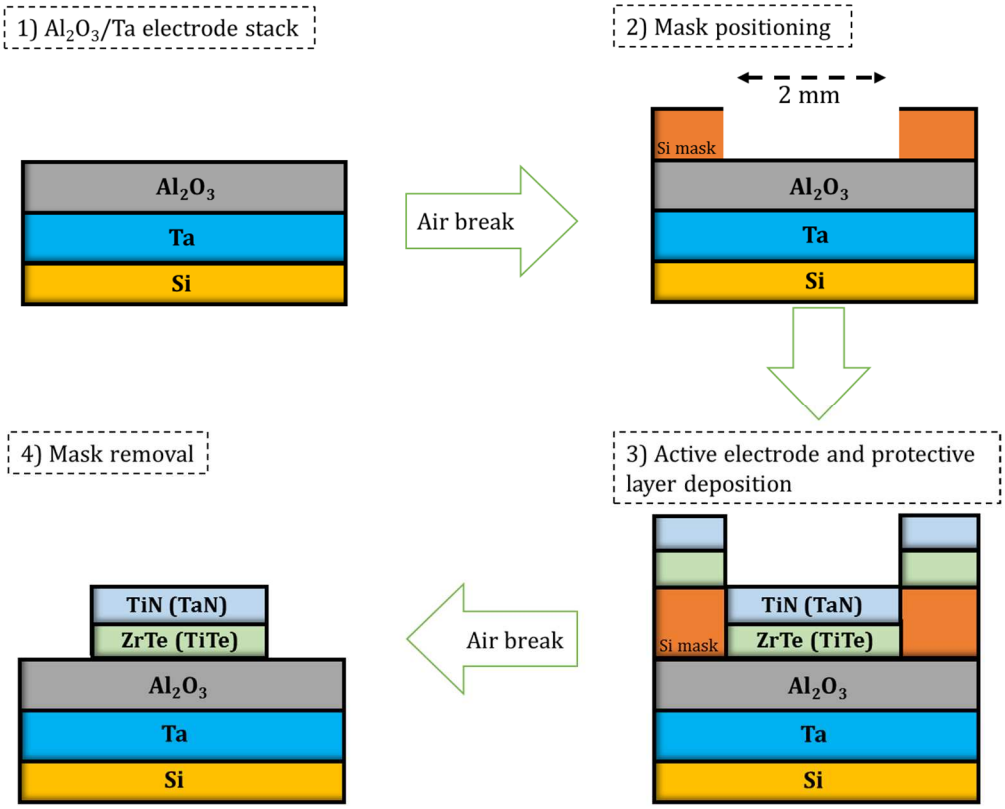

Figure 2.3.Deposition process of the CBRAM cells.

All parameters and methods applied for the deposition of the layers used in this work were defined by the Department of Deposits (SDEP). The deposition of the active electrodes used a co-sputtering method that consists in sputtering two targets at the same time to form the alloy. In this case a target of Zr or Ti and a target of Te were used. The power density was adjusted to obtain the desired stoichiometry of 60% Te and 40% Zr (Ti). The parameters used for TiN, TaN, Ta and Al_2O_3 were based on reference tables provided by the EVATEC/OERLIKON Clusterline 200 manufacturer.

Table 2.2. Description of the methods and parameters used for the deposition of each layer.

	Material	Deposition parameters
Protective layer	TiN	• Reactive sputtering of a titanium target, with a power density of 0.7W/cm^2, an Ar flow of 25sccm and a N_2 flow of 35sccm
	TaN	• Reactive sputtering of a tantalum target, with a power density of 5.7W/cm^2, an Ar flow of 40sccm and a N_2 flow of 16sccm.
Active electrode	ZrTe	• Co-sputtering of Zr (Ti) and Te targets using an Ar flow of 40sccm and a power density of 0.5- 0.7 W/ cm^2 and 0.8-1 W/ cm^2 for tellurium and zirconium (titanium) respectively.
	TiTe	
Electrolyte	Al_2O_3	• RF sputtering of an Al_2O_3 target with an Ar flow of 40sccm and a power density of 2.5W/ cm^2
Bottom electrode	Ta	• Sputtering of a tantalum target with a power density of 0.7W/cm^2, an Ar flow of 25sccm.

2.2. Electrical characterization

2.2.1. Ex-situ electrical characterization

The resistive switching was performed in ambient atmosphere using a Keithley 2635B and the Ta bottom electrode was grounded. A linear voltage sweep was applied by an Au wire with minimum contact force on the top electrode as shown in Figure 2.4. A standard electrical connection was not used for the top electrode due to the ultra-thin alumina layer which can be easily short-circuited by mechanical or thermal stress. The electrical contact to the bottom electrode was made with a W tip.

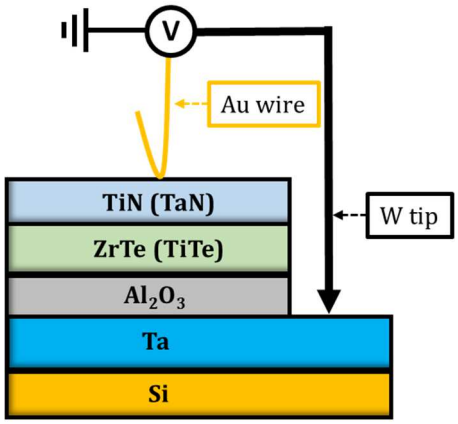

Figure 2.4. Schematic of the setup for electrical characterization of CBRAMs cells.

For the forming and reset processes, the voltage was applied step by step from 0 V until a maximum voltage V_{max} and the current was measured at each step using 0.1 V/s. The compliance current was chosen

low enough to avoid permanent breakdown of the oxide but sufficiently high to induce significant ionic diffusion, facilitating the detection of the defects by XPS and ToF-SIMS analyses. The specific value of this parameter was determined choosing the largest possible compliance current that allowed resetting the sample, i.e. a reversible resistive switching.

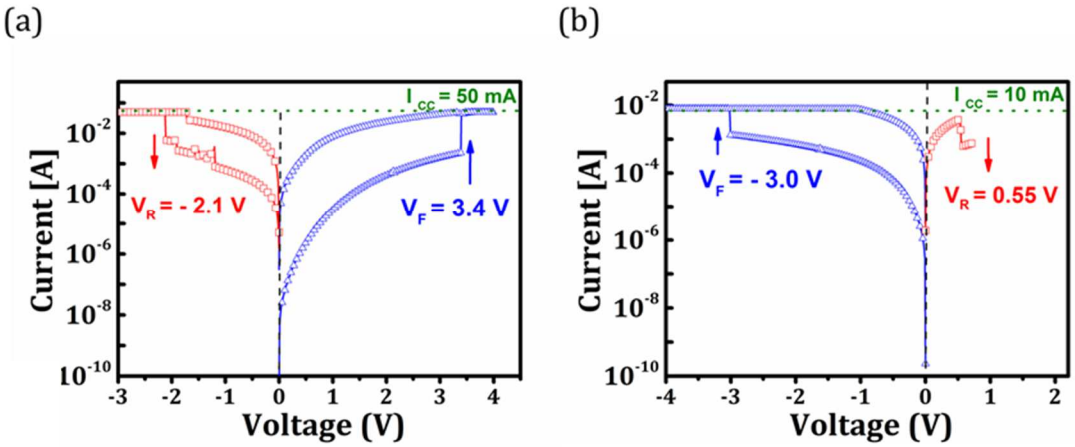

Figure 2.5. Current - voltage (I-V) curve for the (a) direct forming and reset (under negative polarization) and (b) indirect forming and reset (under positive polarization).

Figure 2.5 (a) shows a current-voltage curve characteristic of the resistive memories for the direct forming (i.e under positive polarization) and reset step (i.e. under negative polarization). A reverse forming (i.e. under negative polarization) and a reset under positive polarization were also performed, as shown in Figure 2.5 (b). For the read of the cell resistance state, a ramp was performed from 0 mV to 50 mV, to prevent changes in the structure. The current-voltage curve obtained for the reading is linear as it corresponds to the Ohm's law as shown in Figure 2.6.

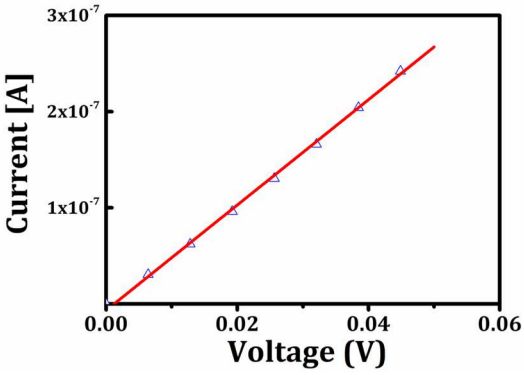

Figure 2.6. Current-voltage curve obtained for the reading of the TaN/ZrTe/Al_2O_3/Ta stack.

The geometry of the samples and the setup used for the electrical characterization make memory cycling less stable in comparison to integrated memories for which the devices are smaller. This instability

can be induced by a possible lateral oxidation of the sample or by not automated electrical measurements which implies a lack of precision.

2.2.2. *In-situ* electrical characterization

We have developed the measurement protocol (mounting and electrical contacts) which allows the electric field to be directly applied to the sample used for XPS, i. e. directly under ultra-vacuum. To achieve the change in resistance *in-situ*, we have developed a way to electrically connect this stack in the ultra-vacuum chamber of the equipment used for the XPS analyses (VersaProbe II). Pictures of the assembly used for *in-situ* switching are presented in Figure 2.7(a) and (b).

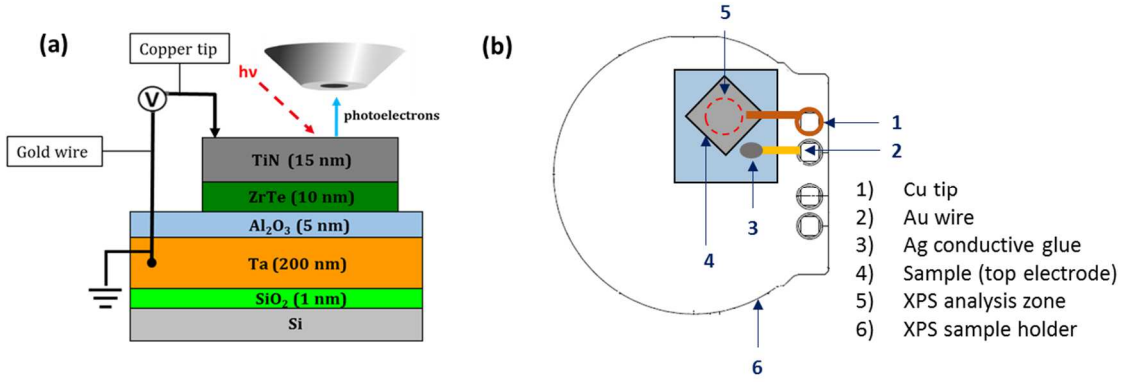

Figure 2.7 . (a) Schematic of the setup for in-situ electrical switching and characterization and (b) Assembly on the XPS sample holder.

The sample is mounted on a specific sample holder adapted for analyses with *in-situ* electrical polarization. This support has contacts located on the side where we can connect conductive wires. These contacts are isolated from the central body of the support by two ceramics. Once this holder is placed in the analysis chamber, it is linked to a connector located on the main frame of the equipment, where a voltage generator can be plugged.

The sample is fixed on the holder via an isolating scotch (ultra-vacuum compatible). The electrical contacts were done locally by approaching the top electrode surface with a copper tip with minimum contact force, the tantalum bottom electrode was grounded and connected with a gold wire using a silver conductive glue as shown in Figure 2.7 (b).

2.3. X-ray photoelectron spectroscopy – XPS

X-ray photoelectron spectroscopy is an important experimental method for the study of the chemical properties and electronic structure of molecules, solids and surfaces. XPS enables the identification of the elemental and chemical composition of the sample through the core levels analysis.

2.3.1. Theory

X-Ray Photoelectron Spectroscopy (XPS) is a surface analysis technique, based upon the photoelectric effect [75,76]. When a material is irradiated with a monochromatic electromagnetic X-ray wave with energy hυ, electrons are ejected with a kinetic energy (Ek) toward the analyzer. This principle is illustrated in Figure 2.8. The energy conservation law (equation 2.1), relates the kinetic energy of the photoemitted electron to its binding energy (BE) and the x-ray photon energy.

$$E_k = h\upsilon - |E_B| \qquad 2.1$$

Where: E_k: kinetic energy of the photoelectron (eV); hυ: photon energy; E_B: binding energy (eV). The electrons are ejected only if their binding energy (E_B) is less than the energy of the incident photons.

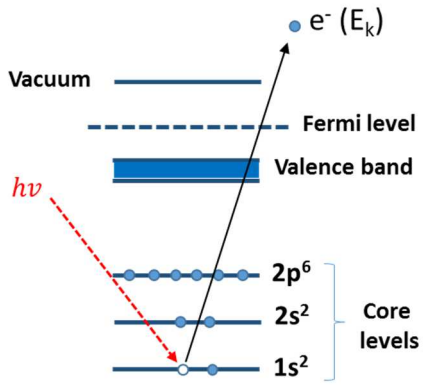

Figure 2.8. Scheme of the issuance of the photoelectric process.

2.3.1.1. Three step model

The photoemission process can be divided into three steps, described in a model known as *three step model* [77]. As shown in Figure 2.9 in the first step, the interaction of the photon with the atom, provides enough energy for the electron to be removed. The second deals with the transport of this photoelectron through the material until it reaches the vacuum level. Third, the photoelectron overcomes the surface potential barrier, in the case of a conducting sample, the work function and is ejected into the vacuum.

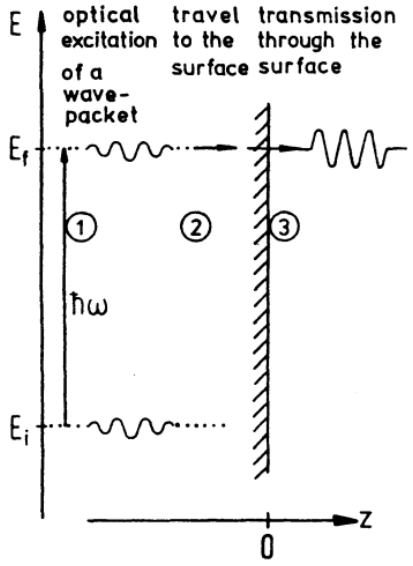

Figure 2.9 Illustration of the Three-step model of the photoemission process, from Hufner et al.[77].

The first step is governed essentially by the Fermi golden rule. For a system with N-electrons, this equation gives the transition probability W_{if} of an electron initially in the initial state i with a wave function ψ_i^N to be excited to a final state f with a wave function ψ_f^N after absorbing a photon with energy *h*ν:

$$W_{if} = \frac{2\pi}{\hbar} \left|\langle \psi_f^N \left| H' \right| \psi_i^N \rangle\right|^2 \delta\left(\mathrm{E}_f^N - \mathrm{E}_i^N - h\nu\right) \qquad 2.2$$

where $\mathrm{E}_i^N = \mathrm{E}_i^{N-1} - \mathrm{E}_B^k$ is the energy values for the initial states and $\mathrm{E}_f^N = \mathrm{E}_f^{N-1} - \mathrm{E}_{kin}$ is the energy values for the final states. E_B^k is the original binding energy of the photoelectron with a kinetic energy of E_{kin} and a momentum k. H' describes a perturbation i.e. the ionizing radiation field. Taking into account H_0 as the Hamiltonian of a solid in the ground state, this perturbation can be written using the dipole approximation:

$$H' = D.E \qquad 2.3$$

Where D is the dipole moment and E the external electric field.

The Fermi golden rule describes the probability of transition for one electron. Thus the description of photoemission intensity inside the material must take into account the contributions of each electron as shown in the relation below:

$$I_{(k,E_{kin})} = \sum_{f,i} w_{f,i} \propto \sum_{f,i} \left|M_{f,i}^k\right|^2 \sum_m \left|c_{m,i}\right|^2 \delta\left(E_{kin} + E_m^{N-1} - E_i^N - h\nu\right) \qquad 2.4$$

where $M_{f,i}^k = < \phi_f^k | H' | \phi_i^k >$ is called one-electron dipole matrix element and $\left|c_{m,i}\right|^2 = \left|\langle \psi_m^{N-1} \left| \psi_i^{N-1} \right\rangle\right|^2$ represents the probability that the remaining (N-1)-electron system is at a eigenstate m

after the ejection of one electron of the initial state i. From this relation it is possible to obtain the flux of photoelectrons that could potentially be detected.

The step 2 is the transfer of the electron towards the surface. During this step, the photoelectron will suffer different interactions as shown in Figure 2.10 (a). In the case I, the electron does not undergo any inelastic scattering and consequently arrives on the surface with its initial energy E_0 and contributes to the main photoemission peak as shown in Figure 2.10 (b). In the case II, the electron undergoes an inelastic scattering and loses a quantized energy arriving at the surface with an energy (E_0 - ΔE): it contributes to the different satellite peaks and inelastic background. In the case III, the electron can also be randomly subjected to several inelastic scattering reactions and then contributes to the secondary electron (SE) background. SE intensity at very low kinetic energy can be orders of magnitude higher than the elastic peaks. Finally, in the case IV, the electron can be absorbed in the solid and never reaches the surface.

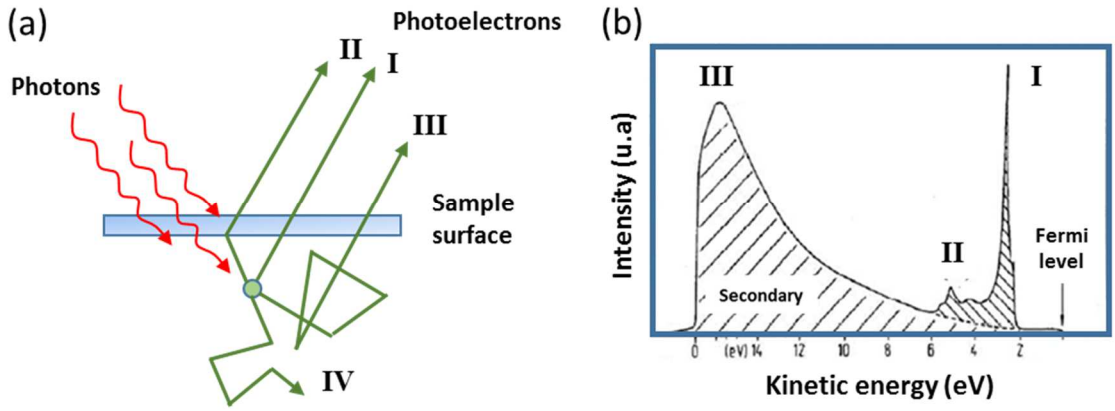

Figure 2.10. (a) Photoelectron-solid interaction process near the surface and b) Schematic representation of a photoemission spectrum.

In the step 3, the photoelectron goes through the surface potential barrier, for a conducting sample the work function, and is ejected into the vacuum. The work function for a solid is defined as the energy gap between the vacuum level and the Fermi level of the sample. For a conductive material connected to the spectrometer the Fermi level of the sample and of the spectrometer (Φ_{sp}) should be equal as shown in Figure 2.11 (a). In this case the energy conservation (equation 2.1), can be written as:

$$E_k = h\upsilon - |E_B| - \Phi_{sp} \qquad 2.5$$

On the other hand, for an insulating material the emission of the photoelectrons causes a positive potential (surface charging effect). Its occurs since there are no free electrons in the insulator and therefore the (virtual) Fermi level of the material and of the spectrometer cannot be equilibrated as illustrated in Figure 2.11 (b) [78,79]. To compensate for sample charging, a beam charge neutralizer can be used or a binding

energy calibration using a reference peak, i.e. the hydrocarbon surface contamination peak C 1*s* located at 284.8 eV [80].

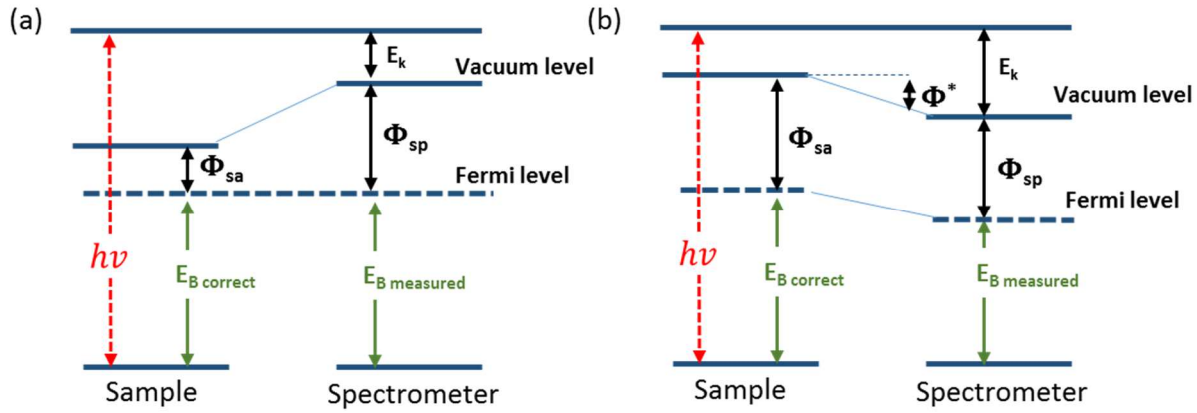

Figure 2.11 Energy level diagram of a XPS experiment for a conducting sample.

The photoemission process can be described also by a more accurate "one-step model" [81,82]. In this model, it is possible to incorporate the three steps showed before into a single Fermi's Golden Rule transition matrix based on a quantum description. However the three-step model is simpler and allows a physically more transparent visualization of the photoemission process.

2.3.1.2. XPS spectra – core level peaks and background

The XPS spectra are the number of photoelectron counts versus their E_k or E_B in a selected specified range. Figure 2.12 shows a typical structure of an XPS spectrum. It consists of relatively narrow core-level photoelectron peaks, peaks originating from X-ray excited Auger emission and a valence band structure. The photoemission background associated to each peak depends on the characteristics of the sample, the excitation source and the transmission characteristics of the instrument. It is formed by the secondary electrons which have lost energy after undergoing inelastic scatterings. For a non-monochromatic radiation of a laboratory X-ray source (X-ray tube) the spectra would be complicated by peak satellites and ghosts.

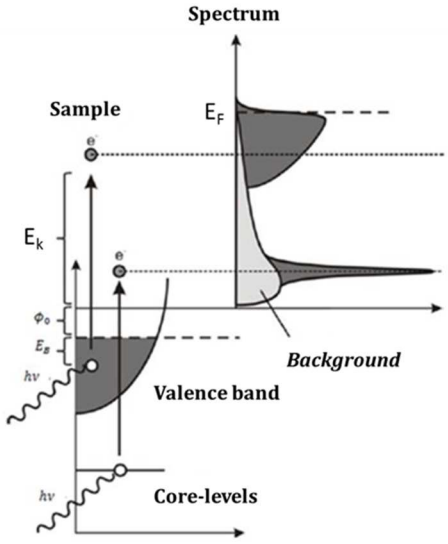

Figure 2.12. Schematic representation of a photoemission spectrum. Adapted from Reinert et al.[83]

The binding energy of the core levels allows the identification of elements present at or near the sample surface. A photoemission peak can be described as the convolution of a Gaussian and a Lorentzian function. The FWHM (full width at half maximum) of the Lorentzian function is related to the lifetime of the core hole by the Heisenberg's uncertainty principle:

$$\Delta E.\Delta\tau \approx \hbar \qquad 2.6$$

where ħ is the Plank constant.

On the other hand the Gaussian function includes the contribution of the resolution of the analyzer, kT and the FWHM of the X-ray line.

For the analysis of the core level spectra, it is essential to remove the continuous background to keep only the photoelectric peak (or no loss peak) contribution. The withdrawal of the spectral background can be done using different methods. For a more precise analysis of the core levels, a non-linear method, known as Shirley, is preferred [84]. In practice the Shirley background is used to correct for inelastic scattering of photoelectrons in the vicinity of the core-level peaks. The Shirley algorithm determines the background intensity as proportional to the integrated peak intensity at higher energy with the condition that the background matches the measured spectrum outside the region of the peak. The Shirley algorithm determines the background using the areas (A1 and A2) as show in Figure 2.13 for a Ti 2*p* spectrum to calculate the background intensity S(E) at energy E:

$$S(E) = I_2 + \kappa \frac{A2\ (E)}{A1(E)+A2\ (E))} \qquad 2.7$$

where k is the step in the background (I_2-I_1).

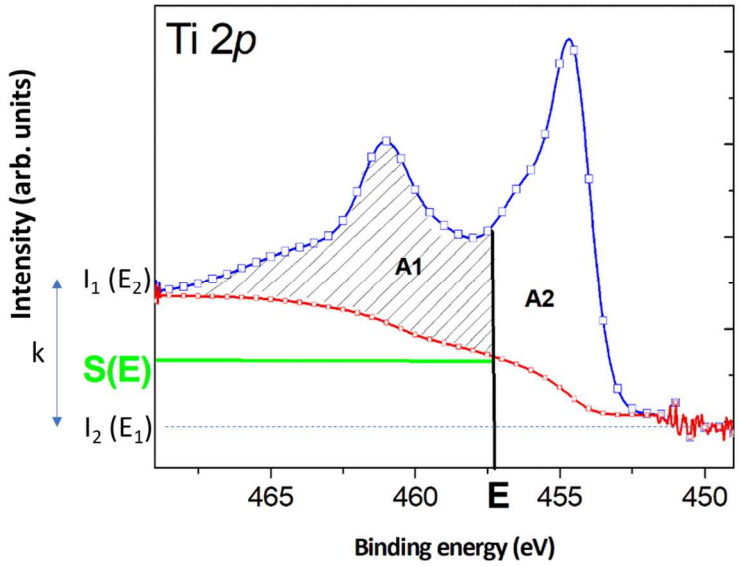

Figure 2.13. Shirley background of a Ti 2*p* spectrum.

2.3.1.3. Chemical shift

XPS allows the identification of the chemical environment of atoms by the chemical core level shift [85]. The binding energy of an electron on a core level depends on the nature of the element and the electronic level considered and can vary depending of the chemical environment. This difference ΔE can be described as:

$$\Delta E = -\Delta\varepsilon + \Delta E_{relaxation} + eV_s + \Delta E_F \quad (2.8)$$

$$\Delta\varepsilon = ke + qV \quad (2.9)$$

The term $-\Delta\varepsilon$ is called chemical shift. It expresses the effect of the chemical environment of the atom considered and reflects the initial state, i.e. before photoemission. Where k is a constant, e is the charge of the atom and V is the potential of neighboring atoms. Considering an atom A in the presence of a ligand B more electronegative (χA < χB), the ligand B attracts the electrons involved in the chemical bond with A. The atom A then reacts by contraction of the deeper localized electronic levels, which increases their binding energy of $-\Delta\varepsilon$ (with $-\Delta\varepsilon > 0$ by convention) as illustrated in Figure 2.14 [86,87].

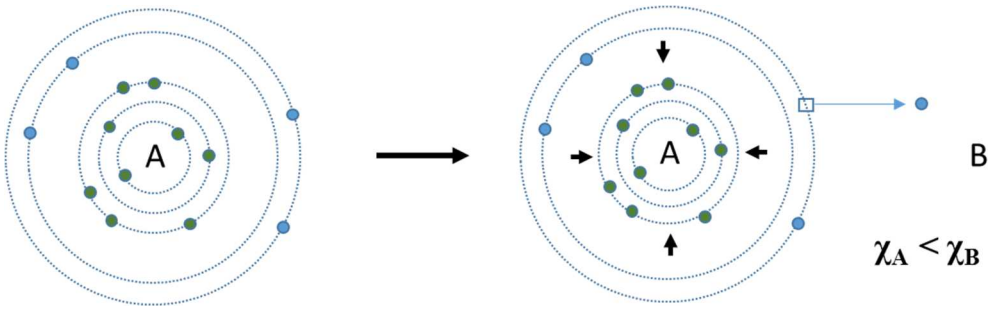

Figure 2.14. Schematic of the initial state effect, before the photoemission. Contraction of the deeper localized electronic levels of atom A in the presence of B.

The term $\Delta E_{relaxation}$ reflects the final state of the system. The binding energy of the core electrons is decreased by the contraction of the more external orbitals after the photoemission as illustrated in Figure 2.15. The contribution of the final state is very difficult to estimate but it is minority. In general, ΔE is estimated taking into account only the term Δε. The term eVs reflects the effect of charges accumulating at the surface for insulating layers. The term $-\Delta E_F$ means a possible change of the position of the Fermi level in the case of insulators and semiconductors. On the photoemission spectra, the chemical shift is materialized by a shift of the peaks.

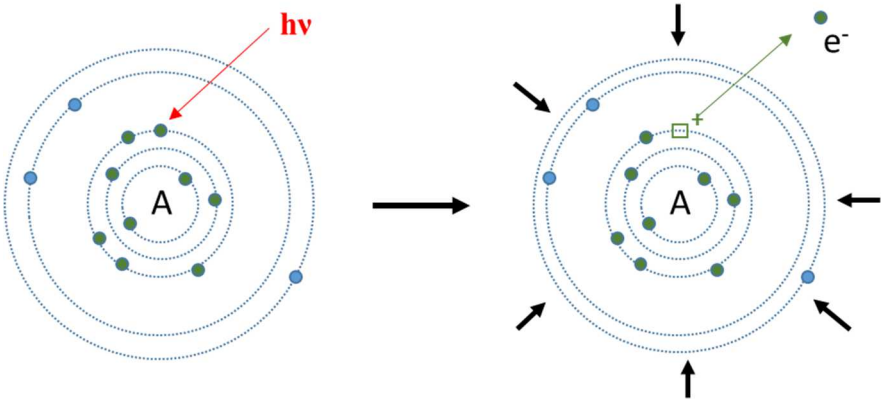

Figure 2.15. Schematic of the final state effect, after the photoemission. Contraction of the more external orbitals.

Figure 2.16 shows a Te $3d_{5/2}$ spectrum of a TiTe layer oxidized on the surface. The oxygen atom is more electronegative than Ti, thereby the binding energy of the TeO_2 contribution is higher than the Ti-Te bulk contribution.

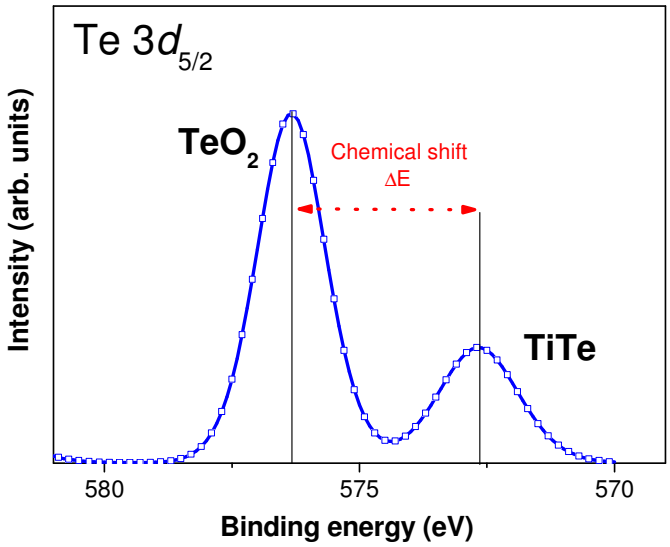

Figure 2.16. Te $3d_{5/2}$ spectrum of a TiTe layer oxidized on the surface.

2.3.1.4. Spin orbit splitting

Core levels in XPS are indicated using firstly the principal atomic quantum number n (n = 1, 2, 3…etc). This number corresponds to the main electronic layers around the nucleus of the atom. The second number is the angular momentum quantum number l (l = 0, 1, 2, 3 i.e. s, p, d, f respectively) and describes the orbital angular momentum of the electron ejected. Finally, there is the angular momentum quantum number (j = l + s) (where s is the spin angular momentum s (s = -½ or ½)). Therefore, core levels are identified by the nomenclature nlj. A doublet related to two possible states with different binding energies is observed for all orbital levels except for s-states (l = 0). This is known as spin-orbit splitting and occurs by the "spin-orbital coupling" between the l and s. The degeneracy of each of these levels is 2j+1 as shown in Table 2.3. The intensity ratio of the peaks is a function of the degeneracy. For example, for a 3*d* spectra, where n is 3 and l is 2, j will be 3/2 and 5/2 and the degeneracy will be 4 and 6 respectively. Thus, the area ratio between $3d_{3/2}$ and $3d_{5/2}$ will be 2:3. Figure 2.17 shows an example of this splitting for the Te 3*d* peak measured on a TiTe layer.

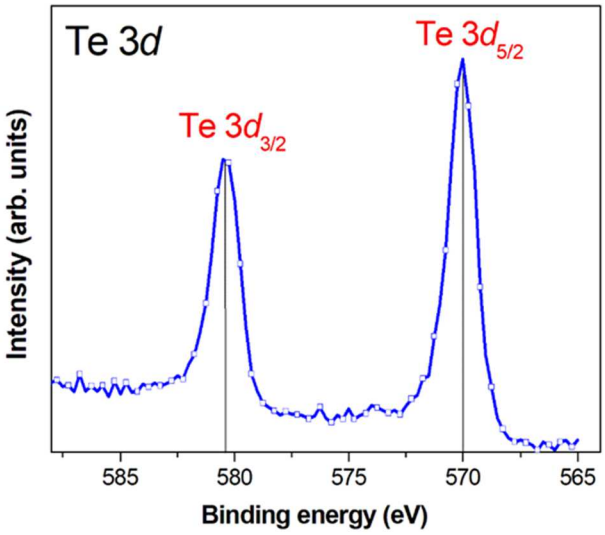

Figure 2.17. Te 3*d* spectrum measured on a TiTe layer and illustration of the 3*d* spin-orbital slitting.

Table 2.3. Spin-orbit splitting j values and ratios of the peak area.

Subshell	j = l ± s		Area ratio
s	1/2		-
p	1/2	3/2	1:2
d	3/2	5/2	2:3
f	5/2	7/2	3:4

2.3.1.5. Semi-quantitative chemical analysis and surface sensitivity

One of the most important information obtained by XPS is the relative chemical composition of the sample. The intensity of a photoemission peak is proportional to the concentration of the corresponding element, after subtraction of the background. For an element x in a homogeneous matrix of i elements, the relative concentration C_x is calculated by the relationship:

$$C_x = \frac{\frac{I_x}{s_x}}{\sum_i \frac{I_i}{s_i}} \qquad 2.10$$

where I_x is the intensity of its characteristic photoemission peak and s is the atomic sensitivity factor. The atomic sensitivity factor is described by:

$$S_A = \sigma_A \lambda_A H_A \left[1 + \frac{\beta_A}{2}\left(\frac{3}{2} sin^2\,\theta - 1\right)\right] \qquad 2.11$$

where H is the transmission function of the spectrometer, β is a factor taking into account the anisotropy of the emission, θ is the angle between the X-rays and the spectrometer, σ is the photoemission cross section and λ is the inelastic mean free path (IMPF).

- **Cross section σ**

The photoionization cross-section represents the probability of ionizing an orbital. It is a key parameter in the quantitative analysis of a material by XPS. The value of this parameter depends on the nature of the atom (atomic number) and the considered core level, as well as the energy of the photon.

The photoionization cross section **σ** for a core level i under a linear polarized light can be described as:

$$\frac{d\sigma_i}{d\Omega} = \left(\frac{\sigma_i}{4\pi}\right)[1 + \beta P_2(\cos\theta) + (\gamma \cos^2\theta + \delta)\sin\theta\cos\varphi] \qquad 2.12$$

Where P_2 (x) is the second order Legendre polynomial, β the energy- and subshell-dependent asymmetry parameter of the photoelectron angular distribution, θ is the angle between the electric field and the photoelectron direction, and φ is the angle between the X-ray direction and the plane passing through the electric field vector and the photoelectron direction[88]. Figure 2.18 shows that the photoionization cross-section decreases with the increase of the photon energy [89,90]. In this work, we have used the theoretical calculations of Trzhaskovskaya et al [89,90] for the HAXPES analyses as shown in Figure 2.18 for Te. On the other hand the quantification of XPS analyses (with a photon energy of 1486.7 eV) was performed using Scofield's values of photoionization cross-sections[91].

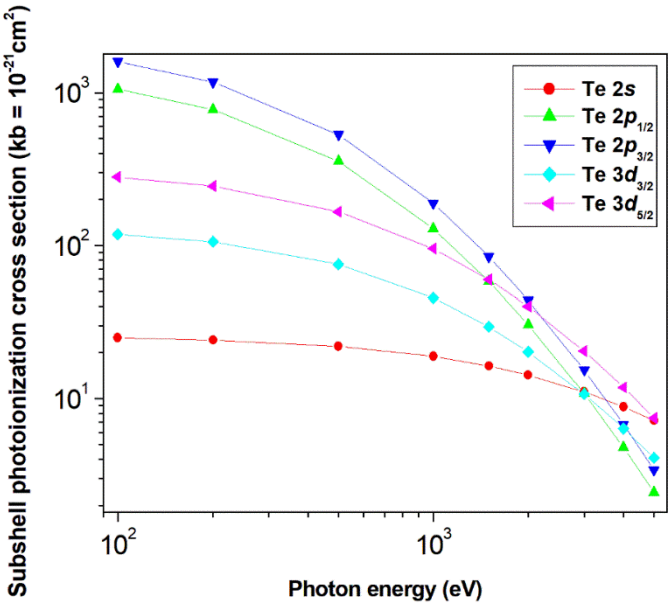

Figure 2.18. Subshell photoionization cross section for Te 2*s*, Te $2p_{1/2}$, Te $2p_{3/2}$, Te $3d_{3/2}$ and Te$3d_{5/2}$ as a function of the photon energy from Trzhaskovskaya et al. [89,90].

- **Inelastic Mean Free Path (IMFP) λ**

The IMPF is the average distance traveled by a photoelectron in the solid between two inelastic collisions. It is a quantity which depends on the material, as well as the kinetic energy of the photoelectron emitted. Therefore, the IMPF will be different for all core level peaks of a given element. The dependence of the IMPF versus the KE of the photoelectron is approximately given by the empirical universal curve [92,93] showed in Figure 2.19 The universal curve is an empirical curve but there are models proposed in the literature that consider the characteristic of the different materials in the IMPF calculation. For example a more accurate value can be calculated by the Tanuma-Penn-Powell (TPP-2M) formula [94]:

$$\lambda = \frac{E}{\left\{E_p^2\left[\beta \ln(\gamma E) - \left(\frac{C}{E}\right) + \left(\frac{D}{E^2}\right)\right]\right\}} \quad \text{(nm)} \qquad 2.13$$

The terms of the equation are given by:

$$\beta = -0.0216 + \frac{0.944}{\left(E_p^2 + E_g^2\right)^{\frac{1}{2}}} + 7.39 \times 10^{-4}\ \rho \qquad 2.14$$

$$\gamma = 0.191\rho^{-0.5} \qquad 2.15$$

$$C = 1.97 - 0.91U \qquad 2.16$$

$$D = 53.4 - 20.8U \qquad 2.17$$

$$U = \frac{N_V\ \rho}{M} = \frac{E_p^2}{829.4} \qquad 2.18$$

where $E_p=28.8(N_v\rho/M)^{1/2}$ is the free electron plasmon energy (in eV), Nv is the number of valence electrons per atom (for elemental solid) or molecule (for compounds), ρ is the density (in $g.cm^{-3}$), M is the atomic or molecular weight and E_g is the bandgap energy (in eV).

As shown in Figure 2.19 for electrons with kinetic energies higher than 70-100 eV, increasing the kinetic energy of the photoelectron increases the IMFP. The tendency is reversed at lower energies (less than 70 eV) since the electron has too low an energy to cause plasmon excitation, consequently the probability of inelastic scattering decreases and the IMFP increases.

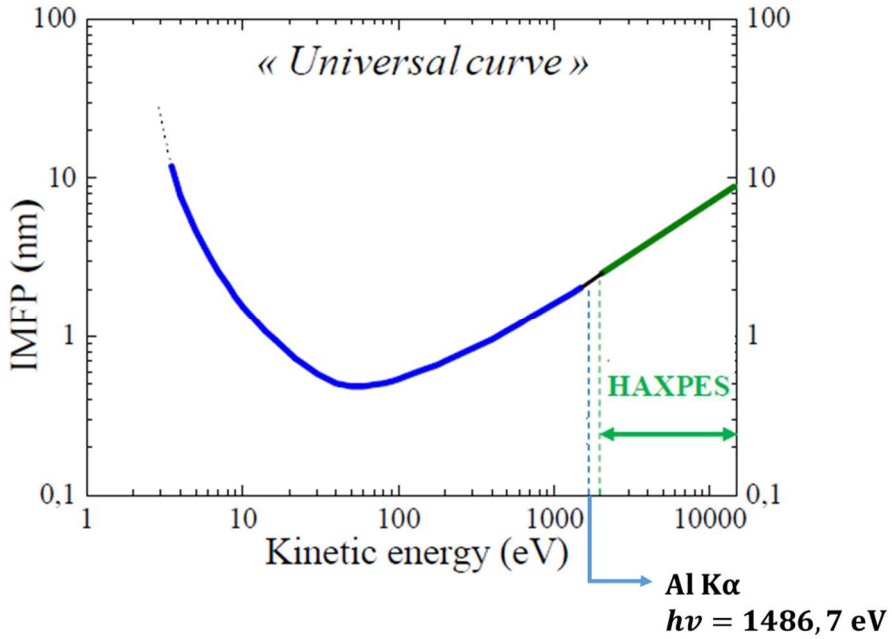

Figure 2.19. Universal curve representing the IMFP as a function of the kinetic energy of the photoelectrons. Adapted from Seah et al. [92].

2.3.1.6. Depth information

The contribution of a surface layer (with a thickness z) to the XPS peak intensity follows the Beer Lambert law [95]:

$$I = I_\infty \left[1 - e^{-z/\lambda sin\theta}\right] \qquad 2.19$$

where θ is the angle between the surface of the sample and the collected electron trajectory, λ is the inelastic mean free path and I_∞ is the intensity collected for an infinite thickness. Figure 2.20 shows the connection between analysis depth and IMFP.

The intensity from buried atoms is attenuated. The value of the inelastic mean free path λ plays a leading role by limiting the thickness of analysis. Finally, as a layer of thickness d = 3 λsinθ contributes to 95% of the measured signal, the analysis depth is estimated by:

$$d = 3\lambda \sin\theta \qquad 2.20$$

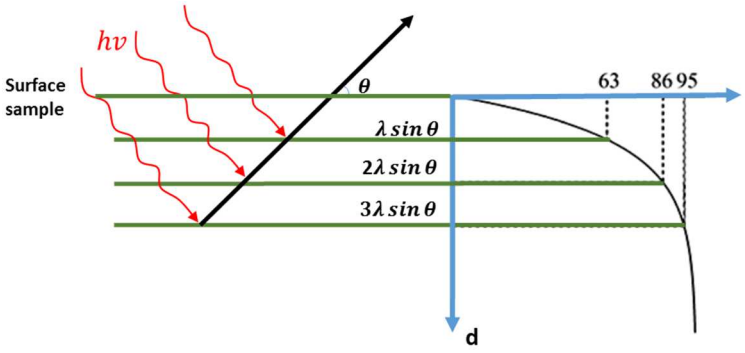

Figure 2.20. Intensity of the emitted electron as a function of depth of analysis.

The thickness probed in laboratory XPS with a monochromatic Al K_α source (hν = 1486.7 eV) never exceeds 10 nm (λ~2-3nm) for normal detection. This makes XPS a surface analysis technique. To increase the depth of analysis, it is necessary to use a source of hard X-rays (typically hν > 2 keV). In these circumstances, the increase of the photoelectron kinetic energy increases their mean free path and consequently increases the analysis depth as shown in the equation 2.20 and Figure 2.19.

However, Figure 2.18 shows that the photoemission cross section decreases at high energies of photons. Therefore, X-ray sources with a high brightness such as synchrotron sources must be used to compensate this decrease thus allowing to increase the depth sensitivity whilst maintaining reasonable statistics.

2.3.2. XPS Instrumentation

2.3.2.1. The ultra-high vacuum

XPS analysis requires an ultra-high vacuum (UHV) (~ 10^{-9} Torr / 10^{-7} Pa) system. It is necessary to prevent the interaction between the ejected photoelectrons and gas molecules between the sample surface and the analyzer, as well as to reduce the presence of contaminants on the samples surface.

2.3.2.2. X-ray sources

- **X-ray tube (laboratory XPS source):**

Figure 2.21 (a) shows a schematic of an X-ray source. A current of a few amperes (2-4 A) passes through a filament of tungsten (cathode). The filament heating causes the emission of electrons by thermionic emission. These electrons are accelerated by a high voltage (typically 10-15 kV) and impinge on the anode (Al or other materials). The electron-anode interaction generates an X-ray emission spectrum, containing background noise, called *bremsstrahlung*, along with the sharp peaks (K-shell emission radiation) related to the electronic structure of the anode metal as shown in the Figure 2.21 (b). In the case of an Al anode, a window also in Al is placed in front of the anode. It reabsorbs part of the *bremsstrahlung* and transmits almost all the Al Kα lines. The X-ray used in this work was Al $K\alpha_{1,2}$ (hv = 1486.6 eV) generated by the electron transition between the 2*p* orbital (L shell) and the 1*s* orbital (K shell).

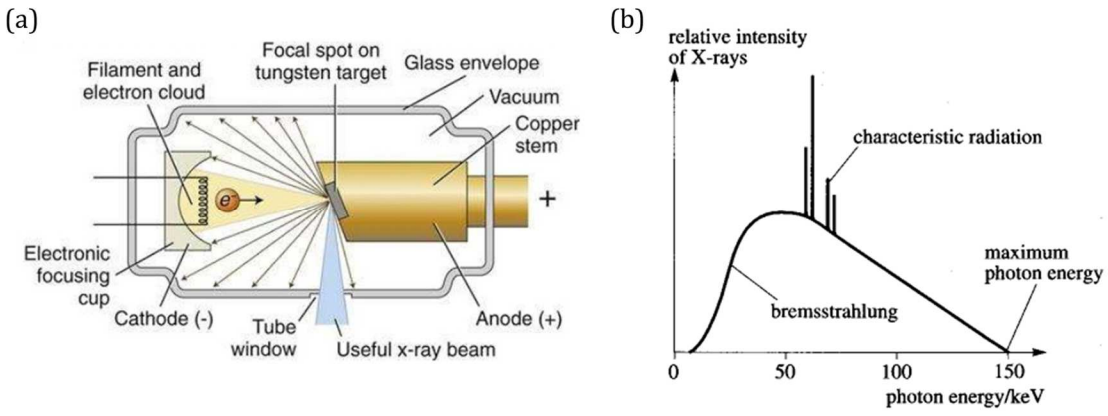

Figure 2.21 (a) Illustration of an X-ray tube source, from [96] (b) X-ray emission spectra.

The photons emitted are not monochromatic and can be selected in energy via a monochromator to improve the resolution and eliminate the annoying satellite rays contribution. The quartz crystal monochromators are based on the diffraction process according to Bragg's law as shown in Figure 2.22. This device decreases the photon flux but improves the energy resolution of the measure. The typical FWHM of a monochromated Al Kα source is 250 meV. However, laboratory sources are limited to a few strong X-ray emission lines: Mo, Al and Si are the most common, all delivering X-rays below 2 keV. For higher energy X-rays, synchrotron radiation is necessary, delivering a continuous spectrum allowing tuning of the photon energy.

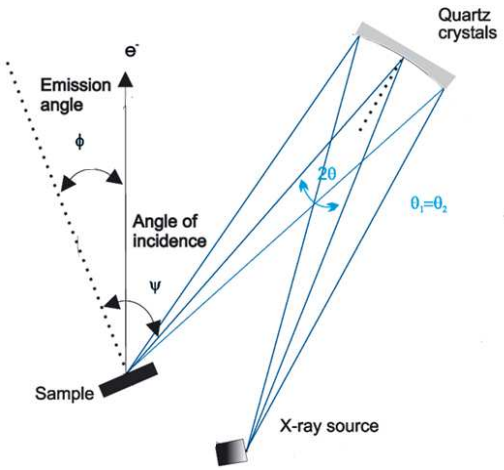

Figure 2.22 (a) Illustration of the working principle of a quartz crystal monochromator. Adapted from Specs [97].

As discussed before in section 2.3.1., for an insulating material the emission of the photoelectrons causes a positive potential (accumulation of positive charges at the surface). For a non-monochromated source there are usually a sufficient number of electrons at the surface of the sample to compensate this accumulation. However, for a monochromated X-ray source there are less electrons to control the charging. Therefore, it is necessary to minimize the positive charges using a low energy electron neutralization source as shown in Figure 2.23. This source is a flood gun that uses thermionic emission of low energy electrons near the sample to compensate the accumulation of charges at the surface [98].

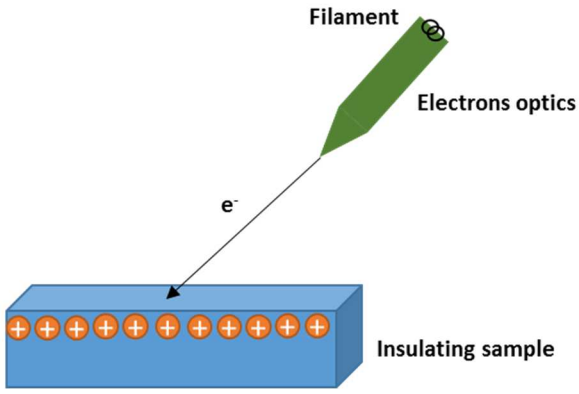

Figure 2.23 Illustration of an electron flood gun.

- **Synchrotron radiation:**

As shown in Figure 2.24, the first part of a synchrotron is constituted of an electron gun and a linear accelerator (preinjector). Electrons emitted by the electron gun, travel into the linear accelerator (Linac) where they are accelerated to higher energies (MeV) depending on the facility. In the booster ring, the

electrons receive a boost in energy and they reach several hundreds of MeV or even few GeV. After this step, the speed of the electrons is approximately the speed of light and they are injected in the storage ring. Once in the storage ring, the electrons are kept circulating with constant energy for many hours producing photons (so-called synchrotron radiation).

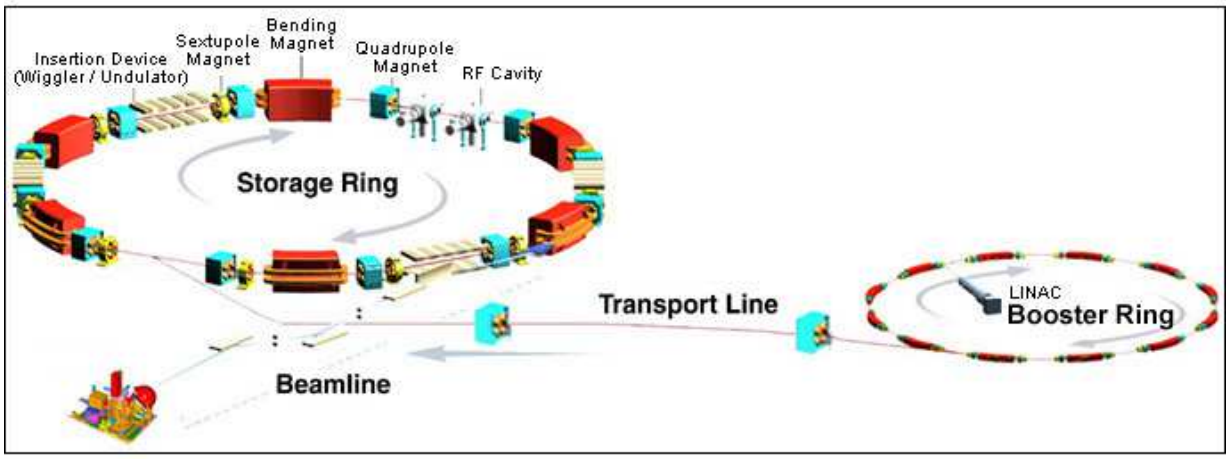

Figure 2.24. Schematic view of a synchrotron radiation facility. Adapted from NSRRC [99].

The storage ring is made of: quadrupole and sextupole magnets, bending magnets, and insertion devices (undulator, wiggler) as shown in Figure 2.25. The electrons are forced to follow a closed orbital trajectory guided by the magnetic field of the bending magnets. During each turn, the electrons lose a part of their energy thus emitting synchrotron light. This energy is regained in the RF cavities. The quadrupole magnets, made of four magnetic poles, are used to focus the electron beam, acting like magnetic lenses. Sextupoles with six magnetic poles rather than four can also be used. An appropriate arrangement of sextupole and quadrupole magnets can improve the focusing system and decreases the beam size. The improvement of the brightness of the synchrotron radiation was made by the insertion of wigglers or undulators in the straight sections of storage ring joining two successive bending magnets. These elements present in the third generation sources, are formed by several permanent magnets that imposes a sinusoidal trajectory to the electrons, generating synchrotron radiation in addition of the bending magnets. The wiggler emits intense radiation over a wide spectral range but the radiation from different wiggles add incoherently of the radiation from each oscillation. On the other hand, in undulators, the small-amplitude oscillations from the passage of a single electron produce a coherent addition of the radiation from each oscillation. As most of the scientific studies usually need a very narrow range of wavelengths the most modern machines preferentially use undulators instead of wigglers[100–103].

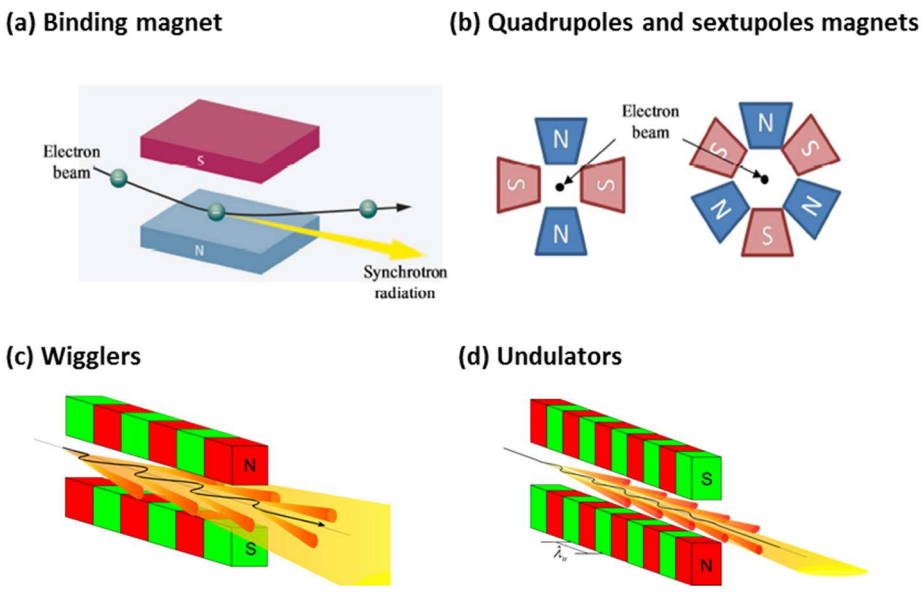

Figure 2.25. Illustration of some main elements found in a storage ring (a) bending magnets, (b) quadrupole and sextupole magnets, from PSI [104] (c) wigglers and (d) undulators, from Desy [105] .

The energy range produced in the storage ring can be between IR to hard X-rays. After the production of the synchrotron radiation, monochromators, filters, mirrors, are used in the beamline to tune the photon beam energy and focus the beam on the sample at the experimental station. Figure 2.26 shows a schematic of the BL15XU (Spring-8) and Galaxies (SOLEIL) beamline. The beamline details are showed in Table 2.4.

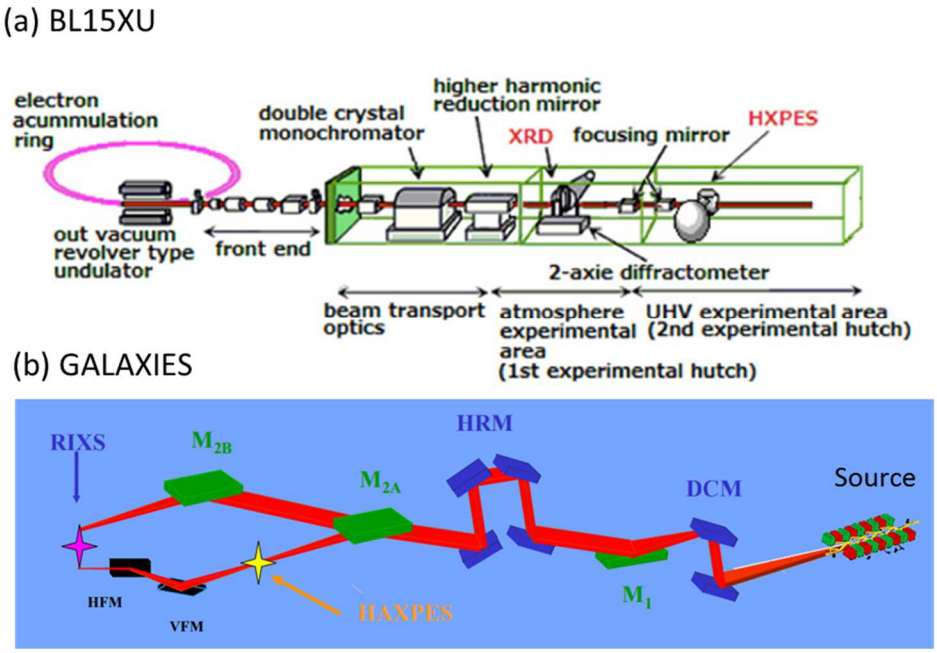

Figure 2.26.Schematic diagram of the (a) BL15XU, from [106] and (b) GALAXIES beamline, from [107].

Table 2.4 BL15XU [106] and GALAXIES beamline[107] details.

Beamline	Beamline	
BL15XU (Spring-8)	Source type	Out vacuum revolver type undulator
	Energy range	Hard X-ray (2.2-10 keV)
	Beam size	40 µm (V) x 70 µm (H)
	Photon flux	~10^{12} photon/s
	Monochromator	Si (111) and Si (311) double-crystal with liquid nitrogen cooling and Si (111) channel-cut monochromators
	Mirrors	Two Rh-evaporated mirrors (70cm length, reflection direction is horizontal)
GALAXIES (SOLEIL)	Source type	U20 in-vacuum undulator, 20 mm magnetic period with 98 periods
	Energy range	2.3–12 keV
	Beam size	30 µm (V) x 80 µm (H) Micro-focusing: 10 µm (V) x 10 µm (H)
	Photon flux	3.0 10^{11} photon/s at 10 keV
	Monochromator	Double-crystal Si (111) liquid-nitrogen-cooled fixed-exit (DCM) monochromator
	Mirrors	Spherical collimating mirror (M1), R = 8.8 km; Si substrate with C and Pd coatings Toroidal focusing mirrors (M2A, M2B), R = 1.29 km, ρ = 30 mm; Si substrate with Pd coating

For the BL15XU beamline, an additional channel-cut monochromator is used to provide high-energy resolution for the HAXPES analysis (less than 250 meV). Therefore X-rays (2-10keV) used for the HAXPES measurements are obtained by the combination of the undulator, a DCM, and a channel-cut monochromator[106].

For the GALAXIES beamline, the first energy selection is performed by a fixed-exit Si (111) double-crystal monochromator (DCM).

2.3.2.3. Electron analyzer system

The electron analyzer system can be divided into three parts:

- **Entrance optics:**

In this part of the system the electrons are collected, transmitted and accelerated or retarded to a pass energy (E_P) and focused toward the entrance slit of the hemispherical analyzer.

- **Analyzer:**

The electron hemispherical analyzer is illustrated in Figure 2.27. It consists of two concentric hemispheres of R_1 and R_2 radius, covered with a conductive coating. The median radius is R_0. The application of a potential difference (V_2-V_1) between the hemispheres gives rise to a radial electric field that defines the trajectory of the photoelectron. The geometry and the potential difference define the pass energy of the analyzer (E_a) according to:

$$E_a = \frac{e\,(V_2 - V_1)}{\left(\frac{R_2}{R_1} - \frac{R_1}{R_2}\right)} \qquad 2.21$$

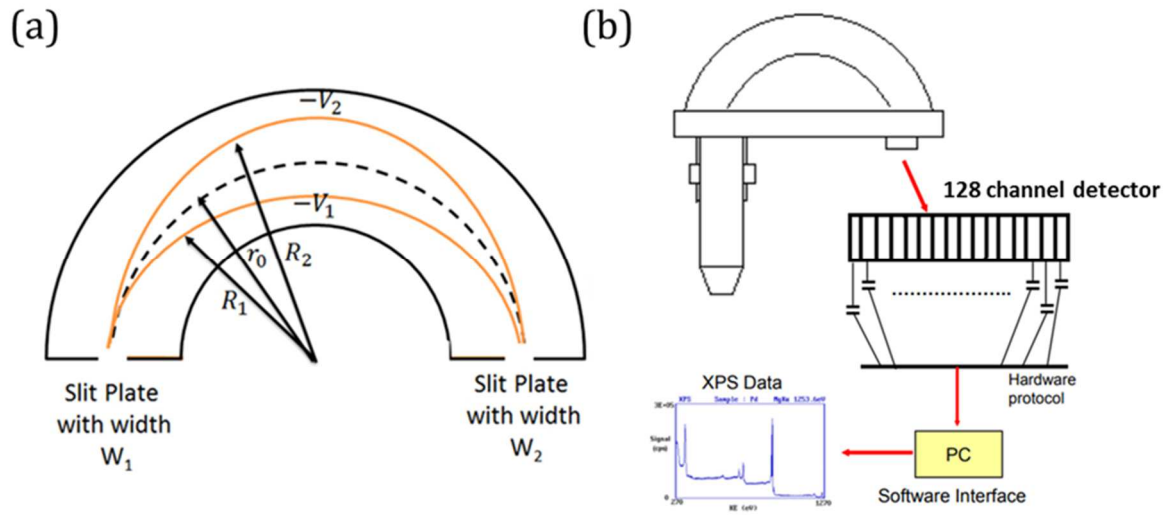

Figure 2.27. Schematic of a (a) hemispherical analyzer geometry, from Santana et al. [108] and (b) analyzer coupled to a 128 channel detector (MCD) (PHI 5000 VersaProbe II (Physical Electronics) detector).

Ea is the energy that must have an electron entering the analyzer to emerge with a median radius trajectory R_0. Electrons with a kinetic energy greater or less than E_a collide with the hemispheres. The analyzer energy resolution $\Delta E_{Analyzer}$ plays a crucial role in the analysis of the binding energies. In practice, the components of a spectrum cannot be separated if their offset in binding energy is less than this resolution.

The $\Delta E_{Analyzer}$ depends on E_a, R_0, the solid angle of the retarding lenses ($\delta\alpha$) and W the entrance slit size as shown in the expression below:

$$\frac{\Delta E}{E_a} = \frac{W}{2R_0} + (\delta\alpha)^2 \qquad 2.22$$

The reduction of the slit size improves the resolution. On the other hand, this reduction degrades the counting rate and therefore the signal-to-noise ratio. A compromise must therefore be found between resolution and intensity for each different analysis.

- **Detector**

In the detector, the electrons are collected and counted using several aligned channeltrons (electron multipliers) or by using a multichannel plate (MCP). For the XPS analysis of this work, the photoemission spectra are obtained using a 128-channel detector (PHI 5000 VersaProbe II) as illustrated in Figure 2.27 (b).

For the HAXPES analysis the photoemission spectra are obtained using a multi-channel plate coupled to a charge coupled device (CCD). This system is used as it yields high speed recording and very high spatial resolution.

2.3.3. XPS in-depth analyses

As we have seen in section 2.3.1., XPS is a surface technique with a limited probing depth, typically < 10 nm. Therefore, for this study, we have used hard X-ray photoelectron spectroscopy (HAXPES) to probe the buried interfaces involved in resistive switching as well as XPS depth profiling using GCIB (gas cluster ion beam) to investigate the elements migration in-depth.

2.3.3.1. Hard X-ray photoelectron spectroscopy – HAXPES

The use of synchrotron radiation has several advantages compared to common laboratory X-ray sources. The increase of the photon energy to hard x-rays (HAXPES) increases the kinetic energy for the same core level emission and hence increases the IMFP giving to HAXPES a higher bulk sensitivity than XPS. Besides that, the synchrotron radiation provides a higher photon flux and the possibility of focusing the X-ray beam into a small spot. The brightness is one of the key parameters to compare the quality of the X-ray beams from different sources. It depends on the number of photons emitted per second (photons/s), the angular divergence of the photons (mrad), the cross-sectional area of the beam (mm^2) and the relevance of spectral distribution (0.1% of the bandwidth- BW) as described in the relation below:

$$\text{Brightness} = \frac{photons/s}{(mrad)^2\ (mm^2{-}area)(0.1\%BW)} \qquad 2.23$$

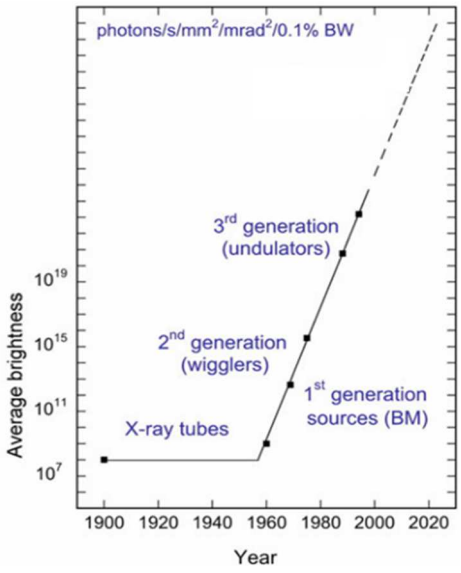

Figure 2.28. Histogram of the synchrotron radiation sources evolution. Adapted from [109].

Figure 2.28 shows a plot of X-ray source brightness from 1900 to the present day. Knowing that the photoionization cross section decays rapidly with increasing photon energy as showed before in Figure 2.18, the advances in high brightness offered by third generation sources shown in Figure 2.28 were crucial to compensate this limitation and allow the study of deeply buried interfaces using hard X-rays[10,100].

Finally, another advantage of the synchrotron radiation is the tunability of the photon energy, allowing to successively probe the system with surface or bulk sensitivity. Figure 2.29 shows a comparison of depth sensitivity at different photons energies for a Si layer oxidized on the surface. The increase of the photon energy promotes an increase of the bulk contribution (grew line) in comparison to the surface layer contribution (red line) in the Si 2*p* spectrum. In the case of the resistive memories mechanism study, HAXPES enables non-destructive analysis of the buried interfaces between realistic electrodes and insulating layer thanks to the much greater probing depth.

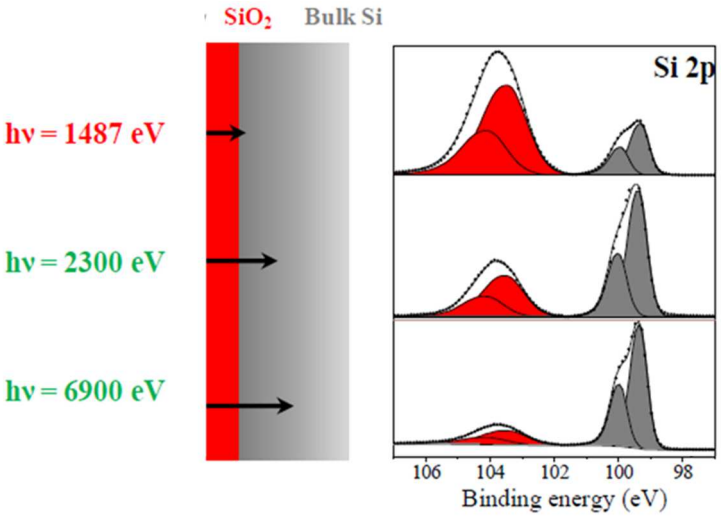

Figure 2.29. Si 2*p* spectrum measured on a Si layer at different photon energies. Adapted from Philippe et al. [110].

- **Recoil effect**

The recoil effect is an important point to take into consideration in HAXPES experiments. This effect is associated with the momentum conservation. The recoil energy ΔE is the transferred energy to the emitter atom of mass M when the photoelectron of mass m is emitted with a kinetic energy Ekin. Taking into account one atom in vacuum, the shift towards higher energies can be estimated as:

$$\Delta E = E_{kin}\left(\frac{m}{M}\right) \qquad 2.24$$

The recoil energy is not important in XPS analysis where the momentum transfer is very low. On the contrary, for HAXPES this effect becomes non negligible and can induce a ΔE comparable to the chemical shifts depending on the mass of the atom analyzed [111,112].

- **Description of the HAXPES set-up used to analyze CBRAM cells**

HAXPES experiments were performed at the BL15XU beamline of the Japan Synchrotron Radiation Research Institute (SPring-8) [106] and at GALAXIES beamline of the Synchrotron SOLEIL (Saint Aubin)[107,113]. Table 2.5 summarizes the characteristics of the HAXPES set-up for each synchrotron source.

Table 2.5 Instrumentation and experimental parameters of HAXPES measurements

Synchrotron	Beamline	Photon energy (eV)	Energy resolution (meV)	Spot size (μm^2)	Analyzer
Spring- 8	BL15XU	7935.7	243	300 x 40	VG Scienta R4000
SOLEIL	GALAXIES*	6900	110	500 x 30	
		8000	160		
		10000	210		

*the experiments were performed using the DCM at third order.

These measures using high energy, high brightness and high resolution have enabled the analysis of the buried layers such as: active electrode, electrolyte and bottom electrode of the CBRAMs cells as well as the interfaces that have a key role in the switching process.

The IMFPs were estimated with the Tanuma equation [94]. These values were obtained by averaging the IMFPs estimated for each layer crossed by the photoelectrons during their transport toward the surface. The average was weighted by the thickness of each layer. For example, the relation below shows the estimation of the λ for Al $1s$ photoelectrons considering a stack of TaN/ZrTe/Al_2O_3.

$$\lambda_{\text{Al } 1s} = \frac{\left[\left(\lambda_{\text{Al},TaN} \times d_{TaN}\right)+\left(\lambda_{\text{Al},ZrTe} \times d_{ZrTe}\right)+\left(\lambda_{\text{Al},Al_2O_3} \times d_{Al_2O_3}\right)\right]}{\left(d_{TaN}+ d_{ZrTe}+ d_{Al_2O_3}\right)} \quad 2.25$$

where $\lambda_{\text{Al},TaN}$, $\lambda_{\text{Al},ZrTe}$ and $\lambda_{\text{Al},Al_2O_3}$ are the IMFPs estimated in the TaN , ZrTe and Al_2O_3 layers respectively as well as d_{TaN}, d_{ZrTe} and $d_{Al_2O_3}$ are the thickness of each layer.

2.3.3.2. Depth profiling - GCIB

As XPS is a surface analysis technique, sputtering using conventional monoatomic ions beams is often used to probe the bulk of materials. XPS combined with sputtering to etch the material between analyses cycles, i.e. XPS depth-profiling enables the study of multilayer samples and provides information of the element's distribution. However, the use of monoatomic ion beam may cause preferential sputtering which change the chemical composition of the probed material. Preferential sputtering occurs in multi-component samples where an element will sputter more efficiently than the others. This phenomenon is governed mainly by the atomic mass and binding energy of the sputtered atom. Usually preferential sputtering occurs for atoms with low mass and low surface binding energy[114,115].

Recently, the cluster ion sputtering system has received attention as an alternative method to solve the problems related to the chemical damages occurring during monoatomic ion sputtering. The advantage of a sputtering process with gas cluster ion beams (GCIB) is that they involve low-energy individual atomic interactions decreasing the preferential sputtering. The energy of each atom in a cluster is equal to the total energy of the cluster divided by the number of atoms therefore a cluster ion beam produces low-energy irradiation effects. For example, a cluster ion with 1000 atoms and a total energy of 10 keV, has individual atoms with an energy of only 10 eV. It is difficult, to obtain a monoatomic ion beam with low energy and high ion current, taking into account the divergence caused by the space charge effects. Thus, the use of GCIB can be very useful as a low-damage method of sputtering. [116].

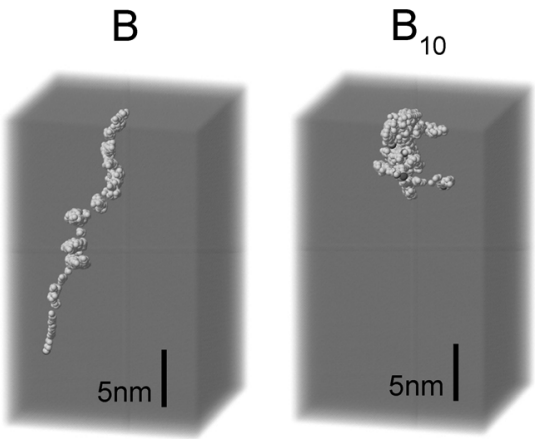

Figure 2.30. Comparison of the impact of a monomer ion beam (B) and a cluster ion beam (B_{10}), from Toyoda et al. [117].

For the impact of gas cluster ions, thousands of atoms simultaneously bombard the sample promoting multiple collisions near the surface. This process induces different irradiation effects in comparison to monomer ions such as: amorphous formation, penetration depth, sputtering, and energy deposition.

Figure 2.30 shows a molecular dynamics simulation (MDS) of the impact of a B monomer and B_{10} cluster ion into Si with energy of 5 keV. The comparison shows significant differences in the penetration and in the displacements produced. For B_{10} the penetration range is shallower and only the extreme surface is damaged, whereas for a similar energetic monoatomic ion beam, the primary ions penetrated deeper into the sample. [116]. While monomer ions promote a linear-cascade collision, the GCIB impact causes multiple collisions, i.e. nonlinear collisions near the surface. As a consequence, this method of sputtering results in a high sputtering yield, lateral sputtering and low-damage processing.

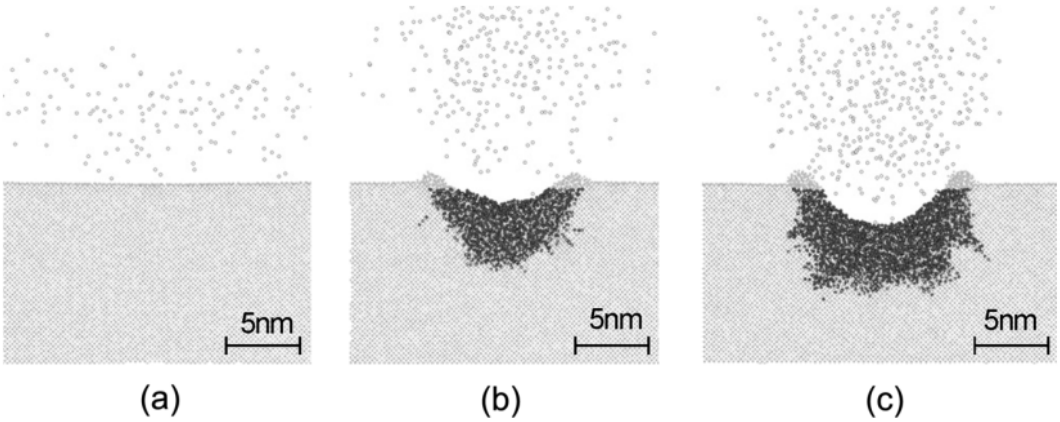

Figure 2.31. Impact of the energy per atom on the solid surface for: (a) 1 eV/atom, (b) 5 eV/atom, and (c) 10 eV/atom, from Toyoda et al. [117].

The appropriate energy and amount of atoms have to be selected according to the studied material. First of all, a sufficiently high number of atoms composing the cluster has to be chosen to reduce the deterioration depth. Another important parameter to take into account is the energy per atom. When too high, damage will be gendered. When too low, there is a risk that the incident energy doesn't overcome the surface binding energies and that nothing will be sputtered as show in Figure 2.31.

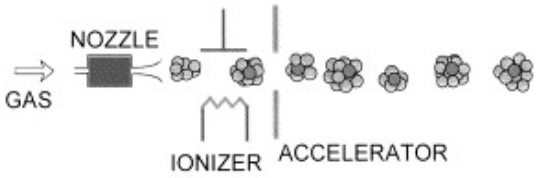

Figure 2.32. Diagram of the cluster ion beam irradiation system. Adapted from Yamada et al. [116].

Figure 2.32 shows a schematic diagram of the cluster ion beam iyamadarradiation system. Adiabatic expansion of a high-pressure gas through a nozzle is utilized for the formation of Ar gas cluster beams. When a supersonic flow ejects from the nozzle, shockwaves are generated. These shockwaves disturb the generation of neutral cluster beams. To avoid formation of such shockwaves, the skimmer (Nozzel) was developed. The skimmer extracts the core of the supersonic flow and the cluster beam is introduced into high vacuum. The neutral clusters are ionized by the electron bombardment. The ionizer consists of filaments and anode. Electrons ejected from hot filaments are accelerated toward the neutral cluster beam and ionize clusters. The ionized clusters are then extracted and accelerated towards targets. When an energetic cluster of several hundreds of atoms impacts upon a surface, it interacts nearly simultaneously with many target atoms and deposits higher energy into a very small volume of the target material.

2.3.3.3. Description of the XPS sputtering method applied to analyze CBRAM cells

XPS depth profiling was performed using a PHI 5000 VersaProbe II (Physical Electronics) equipped with a monochromatic Al K_α source ($h\nu$ = 1486.7 eV). The pass energy was set to 47 eV, giving an overall energy resolution of 0.75 eV, with an emission angle of 45°. To compensate for sample charging, in particular when analyzing the insulating Al_2O_3 layer, a dual beam charge neutralizer was used. XPS depth profiling was carried out using an argon gas cluster ion beam (GCIB) with 2500 Ar atoms per cluster, a current of 20 nA, a raster area of 2mm*2mm, ensuring uniform sputtering of the analyzed area, and 20 kV accelerating voltage corresponding to an energy of 8 eV per atom.

2.4. Time-of-Flight Secondary Ion Mass Spectrometry - ToF-SIMS

2.4.1. Principles

Time-of-Flight Secondary Ion Mass Spectrometry (ToF-SIMS) is a destructive technique used to identify and dose the chemical composition of solid surfaces. In comparison to most of the existing characterization techniques, it gathers high performances in term of sensibility, chemical and spatial resolutions as shown in Table 2.6.

Table 2.6. ToF-SIMS characteristics [118]

Performance	
Chemical detection	• Full periodic table detected • All molecular species
Sensitivity	• ppm
Mass resolution	• m/dm > 3000 • ex: m/dm = 3971 for $^{30}SiH^{-/+}$ (30.9816 u) and $^{31}P^{-/+}$ (30.9738 u)
Lateral resolution	• <µm
Depth resolution	• ~nm
Samples compatibility	• Analysis of inorganic/organic conductive/insulating materials

ToF-SIMS is a complementary technique to XPS. While XPS depth profiling allows the identification of the chemical states and a semi-quantification of the elements in-depth, ToF –SIMS, in turn, provides in-depth profiles with a high depth resolution (< 1nm) and with a better sensitivity (< 10 ppm) [11]. These characteristics are essential to study the small changes that occur during the resistive switching and the elements diffusion under the bias application.

SIMS consists in bombarding a surface with charged primary ions (mono or polyatomic) of a well-known energy (in the order of keV). Part of these ions are scattered but for the majority of them, they induce collisions, transfer the incident energy to the sample surface, break the atomic bounds and pulverize the top layers. The emitted particles are mainly neutral (99%) but some are still positively or negatively charged ions. Since part of the sample is withdrawn during the analysis, this technique is destructive. The secondary ions detection provides then chemical and elementary information on the top layers of the inspected sample.

ToF-SIMS presents an analysis approach different from the magnetic or quadripolar SIMS for which the ions are successively selected in agreement with their energy. A Time-of-Flight analyzer is here used to measure the time taken by each of the extracted particle to travel through a field-free drift tube under Ultra High Vacuum (UHV). After their projection, the ions are extracted and accelerated by a fixed potential toward this chamber clear of electromagnetic field. The ions travel with a constant speed and are separated according to their mass and charge. The frictional and gravity forces inside the tube are negligible because of the low masses and the high speeds. The high vacuum guarantees the quasi total absence of collisions between ions.

The Time of Flight is directly related to the nature of the ions by the following equation:

$$t_{ToF} \approx L\sqrt{\frac{m}{2zE_0}} \qquad 2.26$$

Where L is the length of the detection chamber, m the ion mass, z the charge of the ion, and E_0 is the secondary ion acceleration voltage. The counts of ions per second detected at the end of the flight can thus be represented on a spectrum and translated into a mass spectrum as shown in Figure 2.33.

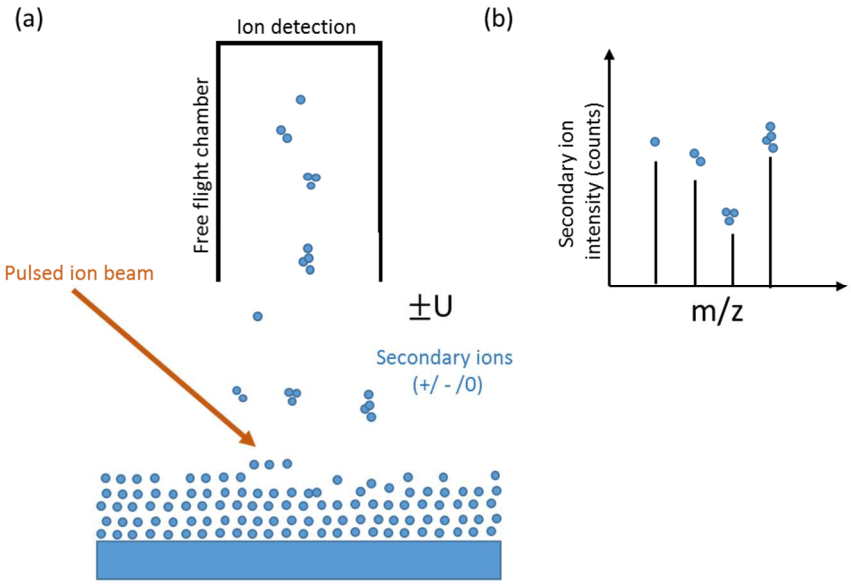

Figure 2.33. (a) Illustration of the ToF-SIMS analysis (b) Mass spectra generated by the pulse of primary ions.

The mass resolution is expressed by the ratio m/Δm and is equivalent to $t_{ToF}/2\Delta_{ToF}$. The Δ_{ToF} is related to the pulse width of primary ions and also to the kinetic energy difference for secondary ions with the same ratio (m/z). This mass resolution can be improved by reducing the pulses width, using a pulse time compression. The mass resolution varies between 300 and 10 000 and depends on the analyzed ion.

In this thesis, measurements were done using the depth profiling mode. To get information about the in-depth sample composition, a "dual beam" is used. The first rastering beam with a low energy (from 150eV to few keV) is used to sputter the sample (i.g. Ar^+ , Ga^+ , Cs^+ or O_2^+). The second one has a higher pulsed energy (15 to 25 keV) and analyzes the top layers. In this way the composition of consecutive layers is evaluated, and a depth profile is realized. The intensity spectrum for different elements is obtained as a function of sputtering time. It can be converted in a thickness unit if we know the erosion speed (V) of the sputtered matter using the following equation:

$$D_{layer} = V\, t_{ToF} \qquad 2.27$$

The Dual Beam cycle is represented on the Figure 2.34. Sometimes it can be necessary to use an electron gun (flood gun) to compensate the charges accumulated on the surface.

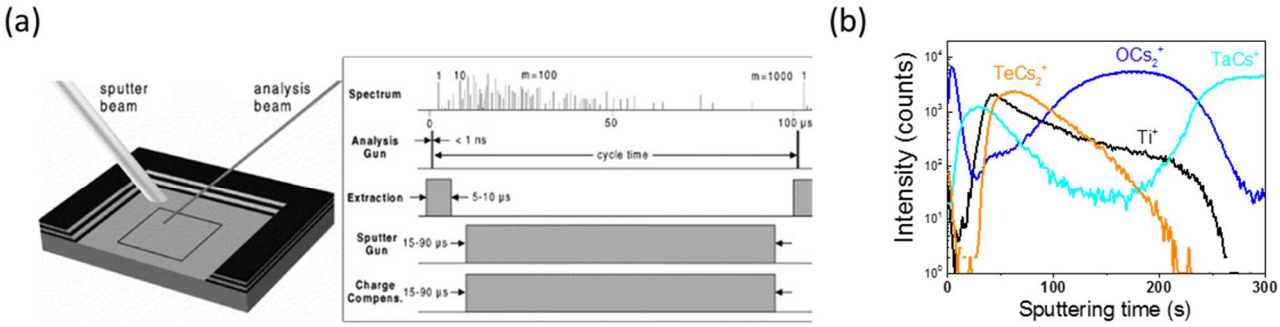

Figure 2.34 (a) ToF-SIMS dual beam depth profiling illustration, from Grehl et al. [119], (b) ToF-SIMS depth profile.

The signal intensity of the detected secondary ions can be expressed by the following formula:

$$I_m = I_p\ y_m\ \alpha^{+/-}\ \theta_m\ \eta \qquad 2.28$$

where I_m is the secondary ion current of species m [A], I_p is the primary ion flux [A/cm²] $\in [10^{-12};10^{-8}]$, y_m is the sputter yield y_m =[emitted ion]/[incident ion], $\alpha^{+/-}$ is the ionization probability$\in [10^{-3};10^{-8}]$, Θ_m is the fractional concentration of species m in the surface layer and η is the transmission of the analysis system $\in$ [0.9;0.95].

The secondary ion current depends on two fundamental parameters: the sputter yield y_m and the ionization probability a. Both are relatively low and vary according to the sample characteristics. The sputter yield is expressed as the ratio between the total number of emitted particles of species m (neutral and ionic) and the total number of primary ions[118].

The processes involved in the atoms ionization are not well understood. Different models have been proposed to explain the ionization process i.e. secondary ions formation mechanism. The two most commonly used models describing ionization are the tunneling model and the bond breaking model. The tunneling model is applied to conductive or semiconducting samples. In this case during the interaction of the primary ions with the surface atoms, there is an exchange of electrons which favors the ionization of the atoms. Whereas for ionic bonds (A^+B^-) the dissociation can be explained by the bond breaking model where the incident energy of the primary ions is sufficient to break the ionic bonding.

A Cesium gun favors the reduction of the top layer and so the extraction of electronegative atoms[120], whereas an oxygen gun promotes the oxidation and thus the extraction of electropositive atoms[121].

Oxidation process with O_2^+: $M \rightarrow M^+ + e^-$ 2.29

Reduction process with Cs^+: $M + e^- + Cs^{\cdot} \rightarrow M^-$ 2.30

In this way we can choose to analyze more specifically negative or positive ions by selecting the appropriate gun. The Figure 2.35 shows the relative efficiency of the sputtering for each atom regarding the primary ion gun.

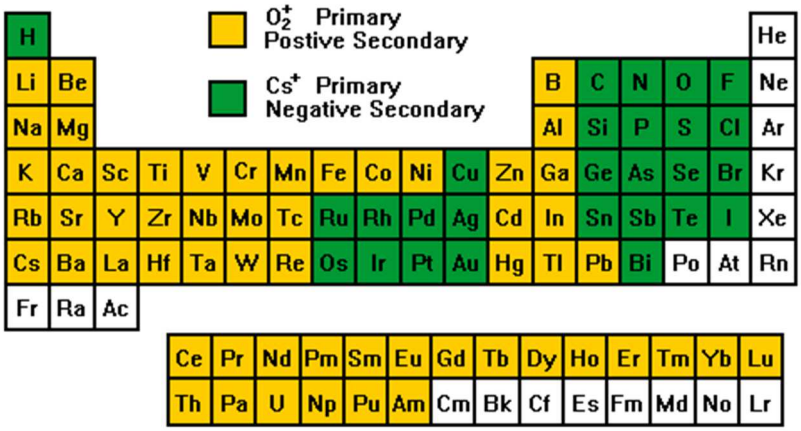

Figure 2.35. The yellow compounds are electropositive and will be better sputtered with O_2^+ into positive ions. The green ones are electronegative and extracted as negative ions with Cs^+, from [122].

There is also a second process consisting in the recombination of neutral chemical species M with the reactive Cs^+. When entering in contact with the surface, the primary ions form some clouds of matter where neutral particles gathered with the incident ones and create MCs^+ or MCs_2^+ compounds as shown below:

Dimer: $M + Cs^+ \rightarrow MCs^+$ 2.31

Trimer: $MCs^+ + Cs^+ \rightarrow MCs_2^+$ 2.32

The ionisation yield for MCs_n^+ is higher in comparison to the atomic element M, but this method is limited only to Cs^+ bombardment[123].

2.4.2. ToF-SIMS instrumentation

Figure 2.36 shows the geometry of the ToF-SIMS V (IONTOF) used in this study with the analysis chamber, the two ion sources tilted at 45° with respect to the normal of the sample, the time of flight analyzer and detector. The instrumentation presented below is related to ToF-SIMS V instrument used to analyze the samples of this thesis.

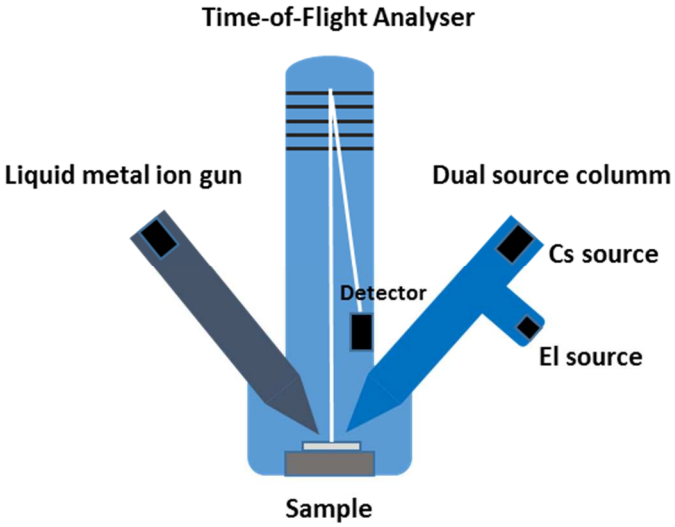

Figure 2.36. Schematic of the ToF-SIMS used in this work with the two ion sources tilted of 45° with respect to the normal of the target.

2.4.2.1. Primary ion guns

There are two kinds of primary ion guns. The analysis sources are pulsed and used to get spectrometric information about the surface. On the other hand, the sputtering sources deliver continuously primary ions in order to dig the surface and get a volume information. Both sources are associated with an optical column composed of electrostatic lenses used to focalize correctly the beam onto the surface.

- **Liquid Metal ion gun (LMIG)**

The Liquid Metal ion gun (LMIG) is used as primary ion source. With this source it is possible to generate monoatomic Ga, and Bi ion beams or polyatomic (i.g. Bi_3^+) ion beams. Figure 2.37 shows a schematic of a LMIG emitter. The first step of the process consists in heating the metal inside of a needle (e.g. Ga, Bi) to a liquid state using a heater filament. A positive voltage (around 10 keV) is applied forming a Taylor cone between the tip of the needle and the extractor due to the potential difference. The stream of positive charged ions induced by the field is then selected by deflection plates to obtain a single type of aggregate in the beam i.e. Bi^+ or Bi_3^+. During this phase, the flux is also deflected to assure the pulsing. The ions entering the first deflection plate with different m/z, travel at different velocities. The ions with desired m/z can be selected by the application of a deflection pulse equal to the time that takes an ion to reach the center of the second plate. A pulsed primary ion beam pulsed is necessary since the analyzer works by measuring the time of flight and the mass resolution depends of the pulse width. The mass resolution is improved by using short pulses (usually 1 ns or less). However, the use of a short pulse decreases the beam intensity. To solve this problem, a relatively longer pulse is applied (~20-40 ns), but with an additional buncher placed after the deflection plates to group the ions. As a result, the ion packet hits the sample over a shorter pulse.

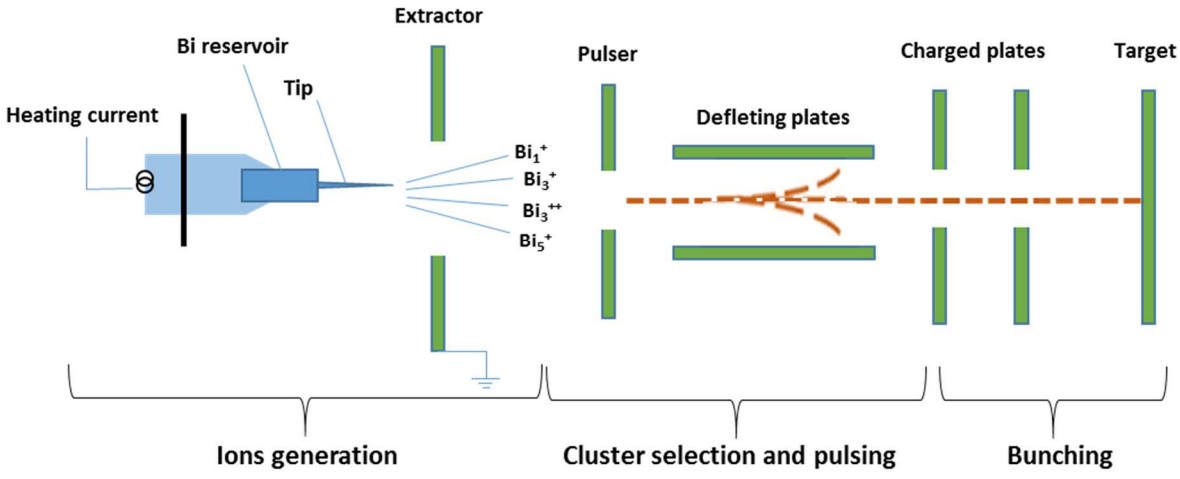

Figure 2.37. Schematic principle of a liquid metal ion gun (LMIG).

- **Ion gun for sputtering**

The Dual Source Column showed in Figure 2.36 is generally equipped with a source of surface ionization (in this case, Cs^+) and another source of ionization by electron impact (EI) (O_2 and Xe). Figure 2.38 (a) shows a schematic of a Cs surface ionization source. This source contains a solid Cs reservoir that generates Cs vapor after being heated. The vapor generated is driven to a heated porous W plug. As the W work function is superior to Cs ionization potential, electrons from Cs are trapped forming Cs positive ions (Cs^+). These ions are then extracted from the W plug surface and injected into the optical column.

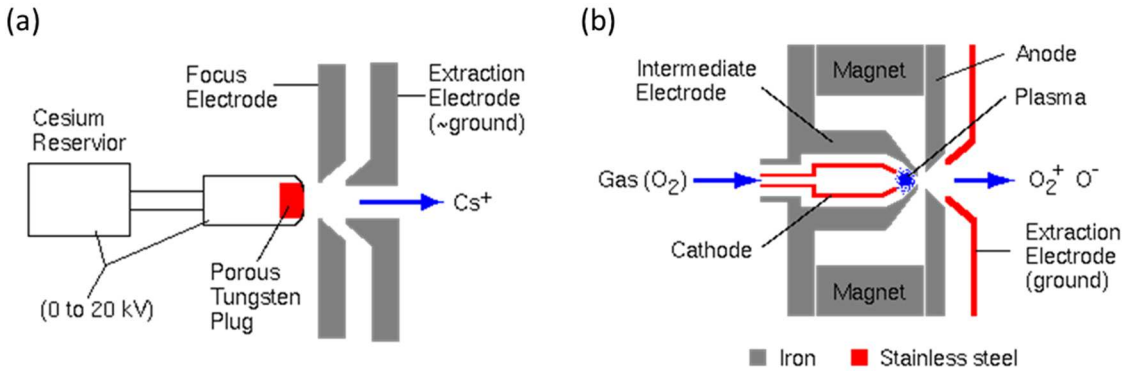

Figure 2.38. Schematic of a) the Cs surface ionization source and b) gas ionization by electron impact source, from [124].

Figure 2.38 (b) shows a schematic of an electron impact ionization source (EI). This technique is used to generate ions from gaseous species such as noble gases (He, Ar, Xe…) or oxygen O_2. Firstly the gas is injected in the source and it is bombarded by an electron flux. The generation of charged particles (i.g. O_2^+) occurs by the impact of electrons with the gas atoms. After that, the ions are injected into the optical column induced by an electric field generated by a reflector.

2.4.2.2. ToF-SIMS analyzer

Figure 2.39 (a) shows the analyzer of the ION-TOF ToF-SIMS 5 instrument. It is composed by a UHV tubular shaped chamber. In this chamber, the secondary ions are separated according to their m / z ratio as descripted in section 2.4.1. An electrostatic mirror, named reflectron, is placed at the extremity of the flight chamber. This device increases the ions separation without needing a tube's length augmentation and thus improves the mass resolution. The first gridless reflectron is used to perform time focusing of the ions, the second is an adjustable reflectron voltage (VDP) employed to compensate the difference of initial kinetic energy between ions with same mass. Ions with the same mass but with different kinetic energies (KE) will

penetrate at different depths in the reflectron. While ions with a higher KE will penetrate deeper in the electrostatic field, the ions with a lower kinetic energy will penetrate less in order to arrive at the same time on the detector as shown in Figure 2.39 (b).

At the end of the analyzer, the secondary ions are post-accelerated by the application of a voltage onto the Multi-Channel Plate detector MCP.

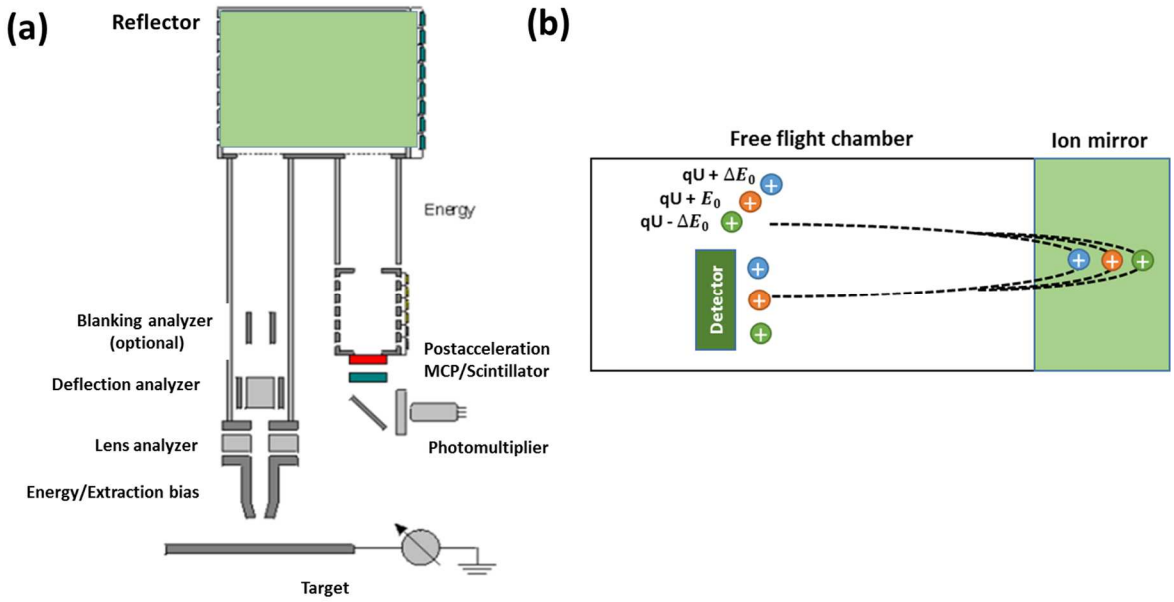

Figure 2.39. Schematic of a (a) TOF analyzer (from ION-TOF SurfaceLab) (b) Principal reflectron.

2.4.2.3. Flood gun

For the analysis of insulating materials, primary ions and pulsed low-energy electrons are used simultaneously to prevent charge accumulation on the sample from primary ion beam. The use of low energy electrons avoids the change in surface potential which disturb secondary ion emission and consequently the time of flight. These low energy electrons are produced by a flood gun as shown in Figure 2.40. It consists mainly in a filament heated with a voltage (around 2.5 V), a Wehnelt electrode for optimization of the electron beam current, and extraction electrodes. The energy of the electrons is determined by the voltage applied to the filament, which is adjustable (0-21 V).

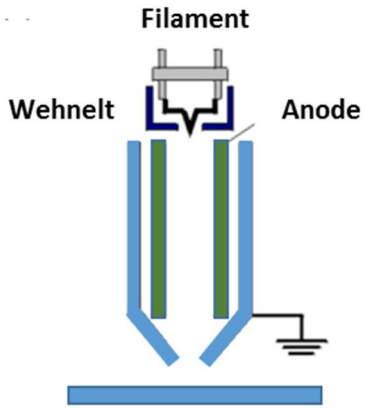

Figure 2.40. Schematic of a flood gun.

2.4.3. ToF-SiMS parameters applied to analyze CBRAM cells

In this thesis ToF-SIMS depth profiling was used to study the ions diffusion during the resistive switching of the CBRAM cells. ToF-SIMS data were collected using an ION-TOF ToF-SIMS 5 instrument. The analysis beam for this study was generated by a 25 keV bismuth source, utilizing a Bi^{3+} rastered over an area of 80 × 80 µm. Cesium ions were used for sputtering, rastered over a 300x300 µm² area, at an impact energy of 500 eV. Both beams were incident at 45°.

The sputter beam was operated at low energy and the primary ion beam at very low current to minimize sputter-induced artefacts and preserve the depth resolution. ToF-SIMS depth profiling was carried out in positive ion data collection mode (M^+) and using MCs^+ or MCs_2^+ clusters.

Chapter 3

3. Direct forming mechanism of Te-based conductive-bridge memories

As described in the chapter 1 the switching mechanism of a CBRAM is based on applying voltage or current pulses to a solid electrolyte. Ionic diffusion from the active electrode into the electrolyte creates a conductive bridge between the two electrodes. Recently, special attention has been drawn to devices containing an elemental semiconductor such as tellurium, operating with reduced currents and less retention failures [8]. The current required to program a standard CBRAM cell is directly related to the conductance of a 1-atom filament (G_{1atom}). For metals, G_{1atom} is comparable to the quantum $G_0=2e^2/h$, whereas for a semiconductor such as Te, it is sub-quantum (0.03 G_0) enabling operation at low currents as shown in Figure 3.1 for Ag- and Te-based cells [8].

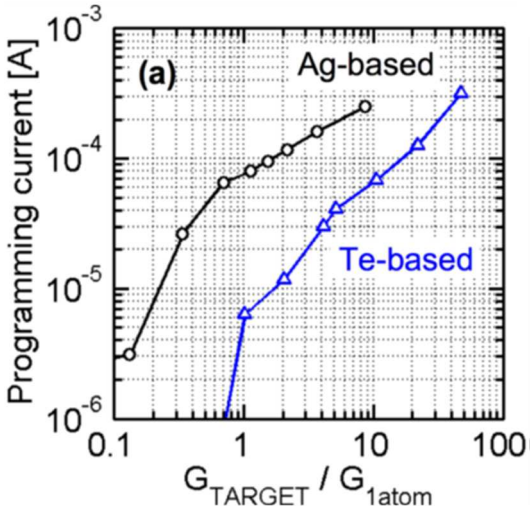

Figure 3.1. Comparison between the median programming current of the subquantum Te-based CBRAM cells and of the Ag-based cells for target conductances ranging from 10 G_{1atom} to 1G_{1atom}. Adapted from [8].

Subquantum CBRAMs based on an Al_2O_3 electrolyte and an active top electrode of a Te binary alloy such as ZrTe, TiTe and HfTe, are the most promising systems reported in the literature, with cell operating current and power as low as 10 µA and 0.01 mW [8]. The conductive bridge of such memory cells was attributed to the migration of tellurium through the alumina. Jameson at al. suggested that a possible mechanism for Te release might be the oxidation of Zr by scavenging from the alumina, yielding a sub-

stoichiometric electrolyte. Oxygen vacancies ($V_O^{\bullet\bullet}$) are thought to provide preferential paths for Te migration across the alumina. These assumptions were based on a detailed analysis of electrical characterizations, but no direct proof has been reported yet in the literature. In this chapter, we bring information about the electrochemical mechanisms involved in resistive switching. In particular, we confirm the key role of the ZrTe/Al_2O_3 interface chemistry in the switching mechanism.

We first investigated electrochemistry of the resistivity change during the direct forming of ZrTe/Al_2O_3 based CBRAMs. The direct forming occurs when a positive bias is applied on the top electrode to form the filament. We have used hard X-ray photoelectron spectroscopy (HAXPES) to probe the buried interface between the ZrTe active electrode and the Al_2O_3 layer. Measurements were performed on as-grown samples and after *ex-situ* forming, referred to as as-grown and formed. In addition, we have used XPS and ToF-SIMS depth profiling to investigate the oxygen, tellurium and zirconium migration. In the second part of this chapter, we have studied the resistive switching for TiTe/Al_2O_3-based devices. TiTe features a retention behaviour controlled by a similar critical conductance as that for ZrTe [8] . The investigation of this memory cell mechanism is important since not all binary alloys of Te favor the formation of a semiconductor filament. For example, in the case of the $CuTe_x$ the filament is formed preferentially by Cu [48]. Therefore, it is necessary to understand the role of the metal and the semiconductor during the resistance switching for each Te-based electrode variant.

3.1. Investigation of ZrTe/Al_2O_3 based CBRAM

The first part of this study will describe the CBRAM samples and the electrical characterization of the resistive switching process. The second part will show the results obtained from the HAXPES experiments performed at the BL15XU beam line of the Japan Synchrotron Radiation Research Institute (SPring-8), using a photon energy of 7.9 keV. The third part is a comparison of HAXPES results using different photon energies to obtain a depth profile of the sample. The experiments were performed at the GALAXIES beamline of the SOLEIL synchrotron using 6.9 keV and 8 keV photon energies. In the last part, we will show the depth profiling results obtained using two methods: laboratory XPS depth profiling analysis carried out with a monochromatic Al Kα source (hν = 1486.7 eV) and an argon gas cluster ion beam (GCIB) and ToF-SIMS depth profiling.

3.1.1. CBRAM sample based on $ZrTe/Al_2O_3$

The memory cells were composed of a 5 nm Al_2O_3 layer sandwiched between two metallic electrodes. The bottom electrode was a 200 nm-thick Ta layer, deposited on a 200 mm Si (100) wafer, followed by the alumina deposition. A ZrTe metallic alloy was then deposited through a mask, to obtain 2 mm diameter active, top electrodes as shown in Figure 3.2. The electrodes and Al_2O_3 layer were deposited by physical vapor deposition.

The ZrTe growth process was optimized to reach a Zr/Te stoichiometry of 40/60 prior to the deposition. The composition was checked by rutherford backscattering spectrometry (RBS). The result of this analysis showed that the ZrTe layer is formed by 60.5 at. % of tellurium and 39.5 at. % of zirconium, with a Te/Zr ratio of 1.5 as expected. The base pressure in the deposition chamber was $5x10^{-4}$ mbar. Finally, a 5 or 15 nm TaN (TiN) capping layer was deposited by reactive sputtering to prevent oxidation of ZrTe when exposed to air. The details of the deposition process are described in chapter 2.

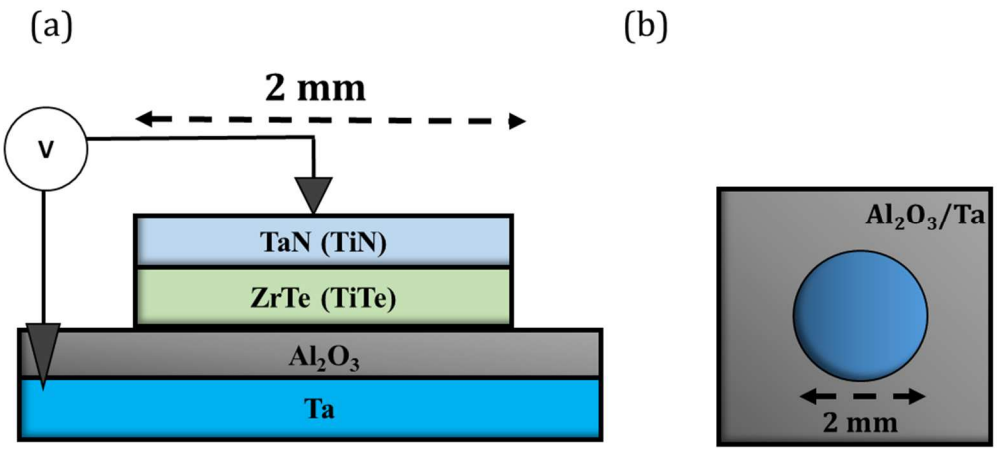

Figure 3.2. (a) Schematic of the setup for electrical characterization and (b) top view of the CBRAM cells.

Table 3.1. summarizes the slightly different stacks prepared for each physical-chemical characterization used to analyze the resistive switching. Measurements were first done with a TaN protective layer. We then changed to TiN in order to better distinguish the signals from the top and bottom electrodes. Their thicknesses were adapted for each experiment taking into account the depth sensitivity of the analyses. These variations can affect the long-term behavior of the devices, such as for example the cycling endurance of the cell. But it is important to mention that these changes do not induce major short-term changes in the mechanism of the memory. Therefore, as the focus of this work was the forming process (the first switch from the HRS to the LRS), the long-term variations can be neglected.

Table 3.1. Sample composition for each physical-chemical characterization.

	Protective layer (5 nm)	Active electrode	Electrolyte (5 nm)	Section
HAXPES (Spring-8)	TaN	ZrTe (15 nm)	Al_2O_3	3.1.3.1
ToF-SIMS				3.1.5
HAXPES (SOLEIL)	TiN	ZrTe (5 nm)		3.1.3.2
XPS depth profiling	TiN (15 nm)	ZrTe (10 nm)		3.1.4

3.1.2. Electrical characterization of the ZrTe/Al_2O_3 based sample

In order to protect the oxide layer from irreversible damage during the bias application, it is necessary to estimate the breakdown voltage of the Al_2O_3 layer. The breakdown voltage defines the maximum voltage that can be applied to an insulator before it becomes conductive. According to McPherson et al. [125] the breakdown voltage of a dielectric material decrease when the dielectric constant (κ) increases and the breakdown field E_{BD} can be estimated from the empirical equation below:

$$E_{BD}\ (\mathrm{MV.cm^{-1}}) = 29.9\ (\kappa)^{-0.65} \qquad 3.1$$

Therefore, taking into account the thickness of 5 nm and a dielectric constant of 9 the estimated voltage breakdown of the Al_2O_3 layer is 3.6 V. This value was used as a reference during the electrical characterization to avoid the irreversible breakdown of the cells.

Forming was performed in ambient atmosphere using a Keithley 2635B. The Ta bottom electrode was grounded. A linear positive voltage sweep between 0 and +4V at 0.1 V/s was applied by an Au tip with minimum contact force on the top electrode, i.e. the tip approach on the top electrode was carefully made to ensure the electrical contact without damaging the surface of the sample (see Figure 3.2 (a)). The electrical contact to the bottom electrode was made with a W tip. Standard electrical connections cannot be used due to the ultra-thin alumina layer which can be easily short-circuited by mechanical or thermal stress.

Figure 3.3 (a) shows the I-V characteristic of the forming step of the TaN/ZrTe/Al_2O_3/Ta stack used to perform the HAXPES analyses at Spring- 8. The current increases abruptly by three orders of magnitude to the 50 mA compliance current at 3.3 V. This is the forming process, during which conductive paths are created through the insulating dielectric layer. The device resistance measured before and after forming are $R_{As\text{-}grown}$ = 2.0x10^7 Ω and R_{Formed} = 2.5x10^2 Ω. The resistance ratio $R_{As\text{-}grown}$ / R_{Formed} = 1.0x10^5 shows a change of five orders of magnitude in the device resistivity after the forming process. Figure 3.3 (b) presents a current - voltage (I-V) curve for the forming and reset processes measured on a similar memory stack. In this curve, it

is possible to observe, by the application of opposite polarity, the reset operation switching the memory from the low-resistance state (LRS) to the high-resistance state (HRS) at -1.4 V.

The compliance current of 50 mA (16 $mA.mm^{-2}$) was chosen low enough to avoid a dielectric breakdown of the oxide but sufficiently high to generate important chemical modifications in the insulating layer or at the interfaces with the electrodes, facilitating the detection [126]. The reset process showed in Figure 3.3 (b) confirms that the oxide was not irreversibly damaged during the bias application and the ability to switch the resistance of the cell using this value of compliance current. As showed in Figure 3.4 a higher I_{cc} = 100 mA was also tested for this sample but the bias application with this I_{cc} caused a permanent breakdown of the oxide i.e. the switching the memory under negative polarization from the low-resistance state (LRS) to the high-resistance state (HRS) was not possible.

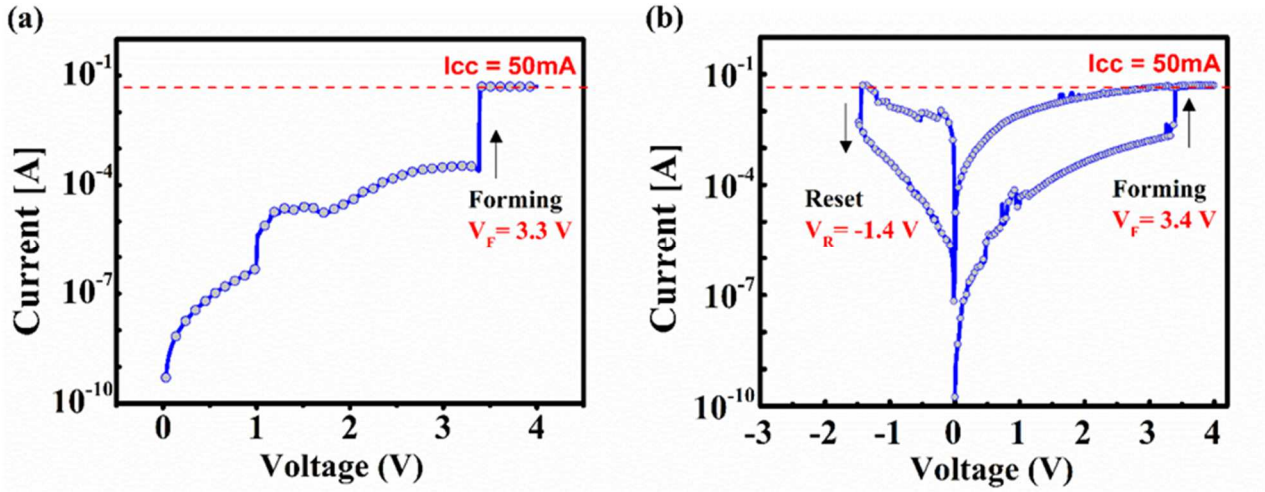

Figure 3.3. (a) Current - voltage (I-V) curve for the forming of the TaN/ZrTe/ Al_2O_3/Ta stack. (b) Current - voltage (I-V) curve for the forming and reset of the TaN/ZrTe/ Al_2O_3/Ta stack used on the Spring- 8 HAXPES measurements.

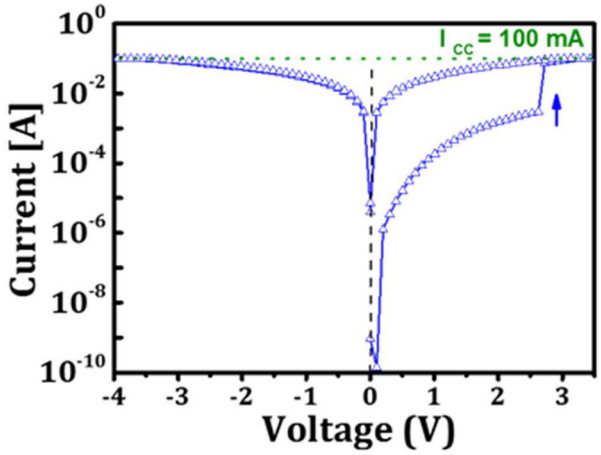

Figure 3.4. (a) Current - voltage (I-V) curve obtained using an I_{cc} = 100 mA for the sample used on the Spring-8 HAXPES measurements.

While an I_{cc}= 50 mA protected the cell used on the Spring- 8 HAXPES measurements of an irreversibly damaged, for the sample used on the HAXPES measurements performed at SOLEIL (see Table 3.1) an I_{cc}= 50 mA led to an irreversible breakdown of the oxide as showed in Figure 3.5 (a). Thus, for this sample we have used an I_{cc} of 8 mA to perform the forming step as described in Table 3.2. The reset process showed in Figure 3.5 (b) confirms that this lower I_{cc} protected the oxide of a permanent breakdown.

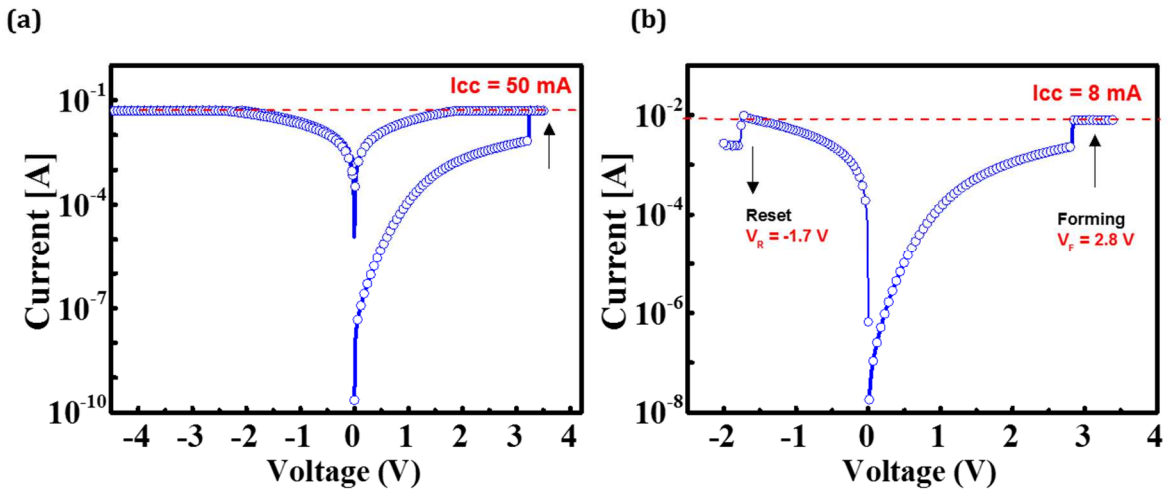

Figure 3.5. (a) Current - voltage (I-V) curve obtained using an I_{cc} = 50 mA and (b) Current - voltage (I-V) curve for the forming and reset of the TiN (5 nm)/ZrTe(5 nm)/Al_2O_3(5 nm)/Ta stack for the sample used on the SOLEIL HAXPES measurements using an I_{cc} = 8 mA.

In this chapter, we focus our attention on the critical forming step which has a key role for the devices operation. Table 3.2 summarizes the results of the electrical characteristics of the samples used for the HAXPES experiments performed at SOLEIL (section 3.1.3.2.) as well as for the XPS (section 3.1.4) and ToF-SIMS (section 3.1.5) experiments.

Table 3.2. Electrical characteristics of the samples analyzed by different experiments

Experiment	$R_{As\text{-}Grown}$ (10^5 Ω)	R_{Formed} (10^2 Ω)	$R_{As\text{-}Grown}/R_{Formed}$ (10^2 Ω)	I_{cc} (mA)	V_F (V)
HAXPES Spring-8	200	2.5	1000	50	3.3
HAXPES SOLEIL	5.0	1.2	40	8.0	2.8
XPS depth profiling	2.5	9.0	2.8	50	3.3
ToF-SIMS depth profiling	1.0	1.4	7.1	50	3.0

Electrical measurements were performed on ten cells. The average forming voltage of 3.0 V and an average reset voltage of -1.2 V are obtained. All the values are below the breakdown voltage of the Al_2O_3 layer, to induce resistive switching without irreversible damages. The average initial and final resistances are of $2.5x10^5\,\Omega$ and $1.4x10^2\,\Omega$ respectively.

3.1.3. Hard X-ray photoelectron spectroscopy (HAXPES) analysis

Using hard X-rays, the electron mean free path is considerably increased providing sufficient depth sensitivity to reach the buried interfaces and thus provide information about the redox processes occurring in the electrode and in the electrolyte region, as described in chapter 2.

This study was divided in two parts. In the first part, the CBRAM cell was analysed using a photon energy of 7.9 keV. This energy made possible the chemical analysis of all layers involved in the resistive switching. The second part was an opportunity to obtain supplementary information about the forming process using different photon energies (at 6.9 keV and 8 keV), thus varying the sampling depth. This experimental approach provided information about the depth distribution of the species in the stack before and after the bias application.

3.1.3.1. HAXPES – 7.9 keV

These HAXPES experiments were performed at the BL15XU beam line of the Japan Synchrotron Radiation Research Institute (SPring-8). A photon energy of 7.9 keV with an overall energy resolution (beamline and spectrometer) of 243 meV were used. The inelastic mean free paths (λ), estimated with the Tanuma equation [94] for Ta $3d_{5/2}$, Al 1*s*, Zr $3p_{3/2}$ and Te $3d_{3/2}$ photoelectrons in the stack, were 10.8, 9.2, 10.7 and 10.4 nm, respectively. These values are obtained by averaging the IMFPs estimated for each layer crossed by the photoelectrons during their transport toward the surface. The average was weighted by the thickness of each layer as described in section 2.3.3.1. Corresponding sampling depths (3λ) of 27.6, 32.1 and 31.2 nm allow probing the ZrTe electrode and alumina layer.

The area of the x-ray spot on the sample surface was 300*40 μm^2. Photoelectrons emitted at an angle of 80° with respect to the surface were collected with a VG Scienta R4000 hemispherical analyzer, with a slit size of 0.5 mm. The binding energy was calibrated relative to the Fermi level measured from a clean gold surface. Subtracted backgrounds for XPS spectra were of Shirley type [84], and the oxide peaks were modeled using a combination of Lorentzian (30%) and Gaussian (70%) functions while the metallic core lines were fitted using a Doniach-Sunjic function [127] using Casa XPS v2.3 software. The peaks fit for each element was made establishing constrains on components positions and fixing the separation between each chemical state. The parameters used to fit the HAXPES peaks are presented in Table A.1 and in Table A.2 (Binding

Energies) in annex A.

HAXPES measurements were performed on as-grown and formed TaN/ZrTe/Al_2O_3/Ta stacks, and also on the bare Al_2O_3/Ta structure outside the top electrode (see Figure 3.2), in order to provide a reference spectrum for aluminum and tantalum present in the electrolyte and bottom electrode. Each peak was normalized relative to the intensity of the background measured at high kinetic energy. The photoelectron recoil effects [111] were estimated from E_{kin} (m/M) where E_{kin} is the photoelectron kinetic energy, m is the electron mass and M the atomic mass. The estimated recoil energy for Ta $3d_{5/2}$, Al 1s, Zr $3p_{3/2}$ and Te $3d_{3/2}$ core levels are 0.018, 0.13, 0.045 and 0.03 eV, respectively. Apart from the recoil of the Al 1s, all are less than the observed energy chemical shifts and can therefore be neglected.

Figure 3.6 shows the Ta $3d_{5/2}$ core level spectrum measured on the bare Al_2O_3/Ta structure outside the top electrode together with the best fit. This spectrum is asymmetric at higher binding energies suggesting the presence of an additional component. Indeed, a second component must be used in this case to obtain a satisfactory fit. The first component is characteristic of metallic Ta at 1731.5 eV [128] and the second component at 1733.4 eV is attributed to tantalum sub-oxide (TaO_x). The latter demonstrates that there is tantalum oxide at the Al_2O_3/Ta interface. The relative areas of these components are given in the Table 3.3. This result shows that the deposition of the alumina layer caused an oxidation of the Ta bottom electrode.

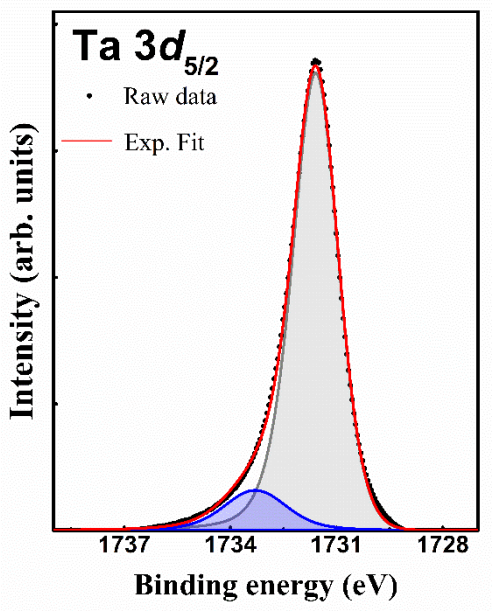

Figure 3.6. (a) Ta $3d_{5/2}$ core level spectrum obtained at 7.9 keV photon energy on the bare Al_2O_3/Ta structure.

Table 3.3. Relative areas (%) of the Ta $3d_{5/2}$ components for the Al_2O_3/Ta stack obtained at 7.9 keV photon energy

	Ta	TaO_x
Al_2O_3/Ta	88.8 ± 8.8	11.2 ± 1.1

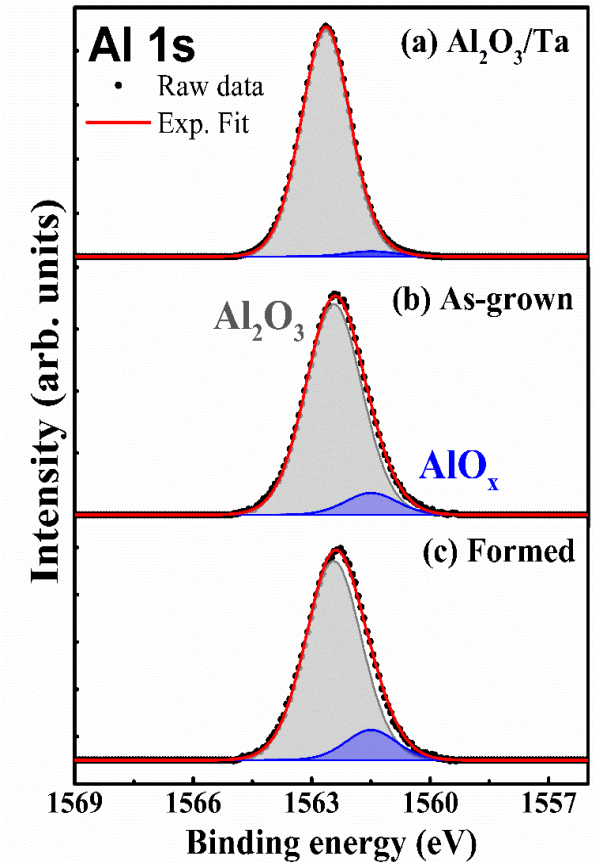

Figure 3.7. Al 1*s* core level peaks obtained by HAXPES on: a) the Al_2O_3/Ta stack, b) as-grown and c) formed states of the TaN/ZrTe/ Al_2O_3/Ta stack.

The Al 1*s* core level spectra outside the top electrode, i. e. for the Al_2O_3/Ta structure, for the as-grown and formed states are represented in Figure 3.7 together with the best fits and the overlap of these spectra is presented in Figure A.1 and A.2 in annex A. As discussed before, the Ta $3d_{5/2}$ spectra measured on the bare Al_2O_3/Ta structure showed an oxidation of the bottom electrode (see Table 3.3) at the Al_2O_3/Ta interface probably due to oxygen scavenging from the overlying Al_2O_3 layer, leading to a reduction of this layer during the deposition process. Therefore, the decomposition of these Al 1*s* spectra took into account two contributions: aluminum sub-oxide (labeled AlO_x) at binding energy (BE) of 1561.5 eV and alumina (Al_2O_3) at 1562.4 eV. The relative areas of these components are given in the Table 3.4.

Table 3.4. Relative areas (%) of the Al 1*s* components for the Al_2O_3/Ta stack, as-grown and formed samples.

	Al_2O_3	AlO_x
Al_2O_3/Ta	97.8 ± 9.7	2.2 ± 0.2
As-grown	91.3 ± 9.1	8.7 ± 0.8
Formed	88.0 ± 8.8	12.0 ± 1.2

These results showed an increase of the sub-oxide contribution (AlO_x at 1561.5 eV) relative to the main contribution (Al_2O_3 at 1562.4 eV) for the as-grown and formed states with respect to the Al_2O_3/Ta structure. Regarding the as-grown state, it means that the ZrTe top electrode deposition gives rise to a significant reduction of the underlying alumina layer.

On forming, our results showed a further reduction of the Al_2O_3 and an increase of the AlO_x contribution (+3.3 %).

Figure 3.8 presents the Zr 3$p_{3/2}$ spectra for as-grown and formed samples the overlap of these spectra is presented in Figure A.3 in annex A. In Al 1*s*, there is a reduced component implying oxygen scavenging by the ZrTe hence probable formation of ZrO_2. Therefore, the spectra have been fitted considering two contributions. The first component at 330.2 eV was fitted using a Doniach-Sunjic [127] function and it is characteristic of the ZrTe alloy. The second component at 332.9 eV was fitted using a Lorentzian-Gaussian function and it is characteristic of ZrO_2[129].

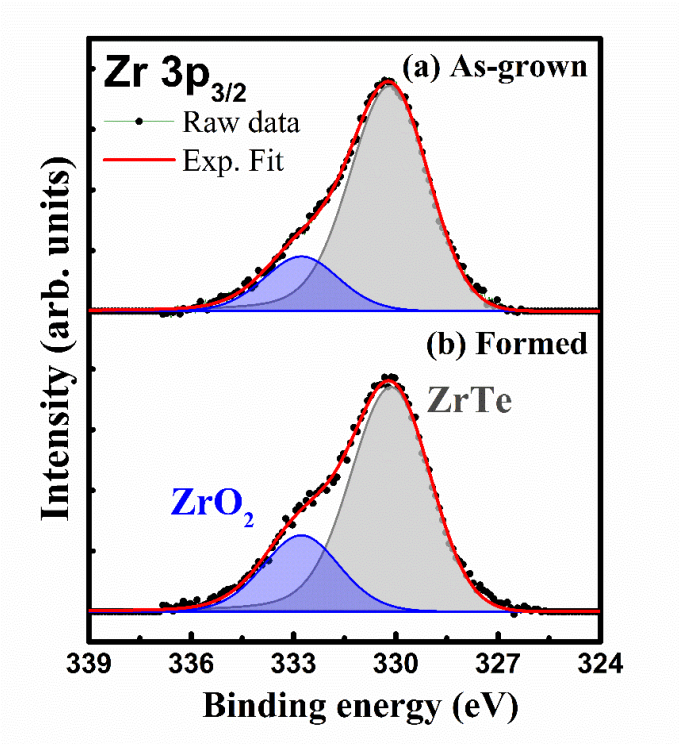

Figure 3.8. Zr 3$p_{3/2}$ core level peaks obtained by HAXPES on: a) as-grown and b) formed states of the TaN/ZrTe/ Al_2O_3/Ta stack.

Table 3.5 shows the relative areas of the two components of the Zr $3p_{3/2}$ spectra for as-grown and formed samples. An increase of the ZrO_2 area (+4.6%) with respect to the main peak was observed after forming, consistent with the alumina reduction previously observed on the Al 1*s* core level.

Table 3.5. Relative areas (%) of the Zr $3p_{3/2}$ components for the as-grown and formed samples.

	ZrTe	ZrO_2
As-grown	79.0 ± 7.9	21 .0 ± 2.1
Formed	74.4 ± 7.4	25.6 ± 2.5

The Te $3d_{5/2}$ core level was not used in our measurements because of the overlap with the Ta *4*s core level. The Te $3d_{3/2}$ spectra measured for as-grown and formed samples are shown in Figure 3.9 the overlap of these spectra is presented in Figure A.4 in annex A. These asymmetrical peaks have been fitted using a Doniach-Sunjic function [127] by taking two contributions, considering that in addition to the Zr-Te bonds, Te-Te bonds are also possible as the Te/Zr ratio higher than 1 (1.5) and the presence of ZrO_2 bring evidence of a Te-rich environment. The first component at 582.6 eV is related with the ZrTe alloy and the second component at 583.4 eV is characteristic of elemental Te[130,131].

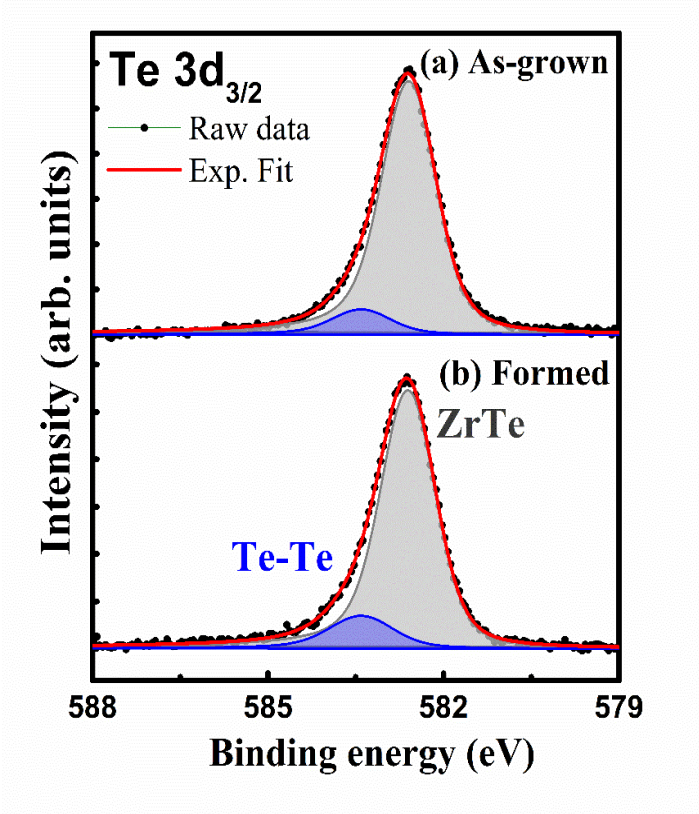

Figure 3.9. Te $3d_{3/2}$ core level spectra of a) as-grown and b) formed states of the TaN/ZrTe/ Al_2O_3/Ta stack.

Table 3.6. Relative areas (%) of the Te $3d_{3/2}$ components for the as-grown and formed samples.

	ZrTe	Te
As-grown	90.8 ± 9.0	9.7 ± 0.9
Formed	86.8 ± 8.6	13.2 ± 1.3

Comparison between the relative areas extracted from as-grown and formed spectra is presented in Table 3.6. This result showed a significant elemental tellurium increase (+3.5 %) during the forming process. This increase was similar to that of the ZrO_2 contribution. Thus it could be related to the detachment and migration of Te [8] or simply formation of Te-Te bonds inside the top electrode as a results of ZrO_2 formation following oxygen uptake from the alumina.

- **Discussion of the HAXPES results – 7.9 keV**

Our results showed that a complex chemical process occurs at the $ZrTe/Al_2O_3$ interface (ZrO_2 formation, Al_2O_3 reduction) yielding to a sub-stoichiometric aluminium oxide and consequential phase separation in ZrTe, giving rise to elemental Te. This behaviour can already be observed during the deposition of the top electrode on the alumina. 8.7% of Al was in a lower oxidation state compared to only 2.2% in the as-deposited Al_2O_3. This suggests a preliminary redox process at the $ZrTe/Al_2O_3$ interface creating oxygen vacancies ($V_O^{\bullet\bullet}$) in the alumina. Indeed, the formation of ZrO_2 is thermodynamically more favourable in comparison with Al_2O_3 formation, as shown by the Ellingham diagram in Figure 3.10[132].

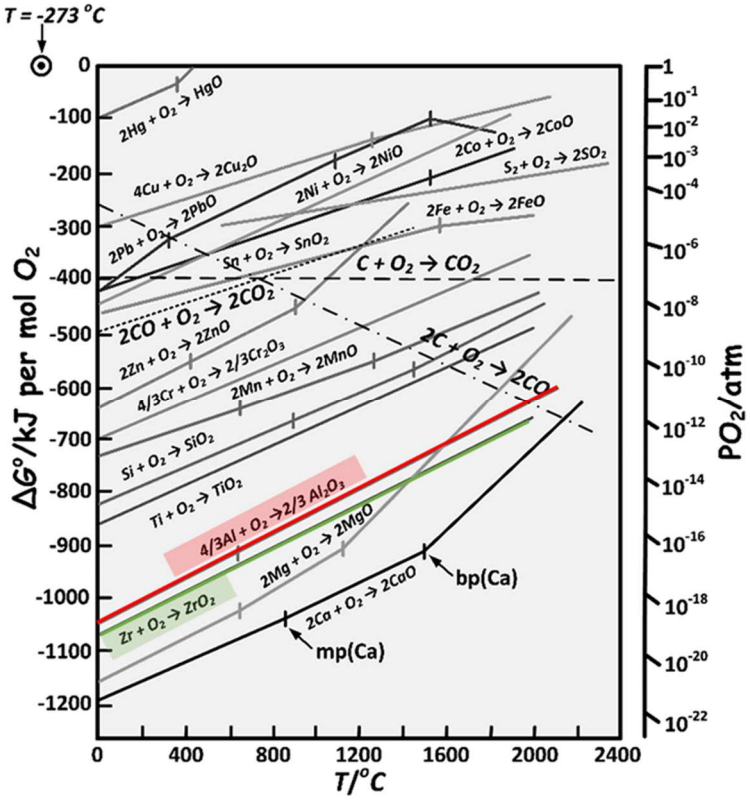

Figure 3.10. Ellingham diagram for the free energy of the formation of metallic oxides. Adapted from Greenwood et al. [132].

The creation of oxygen vacancies ($V_O^{\bullet\bullet}$) during the top electrode deposition process facilitates the creation of low resistance paths presumably via Te diffusion inside the electrolyte. We may consider the presence of oxygen vacancies (defects) in the electrolyte layer as a prerequisite to the forming process of CBRAMs cells. The enhancement of ions diffusion by $V_O^{\bullet\bullet}$ is supported by several studies [51,67,133]. These studies show that the energy cost to insert ions from the active electrode in the electrolyte decreases with the increase of $V_O^{\bullet\bullet}$.

After forming, the $V_O^{\bullet\bullet}$ concentration deduced from the AlO_x component has increased, with 12% Al in lower oxidation state compared to 8.7% in the virgin state. In parallel, the forming process caused Zr oxidation and Te release at the $ZrTe/Al_2O_3$ interface. We consider here that these observations are related to oxygen migration towards the active electrode under positive bias.

These results confirms the mechanism proposed by Jameson et al [8] described by:

$$ZrTe_x + O_2 \rightarrow ZrO_2 + xTe \qquad 3.1$$

This mechanism suggests that the Zr oxidation, by oxygen scavenging from the alumina during the positive bias application, causes a Te release. The Te transport is then assumed by the authors under an applied field through the oxide to create the filament.

Our results show that oxygen vacancies are not restricted to OxRRAMs. Several studies show an hybrid mechanism, i.e. a combination of both CBRAM (ions diffusion) and OxRRAM ($V_O^{\bullet\bullet}$ formation by oxygen transport) mechanisms to form the filament [51,67,68]. For example, according to Saadi et al.[51], the resistance transition can be divided in two stages. The first is the creation of oxygen vacancies and the second is the migration of the ions along $V_O^{\bullet\bullet}$ paths. Assuming this model, in our case, the forming can be divided in: 1) reduction of alumina and the formation of oxygen vacancies inside of the oxide followed by Zr oxidation and Te release at the ZrTe/Al_2O_3 interface, 2) Te migration through $V_O^{\bullet\bullet}$ paths towards the bottom electrode.

The HAXPES results provide a direct evidence of the chemistry of the first step of the proposed mechanism, i.e. Zr oxidation by oxygen scavenging from the alumina and, as a consequence, Te release. However, we must mention here that Zr oxidizes also at the upper TaN/ZrTe interface, due to the very thin TaN capping layer used for HAXPES. The regrowth of Zr oxide during forming is thus also possible due to oxygen insertion at the surface from ambient air. To avoid this external oxygen reservoir, in-situ XPS measurements were developed. The results are shown in chapter 5. Note that we can not rule out a possible Te liberation at the TaN/ZrTe interface, related to Zr oxidation.

- **Multilayer model**

A four-layer capacitor model [134,135] was used to quantify the redox process at the ZrTe/Al_2O_3 interface. We assumed that two distinct layers of ZrO_2 and AlO_x were formed with sharp interfaces yielding the structure shown in Figure 3.11. This is a first attempt to provide a quantitative insight which needs to be improved in the future. We need in particular to take into account the Zr oxide layer at the upper TaN/ZrTe interface for a better quantification. We also assumed that the released Te stays at the interface, and is located at the same level as the interfacial ZrO_2 layer, labelled ZrO_2 + Te-Te in Figure 3.11. This is equivalent to assuming a phase separation in the interfacial layer between the ZrTe and Al_2O_3.

As showed in chapter 2, the contribution of a surface layer (with a thickness d) to the XPS peak intensity follows the Beer Lambert law:

$$I(d) = I_\infty \left[1 - \exp\left(\frac{-d}{\lambda \sin\theta}\right)\right] \qquad 3.2$$

where θ is the angle between the surface of the sample and the collected electron trajectory, λ is the inelastic mean free path and I_∞ is the intensity collected for an infinite thickness.

To calculate the layer thicknesses, we considered the photoelectron intensities from each distinct chemical environment corresponding to Al_2O_3, AlO_x, ZrO_2 and ZrTe, given by the areas of the corresponding components of the Al 1*s* and Zr 3$p_{3/2}$ core level spectra. These intensities were calculated by the following equations, expressing the intensity attenuation for each layer crossed by the photoelectrons:

$$I_{ZrTe} = I^{\infty}_{ZrTe}\left[1-\exp\left(\frac{-d\,ZrTe}{\lambda\,\mathrm{Zr}}\right)\right] \quad 3.3$$

$$I_{ZrO2} = I^{\infty}_{ZrO2}\exp\left(\frac{-d\,ZrTe}{\lambda\,\mathrm{Zr}}\right)\left[1-\exp\left(\frac{-d\,ZrO2}{\lambda\,\mathrm{Zr}}\right)\right] \quad 3.4$$

$$I_{AlOx} = I^{\infty}_{AlOx}\exp\left(\frac{-d\,ZrTe}{\lambda\,\mathrm{Al}}\right)\exp\left(\frac{-d\,ZrO2}{\lambda\,\mathrm{Al}}\right)\left[1-\exp\left(\frac{-d\,AlOx}{\lambda\,Al}\right)\right] \quad 3.5$$

$$I_{Al2O3} = I^{\infty}_{Al2O3}\exp\left(\frac{-d\,ZrTe}{\lambda\,\mathrm{Al}}\right)\exp\left(\frac{-d\,ZrO2}{\lambda\,\mathrm{Al}}\right)\exp\left(\frac{-d\,AlOx}{\lambda\,\mathrm{Al}}\right)\left[1-\exp\left(\frac{-d\,Al2O3}{\lambda\,Al}\right)\right] \quad 3.6$$

where d_{ZrTe}, d_{ZrO2}, d_{AlOx} and d_{Al2O3} are the thicknesses of the ZrTe, ZrO_2, AlO_x and Al_2O_3 layers of the model. We assumed that the inelastic mean free paths of Al 1*s* and Zr 3$p_{3/2}$ photoelectrons were the same in all the layers of the stack and respectively equal to λ_{Al} = 9.2 nm and λ_{Zr} = 10.7 nm. This approximation leads to an uncertainty of ± 1.3 nm in the ZrO_2 layer estimation, considering that the value of λ_{Zr} was obtained by averaging the IMFPs estimated for each layer crossed by the photoelectrons as showed in equation 2.23 without taking into account the contribution of the IMPF estimated in the ZrO_2 layer ($\lambda_{\mathrm{Zr},ZrO_2} = 9.7$ nm). From equations (3.3) and (3.4), we can express the intensity ratio of the ZrO_2 and ZrTe contributions of the Zr 3$p_{3/2}$ core level:

$$\frac{I_{ZrO2}}{I_{ZrTe}} = \frac{I^{\infty}_{ZrO2}}{I^{\infty}_{ZrTe}}\exp\left(\frac{-d\,ZrTe}{\lambda\,\mathrm{Zr}}\right)\frac{1-\exp\left(\frac{-d\,ZrO2}{\lambda\,Zr}\right)}{\left[1-\exp\left(\frac{-d\,ZrTe}{\lambda\,Zr}\right)\right]} \quad 3.7$$

From equations (3.5) and (3.6), we can express the intensity ratio of the Al_2O_3 and AlO_x contributions of the Al 1*s* core level:

$$\frac{I_{Al2O3}}{I_{AlOx}} = \frac{I^{\infty}_{Al2O3}}{I^{\infty}_{AlOx}}\exp\left(\frac{-d\,AlOx}{\lambda\,\mathrm{Al}}\right)\frac{1-\exp\left(\frac{-d\,Al2O3}{\lambda\,Al}\right)}{\left[1-\exp\left(\frac{-d\,AlOx}{\lambda\,Al}\right)\right]} \quad 3.8$$

These ratios enable to estimate the thickness of the interfacial AlO_x and ZrO_2 layers, given that d_{AlOx}+ d_{Al2O3} = 5 nm and d_{ZrO2}+ d_{ZrTe} = 15 nm. We also assumed that the intensities of the semi-infinite blocks of the Al_2O_3 and AlO_x layers were equal. The same assumption was made for the ZrO_2 and ZrTe layers.

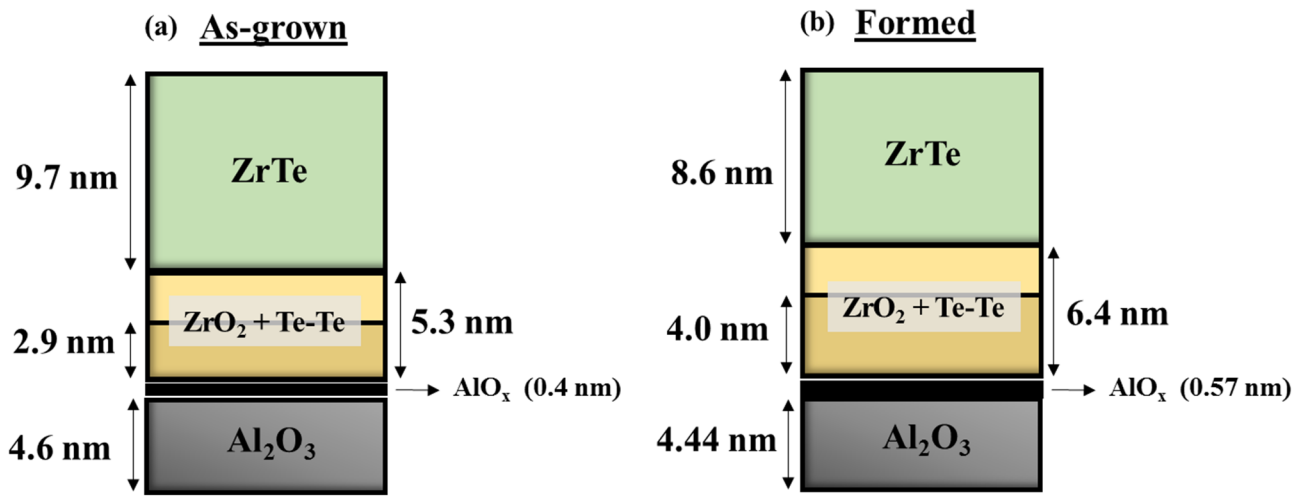

Figure 3.11. Four-layer capacitor model for the (a) as-grown and (b) formed samples.

The thicknesses of the ZrO_2 and AlO_x layers calculated using this model for the as-grown and formed samples are given in Table 3.7.

Similarly, the intensity ratio between the Te and ZrTe contributions extracted from the Te 3$d_{3/2}$ core level can be expressed as follows:

$$\frac{I_{Te}}{I_{ZrTe}} = \frac{I^{\infty}_{Te}}{I^{\infty}_{ZrTe}} \exp\left(\frac{-d\ ZrTe}{\lambda\ \mathrm{Te}}\right) \frac{1-\exp\left(\frac{-d\ Te}{\lambda\ Te}\right)}{\left[1-\exp\left(\frac{-d\ ZrTe}{\lambda\ Te}\right)\right]} \qquad 3.9$$

where $d_{Te\text{-}Te}$ is the thickness of the Te-rich layer formed near the interface and λ_{Te} is equal to 10.4 nm. From this last equation, we calculated the thickness of the interfacial Te-rich layer to be 2.9 and 4.0 nm, for the as-grown and formed samples respectively (see Table 3.7). The Te-rich layer is thinner by half compared to ZrO_2. Therefore, these results show that the ZrO_2 layer thickness was probably overestimated due to an additional ZrO_2 contribution on the Zr 3$p_{3/2}$ peak coming from Zr oxidation at the upper TaN/ZrTe interface. Indeed, the TaN capping layer did not completely prevent oxidation of ZrTe. This large discrepancy between the calculated thickness of the interfacial layer based on the Te or Zr signal is an evidence of the inadequation of this model with a single ZrO_2 layer. We will thus concentrate for further analysis on the Te signal.

Table 3.7. Estimated thicknesses of the ZrTe/ZrO_2+Te/AlO_x/Al_2O_3 stack extracted from the quantitative model and the Al 1s, Zr 3$p_{3/2}$ and Te 3$d_{3/2}$ core-level components intensities.

Sample	d AlO_x (nm)	d ZrO_2 (nm)	d Te (nm)	d ZrTe (nm)
As-grown	0.40	5.3	2.9	9.7
Formed	0.57	6.4	4.0	8.6

After the forming process, we saw an increase of 1.1 nm at the interfacial Te-Te layer (see Figure 3.11 (b)). This trend agrees with the redox process deduced from the detailed analysis of the Te 3$d_{3/2}$ peaks. The

electroforming enhances the Zr oxidation, releasing Te from the alloy. The released Te is confined near the ZrTe/Al_2O_3 with a possible extension inside the alumina. A small increase of the interfacial AlO_x layer was also obtained after the voltage application, confirming the creation of $V_O^{\bullet\bullet}$ inside the alumina layer. Assuming that this is an interfacial effect, our model showed that the AlO_x thickness is 0.17 nm higher after forming but very confined (~2 monolayers). However, this reduction process is probably not only located at the interface, but extends through the whole alumina layer, to achieve the formation of preferential conductive paths. Therefore, the AlO_x thickness obtained with our simplified multilayer model was probably underestimated.

The next section will show a study performed to obtain more insights about the possible Te diffusion during the positive bias application.

3.1.3.2. HAXPES with varying probing depths

A depth profile using different photon energies was performed on a sample TiN (5 nm)/ZrTe (5 nm)/ Al_2O_3 (5 nm)/ Ta (200 nm) (see Table 3.1) to obtain complementary information about the depth distribution of tellurium and zirconium before and after the forming process. These HAXPES analyses were performed at the GALAXIES beamline of the synchrotron SOLEIL[107,113]. The buried interfaces were probed by tuning the inelastic mean free path (λ) using photon energies of 6.9 and 8 keV. The overall energy resolution (beamline and spectrometer) was 110 and 160 meV for 6.9 and 8 keV photon energies respectively. The values of λ are estimated with the Tanuma equation [94] for Zr $2p_{3/2}$ and Te $3d_{3/2}$ photoelectrons and are given in Table 3.8. The X-rays beam spot size on the sample was 500 x 30 μm^2 (with an X-ray incidence angle of 10° with respect to the surface) and photoelectrons emitted at an angle of 80° with respect to the surface were collected with a hemispherical SCIENTA EW4000 electron analyzer. The binding energy was calibrated relative to the Au 4*f* level measured from a clean gold surface and also relative to the Ta $3d_{5/2}$ level measured on the Al_2O_3/Ta interface outside the device areas (as a stable internal reference).

Table 3.8. Inelastic mean free paths for photon energy of 6.9, and 8 keV. The sampling depth is defined to be 3 λ. [88]

	6.9 keV λ (nm)	8.0 keV λ (nm)
Zr $2p_{3/2}$	7.7 ± 1.5	9.4 ± 1.9
Te $3d_{3/2}$	10.1 ± 2.0	11.4 ± 2.3

Each peak was normalized relative to the background intensity measured at high kinetic energy. Figure 3.12 (a) presents the Zr $2p_{3/2}$ spectra fitted considering two contributions obtained by HAXPES at 6.9 keV and 8 keV. The low binding energy (LBE) component at 2222.9 eV was fitted using a Doniach-Sunjic

function and is characteristic of the metallic ZrTe alloy. The second component at 2224.3 eV was fitted using a Lorentzian-Gaussian function and is characteristic of ZrO_2. The relative areas are reported in Table 3.9.

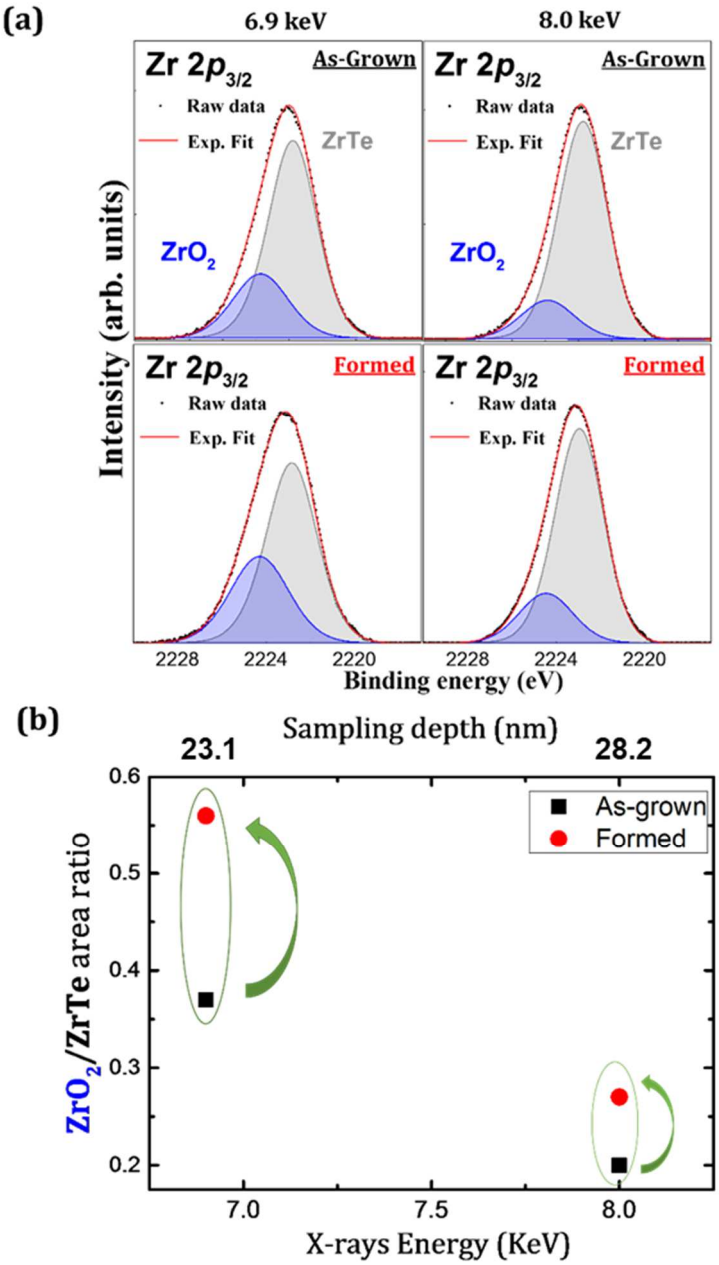

Figure 3.12. (a) Zr $2p_{3/2}$ core level peaks obtained by HAXPES at 6.9 keV and 8 keV on as-grown and formed samples of the TiN/ZrTe/Al_2O_3/Ta stack (b) ZrO_2/ZrTe area ratios extracted from the Zr $2p_{3/2}$ line area ratios measured at 6.9 and 8 keV for as-grown and formed samples.

Table 3.9. Relative areas (%) of the Zr 2$p_{3/2}$ components for the as-grown and formed samples obtained by HAXPES at 6.9 keV and 8 keV.

	6.9 keV		8 keV	
	ZrTe	ZrO_2	ZrTe	ZrO_2
As-grown	72.7 ± 7.2	27.3 ± 2.7	83.2 ± 8.3	16.8 ± 1.6
Formed	64.2 ± 6.4	35.8 ± 3.5	79.3 ± 7.9	20.7 ± 2.0

The redox process occurring at the ZrTe/Al_2O_3 interface is confirmed by the ZrO_2/ZrTe intensity ratio extracted from the Zr 2$p_{3/2}$ line. This ratio is compared at 6.9 and 8 keV photon energies and reported for the as-grown and formed samples in Figure 3.12 (b). During forming, the ZrO_2/ZrTe area ratio increases at all photon energies, indicating Zr oxidation all along the stack. This is related to the upward oxygen movement towards the top electrode attracted by the positive bias as previously discussed in section 3.1.3.1. However, as we can see in Figure 3.12 (b) the ZrO_2/ZrTe area ratio is higher at 6.9 keV (3λ = 23.1 nm) than 8 keV (3λ = 28.2 nm), indicating the presence of ZrO_2 also at the TiN/ZrTe interface. This result shows that surface oxidation is probably dominating the contribution of ZrO_2, thus preventing a detailed analysis of the Zr oxidation at the ZrTe/Al_2O_3 interface. Our results can thus not describe with accuracy the redox process at this buried interface during the resistive swithing. In addition, the Zr oxidation next the surface may also indicate that the capping layer not completely prevent oxidation of ZrTe as we will show in detail in chapter 5.

Figure 3.13 (a) presents the Te 3$d_{3/2}$ spectra fitted with three components obtained by HAXPES at 6.9 keV and 8 keV. The major component at 582.9 eV is related with the ZrTe alloy, the second component at 583.6 eV is characteristic of elemental Te and the last component at 584.9 eV is related with tellurium sub-oxide (TeO_x). The relative areas are reported in Table 3.10. Contrary to the previous analysis presented in section 3.1.3.1., the Te 3$d_{3/2}$ spectrum presents a TeO_x component. This variation can be related to an oxidation of the ZrTe layer caused by oxygen from air. The TaN capping layer has been replaced by TiN which is probably less efficient to prevent oxygen insertion from atmosphere. Except from that, the change of the protective layer do not strongly influence the memory behavior.

More insights about the phenomena taking place during the direct forming are obtained by comparing the Te and ZrTe contributions extracted from the Te 3$d_{3/2}$ line with increasing photon energies. Figure 3.13 (b) shows the Te/ZrTe area ratios measured for the as-grown and formed samples. During forming, the Te contribution is enhanced at 6.9 keV (3 λ = 30.3 nm) and also at 8 keV (3 λ = 34.2 nm). The increase more pronounced at the highest depth suggests a possible diffusion of tellurium through the alumina layer. This result agrees with the previous results that show a release of Te during the forming process and provides evidences of Te migration to create conductive filaments.

As observed for the ZrO_2, the variation of the Te/ZrTe area ratio in-depth also indicated the presence of Te next to the surface. Considering the contribution of the superficial tellurium, it is difficult to quantify with accuracy the release of tellurium at the ZrTe/Al_2O_3 interface after the forming process.

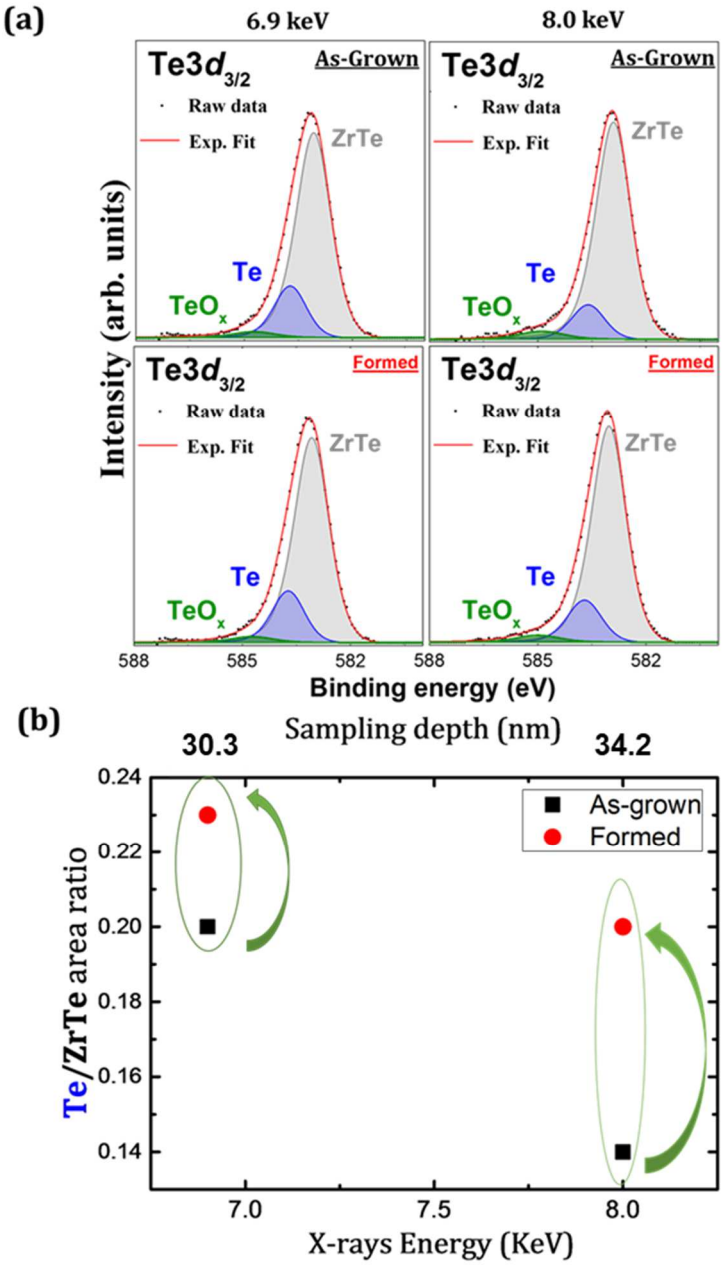

Figure 3.13. (a) Te 3$d_{3/2}$ core level peaks obtained by HAXPES at 6.9 keV and 8 keV on as-grown and formed samples of the TiN/ZrTe/Al_2O_3/Ta stack (b) Te/ZrTe area ratios extracted from the Te 3$d_{3/2}$ line area ratios measured at 6.9 and 8 keV for as-grown and formed samples.

Table 3.10. Relative areas (%) of the Te $3d_{3/2}$ components for the as-grown and formed samples obtained by HAXPES at 6.9 keV and 8 keV.

	6.9 keV			8 keV		
	ZrTe	Te	TeO_x	ZrTe	Te	TeO_x
As-grown	80.9 ± 8.0	16.2 ± 1.6	2.9 ± 2.9	83.3 ± 8.3	12.4 ± 1.2	4.3 ± 0.4
Formed	78.7 ± 7.8	18.3 ± 1.8	3.0 ± 3.0	81.0 ± 8.1	15.5 ± 1.5	3.5 ± 0.3

3.1.4. XPS depth profiling using GCIB

Laboratory XPS depth profiling was performed using a PHI 5000 VersaProbe II (Physical Electronics) equipped with a monochromatic Al K_α source (hν = 1.48 keV). The pass energy was set to 47 eV, giving an overall energy resolution of 0.75 eV, with an emission angle of 45.0°. To compensate for sample charging, in particular when analyzing the Al_2O_3 layer, a dual beam charge neutralizer was used. The charge compensation is necessary in this case as the emission of photoelectrons causes an accumulation of positive charges at the insulator surface after the sputtering of the top electrode. For the HAXPES analysis, the use of a beam neutralizer was not necessary as the Al_2O_3 layer was buried under a conductive layer enabling charges evacuation. XPS depth profiling was carried out using an argon gas cluster ion beam (GCIB) [116] with 2500 Ar atoms per cluster, a current of 20 nA, a raster area of 2mm*2mm, ensuring uniform sputtering of the analyzed area, and 20 kV accelerating voltage corresponding to an energy of 8 eV per atom.

XPS depth profiling was carried out on the as-grown and formed samples to provide information about oxygen, tellurium and zirconium migration along the TiN/ZrTe/Al_2O_3/Ta stack. The analysis was performed on a slightly different stack, with a TiN capping layer of 15 nm and a ZrTe electrode of 10 nm as shown in Table 3.1.

3.1.4.1. Oxygen depth profile

Figure 3.14 shows the XPS atomic concentration sputter depth profiles of oxygen obtained from the O 1*s* core level intensity, for the as-grown and formed samples.

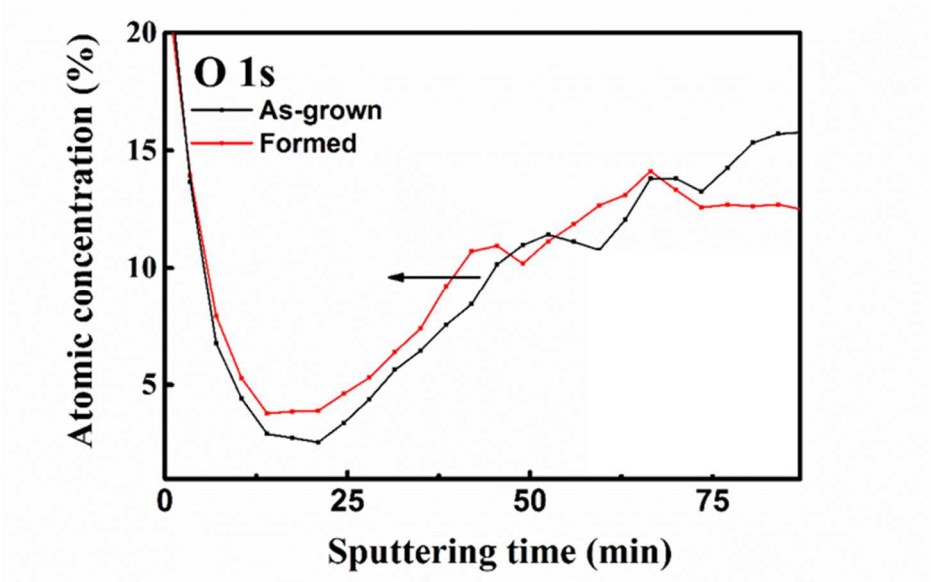

Figure 3.14. XPS depth profiles of oxygen measured on the TiN/ZrTe/Al_2O_3/Ta stack for as-grown and formed samples.

The high oxygen signal before sputtering is due to surface oxidation of the TiN cap and does not influence the subsequent profiling. The onset of the buried oxygen intensity obtained after forming is shifted towards the top electrode compared to the one measured for the as-grown sample. This result indicates oxygen diffusion into the ZrTe layer which is consistent with what is observed on the Zr $3p_{3/2}$ core level spectra, i. e. a decrease of ZrTe component and an increase of ZrO_2.

3.1.4.2. Te and Zr depth profile

Figure 3.15 shows the XPS atomic concentration depth profiles of tellurium and zirconium obtained from the Te 3*d* and Zr 3*d* core level intensities, for the as-grown and formed samples. The Te depth profile obtained after forming is shifted towards the Al_2O_3 layer compared to the one measured for the as-grown sample as shown in Figure 3.15 (a). This result can indicate a Te diffusion in the Al_2O_3 layer which is consistent with the switching mechanism of subquantum CBRAM cells where the conductive bridge is formed by the migration of a semiconductor [8] .

The comparison between the Zr depth profiles for as-grown and formed samples also reveals a possible diffusion of Zr towards the electrolyte layer after the forming process as shown in Figure 3.15 (b). However the interpretation of this result is more complicated since the XPS Zr depth profiles are too much impacted by the sputter-induced burying effect [116].

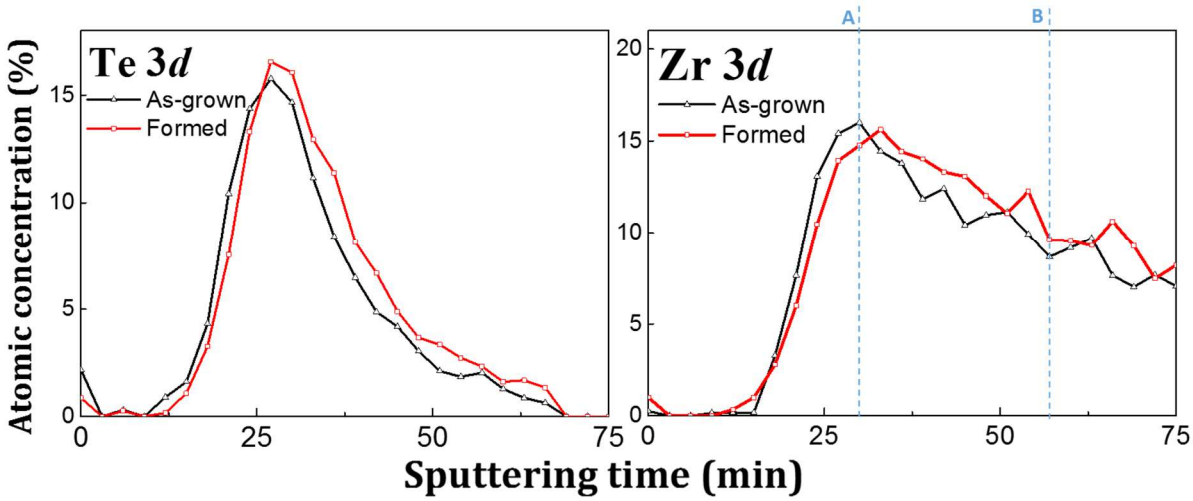

Figure 3.15. XPS depth profiles of (a) Te and (b) Zr measured on the TiN/ZrTe/Al_2O_3/Ta stack for as-grown and formed samples.

3.1.4.3. Zr oxidation analysis

Figure 3.16 (a) and (b) show a comparison between the peak of Zr 3*d* measured at the atomic concentration maximum value of the depth profile (after 30 min of sputtering at point A) and the peak measured at half its maximum value (after 57 min of sputtering at point B) for the as-grown and formed samples. The spin-orbital interaction for Zr 3*d* produces the doublet Zr $3d_{5/2}$ and Zr $3d_{3/2}$. The peaks at 180.4 eV and 182.4 eV correspond to ZrTe alloy and the peaks at 183.5 eV and 185.6 eV correspond to ZrO_2 [136]. Table 3.11 shows the relative areas of the two contributions of the Zr 3d spectra for as-grown and formed samples at the different sputtering times. The ZrO_2 contribution increases (+ 5.5 %) after 57 min of sputtering in comparison to the point A, for the as-grown sample. Assuming that the point A is located in the middle of the ZrTe layer and the point B is located near the ZrTe/Al_2O_3 interface, this result indicates, as showed before in the HAXPES analysis, a Zr oxidation at this interface during the deposition process.

The results for the formed sample showed an increase of the ZrO_2 contribution in both A and B in comparison to as-grown sample, consistent with oxygen migration towards the active electrode under positive bias. In addition the major increase occurred at the point A (+ 12.8%) which may indicate that oxygen diffuses deeply inside ZrTe layer and not only at the interface after the forming process.

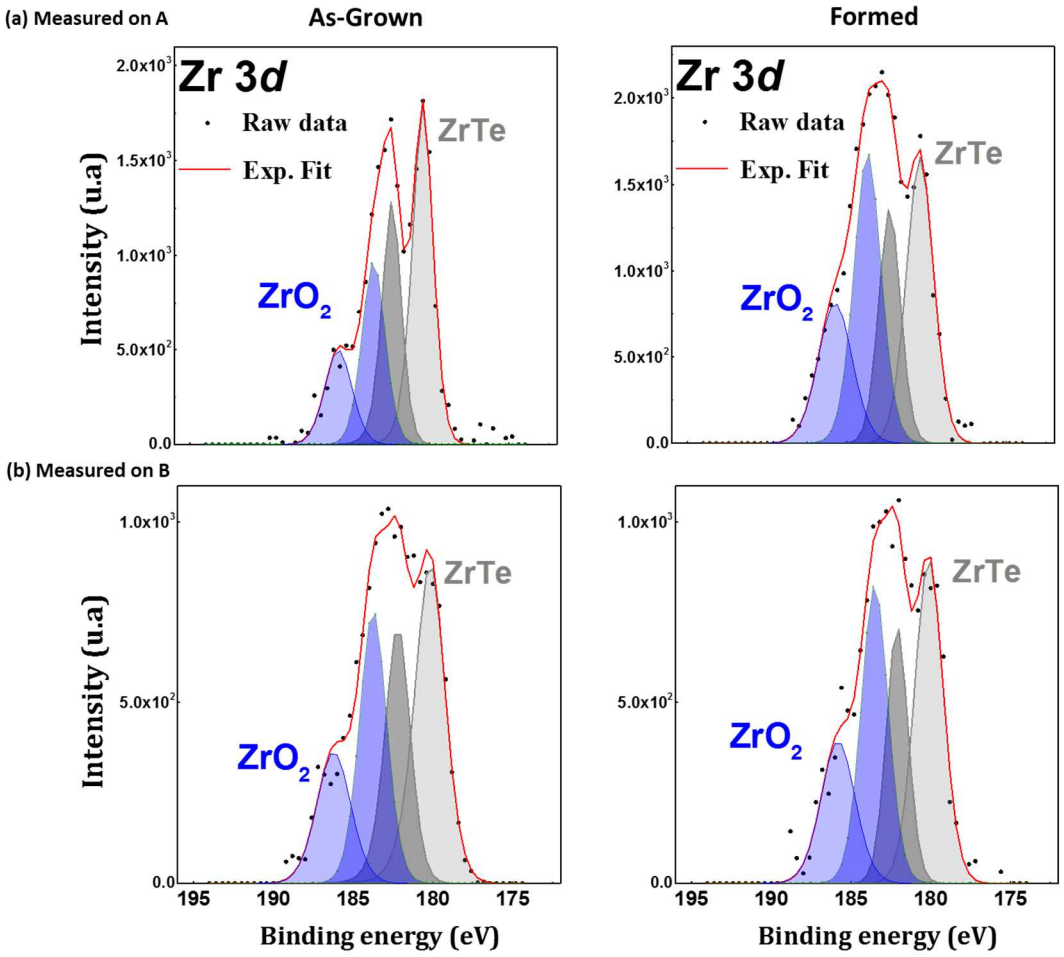

Figure 3.16. Zr 3*d* core level spectra measured after (a) 30 min (at point A) and after (b) 57 min (at point B) of sputtering for as-grown and formed samples.

Table 3.11. Relative areas (%) of the Zr 3*d* components for the as-grown and formed samples measured on A and B.

	Measured on A		Measured on B	
	ZrTe	ZrO_2	ZrTe	ZrO_2
As-grown	63.0 ± 6.3	37.0 ± 3.7	57.5 ± 5.7	42.5 ± 4.2
Formed	50.2 ± 5.0	49.8 ± 4.9	53.5 ± 5.3	46.5 ± 4.6

3.1.5. ToF-SIMS depth profiling

Time-of-flight secondary ion mass spectrometry (ToF-SIMS) is a complementary technique to XPS. While XPS depth profiling allows the identification of the chemical states and a semi-quantification of the elements in-depth as shown in section 3.1.4 , ToF –SIMS, in turn, provides in-depth profiles with a high depth resolution (< 1nm) and with a better sensitivity (< 10 ppm) [11]. These characteristics are essential to study the small changes that occur during the resistive switching and the elements diffusion under the bias

application.

ToF-SIMS was used to study the elemental depth distribution profiles and possible interdiffusion for as-grown and formed samples. Data were collected using an ION-TOF ToF-SIMS 5 instrument. The Bi_3^+ analysis beam was accelerated at 25 keV and rastered over an area of 80 × 80 µm. Cesium ions were used for sputtering, rastered over a 300x300 µm² area, at an impact energy of 500 eV. Both beams were incident at 45°. The intensities of the M^+ ions and MCs_n^+ clusters secondary ions (where M is the element to be analyzed and Cs^+ is the bombarding ion) were used for the analysis.

Figure 3.17 shows the ToF-SIMS depth profiling data for all elements present in the stack for as-grown (solid line) and formed (dash line) samples. The NCs_2^+, Ta^+, OCs_2^+ and Al^+ profiles are rather stable for the two resistive states. The Al and O profiles shows the presence of both elements in the top electrode layer. This result can be explained by a possible crushing of the top electrode by the Au wire during the electrical characterization exposing the insulation layer. In addition, the O depth profile indicates a significant oxidation of all layers of the device. To provide a better visualization of the Te and Zr depth profiles, the comparison between as-grown and formed samples is shown in Figure 3.18 (a) and (b) respectively.

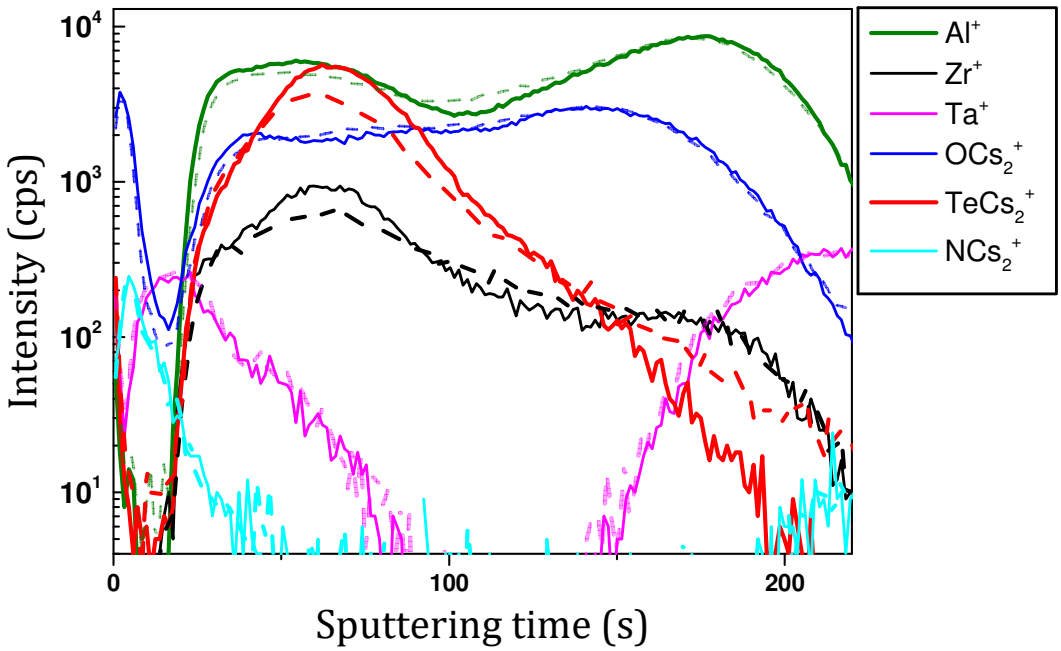

Figure 3.17. ToF-SIMS depth profiles of as-grown (solid line) and formed samples (dash line) for Al^+, OCs_2^+, NCs_2^+, $TeCs_2^+$, Zr^+ and Ta^+.

In both Te depth profiles, we can see some tellurium present at the TaN surface. This diffusion of Te towards the protective layer occurs probably during the deposition process and was observed in all cells. The depth profile of the formed sample shows a decrease of the intensity around 50 -100 s then an increase of

the intensity above 150 s in comparison to the as-grown sample. This shift toward longer sputtering times can be related to a diffusion of Te from the ZrTe layer toward the electrolyte layer after the forming process. This Te diffusion is consistent with the elemental Te release showed by the HAXPES measurements (see Figure 3.9).

The Zr depth profile of the formed sample also showed a small shift towards the bottom electrode but less important than for Te. The presence of ZrO_2 at the ZrTe/Al_2O_3 interface showed before by HAXPES and XPS analyses may act as a barrier and prevent the deeper diffusion of Zr.

ToF-SIMS as well as XPS depth profiling provides evidence of diffusion during the forming process supporting the proposed mechanism based on Te diffusion to form the conducting filament. It is important to note that considering the errors attributed to these destructive analyses these results are used in this work only to provide additional information on the distribution of the elements in the device and to help the global interpretation of the resistive switching study.

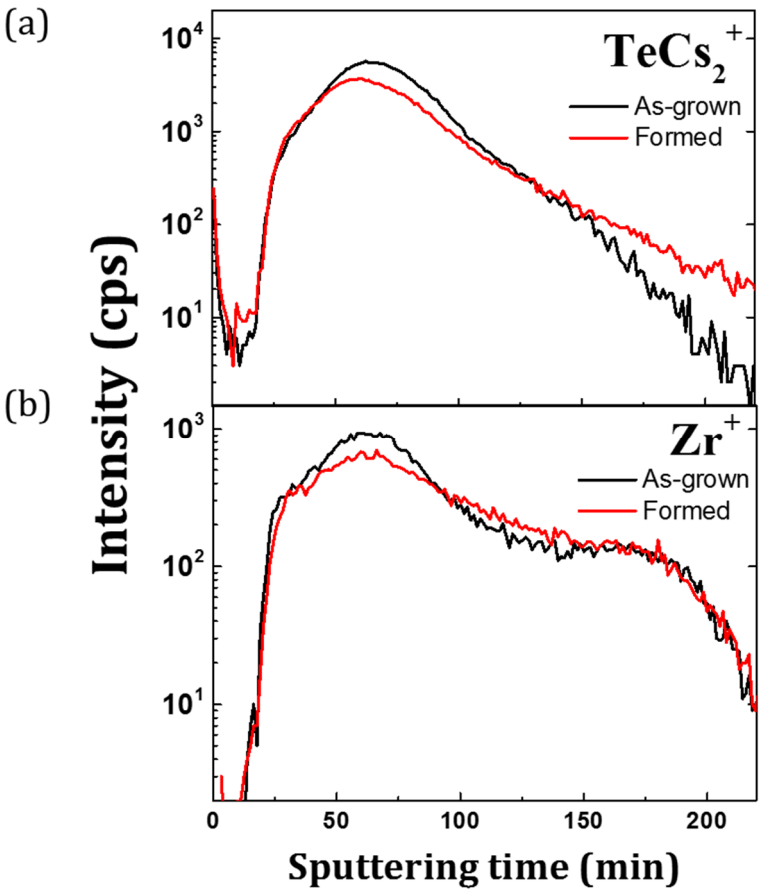

Figure 3.18. ToF-SIMS depth profiles of as-grown (black line) and formed samples (red line) for (a) $TeCs_2^+$, and (b) Zr^+.

3.1.6. Summary of the forming process for $ZrTe/Al_2O_3$ based CBRAM

Based on these results, we suggest the forming mechanism shown schematically in Figure 3.19. For $ZrTe/Al_2O_3$-based devices the results showed the oxidation of Zr together with a correlated alumina reduction during forming. This redox process is related to oxygen scavenging by the active top electrode. This O^{2-} migration leads to the creation of positively charged $V_O^{\bullet\bullet}$ in the alumina, thereby creating favored conductive paths. XPS depth profiling confirmed the oxygen diffusion from the Al_2O_3 towards the ZrTe top electrode. A four-layer capacitor model showed an increase of both the ZrO_2 and AlO_x interfacial layers thicknesses, confirming the redox process located between the active electrode and the electrolyte. Furthermore, the resistance switching caused also an elemental Te increase at the interface $ZrTe/Al_2O_3$. In addition, XPS and ToF-SIMS depth profiling showed evidences of Te migration from the ZrTe layer to alumina layer under positive bias.

Our study clearly showed the correlation of Zr oxidation with the release of Te at the $ZrTe/Al_2O_3$ interface. However, it is more difficult to conclude on the chemical nature of the filament. The HAXPES Te $3d_{3/2}$ spectra showed that the released Te is not ionized. The Te migration through the alumina is thus not directly driven by the electric field and more difficult to explain.

For the sake of consistency with the depth profiles results which showed a possible Te migration towards the electrolyte layer under positive polarization and also with the electrical measurements reported by Jameson et al. [8] which showed a conductance for the ZrTe-based CBRAM equal to $0.03G_0$, below the standard G_0 value, we assume that filaments are made of Te. Thus, a plausible mechanism is that: a) first Te accumulates at the interface and then progressively inside the alumina, b) second, local Te segregation might occur through $V_O^{\bullet\bullet}$, acting as easier diffusion paths towards the bottom electrode. Thus, a hybrid mechanism combining $V_O^{\bullet\bullet}$ formation by oxygen transport with Te migration and filament formation typical of OXRRAMs and CBRAMs, respectively occurs during positive polarization.

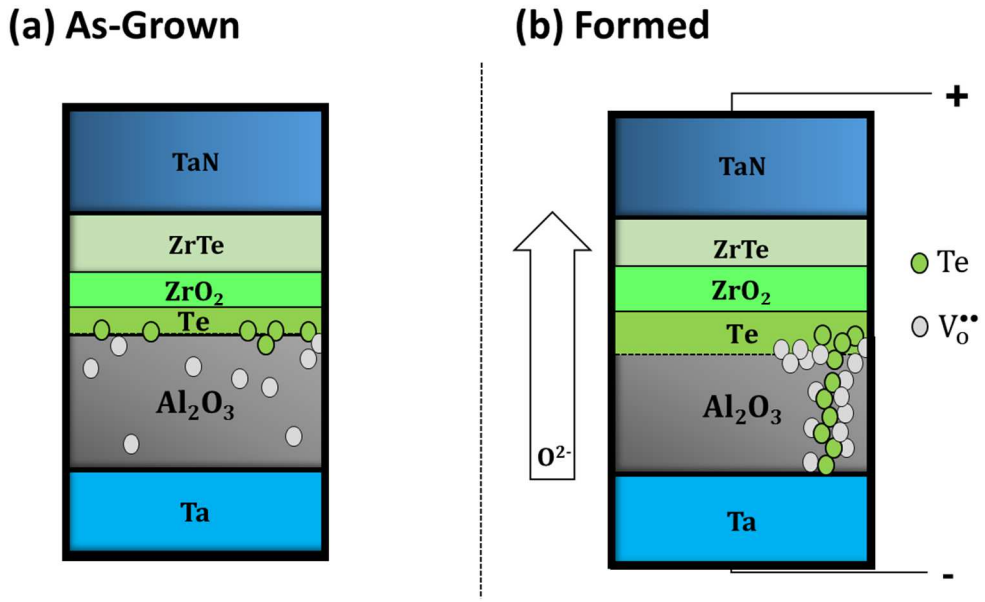

Figure 3.19 Schematic of the (a) as-grown sample and the redox processes and matter transport taking place during (b) forming process in the $ZrTe/Al_2O_3$ - based cells.

3.2. Investigation of $TiTe/Al_2O_3$ based CBRAMs

This section shows the second part of the forming process study, using TiTe as active electrode.

3.2.1. CBRAM based on $TiTe/Al_2O_3$

Same preparation method as $ZrTe/Al_2O_3$ showed in section 3.1.1. The 5 nm TiTe growth process was optimized to reach a Ti/Te stoichiometry of 40/60. Finally, a 5-nm TaN capping layer was deposited by reactive sputtering at 50°C to prevent oxidation of TiTe when exposed to air as shown in Figure 3.2.

3.2.2. Electrical characterization of the $TiTe/Al_2O_3$ based sample

The electrical characterization was performed as for $ZrTe/Al_2O_3$ devices (see section 3.1.2.). The first positive bias application on this cell was performed with a compliance current of 50 mA as shown in Figure 3.20 (a). The current increases abruptly to the 50 mA compliance current at 3.5 V. However, this value of I_{cc} was not enough to prevent a permanent breakdown of the oxide i.e the reset of this sample was not possible under negative polarization.

Based on this result, a second bias application was performed using a lower I_{cc} = 10 mA as shown in Figure 3.20 (b). The current increases abruptly to reach the 10 mA compliance current at 3.3 V. However, as for the first electrical test, the bias application with this I_{cc} caused also a permanent breakdown of the oxide.

Figure 3.20 (c) shows the bias application using an I_{cc} =5mA. The I-V curve shows that during the voltage application up to 4.5 V the current directly reaches the compliance without any clear jump of current. This result demonstrated that this value of I_{cc} is too low thereby preventing the resistive switching of the memory. Table 3.12 summarizes the results of the electrical characteristics of each electrical test using I_{cc} of 50, 10 and 5 mA.

These results show that under these electrical conditions, the TiTe/Al_2O_3 cell does not present a memory behavior i.e a reversible switch of the resistance. This result has motivated the analysis of this memory using other electrical conditions. The electrical tests performed on this cell showed that this memory can be formed under negative polarization with a reset under positive polarization. The analysis of the negative forming will be shown in the next chapter 4 for TiTe and also for ZrTe.

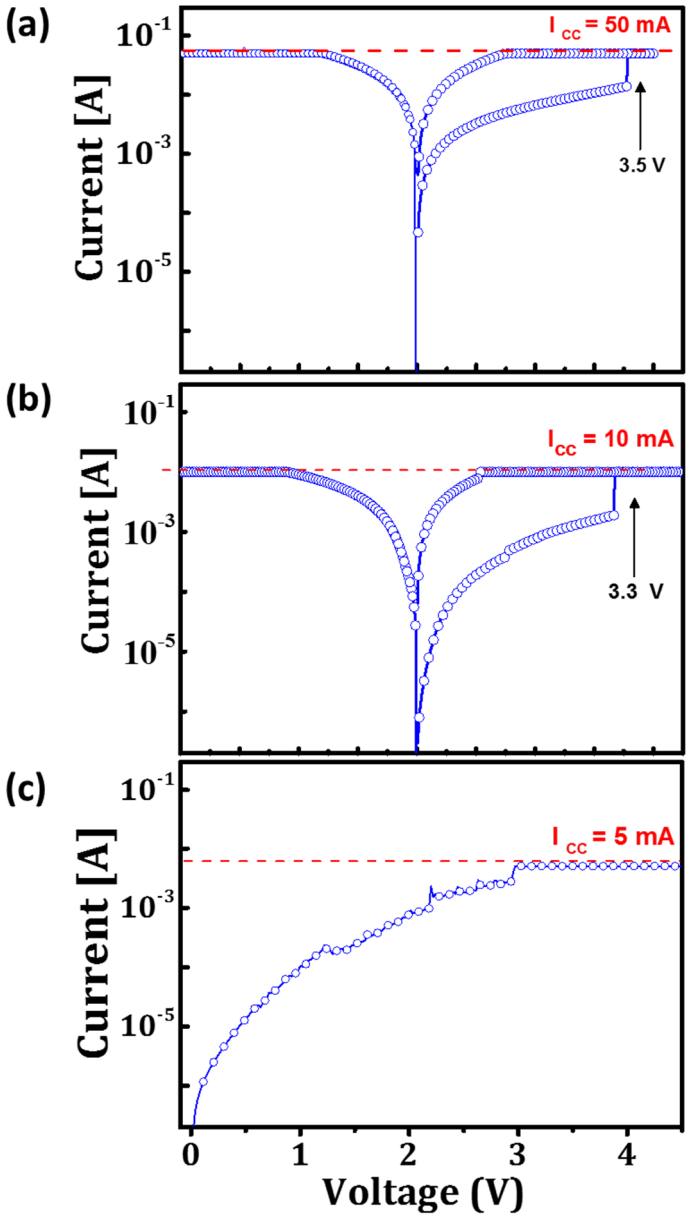

Figure 3.20. Current - voltage (I-V) curves obtained using an (a) I_{cc} = 50 mA, (b) 10 mA and (c) 5 mA for the TaN/TiTe/Al_2O_3/Ta stack.

Table 3.12. Electrical characteristics obtained using 50, 10 and 5 mA as I_{CC}

Experiment	Ri (10^4 Ω)	Rf (10^2 Ω)	Ri/ Rf (Ω)	I_{cc} (mA)	V_F (V)
I	1.7	3.6	47	50	3.5
II	5.0	1.7	300	10	3.3
III	10	1000	1	5	-

3.3. Conclusion

For $ZrTe/Al_2O_3$-based devices, the results showed the oxidation of Zr together with a correlated alumina reduction during forming. This redox process is related to oxygen scavenging by the active top electrode. This oxygen migration leads to the creation of positively charged $V_O^{\bullet\bullet}$ in the alumina, thereby creating favored conductive paths. XPS depth profiling confirmed the oxygen diffusion from the Al_2O_3 towards the ZrTe top electrode. A four-layer capacitor model showed an increase of both the ZrO_2 and AlO_x interfacial layers thicknesses, confirming the redox process located between the active electrode and the electrolyte. Furthermore the resistance switching caused also an elemental Te increase at the interface $ZrTe/Al_2O_3$. Based on these results a plausible mechanism can be described as: a) first Te accumulates at the interface and then some migrates b) second, local Te segregation might occur through $V_O^{\bullet\bullet}$, acting as easier diffusion paths towards the bottom electrode. A hybrid mechanism combining $V_O^{\bullet\bullet}$ formation by oxygen transport with Te migration and filament formation, typical of OXRRAMs and CBRAMs, respectively occurs during positive polarization. This study provides evidence of the physico-chemical phenomena involved during the electroforming process. However, it cannot be excluded that other concurrent physical mechanisms generate or contribute to the resistive switching.

In the case of a cell with TiTe as active electrode, a reversible resistive switching was not possible. However, this cell presents a reversible resistive switching under negative polarisation. The analysis of the forming under negative polarisation and subsequent reset under positive polarisation will be shown in the next chapter.

Chapter 4

4. Reverse forming and reset mechanism of Te-based conductive-bridge memories

In this chapter we investigated the negative forming of Te-based CBRAMs, also called reverse forming, in which a negative voltage is applied to the top electrode and the first reset step i.e. the first transition from LRS to HRS. Negative forming was observed in several standard Cu-based CBRAMs structures [70,71,137] and reported to be related to metal cations and/or oxygen vacancies ($V_O^{\bullet\bullet}$). Compared to positive forming, the device operation is modified and the bottom electrode may also play a role together with the active electrode. To test the validity of this scenario in the case of Te-based CBRAMs, we study the redox phenomena observed in the different layers. We compare results obtained for three samples: as-grown i.e. the pristine device with a HRS, formed i.e. the sample after the first transition between HRS and LRS and reset i.e. the sample after the first transition between LRS and HRS. The aim is to clarify the switching mechanisms and understand the chemical changes at both electrode/electrolyte interfaces for devices with TiTe and ZrTe as active electrodes. The forming process implies a negative bias on the top electrode and so strictly speaking is reverse forming, however, hereafter we will refer to the process simply as forming.

4.1. Investigation of TiTe/Al_2O_3 based CBRAM

The reverse forming was analysed in this case since the positive polarisation caused an irreversible switching of the TiTe/Al_2O_3 cell (see section 3.2). On the contrary, the negative polarization enabled the reset of the memory after the forming process as shown in Figure 4.2 (a). The first part of the analysis will show the electrical characterization of the resistive switching process. The second part will show the results obtained from the HAXPES experiments performed at the GALAXIES beamline of the SOLEIL synchrotron, using a photon energy of 6.9 keV. The third part is a comparison of HAXPES results using different photon energies to obtain a depth profile of the sample using 6.9 keV, 8 keV and 10keV. In the last part, we will show ToF-SIMS depth profiling to study the elemental depth distribution profiles and possible interdiffusion for as-grown, formed and reset samples. In this chapter, the stack is similar to the one used for the positive forming analysis shown in chapter 3: TaN (5 nm)/TiTe (5nm)/Al_2O_3 (5nm)/Ta (200 nm).

4.1.1. Electrical characterization of the TiTe/Al_2O_3 based sample

Firstly, we have performed the voltage application using different values of compliance current (I_{cc}) to determinate the maximum value of this parameter that allows the forming and reset process of the cell. The compliance current was chosen low enough to avoid a dielectric breakdown of the oxide but sufficiently high to generate important chemical modifications in the insulating layer or at the interfaces with the electrodes, facilitating the detection [126]. These tests were done with two different values of I_{cc} such as: 10 mA and 30 mA. As we can observe in the current - voltage (I-V) curve obtained with an I_{cc} of 30 mA in Figure 4.1, the bias application caused a permanent breakdown of the oxide, without any reset at positive bias. However, as showed in Figure 4.2 (a), the current - voltage (I-V) curve obtained with an I_{cc} of 10 mA shows a reversible resistive switching, with a reset at positive bias. Considering this result, an I_{cc} of 10 mA was chosen to analyze these cells. During the forming step, the current increases slowly when applying the negative voltage and then abruptly at the forming voltage (V_F) of -3.0 V to reach the 10 mA compliance current. During the reset step, a positive voltage is applied to the structure until reaching an abrupt decrease of the current at the reset voltage (V_{Reset}) of 0.55 V.

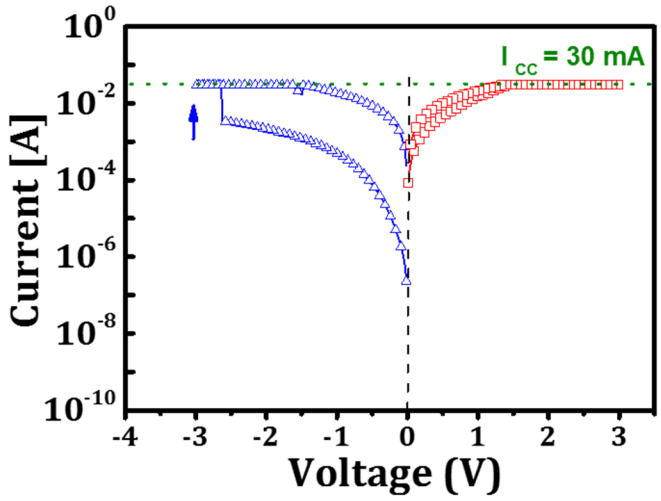

Figure 4.1 Current - voltage (I-V) curve obtained using an I_{cc} = 30 mA for the TaN/TiTe/Al_2O_3/Ta stack.

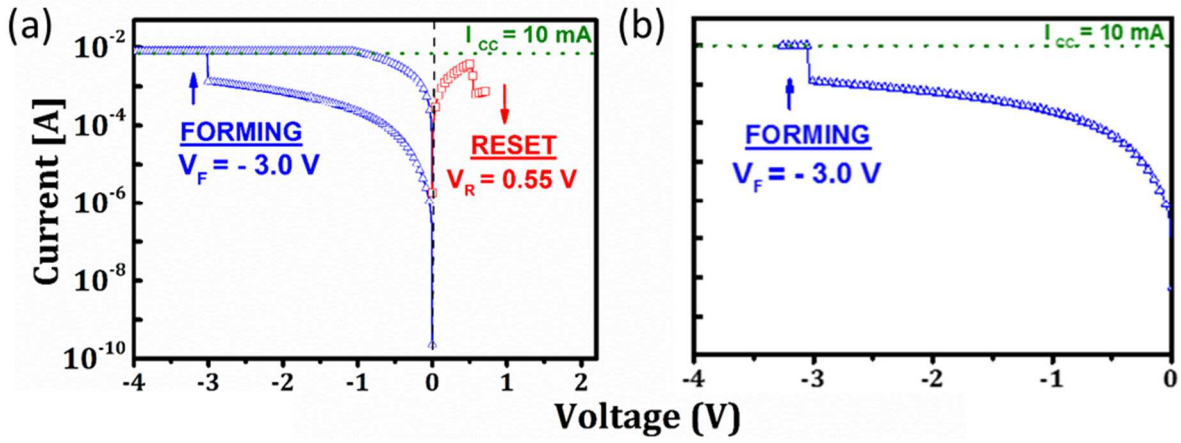

Figure 4.2 Current - voltage (I-V) curve for the (a) forming and reset process of the reset sample and (b) forming process of the formed sample for the TaN/TiTe/Al_2O_3/Ta devices.

The device resistance measured before and after forming are $R_{As\text{-}grown}$ = 3.3x10^4 Ω and R_{Formed} = 1.6x10^2 Ω. The resistance ratio $R_{As\text{-}grown}$ / R_{Formed} = 2.1x10^2 shows a change of two orders of magnitude in the device resistivity by the formation of a conductive path (or paths) in the electrolyte. The resistance measured after reset, R_{Reset} = 5.0x10^3 Ω, confirms the return towards the high resistive state. The HRS/LRS ratio is therefore ~ 3.0x10^1. Note that the resistance ratio is lower than that measured for the forming step, since the initial state is not recovered during the reset.

The current - voltage (I-V) curves presented in Figure 4.2 (a) were measured for the sample after resetting (reset sample). The I-V curve shown in Figure 4.2 (b) was measured on a different sample which had only undergone forming (formed sample). Table 4.1 summarizes the results of the electrical characteristics for the formed and reset samples analyzed by both HAXPES and ToF-SIMS.

Table 4.1. Electrical characteristics of the formed and reset samples analyzed by HAXPES and ToF-SIMS.

Sample	$R_{As\text{-}grown}$ (10^4 Ω)	R_{Formed} (10^2 Ω)	R_{Reset} (10^3 Ω)	$R_{As\text{-}grown}$ / R_{Formed} (10^2)	R_{Formed}/ R_{Reset} (10)	I_{cc} (mA)	V_F (V)	V_{Reset} (V)
Formed	10	1.3	-	7.7	-	10	-3.0	-
Reset	3.3	1.6	5.0	2.0	3.0	10	-3.0	0.55

Taking into account five tests, we can obtain an average forming voltage of -3.0 V and an average reset voltage of 0.6 V. Regarding the resistances, we have an average of as-grown and formed resistances of 2.5x10^5 Ω and 1.4x10^2 Ω respectively. The resistance ratio $R_{As\text{-}grown}$ / R_{Formed} was around 10^2-10^3 and the $R_{As\text{-}grown}$ / R_{Reset} was around 10^1 -10^2.

4.1.2. Hard X-ray photoelectron spectroscopy (HAXPES) analysis

This study was divided in two parts. In the first part, we will show in detail the results obtained by HAXPES at 6.9 keV. At this energy, the results showed a significant structural difference before and after the forming and reset processes. The second part will show the results at different photon energies (at 6.9 keV, 8 keV and 10 keV), thus varying the sampling depth. This experimental approach provided information about the depth distribution of the species in the stack before and after the bias application. HAXPES analyses were performed at the GALAXIES beamline of the synchrotron SOLEIL [107,113]. The overall energy resolution (beamline and spectrometer) was 110, 160 and 210 meV for 6.9, 8 and 10 keV photon energies respectively. The values of λ are estimated with the Tanuma equation [94] for Al 1*s*, Ti 1*s*, Te $3d_{3/2}$ and Ta $3d_{5/2}$ photoelectrons and are given in Table 4.2. The parameters used to fit the HAXPES peaks are presented in Table A.1 and in Table A.2 (Binding Energies) in annex A.

Table 4.2 Inelastic mean free path for photon energy of 6.9, 8 and 10 keV. The sampling depth is defined to be corresponding to 3λ. [88]

	6.9 keV	8.0 keV	10 keV
	λ (nm)	λ (nm)	λ (nm)
Al 1*s*	8.5 ± 1.7	9.8 ± 1.9	12.4 ± 2.4
Ti 1*s*	3.7 ± 0.7	5.0 ± 1.0	8.0 ± 1.6
Te $3d_{3/2}$	9.8 ± 1.9	11.1 ± 2.2	13.7 ± 2.7
Ta $3d_{5/2}$	8.3 ± 1.6	9.7 ± 1.8	12.2 ± 2.3

4.1.2.1. HAXPES – 6.9 keV

HAXPES was performed on the as-grown, formed and reset samples, and also on the bare Al_2O_3/Ta structure outside the top electrode in order to provide reference spectra for tantalum and aluminum.

- **Electrode metal chemistry**

The Ta $3d_{5/2}$ spectrum measured on the Al_2O_3/Ta interface outside the device area is shown in Figure 4.3. The spectrum measured outside the top electrode serves as a reference to distinguish the contribution of the Ta bottom electrode from the signal of the topmost TaN protective layer of the CBRAMs. As showed before for the TaN/ZrTe/Al_2O_3/Ta sample in section 3.1.3 (Figure 3.6), the Ta bottom electrode was oxidized at the Al_2O_3/Ta interface. In this case, the Ta spectrum shows an additional Ta_2O_5 contribution at 1736.7 eV, together with the Ta and TaO_x contributions already observed at 1731.4 eV and 1733.4 eV respectively. This higher oxidation, in comparison to the previous ZrTe/Al_2O_3 cell, is due to an air break after the bottom electrode deposition which caused an additional oxidation.

Figure 4.4 shows the Ta $3d_{5/2}$ spectra of the as-grown, formed and reset samples. The spectra have been fitted with three contributions. The first component is characteristic of metallic Ta at 1731.4 eV, the second component at 1733.4 eV is characteristic of TaN, only present in the capping layer, and tantalum sub-oxide (TaO_x) and the third one at 1736.7 eV is attributed to Ta_2O_5.

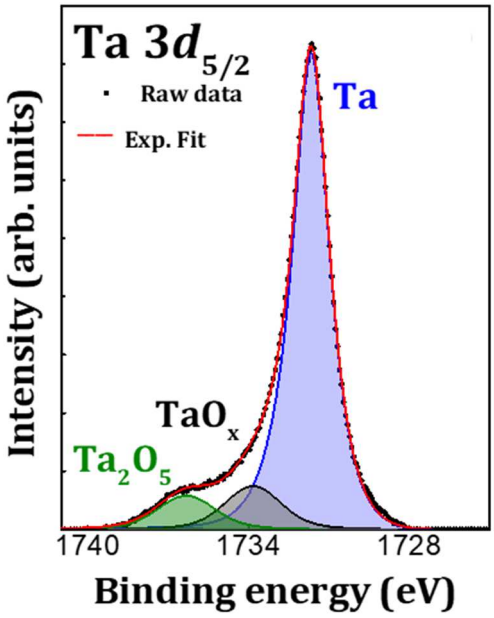

Figure 4.3 Ta $3d_{5/2}$ core level spectrum obtained at 6.9 keV photon energy on the bare Al_2O_3/Ta structure.

The comparison between as-grown, formed and reset spectra showed a decrease of the metallic Ta contribution (- 6.4 %) and an increase in oxidized Ta after forming and, conversely, an increase of metallic Ta (+12 %) accompanied by a decrease of the TaO_x and Ta_2O_5 components after reset (see Table 4.3).

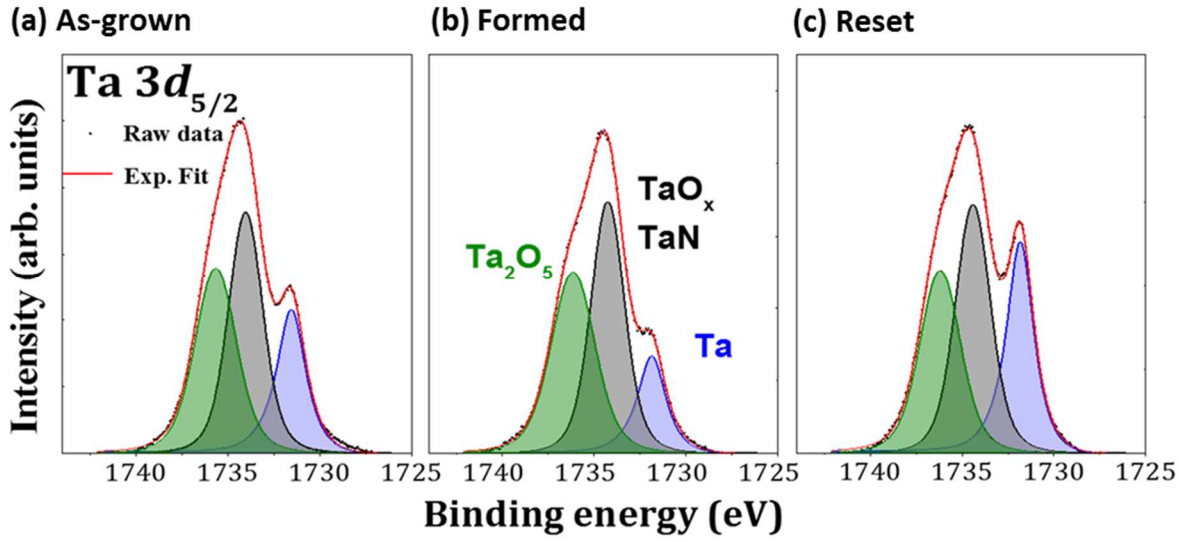

Figure 4.4 Ta $3d_{5/2}$ core level peaks obtained by HAXPES at 6.9 keV on (a) as-grown, (b) formed and (c) reset

sample of the TaN/TiTe/Al_2O_3/Ta stack.

Table 4.3. Relative areas (%) of the Ta $3d_{5/2}$ components measured outside the top electrode and for the as-grown, formed and reset samples.

	Ta	TaO_x or TaN	Ta_2O_5
Al_2O_3/Ta	74.2 ± 7.4	13.3 ± 1.3	12.5 ± 1.2
As-grown	21.0 ± 2.1	41.0 ± 4.1	38.0 ± 3.8
Formed	14.6 ± 1.4	44.0 ± 4.4	41.4 ± 4.1
Reset	26.7 ± 2.6	39.7 ± 3.9	33.6 ± 3.3

Figure 4.5 presents the Ti 1*s* spectra which also have three contributions. The definition of the contributions was made using electronegativity arguments based on the values of binding energies for TiO_2 and Ti^0 found in [138,139]. The low binding energy (LBE) component at 4965.6 eV was fitted using a Doniach-Sunjic function [127] and is characteristic of the metallic TiTe alloy. The second component at 4967.0 eV was fitted using a Lorentzian-Gaussian function and is characteristic of a TiO_x suboxide and the third one at 4968.7 eV is attributed to TiO_2. From these spectra we assumed two interfacial TiO_x and TiO_2 layers at the TiTe/Al_2O_3 interface.

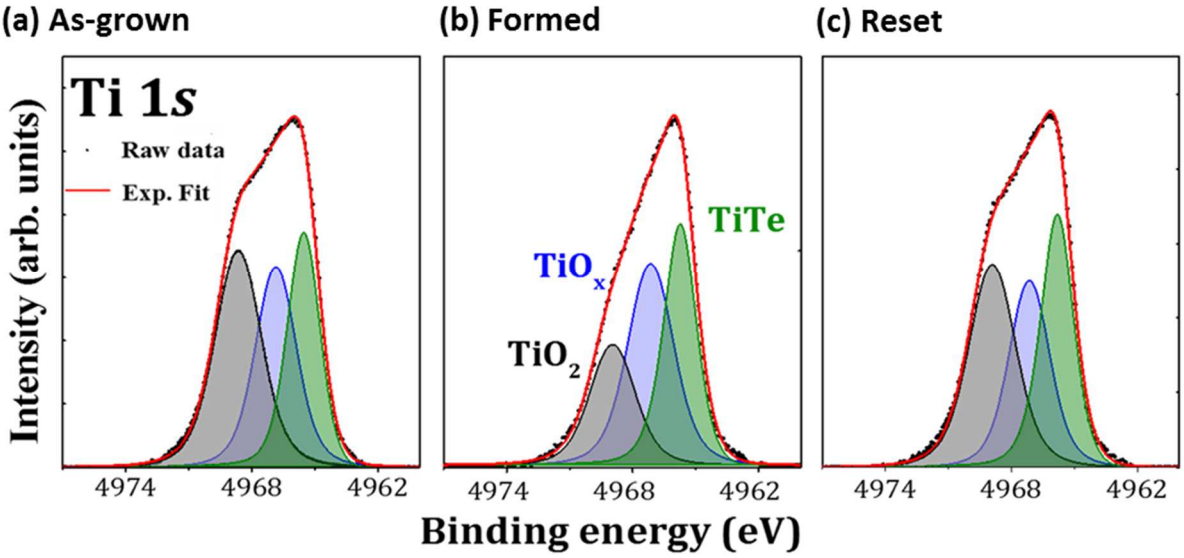

Figure 4.5 Ti 1*s* core level peaks obtained by HAXPES at 6.9 keV on (a) as-grown, (b) formed and (c) reset sample of the TaN/TiTe/Al_2O_3/Ta stack.

The relative areas of each component for as-grown, formed and reset spectra are reported in Table 4.4. We observe a decrease of the TiO_2 area (-9.4 %) after forming. This is consistent with oxygen migration towards the Ta bottom electrode favoring TaO_x oxidation. On the other hand, the reset operation caused an increase of TiO_2 (+ 11.6 %) at the top electrode/Al_2O_3 interface, again consistent with oxygen transport back into the TiTe top electrode, favoring TaO_x reduction at the Al_2O_3/Ta interface. Such a push-pull relationship

has already been reported for OxRRAMs, see for example Berthaud et al. [140]. Furthermore a correlation between oxygen migration and applied voltage on the device has been shown previously for the ZrTe/Al_2O_3 stack under positive forming in chapter 3.

Table 4.4. Relative areas (%) of the Ti 1*s* components for the as-grown, formed and reset samples.

	TiTe	TiO_x	TiO_2
As-grown	32.4 ± 3.2	27.2 ± 2.7	40.4 ± 4.0
Formed	32.5 ± 3.2	36.5 ± 3.6	31.0 ± 3.1
Reset	30.9 ± 3.0	26.5 ± 2.6	42.6 ± 4.2

Thus, the analysis of the Ti and Ta components of the top and bottom electrodes showed that the applied bias causes oxygen migration in the direction of the polarity, driving redox reactions at both top and bottom interfaces. Reduction of the pre-existing TiO_2 at the TiTe/Al_2O_3 interface occurs together with oxidation of TaO_x at the Al_2O_3/Ta interface for forming, consistent with downward oxygen migration. For the positive reset bias, the TiO_x is oxidized at the top interface while at the bottom electrode, TaO_x is reduced, consistent with upwards oxygen migration. These observations, while providing valuable insight into the oxygen push-pull process, do not reveal the filament formation in the resistive switching.

- **Te and electrolyte chemistry**

Figure 4.6 shows the Te 3$d_{3/2}$ spectra. The top electrode is a metallic TiTe alloy but the Te spectra are asymmetric to higher binding energy, suggesting the possible presence of additional components. There are two possibilities for the HBE components: phase separation with formation of elemental Te (semiconductor) and/or oxidation of Te. The spectra have therefore been fitted with three components as showed before for ZrTe/Al_2O_3 samples. The major component at 582.9 eV is related with the TiTe alloy using simple electronegativity arguments, the second component at 583.6 eV is characteristic of elemental semiconductor Te and the HBE component at 584.9 eV is related to the oxide (TeO_x) [130,131].

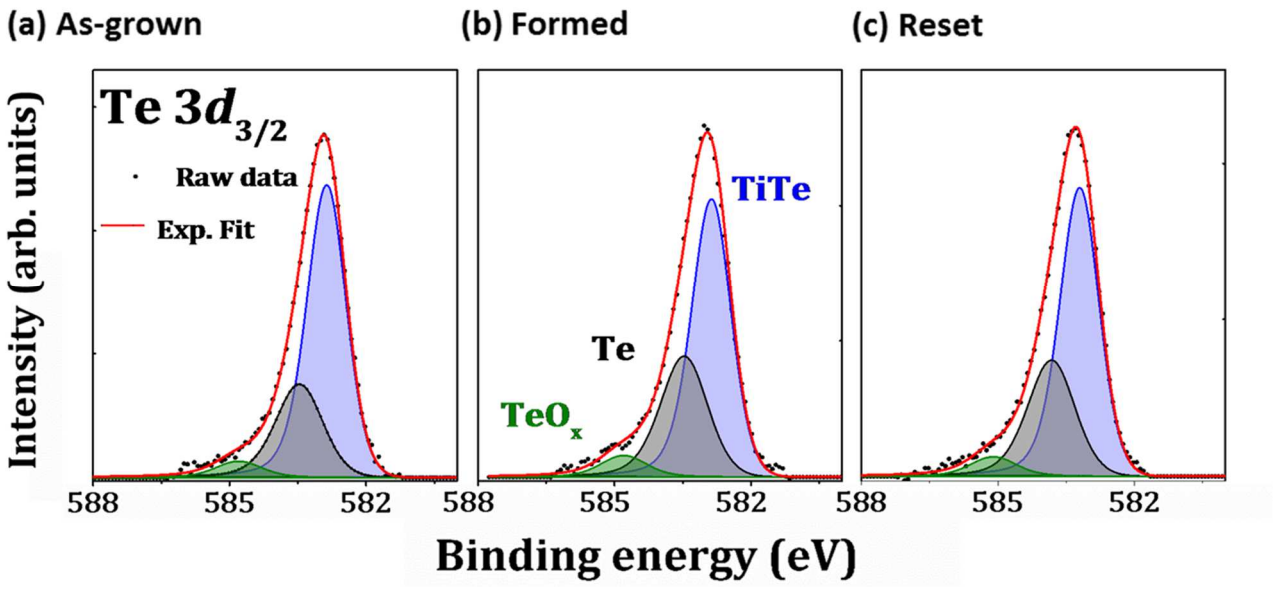

Figure 4.6 Te $3d_{3/2}$ core level peaks obtained by HAXPES at 6.9 keV on (a) as-grown, (b) formed and (c) reset sample of the TaN/TiTe/Al_2O_3/Ta stack.

Table 4.5 shows the relative areas of each contribution in the as-grown, formed and reset spectra. After forming, a decrease in the Ti-Te environment (- 7.2 %) and an increase in elemental Te (+6.6 %) was observed, whereas the reset causes a decrease of elemental Te (-2.7 %) and an increase of the Ti-Te bonds (+2.3 %). Importantly, both formed and reset samples show evidence for increased TeO_x coordination with respect to the pristine sample. This suggests a non-reversible correlation between the increase in elemental Te and oxygen environment.

Table 4.5. Relative areas (%) of the Te $3d_{3/2}$ components for the as-grown, formed and reset samples.

	TiTe	Te	TeO_x
As-grown	69.1 ± 6.9	26.0 ± 2.6	4.9 ± 0.4
Formed	61.9 ± 6.1	32.6 ± 3.2	5.5 ± 0.5
Reset	64.2 ± 6.4	29.9 ± 2.9	5.9 ± 0.5

The reference Al 1*s* spectrum measured outside the top electrode on the Al_2O_3/Ta is shown in Figure 4.7. The Al 1*s* core level spectra for as-grown, formed and reset are shown in Figure 4.8. The Al 1s spectra can be fitted using two components. The two contributions are a sub-oxide (labeled AlO_x) at lower binding energy (BE) of 1561.9 eV and fully oxidized Al_2O_3 at a BE of 1562.7 eV. The relative areas are reported in Table 4.6.

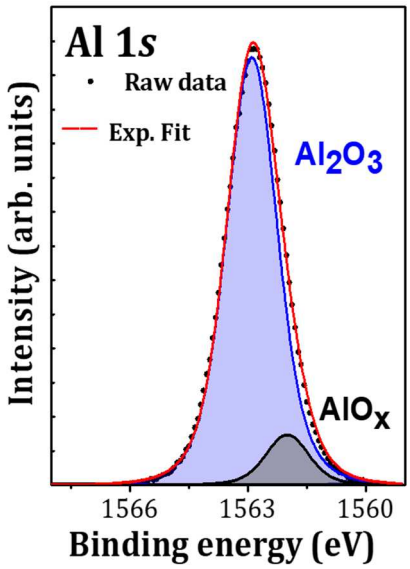

Figure 4.7. (a) Al 1s core level spectrum obtained at 6.9 keV photon energy on the bare Al_2O_3/Ta structure.

The spectrum measured outside the top electrode (see Figure 4.7) showed the alumina reduction near the Ta bottom electrode, consistent with the presence of a TaO_x layer (see Figure 4.3). Comparison between this spectrum and that of the as-grown sample showed an increase of the relative AlO_x contribution (+ 16.2 %) in the latter. This result highlights the additional alumina reduction caused by the top electrode deposition. Pumping of oxygen by the Ti evidenced in Figure 4.5 causes the creation of positively charged oxygen vacancies $V_O^{\bullet\bullet}$ in the electrolyte. This reduction of the electrolyte may play a significant role in the forming process [51,67,68].

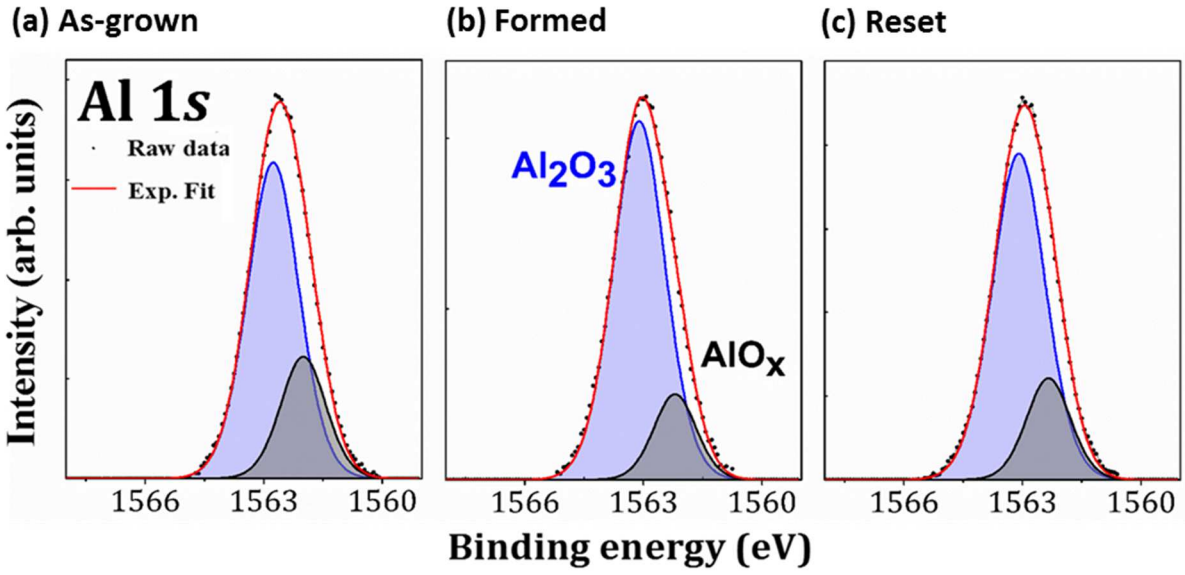

Figure 4.8 Al 1*s* core level peaks obtained by HAXPES at 6.9 keV on (a) as-grown, (b) formed and (c) reset sample of the TaN/TiTe/Al_2O_3/Ta stack.

The sub-oxide contribution (AlO_x at 1561.9 eV) decreases by 9% relative to the main contribution after forming. This is at first sight surprising since forming involves oxygen migration from top to bottom electrode but may be understood if the diffusion results in oxidation of the Al suboxide at the bottom interface. Conversely, application of a positive bias voltage to reset the HRS causes an increase of the AlO_x contribution (+4.2 %) for the reset state compared with the formed sample, consistent with oxygen transport from the electrolyte towards the top electrode, i.e. oxygen scavenging at the top interface.

Table 4.6. Relative areas (%) of the Al 1*s* components measured outside the top electrode and for the as-grown, formed and reset samples.

	Al_2O_3	AlO_x
Al_2O_3/Ta	90.9 ± 9.0	9.1 ± 0.9
As-grown	74.7 ± 7.4	25.3 ± 2.5
Formed	83.7 ± 8.3	16.3 ± 1.6
Reset	79.5 ± 7.9	20.5 ± 2.0

The HAXPES analysis at 6.9 keV therefore shows evidence for oxygen migration towards the bottom electrode during forming and concomitant redox reactions at both interfaces.

- **Multilayer model**

To try to quantify the redox phenomena caused by the forming and reset processes, we have used a multilayer model [135,141] as described in section 3.1.3.1. We assume the presence of distinct layers of TiO_2 and Te at the TiTe/Al_2O_3 upper interface, as shown in Figure 4.9. The layer structure is only a schematic to allow approximate model calculations of equivalent thicknesses. For example, the interface layer of the top electrode could well be a phase separated TiO_x, Te and TiTe. This is a first attempt to provide a quantitative insight which needs to be improved in the future. We need in particular to take into account the Ti oxide layer at the upper TaN/TiTe interface for a better quantification.

We also assume that the released Te mainly stays at the interface. To calculate their respective thicknesses, the intensity ratios extracted from the Ti 1*s* and Te 3$d_{3/2}$ core levels can be expressed using the equation (4.3) and (4.4) as detailed in chapter 3. We assume that d_{TiO2}+ d_{TiTe} = 5 nm and d_{Te}+ d_{TiTe} = 5 nm and that the IMPFs of Ti 1*s* and Te 3$d_{3/2}$ photoelectrons were the same in all the layers of the stack and equal to λ_{Ti} = 3.7 nm and λ_{Te} = 9.8 nm, respectively.

$$\frac{I_{TiO2}}{I_{TiTe}} = \frac{I^{\infty}_{TiO2}}{I^{\infty}_{TiTe}} \exp\left(\frac{-d\,TiTe}{\lambda\,\mathrm{Ti}}\right) \frac{1-\exp\left(\frac{-d\,TiO2}{\lambda\,Ti}\right)}{\left[1-\exp\left(\frac{-d\,TiTe}{\lambda\,Ti}\right)\right]} \qquad 4.3$$

$$\frac{I_{Te}}{I_{TiTe}} = \frac{I^{\infty}_{Te}}{I^{\infty}_{TiTe}} \exp\left(\frac{-d\,TiTe}{\lambda\,\mathrm{Te}}\right) \frac{1-\exp\left(\frac{-d\,Te}{\lambda\,Te}\right)}{\left[1-\exp\left(\frac{-d\,TiTe}{\lambda\,Te}\right)\right]} \qquad 4.4$$

The Ti 1*s* and Te 3$d_{3/2}$ spectra measured at 6.9 keV have been used to estimate respectively the TiO_2 and Te thicknesses, because the changes are more pronounced at this energy. The results obtained for the forming and the reset are summarized in Figure 4.9 and Table 4.7.

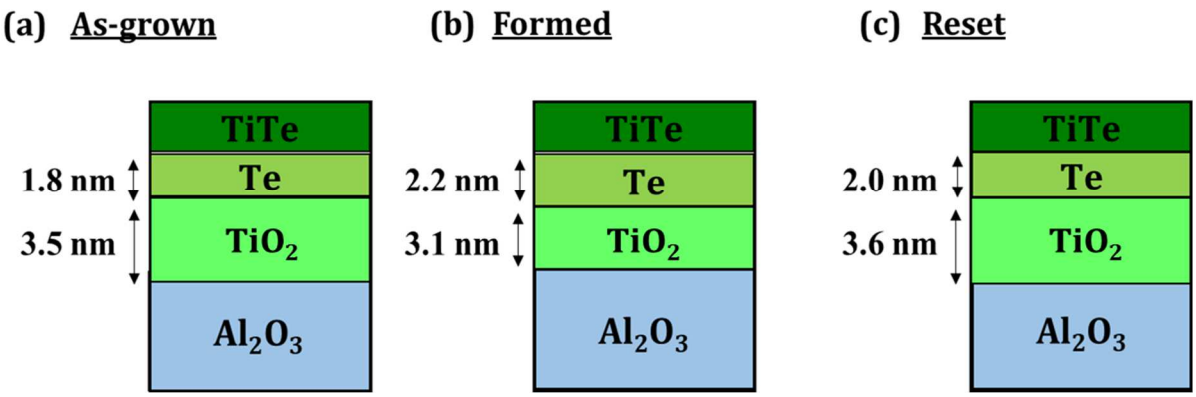

Figure 4.9 Evolution of the thicknesses of the Te and TiO_2 layers during reverse forming and reset in the TaN/TiTe/Al_2O_3/Ta memory stack.

Table 4.7. Estimated thicknesses of the Te and TiO_2 layers extracted from the quantitative model and the Te 3$d_{3/2}$ and Ti 1*s* core-level components intensities.

Sample	d TiO_2 (nm)	d Te (nm)
As-grown	3.5	1.8
Formed	3.1	2.2
Reset	3.6	2.0

After the reverse forming, we see an increase of the interfacial Te-rich layer and a decrease of TiO_2 layer thicknesses of the same order of magnitude (~0.4 nm). This result agrees well with the previous conclusions regarding the accumulation of Te and the accumulation of oxygen vacancies in the TiTe/Al_2O_3 interface. Both phenomena seem to contribute in the same order of magnitude to the resistive switching mechanism. After the reset, the Te-rich layer thicknesses decrease and the TiO_2 layer thicknesses increase of 0.2 nm and 0.5 nm respectively. The dissolution of oxygen vacancies seems to be the major mechanism breaking the conductive paths.

4.1.2.2. HAXPES with varying probing depths

We have performed the same analysis at 8 and 10 keV photon energies in order to vary the depth sensitivity (following the IMFPs given in Table 4.2). Figure 4.10 presents the Ti 1*s* spectra fitted with three components obtained by HAXPES at 8.0 keV and 10 keV. Table 4.8 shows the relative areas of each contribution in the as-grown, formed and reset spectra.

To evaluate the TiTe layer oxidation, the Figure 4.11 (a) shows the evolution of the relative areas (%) of the Ti 1*s* components with increasing photon energies for the as-grown sample. The increase of the relative area of TiO_x and the decrease of the TiO_2 with the increase of the sampling depth indicates a multilayer model based mainly on a TiO_2/TiTe/TiO_x configuration. This result invalidates the model described in the last section that considered only the presence of titatium oxide at the TiTe/Al_2O_3 interface.

Figure 4.11 shows the TiO_2/TiTe area ratio extracted from the Ti 1*s* at 6.9, 8 and 10 keV for the forming (b) and reset (c) steps. During the reverse forming, the TiO_2/TiTe area ratio decreases at all the photon energies, indicating some reduction of the TiO_2 interfacial layer. The opposite trend is observed for the reset at all the photon energies (increase of the TiO_2/TiTe area ratio), showing the oxidation of TiO_x. Changes are most pronounced at 6.9 keV, i.e. for a sampling depth of 11.1 nm, more sensitive to the TiTe.

Table 4.8. Relative areas (%) of the Ti 1*s* components for the as-grown, formed and reset samples obtained by HAXPES at 8.0 keV and 10 keV.

	8.0 keV			10 keV		
	TiTe	TiO_x	TiO_2	TiTe	TiO_x	TiO_2
As-grown	34.6 ± 3.4	35.7 ± 3.5	29.7 ± 2.9	31.0 ± 3.1	42.8 ± 4.2	26.2 ± 2.6
Formed	36.0 ± 3.6	35.4 ± 3.5	28.6 ± 2.8	37.0 ± 3.7	39.7 ± 3.9	23.3 ± 2.3
Reset	34.6 ± 3.4	35.4 ± 3.5	30.0 ± 3.0	32.8 ± 3.2	40.9 ± 4.0	26.3 ± 2.6

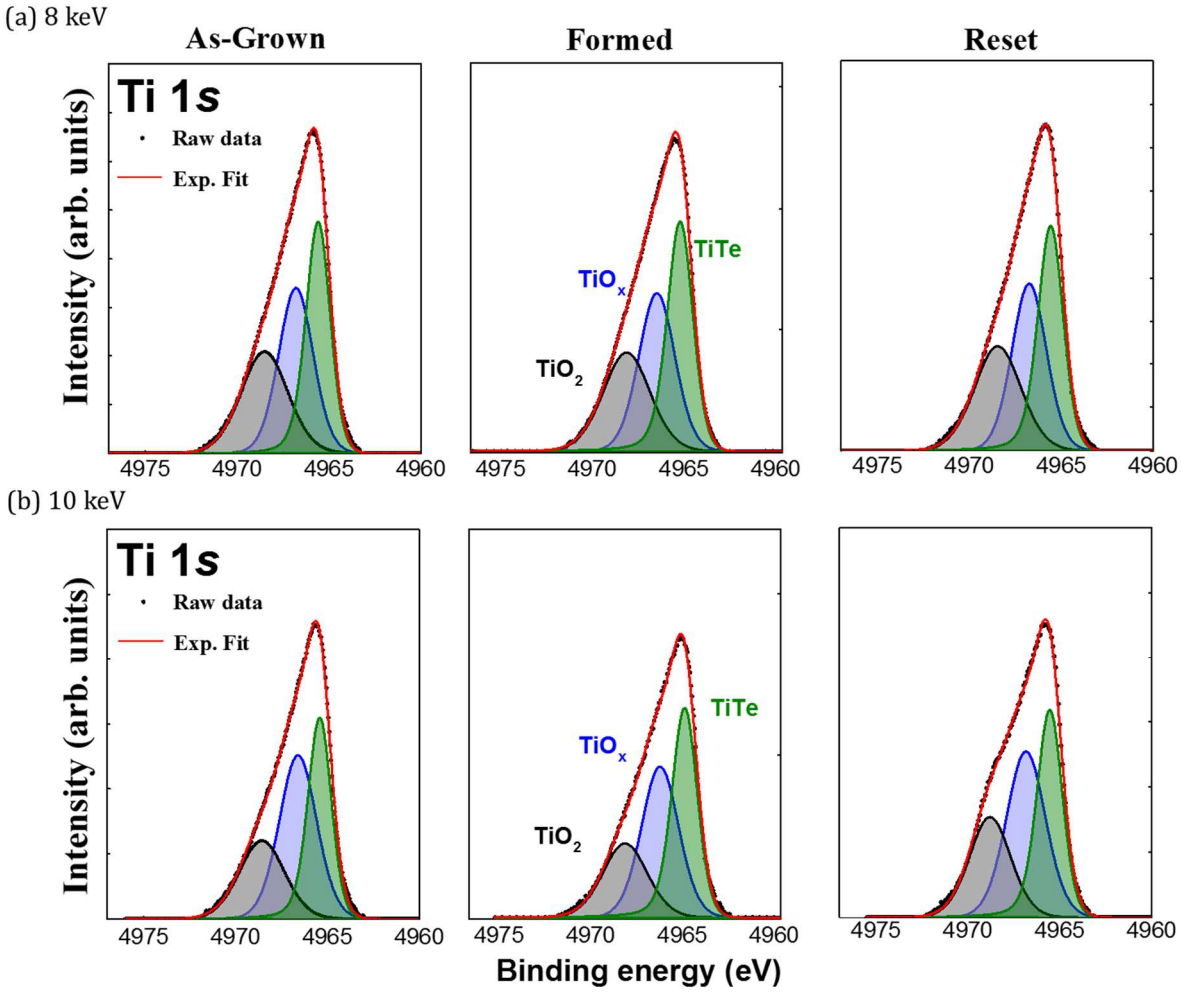

Figure 4.10. (a) Ti 1s core level peaks obtained by HAXPES at 8 keV and 10 keV on as-grown, formed and reset samples of the TaN/TiTe/Al_2O_3/Ta stack.

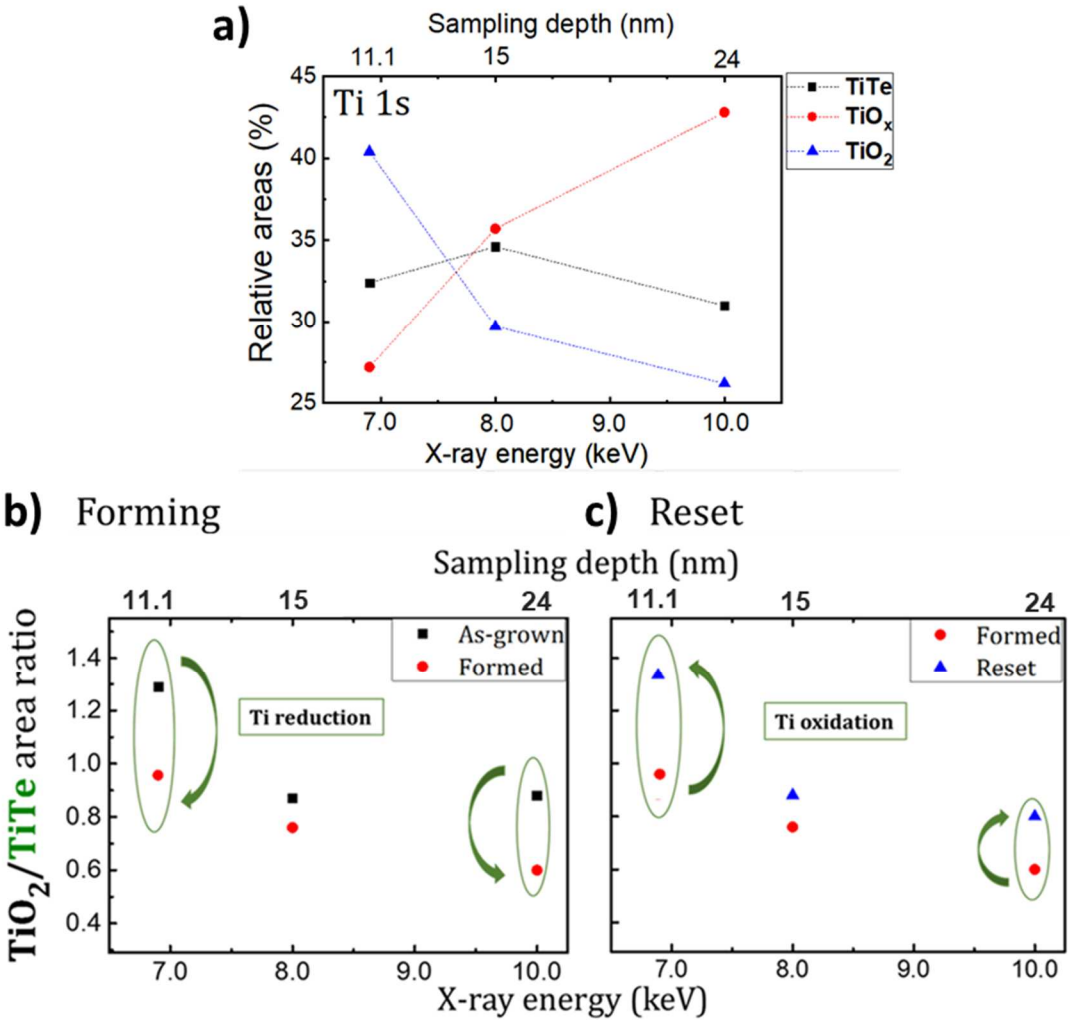

Figure 4.11 (a) Relative areas (%) of the Ti 1*s* components for the as-grown sample obtained by HAXPES at 6.9 keV ,8.0 keV and 10 keV. TiO_2/TiTe area ratios extracted from the Ti 1*s* line measured at 6.9, 8 and 10 keV for (b) as-grown, formed and (c) formed, reset samples.

Figure 4.12 presents the Te $3d_{3/2}$ spectra fitted with three components obtained by HAXPES at 8.0 keV and 10 keV. Table 4.9 shows the relative areas of each contribution in the as-grown, formed and reset spectra. The Te/TiTe area ratios are plotted in Figure 4.13 as a function of photon energy and sampling depth (3λ). On forming, the Te contribution is enhanced at 6.9 keV (3λ = 29.4 nm) at the expense of the TiTe component whereas almost no changes are observed at higher energies (8 keV and 10 keV), more sensitive to regions deeper in the stack. Te is liberated in the TiTe electrode and accumulates near the interface with Al_2O_3. After the reset, there is a decrease of the Te/TiTe ratio for the lowest photon energies (6.9 keV and 8 keV), most sensitive to the TiTe/Al_2O_3 interface. We suggest that this may reflect Te partially driven back into the TiTe.

Table 4.9. Relative areas (%) of the Te $3d_{3/2}$ components for the as-grown and formed samples obtained by HAXPES at 8 keV and 10 keV.

	8 keV			10 keV		
	TiTe	Te	TeO_x	TiTe	Te	TeO_x
As-grown	66.7 ± 6.6	25.1 ± 2.5	8.2 ± 0.8	67.0 ± 6.7	27.2 ± 2.7	5.8 ± 0.5
Formed	66.1 ± 6.6	24.5 ± 2.4	9.4 ± 0.9	69.0 ± 6.9	24.8 ± 2.4	6.0 ± 0.6
Reset	69.3 ± 6.9	21.7 ± 2.1	9.0 ± 0.9	67.2 ± 6.7	27.0 ± 2.7	5.8 ± 0.5

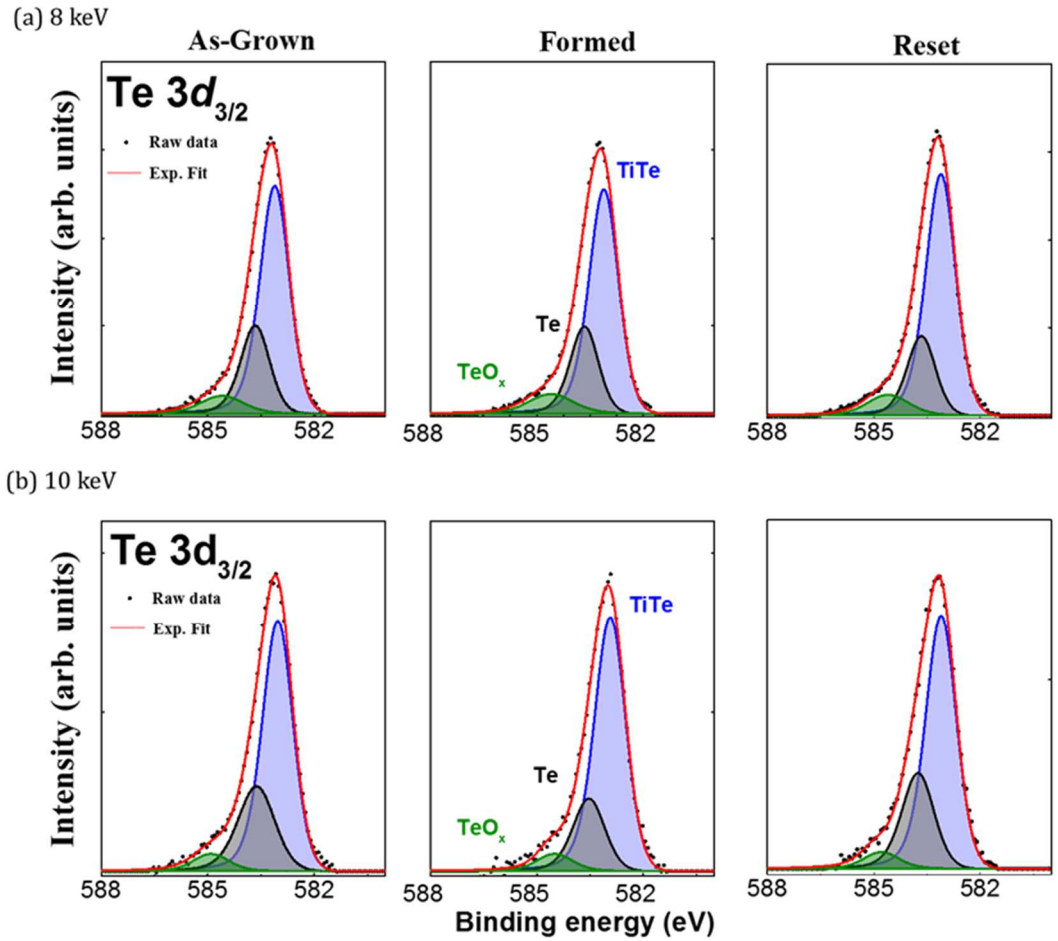

Figure 4.12. (a) Te $3d_{3/2}$ core level peaks obtained by HAXPES at 8 keV and 10 keV on as-grown, formed and reset samples of the TaN/TiTe/Al_2O_3/Ta stack.

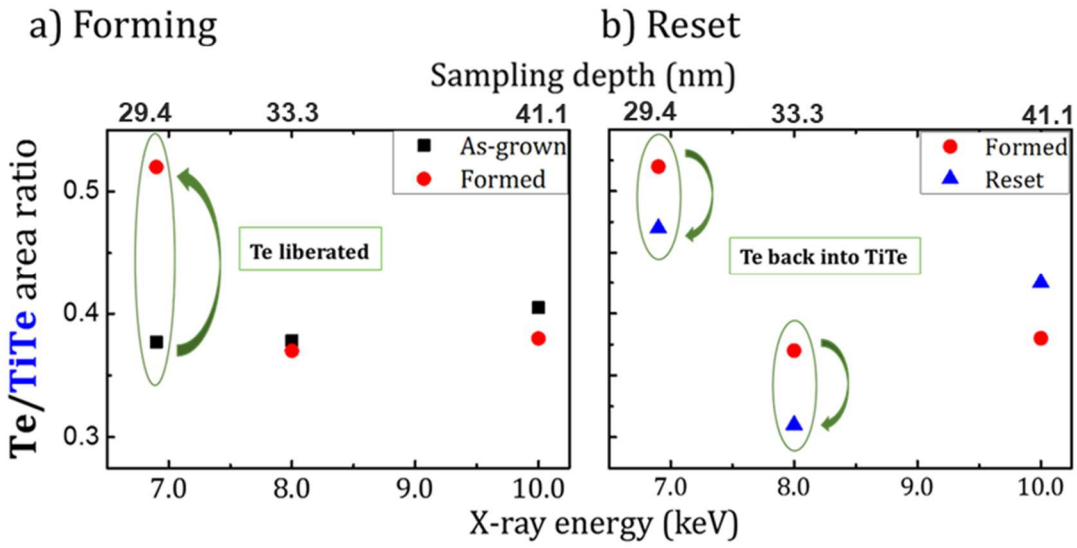

Figure 4.13. Te/TiTe area ratios extracted from Te $3d_{3/2}$ measured at 6.9, 8 and 10 keV for (a) as-grown, formed and (b) reset samples.

- **Discussion of the HAXPES analyses**

Considering the TiTe/Al_2O_3 and Al_2O_3/Ta interfaces, two distinct ion transport mechanisms appear to be at work during the forming and reset stages. The reduction of the pre-existing TiO_2 layer at the TiTe/Al_2O_3 interface (see Figure 4.5) after forming is correlated with the oxidation of the pre-existing TaO_x layer at the bottom electrode (see Figure 4.4), acting as an oxygen getter. These results are consistent with an oxygen transport towards the bottom electrode and probably an increase of the $V_O^{\bullet\bullet}$ concentration near the TiTe/Al_2O_3 interface. In turn, the oxidation of the alumina layer deduced from the decrease of the AlO_x component after the forming process (- 9%) shown in Figure 4.8 may be related to the oxidation of the alumina layer near of the Al_2O_3/Ta interface caused by the diffusion of O^{-2} driven by the electric field.

The electrochemical reactions that occurs at each interface, based on these results, can be described as:

At the TiTe/Al_2O_3 interface:

$$TiO_x + 2x\,e^- \leftrightarrow TiO_{x/2} + {}^{x}/_{2}\,O^{2-} \qquad 4.1$$

At the Al_2O_3/Ta interface:

$$TaO_{x/2} + {}^{x}/_{2}\,O^{2-} \leftrightarrow TaO_x + 2x\,e^- \qquad 4.2$$

The reverse phenomena (TiO_x oxidation and TaO_x reduction) are observed during the reset, showing oxygen movement from Al_2O_3/Ta interface to TiTe layer. During the reset, the alumina is reduced at the Al_2O_3/Ta bottom interface due to oxygen migration towards the top electrode whereas oxygen is injected

into the interface layer with the TiTe electrode which acts as a getter. The results are consistent with an oxygen transport across the stack, driven by the polarity of the applied bias. They suggest push-pull redox reactions happening at the interfaces with the top and bottom electrodes as a function of bias[140]. The key point is that the field induces matter transport and redox reactions at both top and bottom electrode/electrolyte interfaces. Thus, both top and bottom electrode should be considered as active with respect to oxygen transport (getters and reservoirs). These results denote a pure OxRRAM mechanism with $V_O^{\bullet\bullet}$ formation inside of the oxide by oxygen transport. As described by Molas et al.[67], for a Cu-based cell, a pre-forming under negative polarization can be used to improve the resistive switching of a CBRAM inducing oxygen vacancies in the oxide and facilitating the injection of Cu ions inside the electrolyte during the subsequent cycles of the cell.

A combination of both CBRAM and OxRRAM mechanisms is also possible[67,70]. The Te /TiTe intensity ratio analysis is consistent with significant Te release during forming and possible Te diffusion. The intensity ratio suggests an accumulation of elemental tellurium at the TiTe/Al_2O_3 interface after the forming process (see Figure 4.13). Te release was favored by the oxidation of Zr in the case of standard forming of ZrTe-based CBRAMs as shown in chapter 3 [9]. Here, however, the mechanism may be different because TiO_2 is reduced at the TiTe/Al_2O_3 interface because of oxygen transport during the forming whereas the Ti metal peak intensity is unchanged. The driving force for Te migration might be the electric field, pushing Te^{2-} towards the bottom electrode. Indeed, Te is known to be negatively ionized in TiTe or ZrTe alloys because of the higher Te electronegativity (2.1) than Ti/Zr (1.6/1.5). This is consistent with the increase of Te in the elemental form in the Te $3d_{3/2}$ spectra and the slight decrease after resetting. Te which has separated out at the interface or even migrated inside Al_2O_3 is also more likely to have an environment including some oxygen atoms, which could well explain the increase in the TeO_x component after forming. The major changes in the Te intensities happen during forming and are not recovered during the reset, evidence that the forming process is not fully reversible and that Te does indeed participate in the resistive switching.

It is important to note that even if the proposed mechanism considers only the changes at the alumina interfaces, the results with the variation of the probing depth (section 4.1.2.2.) showed also the presence of titanium oxide at the TaN/TiTe interface. Therefore, the preliminary multilayer model proposed in section 4.1.2.1. can not describe with accuracy the changes in the structure caused by the resistive switching. Indeed, our results showed that the redox process is not limited to the interface and probably occurs across the entire TiTe layer.

To better understand the possible O and Te diffusion during the resistive switching a ToF-SIMS depth profile was performed on the three samples in the next section 4.1.3.

4.1.3. ToF-SIMS depth profiling

Time-of-flight secondary ion mass spectrometry (ToF-SIMS) was used to study the elemental distribution depth profiles and possible interdiffusion of tellurium and oxygen during the resistive switching for as-grown, formed and reset samples. ToF-SIMS data were collected using an ION-TOF ToF-SIMS 5 instrument using the same experimental parameters as mentioned in section 3.1.5. Figure 4.14 shows the ToF-SIMS depth profiling data for all elements presents in the stack for as-grown (solid line), formed (dash line) and reset (dot line) samples. To provide a better visualization of the O, Te and Zr depth profiles, the comparisons between as-grown, formed and reset samples are shown in Figure 4.15 and Figure 4.16 (a) and (b) respectively.

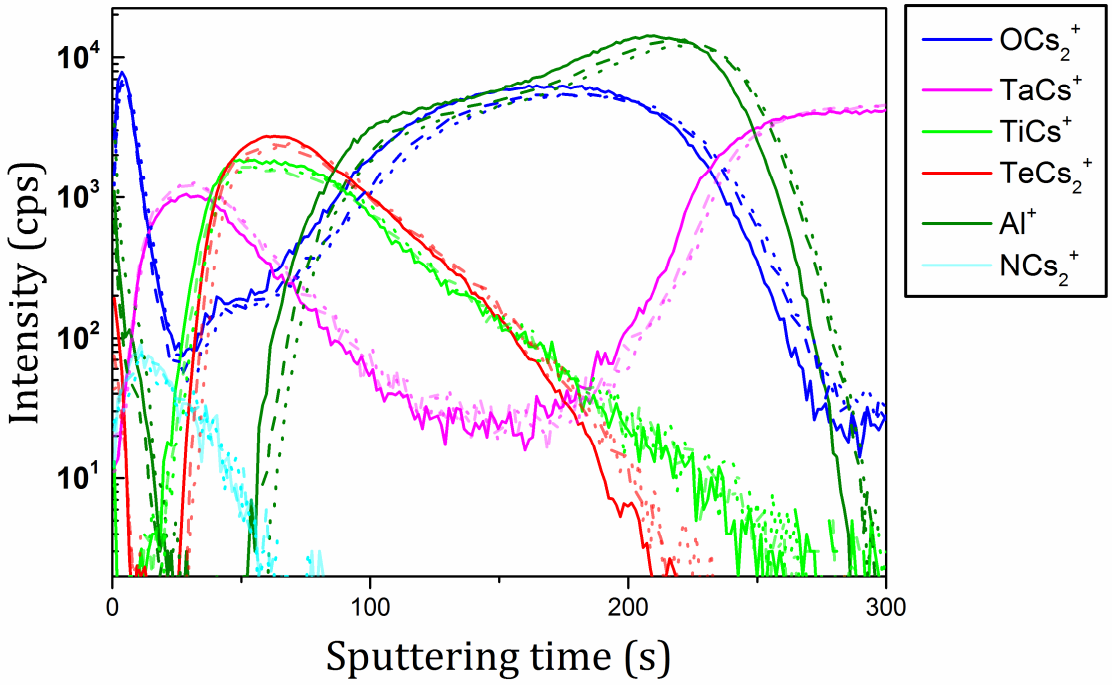

Figure 4.14. ToF-SIMS depth profiles of as-grown (solid line), formed (dash line) and reset (dot line) samples for Al^+, OCs_2^+, NCs_2^+, $TeCs_2^+$, $TiCs^+$ and $TaCs^+$.

4.1.3.1. Oxygen depth profiling

Figure 4.15 shows the oxygen and tantalum ToF-SIMS profiles in the MCs_n^+ mode (OCs_2^+ and $TaCs^+$) for as-grown, formed and reset samples. The $TaCs^+$ depth profiles (dotted lines) were used in order to guide the eye and define the top (TaN) and bottom (Ta) electrodes and thus to facilitate the analysis of the oxygen distribution in the stack.

The formed sample depth profile (red line) showed a shift of the oxygen content towards the bottom electrode in comparison to as-grown (black line). This shift is correlated with the HAXPES analysis that shows

an oxygen movement from the upper negatively biased electrode towards the bottom electrode driven by the electric field. The variation in the oxygen content is not so pronounced for the reset sample in comparison to formed since the reset process causes smaller changes in the structure than the forming process [1,22].

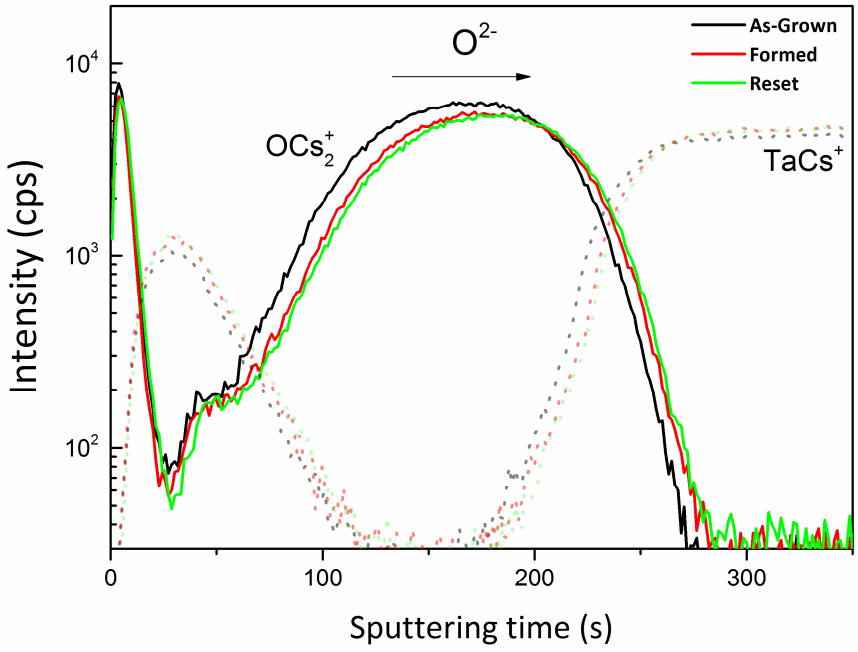

Figure 4.15. ToF-SIMS depth profiles of as-grown, formed and reset samples for OCs_2^+ and $TaCs^+$.

4.1.3.2. Te and Ti depth profiling

Figure 4.16 (a) shows the tellurium ToF-SIMS depth profiling data in the MCs_n^+ mode ($TeCs_2^+$) for as-grown, formed and reset samples. The formed depth profile shows a shift towards longer sputtering times in comparison to as-grown. This shift can be related to a diffusion of tellurium from the TiTe layer towards the electrolyte layer after the forming process. This tellurium diffusion is consistent with the elemental Te release proposed for subquantum CBRAMs based on HAXPES measurements. The major changes happen again during forming, confirming that the initial state is not completely recovered during the reset. On the other hand, the $TiCs^+$ profiles shown in Figure 4.16 (b) are rather stable for the three resistive states.

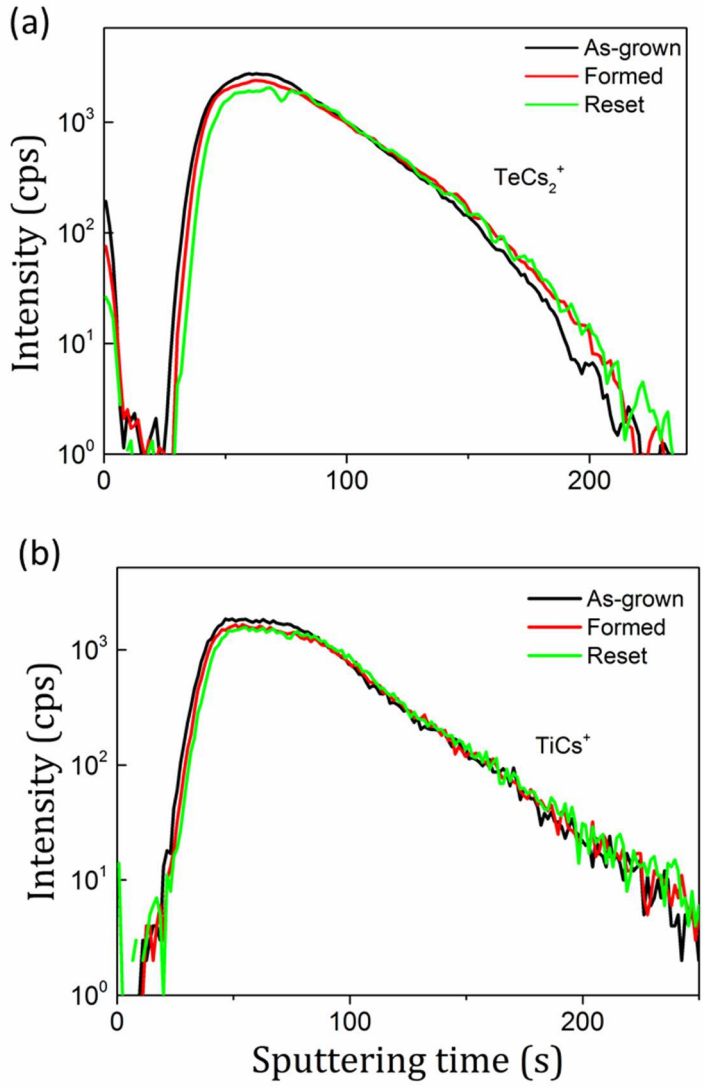

Figure 4.16. ToF-SIMS depth profiles of as-grown, formed and reset samples for (a) $TeCs_2^+$ and (b) $TiCs^+$.

4.1.4. Summary of the reverse forming and reset process for $TiTe/Al_2O_3$ based CBRAM

On the basis of these results, we suggest the forming and reset mechanisms which are shown schematically in Figure 4.17. During forming, we think there is coexistence of interfacial redox processes and localized diffusion mechanisms. Redox processes take place at both $TiTe/Al_2O_3$ and Al_2O_3/Ta interfaces. TaO_x at the bottom electrode is oxidized, with a correlated TiO_x reduction at the top electrode. These redox processes are activated by oxygen migration, the O^{2-} ions drifting downwards under the negative bias applied on the top TaN electrode. A corresponding increase of the oxygen vacancies concentration at the $TiTe/Al_2O_3$ interface is assumed. This oxygen migration was confirmed by the oxygen ToF-SIMS depth profiles for as-grown and formed samples, as shown in Figure 4.15.

In parallel, the HAXPES spectra highlight the accumulation of Te at the TiTe/Al_2O_3 interface. Similarly, to oxygen, Te^{2-} might also drift inside the alumina under the applied field. This migration of Te was evidenced by the shift towards the bottom electrode of the Te ToF-SIMS depth profiling (see Figure 4.16 (a)). Considering a hybrid mechanism, a possible physical interpretation of the forming mechanism is thus the coexistence of phenomena typical of both CBRAMs (Te migration) and OxRRAMs ($V_O^{\bullet\bullet}$ formation by oxygen transport). Thus, the resistive switching mechanism is possibly related to the presence of $V_O^{\bullet\bullet}$ inside the alumina but also to Te drift [70,71,137].

The ions and $V_O^{\bullet\bullet}$ transport mechanisms are reversed during the reset a) TaO_x reduction and TiO_x oxidation following the oxygen movement towards the top electrode, b) less free Te is observed probably because driven back into the top electrode, reforming the TiTe alloy. Both the recombination of oxygen ions with $V_O^{\bullet\bullet}$ at the TiTe/Al_2O_3 interface by reoxidation and the loss of Te near TiTe might help to switch back the structure in a high resistance state.

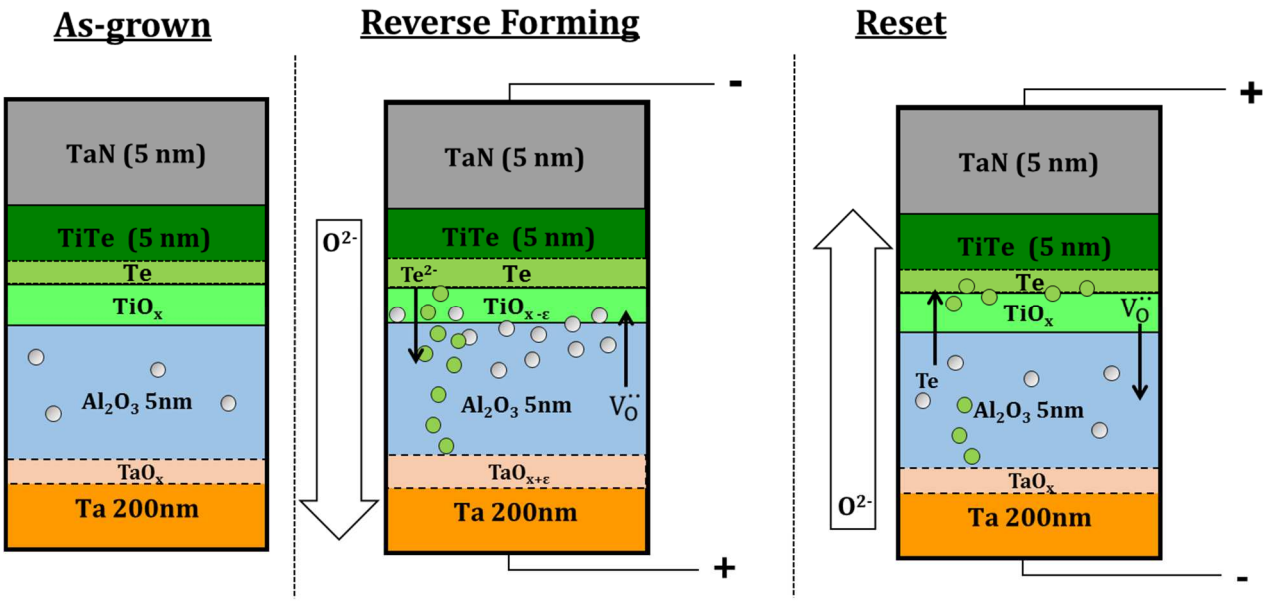

Figure 4.17 Schematic of the (a) as-grown sample and the redox processes and matter transport taking place during (b) forming and (c) reset in the TaN/TiTe/Al_2O_3/Ta stack.

This work provides evidence that the OxRRAM mechanism occurs in the TiTe/Al_2O_3-based CBRAM when a negative voltage is applied on the device. In addition, the results showed a Te release from the top electrode during the forming process. Note that the increase of the elemental Te does not necessarily imply migration, it may also be due to the formation of Te-Te bonds inside the top electrode. In this case only the formation of oxygen vacancies inside of the electrolyte then an OxRRAM behavior may explain the resistive switching of the forming process.

4.2. Investigation of $ZrTe/Al_2O_3$ based CBRAM

This section shows the second part of the reverse forming and reset processes study using ZrTe as active electrode. In this study we used a similar sample than for the positive forming analysis shown in chapter 3 for the SOLEIL measurements: TiN (5 nm)/ZrTe (5nm)/Al_2O_3 (5nm)/Ta (200 nm) stack.

4.2.1. Electrical characterization of the $ZrTe/Al_2O_3$ based sample

The definition of the compliance current was performed as showed in section 4.1.1. The I_{cc} = 10 mA was chosen since this value protected the oxide of a permanent breakdown. The typical I-V curves measured under ambient atmosphere for the TiN/ZrTe/Al_2O_3/Ta devices are shown in Figure 4.18 (a) for the forming and reset steps (reset sample). The I-V curve shown in Figure 4.18 (b) was measured on a different sample which had only undergone forming (formed sample). During the forming step, the current increases slowly when applying the negative voltage and then abruptly at the forming voltage (V_F) of -3.8 V to reach the 10 mA compliance current. During the reset step, a positive voltage is applied to the structure until reaching an abrupt decrease of the current at the reset voltage (V_{Reset}) of 0.6 V.

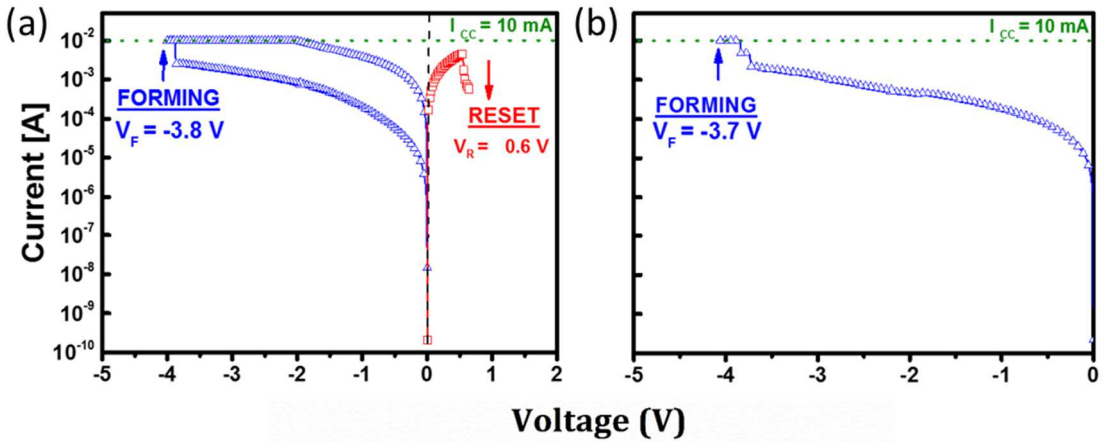

Figure 4.18. Current - voltage (I-V) curves for the (a) forming and reset process of the reset sample and (b) forming process of the formed sample for the TiN/ZrTe/Al_2O_3/Ta devices.

The device resistance measured before and after forming are equal to $R_{As\text{-}grown}$ = 1.25x10^4 Ω and R_{Formed} = 1.18x10^2 Ω. The corresponding resistance ratio $R_{As\text{-}grown}$ / R_{Formed} = 1.1 10^2 shows a significant change of the devices resistivity by the formation of a conductive path (or paths) in the electrolyte. The resistance measured after reset, R_{Reset} = 1.1x10^4 Ω, confirms the return towards the high resistive state. The HRS/LRS ratio is therefore ~ 9.4x10^1.

Table 4.10 summarizes the results of the electrical characteristics for the formed and reset samples analyzed by both HAXPES and ToF-SIMS.

Table 4.10. Electrical characteristics of the formed and reset samples analyzed by HAXPES and ToF-SIMS

Sample	$R_{As\text{-}grown}$ ($10^4\,\Omega$)	R_{Formed} ($10^2\,\Omega$)	R_{Reset} ($10^4\,\Omega$)	$R_{As\text{-}grown}$ / R_{Formed} (10^1)	R_{Formed}/ R_{Reset} (10^1)	I_{cc} (mA)	V_F (V)	V_{Reset} (V)
Formed	1.0	1.42	-	7.0	-	10	-3.7	-
Reset	1.25	1.18	1.1	11.0	9.4	10	-3.8	0.6

Taking into account three tests, we can obtain an average forming voltage of -3.7 V and an average reset voltage of 0.6 V. Regarding the resistances, we have an average of as-grown and formed resistances of $1.0x10^4\,\Omega$ and $1.3x10^2\,\Omega$ respectively. The resistance ratio $R_{As\text{-}grown}$ / R_{Formed} was around 10^1-10^2.

Note that the V_F measured for this sample was higher than the breakdown voltage value estimated (3.6 V) for an alumina layer of 5 nm (see section 3.1.1.). However, the reset step shown in Figure 4.18 (a) demonstrates that the oxide has not undergone an irreversible damage during the negative bias application and can be partially erased by applying the opposite polarity to the structure.

4.2.2. Hard X-ray photoelectron spectroscopy (HAXPES) analysis

This study was divided in two parts. In the first part, we will show in detail the results obtained by HAXPES at 8.0 keV. At this energy the results showed a significant structural difference before and after the forming and reset process. The second part will show the results at different photon energies (at 6.9 keV, 8 keV and 10 keV), thus varying the sampling depth. The values of λ are estimated with the Tanuma equation [94] for Al 1*s*, Zr $2p_{3/2}$, Te $3d_{3/2}$ and Ta $3d_{5/2}$ photoelectrons and are given in Table 4.11. The parameters used to fit the HAXPES peaks are presented in Table A.1 and in Table A.2 (Binding Energies) in annex A.

Table 4.11 Inelastic mean free path for photon energy of 6.9, 8 and 10 keV. The sampling depth is defined to be 3 λ. [88]

	6.9 keV	8.0 keV	10 keV
	λ (nm)	λ (nm)	λ (nm)
Al 1*s*	8.8 ± 1.8	10.0 ± 2.0	12.6 ± 2.5
Zr $2p_{3/2}$	7.7 ± 1.5	9.4 ± 1.9	11.6 ± 2.3
Te $3d_{3/2}$	10.1 ± 2.0	11.4 ± 2.3	14.0 ± 2.8
Ta $3d_{5/2}$	8.5 ± 1.7	10.0 ± 2.0	12.5 ± 2.5

4.2.2.1. HAXPES – 8.0 keV

HAXPES was performed on the as-grown, formed and reset samples, and also on the bare Al_2O_3/Ta structure outside the top electrode in order to provide reference spectra for aluminum.

- **Electrode metal chemistry**

The characterization of the bottom electrode was made by analyzing the Ta $3d_{5/2}$ spectra showed in Figure 4.19. The spectra have been fitted considering three contributions. The first contribution is characteristic of Ta at 1731.4 eV, the second component at 1733.4 eV is characteristic of tantalum sub-oxide (TaO_x) and the third component at 1736.7 eV is characteristic of Ta_2O_5. The deconvolution procedure for the as-grown spectrum highlights the presence of tantalum oxide at the Al_2O_3/Ta interface. The comparison between as-grown, formed and reset spectra showed a decrease of the metallic Ta contribution (- 2.7 %) and an increase in oxidized Ta after forming and, conversely, an increase of metallic Ta (+ 2.0 %) accompanied by a decrease in the TaO_x and Ta_2O_5 after reset (see Table 4.12).

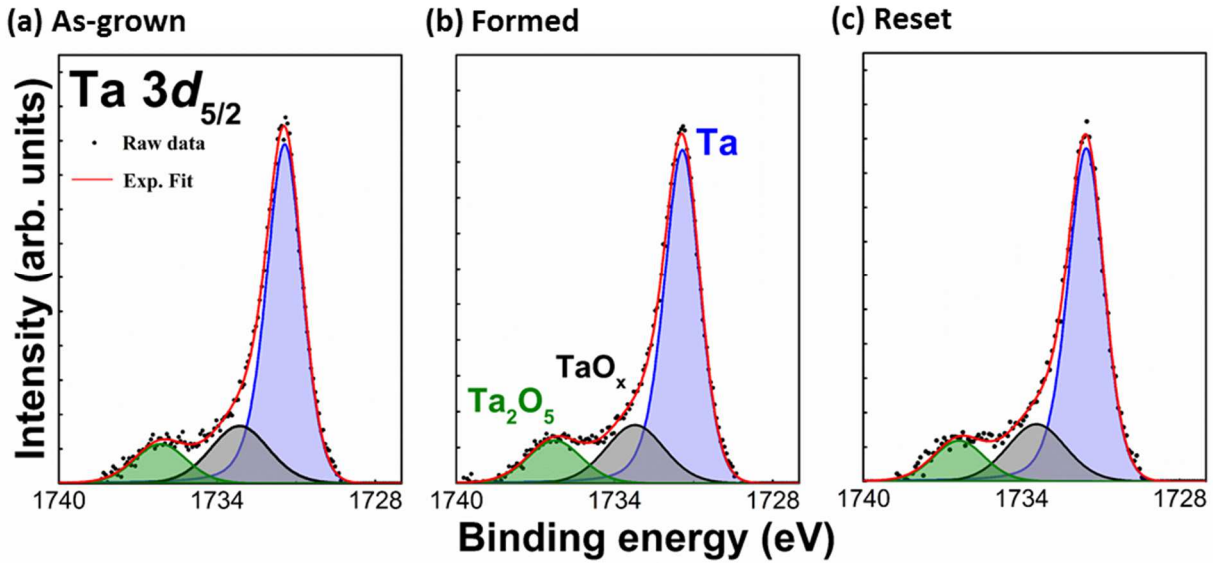

Figure 4.19 Ta $3d_{5/2}$ core level peaks obtained by HAXPES at 6.9 keV on as-grown, formed and reset sample of the TiN/ZrTe/Al_2O_3/Ta stack.

Table 4.12 Relative areas (%) of the Ta $3d_{5/2}$ components measured outside the top electrode and for the as-grown, formed and reset samples.

	Ta	TaO_x	Ta_2O_5
As-grown	74.4 ± 7.4	16.3 ± 1.6	9.3 ± 0.9
Formed	71.7 ± 7.1	17.8 ± 1.7	10.5 ± 1.0
Reset	73.7 ± 7.3	16.7 ± 1.6	9.6 ± 0.9

Figure 4.20 presents the Zr $2p_{3/2}$ spectra measured at 8 keV for as-grown, formed and reset samples. As shown before in section 3.1.3., a preliminary redox process at the ZrTe/Al_2O_3 causes the Zr oxidation by oxygen scavenging from the alumina layer. Therefore, the deconvolution of these Zr $2p_{3/2}$ spectra have been done considering two contributions. The first component at 2222.8 eV was fitted using a Doniach-Sunjic [127] function and it is characteristic of the ZrTe alloy. The second component at 2224.3 eV was fitted using a Lorentzian-Gaussian function and it is characteristic of ZrO_2.

A comparison between the relative areas of each component for the as-grown, formed and reset spectra is presented in Table 4.13. We can observe a decrease of the ZrO_2 area (-5.5 %) with respect to the main peak after negative forming. This result is consistent with the increase of TaO_x and Ta_2O_5 contributions shown in the Table 4.12 and highlights an oxygen migration, probably in the O^{2-} form, towards the bottom electrode. On the other hand, the reset operation (positive polarization) caused an increase of ZrO_2 contribution (+ 6.8 %) again consistent with oxygen transport back into the ZrTe top electrode, favoring TaO_x reduction at the Al_2O/Ta interface. Note that the ZrO_2 component includes again a contribution related to the Zr oxidation at the TiN/ZrTe interface which partially hide the redox phenomenon occurring at the buried ZrTe/Al_2O_3 interface.

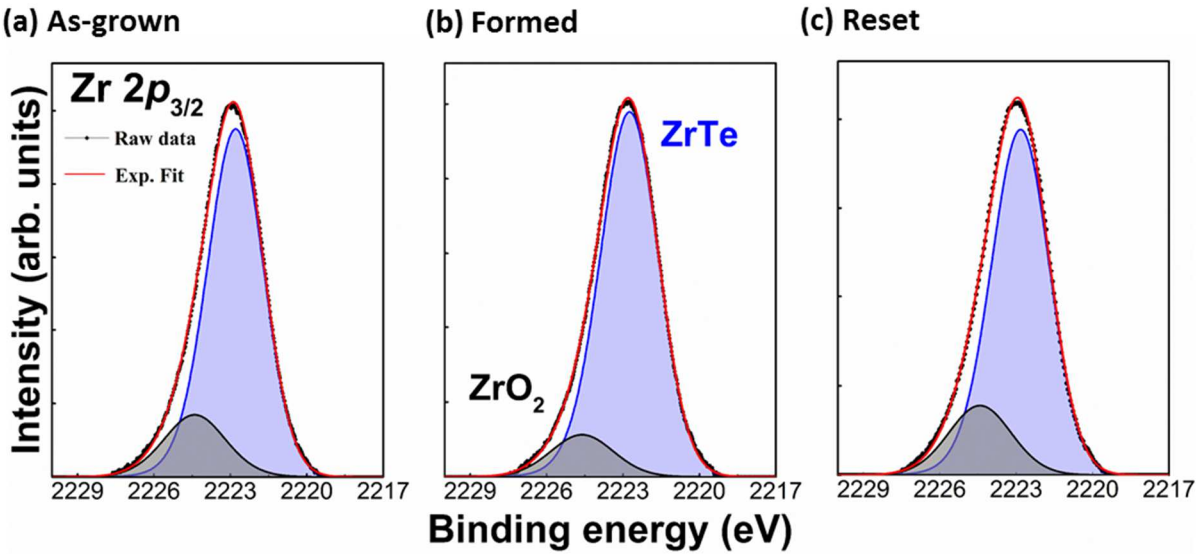

Figure 4.20 (a) Zr $2p_{3/2}$ core level peaks obtained by HAXPES at 8 keV on as-grown, formed and reset sample of the TiN/ZrTe/Al_2O_3/Ta stack.

Table 4.13. Relative areas (%) of the Zr $2p_{3/2}$ components for the as-grown, formed and reset samples obtained by HAXPES at 8 keV.

	ZrTe	ZrO_2
As-grown	83.2 ± 8.3	16.8 ± 1.6
Formed	88.7 ± 8.8	11.3 ± 1.1
Reset	81.9 ± 8.1	18.1 ± 1.8

- **Te and electrolyte chemistry**

The Te $3d_{3/2}$ spectra measured for the three different states are shown in Figure 4.21. These peaks have been fitted considering three contributions. The major component at 582.9 eV is related with the ZrTe alloy, the second component at 583.6 eV is characteristic of elemental Te (semiconductor) and the last component at 584.9 eV is related with tellurium sub-oxide (TeO_x) [130,131].

Table 4.14 shows the relative areas comparison extracted from as-grown, formed and reset spectra. After the forming operation, as a result of negative polarization, a decrease in the Zr-Te bonds (- 6.1 %) and an elemental tellurium increase (+ 6.9 %) was observed. In turn the reset operation causes the reverse process with a reduction of elemental tellurium (-2.3%) and an increase of the ZrTe bonds (+2.2%). Note that changes are again less pronounced for the reset process such as for TiTe.

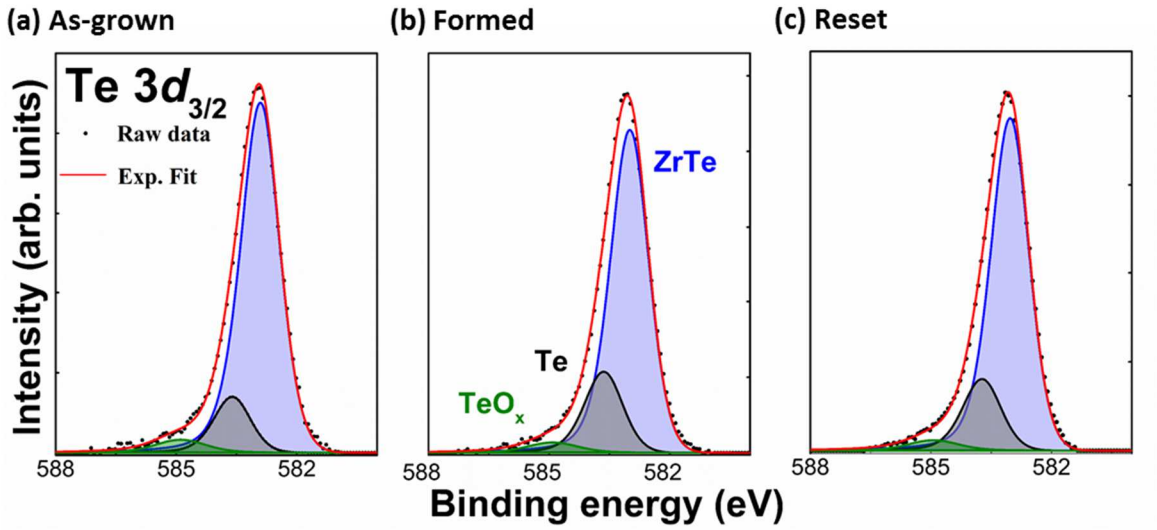

Figure 4.21 Te $3d_{3/2}$ core level peaks obtained by HAXPES at 8 keV on: a) as-grown, b) formed and c) reset states of the TiN/ZrTe/Al_2O_3/Ta stack.

Table 4.14. Relative areas (%) of the Te $3d_{3/2}$ components for the as-grown, formed and reset samples obtained by HAXPES at 8 keV.

	ZrTe	Te	TeO_x
As-grown	83.3 ± 8.3	12.4 ± 1.2	4.3 ± 0.4
Formed	77.2 ± 7.7	19.3 ± 1.9	3.5 ± 0.3
Reset	79.4 ± 7.9	17.0 ± 1.7	3.6 ± 0.3

The Al 1*s* reference spectrum measured outside the top electrode on the Al_2O_3/Ta is shown in Figure 4.22. The Al 1*s* core level spectra for as-grown, formed and reset are shown in Figure 4.23. The decomposition of these Al 1*s* spectra took into account two contributions: aluminum sub-oxide (labeled AlO_x) at binding energy (BE) of 1561.9 eV and fully oxidized Al_2O_3 at 1562.7 eV. The relative areas of these components are given in Table 4.15.

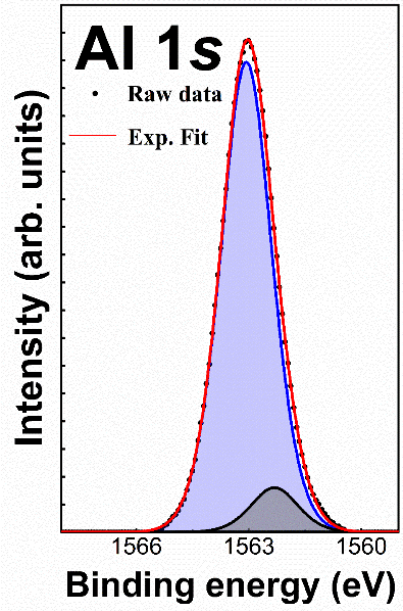

Figure 4.22. (a) Al 1s core level spectra obtained at 8.0 keV photon energy on the bare Al_2O_3/Ta structure.

The comparison between the spectrum measured on the bare Al_2O_3/Ta structure and that of the as-grown sample showed an increase of the relative AlO_x contribution (+ 9.9 %) in the latter. This result highlights the additional alumina reduction caused by the top electrode deposition. Pumping of oxygen by the Zr evidenced in Figure 4.20 causes the creation of positively charged oxygen vacancies $V_O^{\bullet\bullet}$ in the electrolyte.

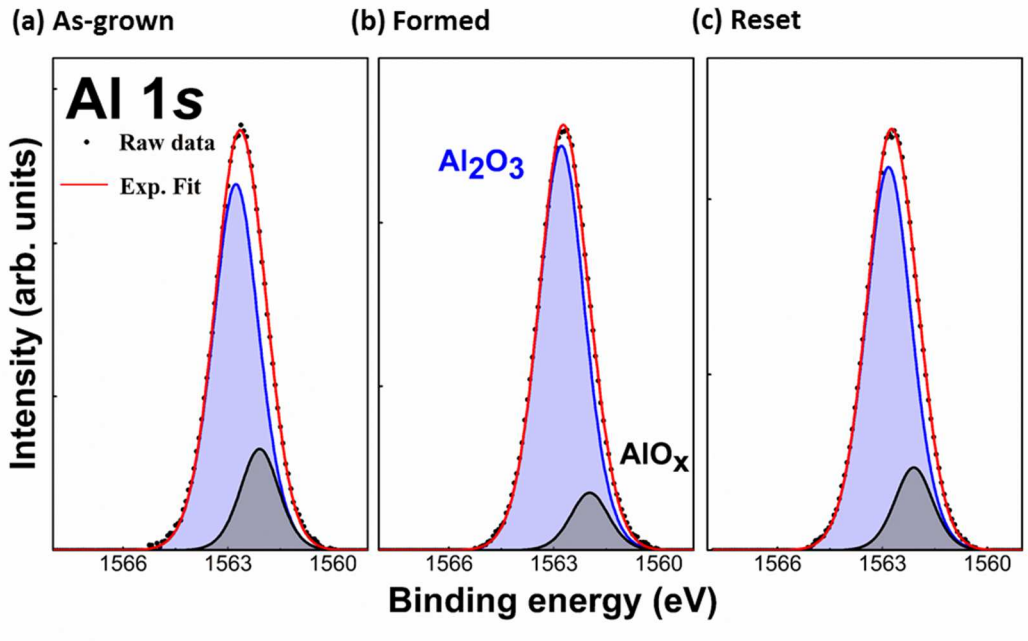

Figure 4.23 Al 1*s* core level peaks obtained by HAXPES at 8 keV on: a) as-grown, b) formed and c) reset states of the TiN/ZrTe/Al_2O_3/Ta stack.

Table 4.15. Relative areas (%) of the Al 1s components for the as-grown, formed and reset samples.

	Al_2O_3	AlO_x
Al_2O_3/Ta	91.9 ± 9.1	8.9 ± 0.8
As-grown	81.2 ± 8.1	18.8 ± 1.8
Formed	89.6 ± 8.9	10.4 ± 1.0
Reset	84.9 ± 8.4	15.1 ± 1.5

These results showed also a decrease of the sub-oxide contribution (AlO_x at 1561.9 eV) relative to the main contribution (Al_2O_3 at 1562.7 eV) for the formed state with respect to the as-grown stack (-8.4 %). After the reset process the results showed an increase of the AlO_x contribution (+ 4.7 %).

- **Multilayer model**

To try to quantify er quantify the redox phenomena caused by the forming and reset processes, we have used a multilayer model [135,141]. We assume the presence of distinct layers of ZrO_2 and Te at the ZrTe/Al_2O_3 upper interface, and of TaO_y (TaO_y = TaO_x + Ta_2O_5) at the Al_2O_3/Ta interface as shown in Figure 4.24. In this case, the calculation of the TaO_y layer thicknesses was possible since the Ta $3d_{5/2}$ spectra only presents the contribution of the Ta bottom electrode. The layer structure is only a schematic to allow approximate model calculations of equivalent thicknesses. For example, the interface layer of the top electrode could well be a phase separated ZrO_2, Te and ZrTe and the interface layer of the bottom electrode could be a phase separated TaO_y and Ta.

We also assume that the released Te mainly stays at the interface. To calculate their respective thicknesses, the intensity ratios extracted from the Zr $2p_{3/2}$,Te $3d_{3/2}$ and Ta $3d_{5/2}$ core levels can be expressed using the equation (4.7), (4.8) and (4.9) as detailed in section 3.1.3.1. We assume that d_{ZrO2}+ d_{ZrTe} = 5 nm, d_{Te}+ d_{ZrTe} = 5 nm and d_{TaOy}+ d_{Ta} = ∞ nm and that the IMPFs of Zr $2p_{3/2}$, Te $3d_{3/2}$ and Ta $3d_{5/2}$ photoelectrons were the same in all the layers of the stack and equal to λ_{Ti} = 9.4 nm, λ_{Te} = 11.4 nm and , λ_{Te} = 10.0 nm , respectively.

$$\frac{I_{ZrO2}}{I_{ZrTe}} = \frac{I^{\infty}_{ZrO2}}{I^{\infty}_{ZrTe}} \exp\left(\frac{-d\ ZrTe}{\lambda\ \mathrm{Zr}}\right) \frac{1-\exp\left(\frac{-d\ ZrO2}{\lambda\ Zr}\right)}{\left[1-\exp\left(\frac{-d\ ZrTe}{\lambda\ Zr}\right)\right]} \quad 4.7$$

$$\frac{I_{Te}}{I_{ZrTe}} = \frac{I^{\infty}_{Te}}{I^{\infty}_{ZrTe}} \exp\left(\frac{-d\ ZrTe}{\lambda\ \mathrm{Te}}\right) \frac{1-\exp\left(\frac{-d\ Te}{\lambda\ Te}\right)}{\left[1-\exp\left(\frac{-d\ ZrTe}{\lambda\ Te}\right)\right]} \quad 4.8$$

$$\frac{I_{Ta}}{I_{TaOy}} = \frac{I^{\infty}_{Ta}}{I^{\infty}_{TaOy}} \exp\left(\frac{-d\ TaOy}{\lambda\ \mathrm{Ta}}\right) \frac{1}{\left[1-\exp\left(\frac{-d\ TaOy}{\lambda\ Ta}\right)\right]} \quad 4.9$$

The Zr $2p_{3/2}$, Te $3d_{3/2}$ and Ta $3d_{5/2}$ spectra measured at 8.0 keV have been used to estimate

respectively the ZrO_2, Te and TaO_y thicknesses, because the changes are more pronounced at this energy. The results obtained for the forming and the reset are summarized in Figure 4.24 and Table 4.16.

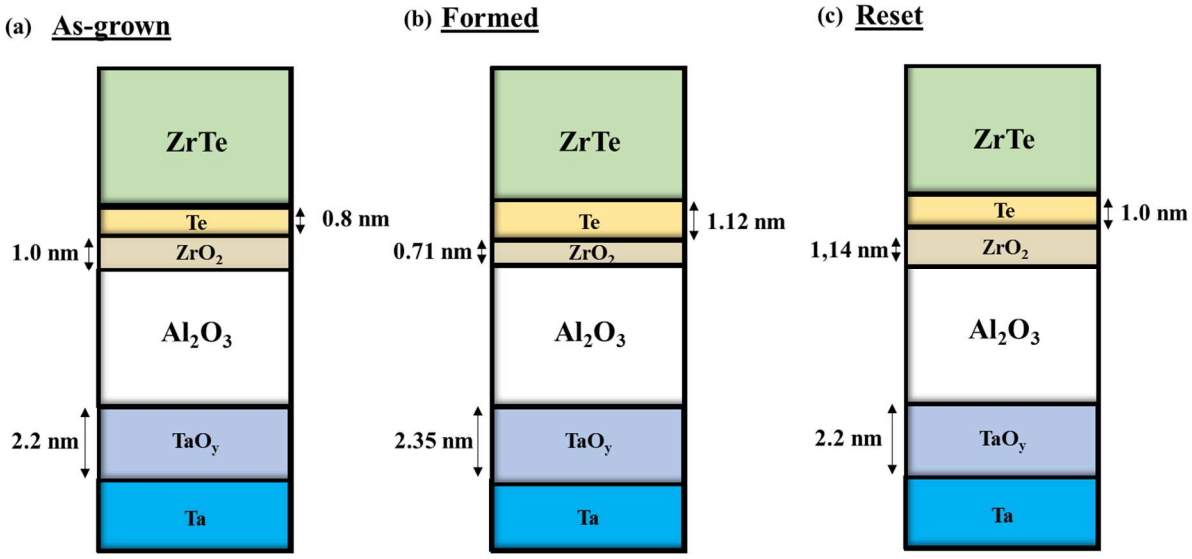

Figure 4.24 Evolution of the thicknesses of the Te, ZrO_2 and TaO_y layers during reverse forming and reset in the TiN/ZrTe/Al_2O_3/Ta memory stack.

Table 4.16. Estimated thicknesses of the TiTe/Te and TiTe/TiO_2 stacks extracted from the quantitative model and the Te 3$d_{3/2}$, Zr 2$p_{3/2}$ and Ta 3$d_{5/2}$ core-level components intensities.

Sample	d ZrO_2 (nm)	d Te (nm)	d TaO_y (nm)
As-grown	1.0	0.80	2.20
Formed	0.71	1.12	2.35
Reset	1.14	1.0	2.20

After the forming, we see an increase of the interfacial Te-rich layer and a decrease of ZrO_2 layer thicknesses of the same order of magnitude (~0.3 nm). This result agrees well with the previous conclusions regarding the accumulation of Te and the accumulation of oxygen vacancies in the ZrTe/Al_2O_3 interface. Both phenomena seem to contribute in the same order of magnitude to the resistive switching mechanism. In addition, we have an increase of TaO_y layer thickness (0.15 nm). This result agrees with the migration of O^{2-} towards the bottom electrode driven by the electric field. After the reset, the Te-rich layer and TaO_y thicknesses decrease (-0.12 and -0.15 nm) and the ZrO_2 layer thickness increases of 0.4 nm. The dissolution of oxygen vacancies seems again to be the major mechanism breaking the conductive paths.

It is important to note that considering only the contribution of ZrO_2 at the ZrTe/Al_2O_3 interface is an approximation. This model can not describe with accuracy the redox process during the resistive swithing as showed before in section 3.1.3.2.

4.2.2.2. HAXPES with varying probing depths

We have performed the same analysis at 6.9 and 10 keV photon energies in order to vary the depth sensitivity. Figure 4.25 presents the Zr $2p_{3/2}$ spectra fitted with two components obtained by HAXPES at 6.9 keV and 10 keV. Table 4.17 shows the relative areas of each contribution in the as-grown, formed and reset spectra.

Figure 4.26 shows the ZrO_2/ZrTe area ratio extracted from the Zr $2p_{3/2}$ at 6.9, 8 and 10 keV for the forming (a) and reset (b) steps. During the forming, the ZrO_2/ZrTe area ratio decreases at 8 keV whereas almost no changes are observed at 6.9 keV and 10 keV. Again, the ZrO_2/ZrTe area ratio is higher at 6.9 keV than 10 keV, confirming the presence of ZrO_2 also at the TiN/ZrTe interface. Changes are most pronounced at 8 keV, i.e. for a sampling depth of 28.2 nm, indicating that Zr reduction mainly occurs at the buried ZrTe/Al_2O_3 interface. The increase of the ZrO_2/ZrTe area ratio is observed for the reset at all the photon energies showing that the oxygen is re-injected into the top electrode, under the effect of the positive bias.

Table 4.17. Relative areas (%) of the Zr $2p_{3/2}$ components for the as-grown, formed and reset samples obtained by HAXPES at 6.9 keV and 10 keV.

	6.9 keV		10 keV	
	ZrTe	ZrO_2	ZrTe	ZrO_2
As-grown	72.7 ±7.2	27.3 ± 2.7	79.7 ± 7.9	20.3 ± 2.0
Formed	73.0 ± 7.3	27.0 ± 2.7	80.9 ± 8.0	19.1 ± 1.9
Reset	70.5 ± 7.0	29.5 ± 2.9	79.3 ± 7.9	20.7 ± 2.0

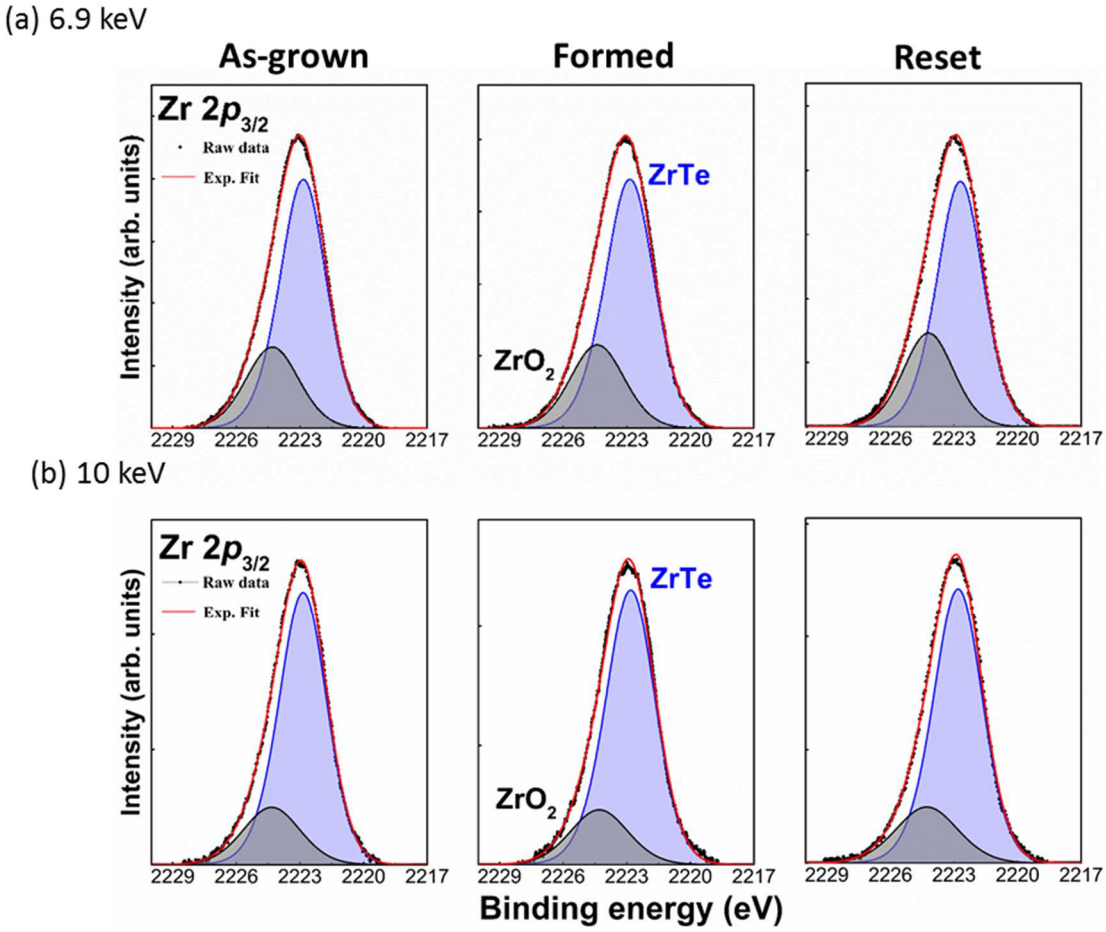

Figure 4.25. (a) Zr $2p_{3/2}$ core level peaks obtained by HAXPES at 6.9 keV and 10 keV on as-grown, formed and reset samples of the TaN/TiTe/Al_2O_3/Ta stack.

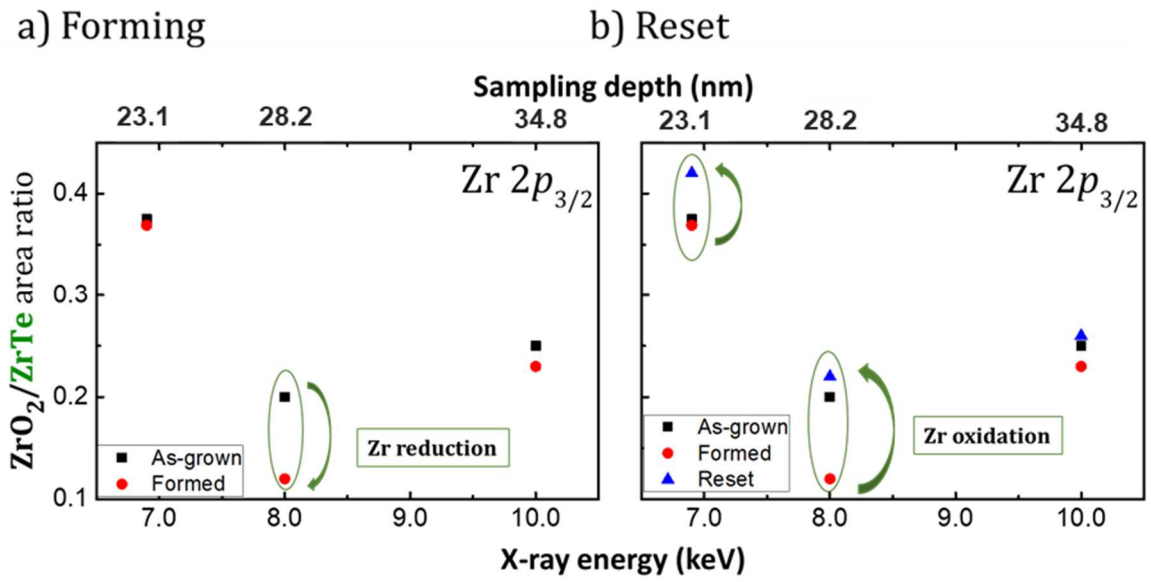

Figure 4.26. ZrO_2/ZrTe area ratios extracted from Zr $2p_{3/2}$ measured at 6.9, 8 and 10 keV for (a) as-grown, formed and (b) reset samples.

Figure 4.27 presents the Te $3d_{3/2}$ spectra fitted with three components obtained by HAXPES at 6.9 keV and 10 keV. Table 4.18 shows the relative areas of each contribution in the as-grown, formed and reset spectra. The Te/ZrTe area ratios are plotted in Figure 4.28 as a function of photon energy and sampling depth (3λ). After the forming, the Te/ZrTe area ratio increased at all the photon energies but mainly at 8 keV. This result agrees with the previous observations for TiTe that show a release of Te during the forming process. After the reset, there is a decrease of the Te/ZrTe area ratio also at all the photon energies.

Table 4.18. Relative areas (%) of the Te $3d_{3/2}$ components for the as-grown and formed samples obtained by HAXPES at 6.9 keV and 10 keV.

	6.9 keV			10 keV		
	ZrTe	Te	TeO_x	ZrTe	Te	TeO_x
As-grown	80.9 ± 8.0	16.2 ± 1.6	2.9 ± 0.2	73.1 ± 7.3	19.7 ± 1.9	7.2 ± 0.7
Formed	79.7 ± 7.9	17.6 ± 1.7	2.7 ± 0.2	71.6 ± 7.1	21.7 ± 2.1	6.7 ± 0.6
Reset	81.2 ± 8.1	15.5 ± 1.5	3.3 ± 0.3	76.7 ± 7.6	17.6 ± 1.7	5.7 ± 0.5

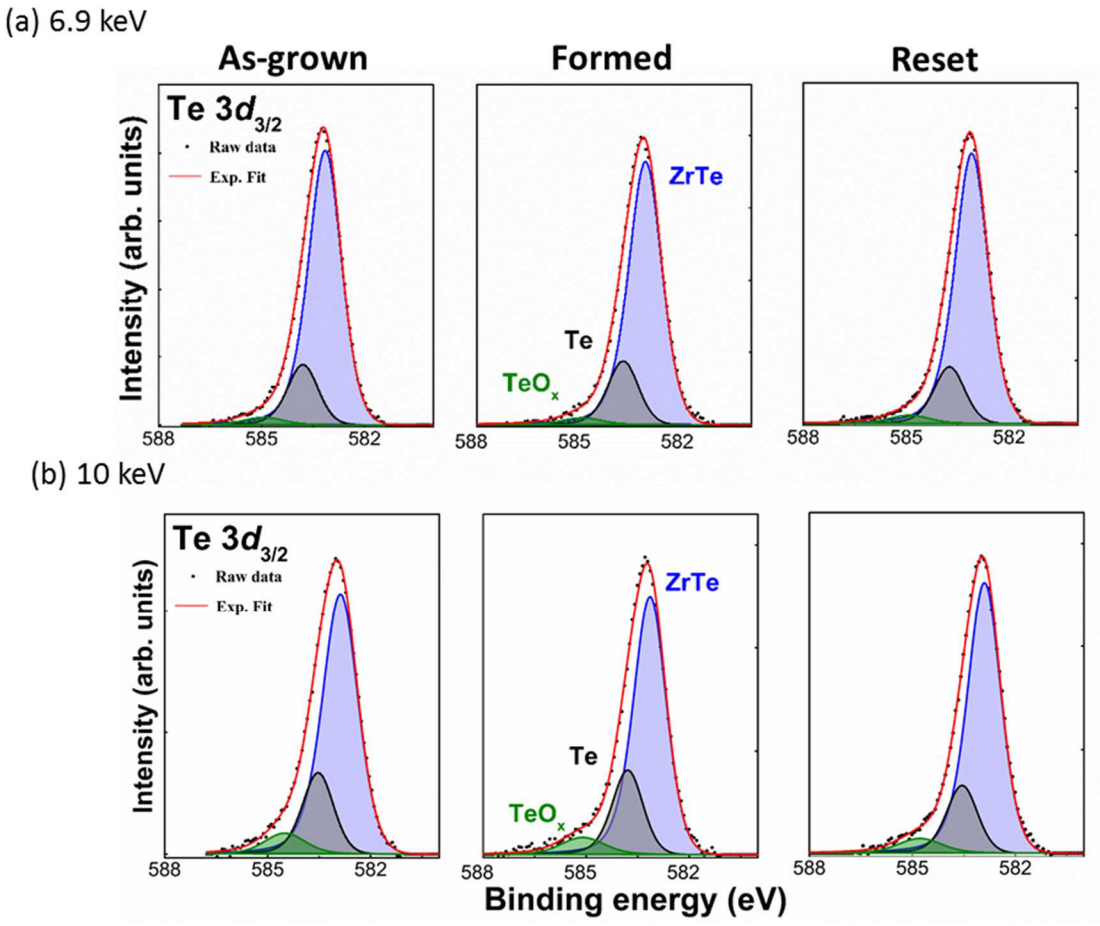

Figure 4.27. (a) Te $3d_{3/2}$ core level peaks obtained by HAXPES at 6.9 keV and 10 keV on as-grown, formed and reset samples of the TaN/TiTe/Al_2O_3/Ta stack.

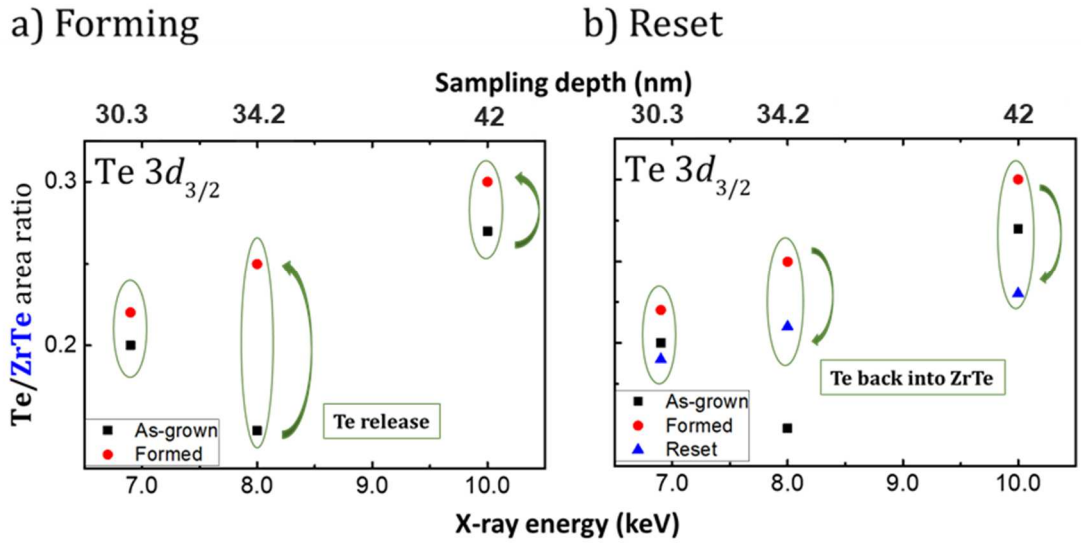

Figure 4.28. Te/ZrTe area ratios extracted from Te $3d_{3/2}$ measured at 6.9, 8 and 10 keV for (a) as-grown, formed and (b) reset samples.

- **<u>Discussion of the HAXPES analyses</u>**

Our results showed a preliminary redox process at the ZrTe/Al_2O_3 interface during the top electrode deposition process. As showed before in section 3.1.3.1, Zr scavenges the oxygen, leading to a reduction of the dielectric layer.

After the forming process, the analysis of the Zr and Ta components of the top and bottom electrodes (Zr reduction and Ta oxidation) showed a mechanism similar to that described for TiTe/Al_2O_3 samples, i.e. the applied bias causes oxygen migration in the direction of the polarity, driving redox reactions at both top and bottom interfaces. The application of a negative bias voltage causes also an oxygen reinsertion in the alumina layer. As discussed before for TiTe/Al_2O_3 devices, the migration of O^{2-} towards the bottom electrode causes an oxidation of the Al suboxide at the bottom Al_2O_3/Ta interface.

The electrochemical reactions that occur at each interface during the forming process, based on these results, can be described as:

At the ZrTe/Al_2O_3 interface:

$$ZrO_x + x\,e^- \leftrightarrow Zr^{x+} + x\,O^{2-} \quad (4.5)$$

At the Al_2O_3/Ta interface:

$$TaO_{x/2} + {}^{x}/_{2}\,O^{2-} \leftrightarrow TaO_x + 2x\,e^- \quad (4.6)$$

The reverse phenomena (ZrO_2 oxidation and TaO_x reduction) are observed during the reset, showing oxygen movement from Al_2O_3/Ta interface to ZrTe layer. In addition, we can see an increase of the AlO_x contribution (+4.7 %) for the reset state in comparison with the formed sample. Thus a reduction of the alumina layer occurs next to the interface with Ta bottom electrode due to oxygen migration towards the top electrode. Oxygen is injected into the interfacial layer with the ZrTe electrode which acts as a getter.

After the forming, the Te/ZrTe area ratio increased at all the photon energies. This result agrees with the previous results that show a release of Te and possible diffusion during the forming process. After the reset the Te/ZrTe area ratio decreased at all photon energies. We suggest that this may reflect Te partially driven back into the TiTe.

Based on these results a combination of OxRRAM (creation of $V_O^{\bullet\bullet}$ in the oxide) and CBRAM (Te migration) mechanism is also possible to explain the resistive switching of ZrTe/Al_2O_3 samples.

4.2.3. Summary of the reverse forming and reset process for ZrTe/Al_2O_3 based CBRAM

Based on these results, we suggest a similar forming mechanism than the one proposed for TiTe-based cells, as shown schematically in Figure 4.29. The main difference is a reduced oxidation of the ZrTe active electrode in the as-grown state. The ZrO_2 thickness is equal to 1 nm compared to 3.5 nm of TiO_2 for TiTe. There is thus less oxygen scavenging from the alumina with less oxygen vacancies at the ZrTe/Al_2O_3 interface. Considering that these defects are a prerequisite for the forming of such CBRAM cells, this is consistent with the higher $|V_F|$ needed for ZrTe (3.7 V instead of 3V).

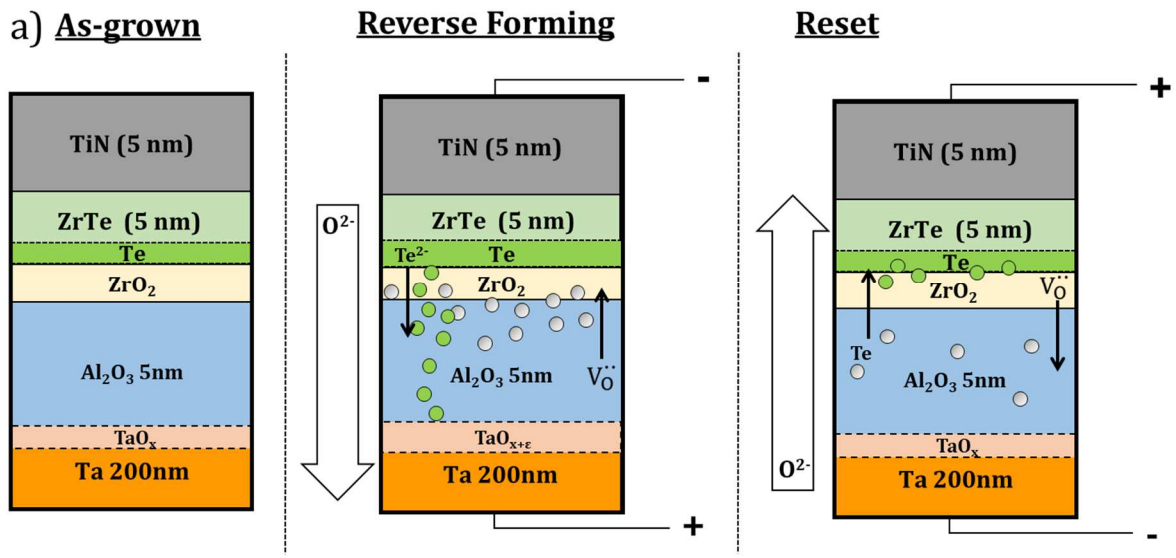

Figure 4.29 Schematic of the redox processes and matter transport taking place during the forming and reset process in the TiN/ZrTe/Al_2O_3/Ta stack.

Our results showed an increase of the $|V_F|$ under negative polarisation (3.7 V) in comparison to the $|V_F|$ measured under positive polarisation (3.0 V). We know that a positive bias causes an oxygen migration towards the top electrode and consequently a Zr oxidation. The positive forming, based on this Zr oxidation and Te release, is easy to induce because the formation of ZrO_2 is thermodynamically more favourable in comparison with Al_2O_3, as shown by the Ellingham diagram in Figure 3.9.

Regarding the reverse forming, the oxygen scavenging is related to the less favourable oxidation of Ta bottom electrode and thus harder to induce. Therefore, our results showed that a positive forming is more adapted to $ZrTe/Al_2O_3$ cells considering the interest of decreasing power consummation during this step.

4.3. Conclusion

In summary, it can be concluded that in the reverse forming of Te-based subquantum CBRAMs, the Ta bottom electrode acts as an oxygen getter creating oxygen vacancies at the Ti(Zr)Te/ Al_2O_3 interface. The oxygen movement in the form of O^{2-} is driven by the electric field from the upper negatively biased electrode towards the bottom one. Forming also causes an accumulation of elemental Te near the top interface. Te^{2-} might also be pushed inside the alumina by the electric field. On reset there is a partial recombination of oxygen ions with $V_O^{\bullet\bullet}$ near Ti(Zr)Te/Al_2O_3 interface together with a loss of Te. These results strongly suggest that CBRAM (Te transport) and OxRRAM ($V_O^{\bullet\bullet}$ migration) mechanisms coexist in these Te-based memory cells.

Chapter 5

5. *In-situ* chemical investigation of the direct forming by X-ray photoelectron spectroscopy

In this chapter, we investigate the forming process performed *in-situ*, i. e. under ultra high vacuum, to get closer to real operating conditions. X-ray photoelectron spectroscopy is performed to analyse the surface and bulk chemical composition, by combining standard and depth profiling measurements. Results are compared with forming under air exposure (*ex-situ* forming) to highligth the role of oxygen from air on the resistive swithing.

5.1. Investigation of $ZrTe/Al_2O_3$ based CBRAM

Here, we further investigate the role of oxygen in resistive switching, in particular the impact of oxygen from air. The results shown in chapter 3 and 4 provide evidences that the forming mechanism for Te-based CBRAMs is based on the coexistence of phenomena typical of both CBRAMs (Te migration) and OxRRAMs ($V_o^{\bullet\bullet}$ formation by oxygen transport). Therefore, when performing resistive switching in such devices, we can not rule out a possible impact of the environment, typically ambient air, on the resistive switching mechanism. Indeed, this environment provides an additional oxygen reservoir which might influence the internal oxygen scavenging processes and oxygen vacancies formation in the oxide layer. As a consequence, oxygen movements and corresponding oxidation/reduction processes might be modified. This has already been mentioned in the literature for standard OxRRAMs[12–14] . D. S. Jeon et al. [12] have reported that the external oxygen from air can be incorporated in the top electrode under positive bias application, causing chemical oxidation at the interface with the oxide layer and consequently retarding the accumulation of oxygen vacancies responsible by the resistive switching. L. Goux et al. [14] showed that the thickness of the top electrode and the operating environment have strong influence on the resistive switching and on the stability of the device. In addition, Ding et al.[13] showed that under positive polarization in vacuum conditions, some oxygen outgases into the ambient air increasing the oxygen vacancies concentration in the oxide and also at the top electrode/ oxide interface, resulting in a V_{set} decrease. This analysis shows that, under vacuum, the oxygen scavenging at the top interface is enhanced, facilitating the forming process.

We use X-ray photoelectron spectroscopy with *in-situ* electrical biasing to highlight the influence of the environment on forming of Te-based CBRAMs. With this technique, it is possible to analyse the variation of the surface top electrode oxidation caused by the bias application. XPS depth profiling also provides information about the depth distribution of elements. In this chapter, we compare surface and bulk chemical changes in a Te-based CBRAM during *in-situ* and *ex-situ* forming. Using a specific sample holder, we directly combine *in-situ* electrical biasing with XPS standard and depth profiling measurements. Spectra are acquired before and after the forming step, corresponding to the transition between the virgin state (VS) and the low resistive state (LRS). This work is important to clarify the influence of the atmosphere on CBRAMs resistive switching.

5.1.1. CBRAM sample used for in-situ analysis

In this study we used a similar sample to that for the positive forming analysis shown in chapter 3 for the Spring-8 experiment: TiN (15 nm)/ZrTe (10nm)/Al_2O_3 (5nm)/Ta (200 nm) stack. To facilitate the positioning of the electrical contact on the top electrode (as shown below in Figure 5.2) a square sample was used for this analysis as shown in Figure 5.1.

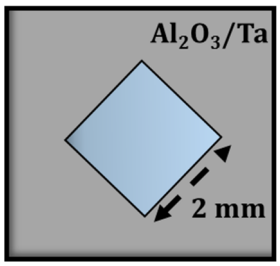

Figure 5.1. Top-view of the sample used in the *in-situ* analysis.

5.1.2. In-situ electrical switching assembly

In-situ forming was performed in the XPS analysis chamber using a specific sample holder (see Figure 5.2) from ULVAC-PHI, allowing *in-situ* electrical connections directly in the analysis chamber. Two electrical contacts were performed on the memory cell. The bottom Ta electrode was connected using a gold wire and conductive silver paste. The top electrode was contacted approaching a copper tip on the TiN surface. The memory device was insulated from the grounded sample holder with an insulating scotch tape. Once inserted in the chamber, the electrical switching was performed in ultra-high vacuum (UHV), using an external power supply, in our case a Keithley 2635B.

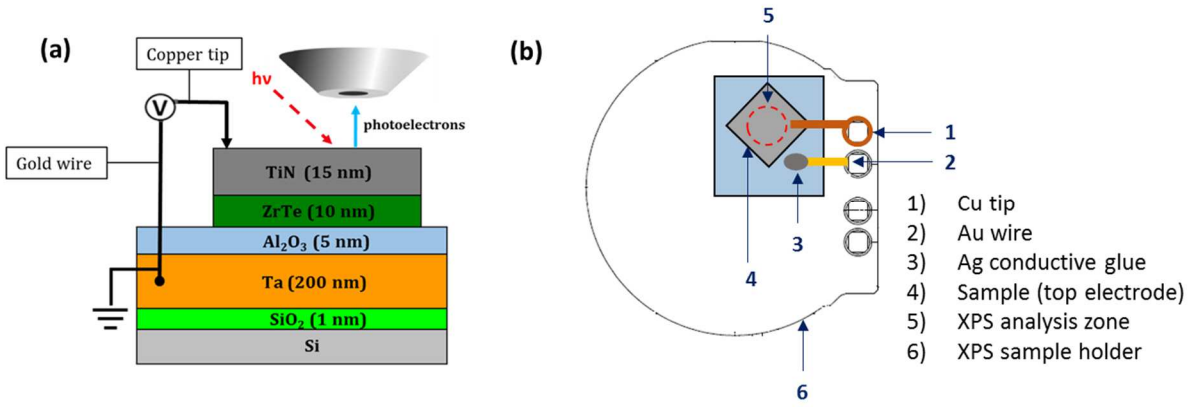

Figure 5.2. (a) Schematic of the setup for *in-situ* electrical switching and characterization (b) Assembly on the XPS sample holder.

5.1.3. Electrical characterization: *Ex-situ* and *In-situ*

The I-V curves measured under ambient atmosphere and under ultra-high vacuum are shown in Figure 5.3 for the forming process. For the *in-situ* forming (red line), a linear voltage sweep was applied via the Cu tip on the TiN (see Figure 5.2) at 0.1 V/s, between 0 and 3 V inside the XPS chamber, i. e. under ultra-high vacuum. As for the positive forming performed on a similar sample in section 3.1.2, a compliance current of 50 mA (12 mA.mm^{-2}) was chosen in order to avoid permanent breakdown of the oxide. The *ex-situ* forming (blue line) was performed using the same parameters and assembly but with a voltage application in ambient atmosphere.

The device resistance measured before and after forming under air are equal to $R_{As\text{-}grown} = 5.0x10^4\ \Omega$ and $R_{Formed} = 8.7x10^1\ \Omega$, yielding to a resistance ratio of $R_{As\text{-}grown}/R_{Formed} = 5.7x10^2$. This ratio confirms a significant change of the devices resistivity by the formation of conductive paths in the electrolyte. Regarding the forming performed in-situ, the resistances measured before and after forming are equal to $R_{As\text{-}grown} = 3.3x10^5\ \Omega$ and $R_{Formed} = 6.8x10^1\ \Omega$. The ratio $R_{As\text{-}grown}/R_{Formed}$ is equal to $4.8x10^3$. Note that the resistance window is higher by one order of magnitude in this latter case. This shows, together with the lower V_F, that ultra-high vacuum seems to favor the forming. Table 5.1 summarizes the electrical characteristics of the *ex-situ* and *in-situ* formed samples.

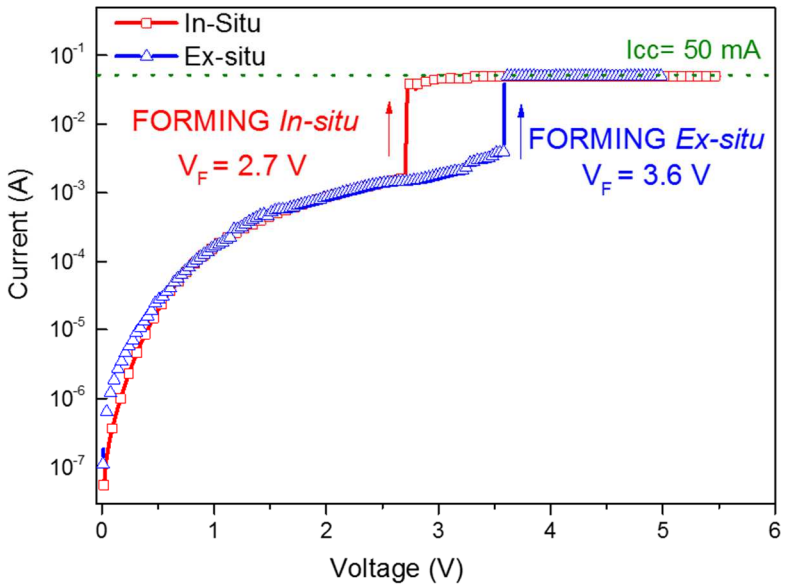

Figure 5.3. Current - voltage (I-V) curves for the forming of the TiN/ZrTe/ Al_2O_3/Ta stack under ambient air (blue) and under ultra-high vacuum (red).

Table 5.1. Electrical characteristics of the formed Ex-situ and In-situ samples.

Sample	$R_{As\text{-}grown}$ ($10^4\,\Omega$)	R_{Formed} ($10^1\,\Omega$)	$R_{As\text{-}grown}$ / R_{Formed} (10^2)	I_{cc} (mA)	V_F (V)
Ex-situ	5.0	8.7	5.7	10	2.5
In-situ	33	6.8	48	10	3.5

Taking into account three tests, we can obtain an average *in-situ* forming voltage of 2.5 V and an average ex-situ forming voltage of 3.5 V. This average considers only the electrical characterizations done using this assembly. Note that the electrical contacts for the *ex-situ* forming used in this study were different from those used in the measurements shown in chapter 3 and 4. Regarding the resistances, we have an average of as-grown and formed resistances of $2.5x10^5\,\Omega$ and $1.4x10^2\,\Omega$ respectively. The resistance ratio $R_{As\text{-}grown}$ / R_{Formed} was around 10^2-10^3 and the $R_{As\text{-}grown}$ / R_{Reset} was around 10^1 -10^2.

5.1.4. X-ray photoelectron spectroscopy analysis

5.1.4.1. Surface analysis

Laboratory XPS was performed using a PHI 5000 VersaProbe II (ULVAC-PHI) equipped with a monochromatic Al Kα source (hν = 1486.7 eV). The pass energy was set to 23.5 eV, giving an overall energy resolution of 0.5 eV, with an emission angle of 45°. Subtracted backgrounds for XPS spectra were of Shirley type, and the peaks were modeled using a Doniach-Sunjic function [127] and a combination of Lorentzian (30%) and Gaussian (70%) functions using Casa XPS v2.3 software. The sampling depths (3λsinθ) are estimated to be 4.2 nm and 3.8 nm respectively for Ti 2*p* and O 1*s* photoelectrons in TiN, using inelastic mean free paths of 2.0 nm and 1.8 nm estimated from the TTP-2M formula [94].

XPS measurements were performed on as-grown, *ex-situ* and *in-situ* formed states of the TiN/ZrTe/Al_2O_3/Ta stack. The Ti 2*p* core level spectra measured in each case are presented in Figure 5.4. The decomposition of these Ti 2*p* spectra takes into account three contributions in agreement to[142]: 1) Ti oxide (TiO_2) at binding energy (BE) of 458.6±0.2 eV, 2) Ti oxinitride (TiO_xN_y) and/or TiO_x at 457.2±0.2 eV, 3) Ti nitride (TiN) at 455.7±0.2 eV. Both TiO_2 and TiO_x/TiO_xN_y peaks are related to surface and subsurface oxidation of TiN under air exposure. Note that shake-up features may also contribute to the intensity of these two peaks. The relative areas of these components are given in Table 5.2.

Table 5.2. Relative areas (%) of the Ti 2*p* components for the as-grown, ex-situ and in-situ formed samples.

	TiN (%)	TiO_x/TiO_xN_y (%)	TiO_2 (%)
As-grown	32.4	26.6	41.0
Ex-situ	34.3	21.6	44.1
In-situ	28.8	36.5	34.7

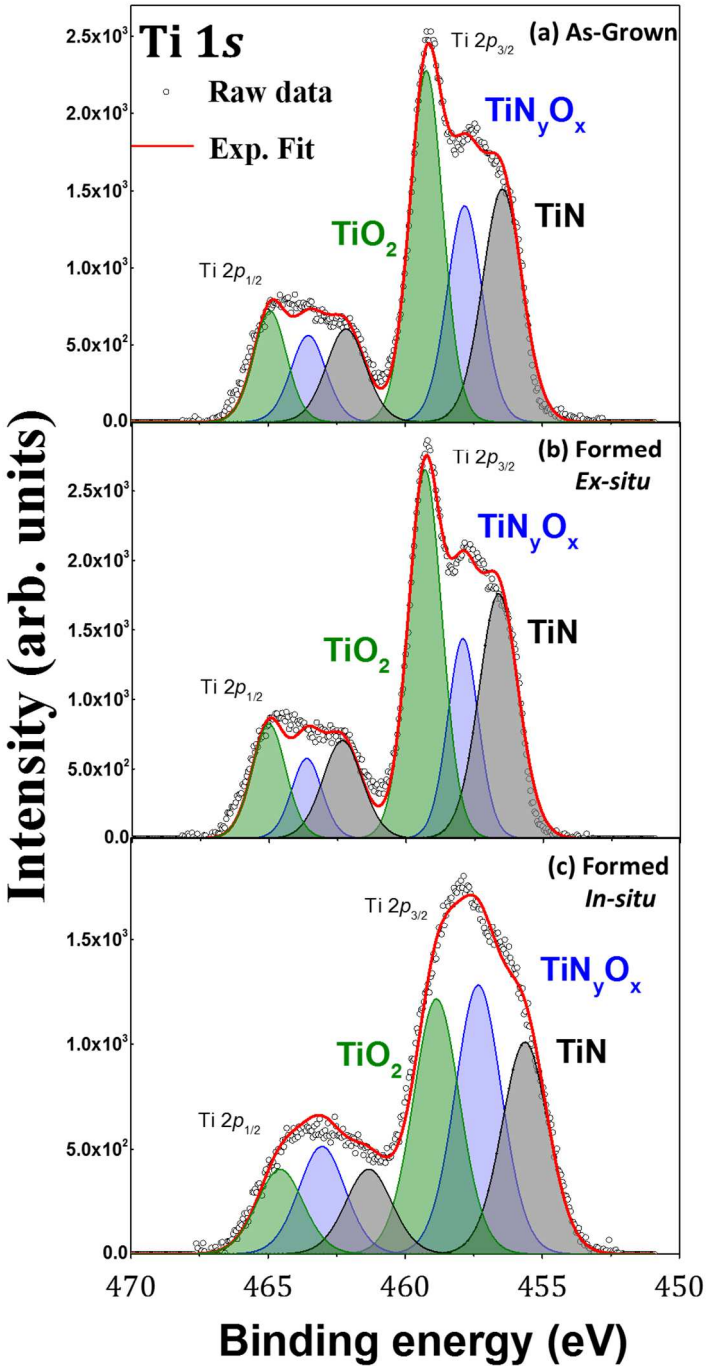

Figure 5.4. Ti 2*p* core level peaks obtained by XPS on the: a) as-grown, b) *ex-situ* and c) *in-situ* formed states of the TiN/ZrTe/ Al_2O_3/Ta stack.

These results show some changes between the as-grown state and both formed states. During *ex-situ* forming, an increase of both TiO_2 (+ 3.1 %) and TiN (+1.9) is observed at the expense of TiO_xN_y (-5 %). During *in-situ* forming, TiO_xN_y increases (+9.9 %) at the expense of both TiN (-3.6 %) and TiO_2 (- 6.3 %)

contributions.

The O 1*s* core level spectra measured in each case are presented in Figure 5.5. The decomposition of these O 1*s* spectra takes into account three contributions. The contribution at 532.6 ±0.2 eV is attributed to the surface hydroxyl groups, hydrocarbon contamination and/or chemisorbed water molecules on the surface of the top electrode. The contribution at 530.1 ±0.2 eV is related to TiO_2 in agreement with [143,144]. The component at 531.4 ±0.2 eV can be assigned to oxygen bonded to Ti^{2+} and Ti^{+3} (i.e. titanium suboxide) based on the work of Carley et al. [143]. Note that this component at 531.4 eV could be also related to a Ti oxynitride (TiO_xN_y). The relative areas of these components are given in Table 5.3.

After the *ex-situ* forming, we can see an increase of the TiO_2 (+ 6.5 %) and TiO_x/TiO_xN_y (+ 6.0 %) contributions. In turn after *in-situ* forming, the results show a decrease of the TiO_2 contribution (-7.4 %) and an increase of the TiO_x/TiO_xN_y contribution (+17.7 %). These results are correlated with those obtained with the Ti 2*p* spectra. The forming performed under air caused an increase of the TiO_2 component for both Ti 2*p* and O 1*s*. For the forming performed under vacuum, the increase of TiO_x/TiO_xN_y is also observed in both spectra.

Table 5.3. Relative areas (%) of the O 1*s* components for the as-grown, *ex-situ* and *in-situ* formed samples.

	C-O/H-O (%)	TiO_xN_y/TiO_x (%)	TiO_2 (%)
As-grown	37.5	17.5	45.0
Ex-situ	25.0	23.5	51.5
In-situ	27.2	35.2	37.6

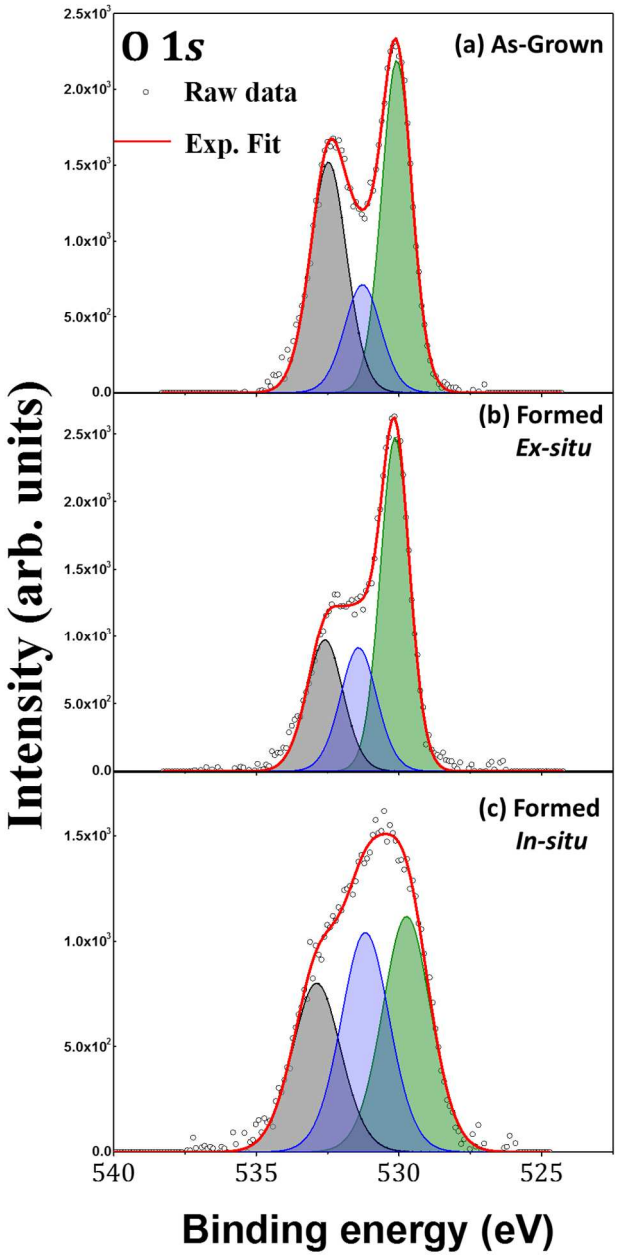

Figure 5.5. O 1*s* core level peaks obtained by XPS on the: a) as-grown, b) *ex-situ* and c) *in-situ* formed states of the TiN/ZrTe/ Al_2O_3/Ta stack.

5.1.4.2. XPS depth profiling

XPS depth profiling was carried out on the as-grown and formed samples to provide information about elements migration along the stack. Measurements were carried out using an argon gas cluster ion beam (GCIB) with 2500 Ar atoms per cluster, a current of 20 nA and 20 kV accelerating voltage corresponding to an energy of 8 eV per atom. Quantification was performed using tabulated relative sensitivity factors [145] with 20 % of uncertainty.

Figure 5.6 shows the in-depth concentration profiles obtained from the O 1*s*, Ta 4*f*, Te3$d_{5/2}$, Ti 2*p* and Zr 3*d* core levels intensity, for the *ex-situ* and *in-situ* forming. The Al signal was not measured due to the low sensitivity of the Al 2*p* core level, yielding to a poor signal to noise ratio when performing short acquisitions, as necessary for depth profiling.

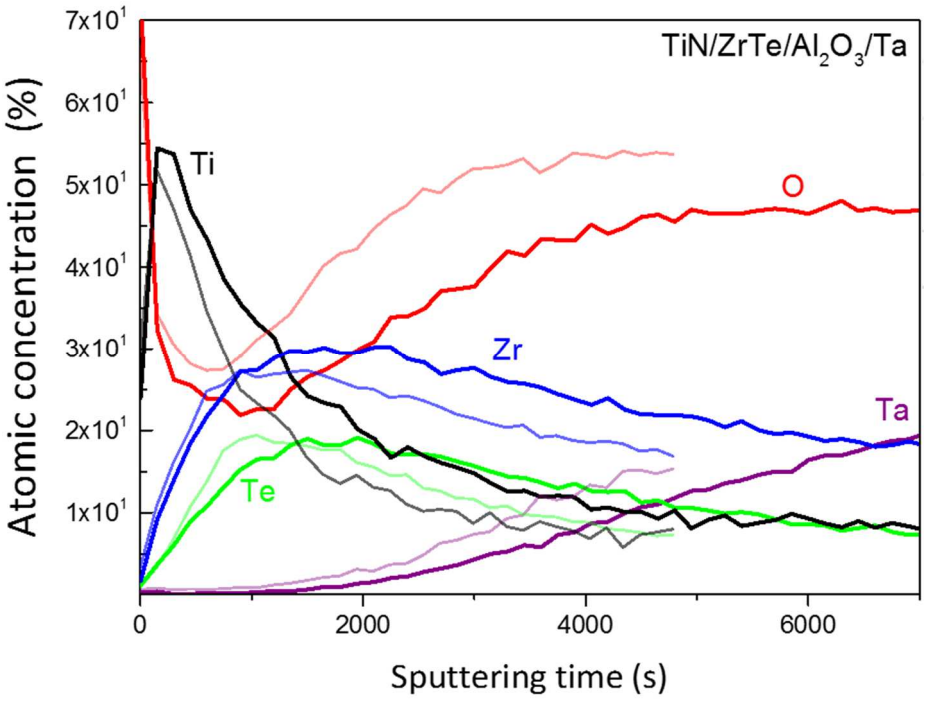

Figure 5.6. XPS depth profiles measured on the *ex-situ* (thick line) and *in-situ* (thin line) formed samples of the TiN/ZrTe/Al_2O_3/Ta stack.

For both *ex-situ* and *in-situ* forming, a high oxygen signal is detected at the surface showing TiN oxidation and confirming the previous XPS analysis. The oxygen intensity increases again when reaching the alumina. The rising edge of this oxygen profile is shifted towards the surface for the *in-situ* forming compared to *ex-situ* forming. Similar but smaller change are also observed for the Te and Ta profiles. On the contrary, the falling edges of Zr and Ti profiles are shifted towards the bottom Ta electrode.

5.1.5. Summary of the operating environment effect on the resistive switching for ZrTe/Al_2O_3 based CBRAMs

The environment seems to play a key role on the forming of the TiN/ZrTe/Al_2O_3/Ta stack. Under ambient air, the oxidation of the TiN capping layer is enhanced by oxygen insertion, yielding to a regrowth of the TiO_2 layer present at the extreme surface under bias application. The increase of the TiO_2 contribution after *ex-situ* forming was observed in both Ti 2*p* and O 1*s* spectra. The external oxygen reservoir from ambient

air causes the surface oxidation, following the reaction:

$$TiO_{x/2} + {}^{x}/_{4}\ O_2 \quad \leftrightarrow TiO_x. \qquad 5.1$$

The reversed phenomenon is observed when forming the sample under UHV. The decrease of TiO_2 contribution for both Ti 2*p* and O 1*s* spectra is probably due to oxygen desorption in the chamber. Furthermore, the increase of TiO_xN_y can be explained by the combination of two phenomena: 1) TiO_2 reduction at the TiN surface caused by the oxygen outgas and 2) oxygen migration (O^{2-} ions) from the underlying ZrTe and Al_2O_3 layers towards the TiN, under the electric field causing the oxidation of the top electrode.

In the chapter 3, we have reported oxygen scavenging from Al_2O_3 by the ZrTe active electrode under the electric field. This phenomenon yields to Zr oxidation and creation of oxygen vacancies in the oxide favoring subsequent Te release at the ZrTe/Al_2O_3 interface, with possible diffusion in the alumina. The XPS oxygen profiles measured here show an enhanced oxygen movement towards the active ZrTe electrode in the case of *in-situ* forming. Thus, the oxygen scavenging by the active ZrTe electrode, which is a critical step to switch the memory to a low resistance state, seems to be favoured under UHV, i. e. without any external oxygen reservoir. A possible interpretation of these results is: 1) there is no further oxidation of the TiO_2 layer by oxygen insertion from air during forming under UHV, 2) this TiN capping is thus more efficient to prevent oxidation of the active electrode, which in turns acts as a better oxygen getter to pump oxygen from Al_2O_3.

This interpretation, based on XPS results, is consistent with the electrical behaviour of the TiN/ZrTe/Al_2O_3/Ta stack. Under ambient air, the V_F was higher (3.5 V) in comparison to the forming under ultra-high vacuum (2.7 V). This difference can be related to the oxygen vacancies concentration in the oxide, as shown in Figure 5.7. Under vacuum, the oxygen outgas to the vacuum ambient increases the oxygen vacancies in the oxide facilitating the formation of the conductive filaments and consequently decreasing the V_F. Under ambient air, the insertion of oxygen, showed by the top electrode oxidation, may also oxidize the active electrode decreasing the oxygen scavenging from Al_2O_3 by ZrTe and thereby retarding the forming process.

These results show that both the decrease of V_F and the increase of the resistance window are promoted under UHV. The role of oxygen from air is thus not negligible in the forming of such Te-based CBRAMs.

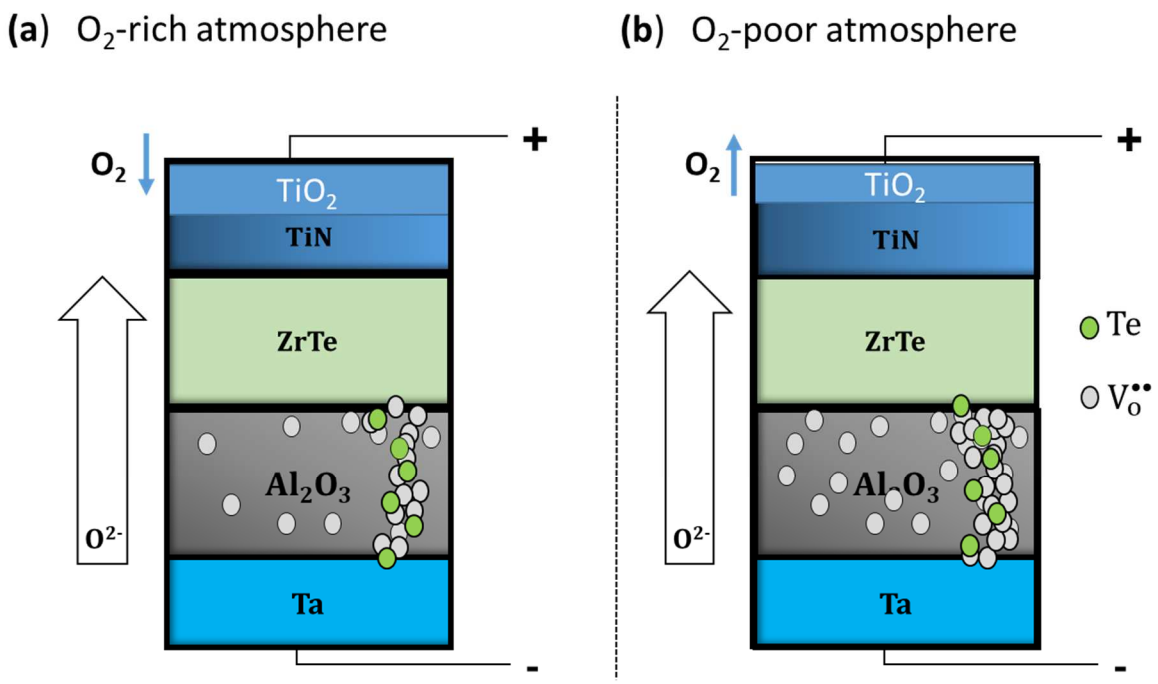

Figure 5.7. XPS depth profiles measured on the *ex-situ* (thick line) and *in-situ* (thin line) formed samples of the TiN/ZrTe/Al_2O_3/Ta stack.

5.2. Conclusion

A precise control of the resistive switching of Te-based CBRAMs is needed for their integration in future memory devices. We have shown that the atmosphere plays a key role in the forming of the TiN/ZrTe/Al_2O_3/Ta structures. Forming the memory stack under ambient air seems to enhance the TiN oxidation by insertion of oxygen from air. This phenomenon can be reduced by performing forming under UHV, as shown by in-situ XPS measurements. By decreasing oxygen insertion from air in the capping layer, the forming mechanism based on oxygen scavenging by ZrTe from Al_2O_3 is favored. This oxygen pumping is enhanced under UHV as shown by XPS depth profiling. This is consistent with a lower forming voltage and higher resistance window. Preventing oxidation of TiN is thus crucial to control the resistive switching of these devices.

Conclusion and perspectives

Conducting bridge random access memories (CBRAMs) are interesting candidates for the next generation of non-volatile memories. Data storage principle is based on switching the resistivity between two high and low resistance states by applying voltage or current pulses. These cells have a simple structure composed by an active electrode (source of ions), a solid electrolyte (insulator layer) and a bottom electrode. Under electrical bias, a conductive path is assumed to be created by ions diffusion from the active electrode into the solid electrolyte [1]. This mechanism has to be better understood to improve their performances but observation of the involved chemical processes is a real challenge. Recently, special attention has been drawn to devices containing an elemental semiconductor such as tellurium, operating with reduced currents and less retention failures, and thus favorable for low-power applications. For these Te-based subquantum CBRAMs, the filament is thought to contain Te, a semiconductor, instead of a metal. This assumption was based on a detailed analysis of electrical characterisations but no direct proof of the chemistry of the filament has been reported in the literature. Therefore, studies about the electrochemical mechanisms involved in the resistive switching are essential for the future development of this type of CBRAM.

The aim of this thesis was the study of subquantum Al_2O_3-based CBRAMs with two different active electrodes: TiTe and ZrTe to investigate the electrochemical reactions and ionic transport involved in the forming process i.e. filament creation. This is a crucial step during which most of the chemical and structural modifications occur and which defines the final properties of the devices. In addition, to better understand the cycling of the cell, the switching between the LRS to the HRS, known as the RESET step was also investigated. The main difficulty of this study is the small amount of net change due to the filament formation. Moreover, the changes most likely occur in a thin layer buried under a thicker top electrode. This requires non-destructive characterization methods able to probe through thick capping layers with high sensitivity. In this work, we use hard X-ray photoelectron spectroscopy to probe the buried interface between the active electrode (ZrTe or TiTe) and the Al_2O_3 layer. Using hard X-rays, the electron mean free path is considerably increased providing sufficient depth sensitivity to reach the buried interface and thus providing information about the redox processes occurring there. We have also used XPS depth profiling using a gas cluster ion beam and ToF-SIMS depth profiling to get complementary information about the elements distribution through the sample.

In chapter 3, we have investigated the electrochemistry of the resistivity change during the direct forming of ZrTe/Al_2O_3 based CBRAMs. The direct forming occurs when a positive bias is applied on the top electrode to form the filament. Measurements were performed on as-grown samples and after *ex-situ* forming. The results showed the oxidation of Zr together with a correlated alumina reduction during forming. This redox process was related to oxygen scavenging by the active top electrode. This O^{2-} migration leads to the creation of positively charged $V_O^{\bullet\bullet}$ in the alumina, thereby creating favored conductive paths. XPS depth profiling confirmed the oxygen diffusion from the Al_2O_3 towards the ZrTe top electrode. A four-layer capacitor model showed an increase of both the ZrO_2 and AlO_x interfacial layers thicknesses, confirming the redox process located between the active electrode and the electrolyte. Furthermore the resistance switching caused also an elemental Te increase at the ZrTe/Al_2O_3 interface. In addition XPS and ToF-SIMS depth profiling showed evidences of Te migration from the ZrTe layer to alumina layer under positive bias.

Based on these results, a plausible mechanism can be described as: a) first Te accumulates at the interface and then some migrates b) second, local Te segregation might occur through $V_O^{\bullet\bullet}$, acting as easier diffusion paths towards the bottom electrode. A hybrid mechanism combining $V_O^{\bullet\bullet}$ formation by oxygen transport with Te migration and filament formation, typical of OXRRAMs and CBRAMs respectively, may occur during positive polarization. However, it is more difficult to conclude on the chemical nature of the filament. The HAXPES Te 3$d_{3/2}$ spectra showed that the released Te is not ionized. The Te migration through the alumina is thus not directly driven by the electric field and more difficult to explain. In the last part of chapter 3, we have investigated the resistance switching of TiTe/Al_2O_3 based CBRAMs. Results showed that, under positive polarization, this cell does not present a memory behavior, i.e a reversible switch of the resistance. However, this memory can be successfully formed under negative polarization with a reset under positive polarization.

Considering this fact, in chapter 4, we have investigated the negative forming of Te-based CBRAMs, also called reverse forming, in which a negative voltage is applied to the top electrode together with the first reset step, i.e. the first transition from LRS to HRS. In summary, it can be concluded for both ZrTe and TiTe/Al_2O_3-based cells that in the reverse forming, the Ta bottom electrode acts as an oxygen getter creating oxygen vacancies accumulating at the Ti(Zr)Te/ Al_2O_3 interface. The oxygen movement in the form of O^{2-} is driven by the electric field from the upper negatively biased electrode towards the bottom one. Forming also causes an accumulation of elemental Te near the top interface. Te^{2-} might also be pushed inside the alumina by the electric field. On reset, there is a partial recombination of oxygen ions with $V_O^{\bullet\bullet}$ near the Ti(Zr)Te/Al_2O_3 interface together with a loss of Te. These results strongly suggest that CBRAM (Te transport) and OxRRAM ($V_O^{\bullet\bullet}$ migration) mechanisms coexist in these Te-based memory cells.

In-addition, our results showed an increase of the $|V_F|$ under negative polarisation (3.7 V) in comparison to the $|V_F|$ measured under positive polarisation (3.0 V) for ZrTe/Al_2O_3-based cells. This can be explained by the fact that the formation of ZrO_2 induced by the oxygen migration towards the top electrode under positive polarisation is thermodynamically more favourable in comparison with the reverse forming, where the oxygen scavenging is related to the less favourable oxidation of Ta bottom electrode. These results showed that positive forming is more adapted to ZrTe/Al_2O_3cells, considering the interest of decreasing power consummation during this step.

The results shown in chapter 3 and 4 provide evidences that the oxygen is also involved in the forming mechanism of Te-based CBRAMs. Therefore, when performing resistive switching in such devices, we cannot rule out a possible impact of the ambient air, on the resistive switching mechanism. The chapter 5 is thus focused on the investigation of the forming process performed in-situ, i. e. under ultra high vacuum, to highlight the role of the surface and interface oxidation on the resistive switching mechanism for TiN/ZrTe/Al_2O_3/Ta structures. The study showed that forming under ambient air seems to enhance the TiN oxidation by insertion of oxygen from air. This phenomenon can be reduced by forming the structure under UHV, as shown by in-situ XPS measurements. By decreasing oxygen insertion from air in the capping layer, the forming mechanism based on oxygen scavenging by ZrTe from Al_2O_3 is favored. This oxygen pumping is enhanced under UHV as shown by XPS depth profiling. This is consistent with the lower forming voltage and higher resistance window measured for in-situ forming.

This thesis showed the interest of combining X-ray photoelectron spectroscopy-based techniques and ToF-SIMS for the investigation of CBRAMs. With these techniques, it was possible to investigate the diffusion and redox processes occurring during resistive switching, highlighting the role of the oxygen in the mechanism of Te-based CBRAM cells. We have been able to better understand the electrochemical processes involved in both forming and reset of these structures, showing the key role of the electrode/electrolyte interfaces. A major conclusion is the coexistence of both CBRAM (Te transport) and OxRRAM ($V_O^{\bullet\bullet}$ migration) mechanisms in resistance switching. The in-situ tests showed that the choice of a good capping layer is also crucial to control the resistive switching of these devices for their integration in future memory devices.

- **Perspectives**

Analysis:

- Operando HAXPES with in-situ electrical biasing: resistive switching by in-situ electrical polarization was also tested in the analysis chamber of the GALAXIES beamline at SOLEIL synchrotron. However the vertical configuration of the sample holder made the electrical contacts with the memory device ineffective. Therefore it is necessary to develop a measurement protocol specific for vertical supports. The use of a more depth sensitive technique can bring information about the role of the ambient air on the resistive switching.

- Endurance failure: further work can be done to analyze the structural changes involved on the gradual loss of R_{HRS}/R_{LRS} ratio with steady decrease in R_{HRS}. This study could be based on the comparison between an as-grown sample and a sample after 10^n switching cycles using HAXPES and ToF-SIMS analyses. A study of the physical mechanisms involved in this failure can improve the endurance characteristics in order to allow CBRAM industrialization.

- TEM/STEM: This thesis brought evidences about the electrochemistry mechanism involved in the forming process, but a study of the filament nature and morphology is necessary. For that, a high spatial resolution technique such as transmission electron microscopy (TEM) combined with local chemical analyses using electron energy-loss spectroscopy (EELS) and/or energy-dispersive X-ray spectroscopy (EDS), can be interesting to observe the composition of the filament. This work is developed for OxRRAMs analyses by the LETI microscopy group[146]. It is very promising but the principal challenge of this technique remains the preparation of a TEM lamella containing the nanometer-sized filament.

Sample

- Jameson et al [8] also suggested HfTe as an interesting alternative for subquantum CBRAMs. Therefore a study of this alloy as active electrode can be interesting for futures investigations.

- The development of a sample geometry to avoid the oxidation of the stack can be interesting to increase the stability of the cell allowing the memory cycling and the endurance study discussed above.

Annex A

A.1. Overlapping of the HAXPES spectra obtained at 7.9 keV photon energy at Spring-8

- **Al 1*s***

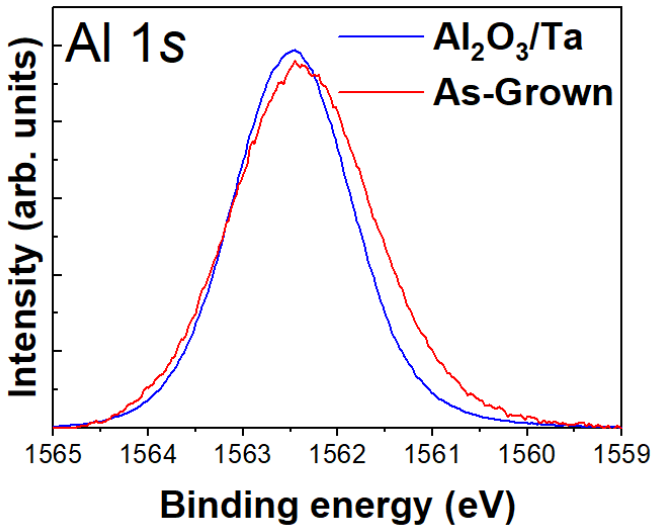

Figure A.1. Overlap of Al 1s core level peaks obtained at 7.9 keV photon energy on the bare Al_2O_3/Ta and on the as-grown sample.

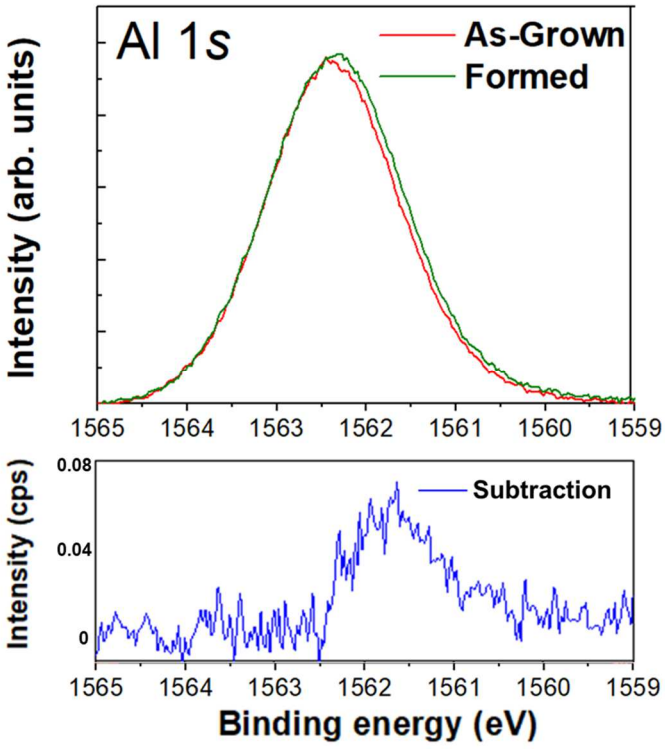

Figure A.2. Overlap of Al 1s core level peaks obtained at 7.9 keV photon energy on the as-grown and formed samples and XPS difference spectra between as-grown and formed spectra.

- **Zr 3$p_{3/2}$**

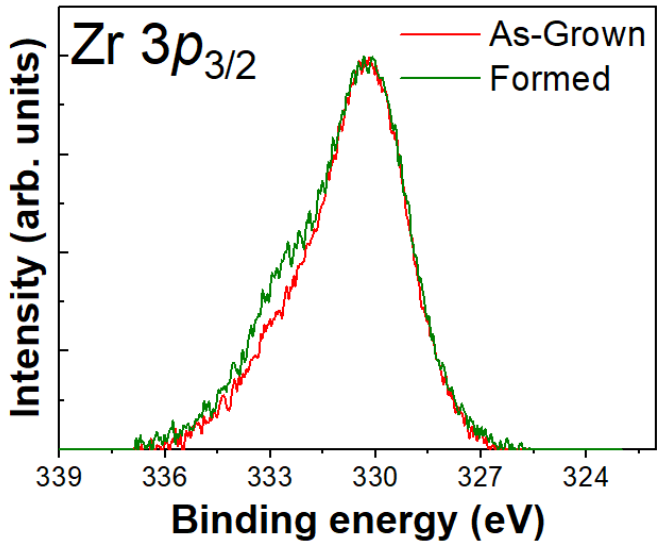

Figure A.3. Overlap of Zr $3p_{3/2}$ core level peaks obtained at 7.9 keV photon energy on the as-grown and formed samples.

- **Te 3$d_{3/2}$**

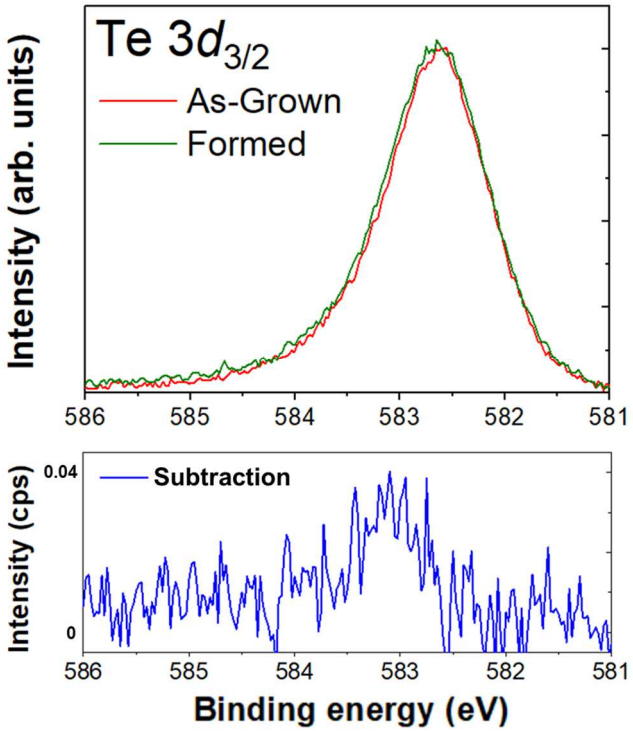

Figure A.4. Overlap of Te $3d_{3/2}$ core level peaks obtained at 7.9 keV photon energy on the as-grown and formed samples, and XPS difference spectra between as-grown and formed spectra.

A.2. Parameters used to fit the HAXPES peak

The peaks fit for each element was made establishing constrains on components positions and fixing the separation between each chemical state. The parameters used to fit the HAXPES peaks are present in table A1.

Table A.1. Parameters used to fit the HAXPES peak.

	Components	**FWHM (eV)**	**Line shape**
Al 1s	AlO_x	1.5	GL(30)
	Al_2O_3	1.6	GL(30)
Ta 3d5/2	Ta	1.8	DS(0.02,250)
	TaO_x	2.2	GL(30)
	Ta_2O_5	2.7	GL(30)
Te 3d$_{3/2}$	ZrTe	1.0	DS(0.03,400)
	Te	1.2	DS(0.03,400)
	TeO_x	1.2	GL(30)
Zr 2p$_{3/2}$	ZrTe	2.5	DS(0.02,400)
	ZrO_2	2.8	GL(30)
Zr 3p$_{3/2}$	ZrTe	2.8	DS(0.02,400)
	ZrO_2	3.0	GL(30)
Ti 1s	TiTe	1.8	DS(0.01,450)
	TiO_x	2.5*	GL(30)
	TiO_2	2.3	GL(30)

* 2.6 eV to the formed sample.

Table A.2 Binding energies (eV) of the Ta 3$d_{5/2}$, Ti 1*s*, Te 3$d_{3/2}$, Al 1*s* and Zr 2$p_{3/2}$ components measured for the as-grown, formed and reset samples obtained at Soleil.

	Components	**Binding energies (eV)**		
		As-Grown	**Formed**	**Reset**
Ta 3*d*$_{5/2}$	Ta	1731.5	1731.7	1731.7
	TaOx or TaN	1734.1	1734.2	1734.2
	Ta_2O_5	1735.8	1736.0	1736.0
Ti 1*s*	TiTe	4965.5	4965.7	4965.7
	TiO_x	4966.9	4967.1	4967.1
	TiO_2	4968.7	4968.9	4968.9
Te 3*d*$_{3/2}$	TiTe/ZrTe	582.9	583.1	583.1
	Te	583.5	583.7	583.7
	TeO_x	584.8	585.0	585.0
Al 1s	AlO_x	1562.0	1562.2	1562.2
	Al_2O_3	1562.8	1563.0	1563.0
Zr 2*p*$_{3/2}$	ZrTe	2222.8	2222.8	2222.8
	ZrO_2	2224.3	2224.3	2224.3

Publication list

M. K Mendes, E. Martinez, J.M. Ablett, M. Veillerot, R. Gassilloud, M. Bernard, O. Renault, J. P. Rueff, N. Barrett, Chemistry of resistivity changes in TiTe/Al_2O_3 conductive-bridge memories, submitted to Scientific reports (Accepted for publication).

M.K. Mendes, E. Martinez, A. Marty, M. Veillerot, Y. Yamashita, R. Gassilloud, M. Bernard, O. Renault, N. Barrett, Forming mechanism of Te-based conductive-bridge memories, Appl. Surf. Sci. 432 (2018) 34–40.

Oral presentation:

M. K Mendes, E. Martinez, M. Bernard, M. Veillerot, J.M. Ablett, N. Barrett, Étude du fonctionnement des mémoires résistives à base de Te par photoémission à haute énergie, 8 eme conférence francophone sur les spectroscopies d'électrons - ELSPEC'2018.

M. K Mendes, E. Martinez, O. Renault, R. Gassilloud, M. Bernard, M. Veillerot, J.M. Ablett, N. Barrett, Hard X-ray Photoelectron Spectroscopy Study of the Resistive Switching in Te-based Conductive Bridging Random Access Memories, AVS 64th International Symposium & Exhibition 2017.

M. K Mendes, E. Martinez, O. Renault, R. Gassilloud, M. Bernard J.M. Ablett, N. Barrett, Hard X-ray photoelectron spectroscopy study of the resistive switching in TiTe/Al_2O_3 Conductive Bridge Random Access Memories, ECASIA - European Conference on Applications of Surface and Interfaces Analysis 2017.

M.K. Mendes, E. Martinez, A. Marty, M. Veillerot, Y. Yamashita, R. Gassilloud, M. Bernard, O. Renault, N. Barrett, Origin of resistivity changes in CBRAMs studied by X-ray photoelectron spectroscopy, ECOSS 32 - European Conference on Surface Science 2016.

Poster presentation:

M. K Mendes, E. Martinez, O. Renault, R. Gassilloud, M. Bernard, J.M. Ablett, N. Barrett, Electrochemistry of Resistivity Changes In TaN/TiTe/Al_2O_3/Ta Conducting Bridge Random Access Memories, 12th SOLEIL users' meeting 2017. **(Prize Roger FOURME – best student poster)**

M. K Mendes, E. Martinez, J.M. Ablett, R. Gassilloud, M. Bernard, O. Renault, J. P. Rueff , N. Barrett, Electrochemistry of Resistivity Changes In Te-based conductive-bridge memories, E-MRS 2018 Spring Meeting. **(Best poster award (2nd best poster) - "Solid state ionics")**

Summary in French

Les mémoires résistives à accès aléatoire (RRAMs) sont des candidates intéressantes pour la prochaine génération de mémoires non-volatiles en raison de leur structure simple, leur forte densité de stockage potentielle et une faible puissance consommée [1-3]. Le principe de stockage de données repose sur la commutation de la résistivité entre des états de résistance élevées (HRS) et faibles (LRS) en appliquant des impulsions de tension ou de courant. Parmi celles-ci, les mémoires à pont conducteur (CBRAMs) sont une option prometteuse comme le montrent certains démonstrateurs industriels préliminaires [4-6]. Ces cellules sont composées d'une électrode active, d'un électrolyte solide (couche isolante) et d'une électrode inférieure. Leur mécanisme de commutation résistive est basé sur la formation / dissolution électrochimique de filaments conducteurs dans la couche d'électrolyte solide, formant un pont entre les deux électrodes. La formation de ces filaments se produit par la dissolution du métal présent dans l'électrode active selon $M \rightarrow M^{z+} + ze^-$, la migration des cations métalliques à l'intérieur de la couche d'électrolyte et la réduction du M^{z+} à la surface de l'électrode inférieure selon: $M^{z+} + ze^- \rightarrow M$. Ce modèle est adopté pour expliquer la commutation résistive, cependant, les mécanismes physiques responsables de ces phénomènes n'ont pas été entièrement compris.

Les CBRAMs améliorent l'endurance au cyclage tout en conservant une bonne mise à l'échelle et une vitesse de fonctionnement élevée. Cependant, cette technologie présente encore plusieurs problèmes, notamment une tension de commutation élevée, la chimie complexe du processus de « forming » et une consommation d'énergie élevée. Par conséquent, une meilleure connaissance du mécanisme de commutation résistive ainsi que l'exploration de nouveaux matériaux est essentielle pour le développement futur du dispositif.

Récemment, une attention particulière a été portée sur l'utilisation de dispositifs contenant un semi-conducteur élémentaire tel que le tellure, fonctionnant avec des courants plus faibles tout en conservant de bonnes propriétés de rétention. Dans ces « subquantum CBRAMs », on pense que le filament contient du tellure. Le courant requis pour programmer une cellule CBRAM standard est directement lié à la conductance d'un filament à 1 atome (G_{1atom}). Pour les métaux, G_{1atom} est comparable au $G_0=2e^2/h$ [7], alors que pour un semi-conducteur tel que le tellure, c'est un sous-quantum (0,03 G_0) qui permet un fonctionnement à faibles courants. Les « subquantum CBRAMs » basées sur un électrolyte en Al_2O_3 et une électrode supérieure active composée d'un alliage binaire tel que ZrTe, TiTe et HfTe, sont les systèmes les plus prometteurs rapportés dans la littérature, avec un courant de fonctionnement et une puissance aussi bas que 10 µA et 0,01 mW [8].

Le but de cette thèse est l'étude de l'électrochimie des processus de « forming » et de « reset » des

CBRAMs à base de ZrTe (TiTe) / Al_2O_3. La création de filaments, appelée « forming », est un processus irréversible nécessaire pour activer les cycles d'écriture / effacement (SET / RESET) de la cellule mémoire. C'est une étape clé à maîtriser pour l'optimisation des cellules CBRAMs [4,6]. Obtenir plus d'informations sur la formation de filaments faciliterait le contrôle et la fabrication de ces cellules mémoire. Il est également nécessaire de mieux comprendre le cyclage de la cellule. Ainsi, non seulement l'étape de « forming » doit être étudiée, mais aussi la commutation entre l'état de résistance faible et l'état de résistance élevée, connue sous le nom d'étape de « reset ».

Pour étudier la chimie du changement de résistivité dans de telles CBRAMs à base de Te, nous avons utilisé la spectroscopie de photoélectrons par rayons X de haute énergie (HAXPES) qui permet une analyse non destructive des interfaces enterrées entre des électrodes métalliques et une couche isolante, grâce à la profondeur sondée. La sensibilité élevée de cette technique est également cruciale en raison des petits changements attendus dans le signal lors de la commutation résistive par rapport à ceux de la matrice environnante. L'XPS en mode profilage en profondeur utilisant des faisceaux d'ions à agrégats gazeux (GCIB) en tant que technique de pulvérisation, a également été utilisé pour étudier la répartition en profondeur des éléments. En outre, le profilage en profondeur en spectrométrie de masse par ions secondaires à temps de vol (ToF-SIMS) a été utilisé comme technique complémentaire pour fournir des profils avec une résolution en profondeur élevée (<1nm) et une meilleure sensibilité (<10 ppm) [11]. Pour étudier l'impact possible de l'environnement sur la commutation résistive de ces cellules, la spectroscopie de photoélectrons par rayons X avec polarisation électrique in situ (sous ultravide) a été utilisée pour mettre en évidence le rôle de l'oxydation de surface et d'interface dans le processus de « forming ». Pour cela, un montage a été développé en utilisant un porte-échantillon spécifique permettant l'application de la polarisation directement dans la chambre d'analyse de l'XPS.

Le travail de thèse a été réalisé dans le cadre d'une collaboration entre la Plateforme de NanoCaractérisation (PFNC) du CEA Grenoble et l'Institut Rayonnement-Matière du CEA Saclay (IRAMIS). Tous les échantillons ont été fabriqués et optimisés par le Département des Dépôts (SDEP). Les analyses par spectroscopie de photoélectrons par rayons X de haute énergie (HAXPES) ont été effectuées sur la ligne de lumière GALAXIES du synchrotron SOLEIL et sur la ligne BL15XU de l'Institut japonais de recherche sur le rayonnement synchrotron (SPring-8).

- Le chapitre 1 présente les concepts clés liés aux mémoires résistives à accès aléatoire (RRAMs): les avantages et les caractéristiques, les processus physiques impliqués dans la commutation résistive, la théorie filamentaire et l'influence des paramètres d'entrée sur la caractérisation des performances. Une description des mécanismes et caractéristiques des CBRAMs et OXRRAMs est présentée. La dernière

partie montre une description des cellules « subquantum CBRAMs » basées sur Te qui sont l'objet de ce manuscrit ainsi que la problématique de cette thèse.

- Le chapitre 2 fournit une description des techniques de caractérisation, des méthodes expérimentales ainsi que de la préparation des échantillons: méthodes de croissance et fabrication des échantillons pour les études ex-situ et in-situ des cellules mémoire. Les principes de la spectroscopie de photoémission sont présentés avec les spécificités de la spectroscopie de photoémission par rayons X durs. En outre, ce chapitre décrit les principes du ToF-SIMS.

Les résultats expérimentaux sont présentés et discutés dans les trois chapitres suivants.

- Dans le chapitre 3, nous avons étudié l'électrochimie du changement de résistivité lors du « forming » direct d'une CBRAM à base de ZrTe /Al_2O_3. Ce « forming » direct se produit lorsqu'une polarisation positive est appliquée sur l'électrode supérieure pour créer le filament. Les mesures ont été effectuées sur des échantillons vierge et après le processus de « forming » ex-situ. Dans la deuxième partie de ce chapitre, nous avons étudié la commutation résistive pour les dispositifs à base de TiTe / Al_2O_3. Pour les dispositifs basés sur ZrTe / Al_2O_3, les résultats ont montré l'oxydation du Zr avec une réduction de l'alumine pendant le processus de « forming ». Ce processus redox était lié au pompage de l'oxygène par l'électrode supérieure active. Cette migration d'O^{2-} conduit à la création de lacunes d'oxygène chargées positivement dans l'alumine, créant ainsi des chemins conducteurs. La profilométrie XPS a confirmé la diffusion de l'oxygène de l'Al_2O_3 vers l'électrode supérieure ZrTe. Un modèle de condensateur à quatre couches a montré une augmentation des épaisseurs des couches interfaciales ZrO_2 et AlO_x, confirmant le processus redox situé entre l'électrode active et l'électrolyte. De plus, le changement de résistance a également provoqué une augmentation de Te élémentaire à l'interface ZrTe / Al_2O_3. De plus, les profils XPS et ToF-SIMS ont montré des preuves de migration de Te depuis la couche de ZrTe vers la couche d'alumine sous l'effet d'une polarisation positive.

  Sur la base de ces résultats, un mécanisme plausible peut être décrit comme suit: a) le Te s'accumule à l'interface et ensuite migre b) la ségrégation locale de Te peut se produire au niveau des lacunes d'oxygène, facilitant la diffusion vers l'électrode inferieure. Un mécanisme hybride combinant la formation de lacunes d'oxygène par la migration d'oxygène avec la migration de Te, typique des OXRRAMs et des CBRAMs, peut se produire pendant la polarisation positive. Cependant, il est plus difficile de conclure sur la nature chimique du filament. Les spectres HAXPES de la raie Te $3d_{3/2}$ ont montré que le Te libéré n'est pas ionisé. La migration de Te à travers l'alumine n'est donc pas directement entraînée par le champ électrique et plus difficile à expliquer. Les résultats pour TiTe/Al_2O_3 ont montré qu'en polarisation positive, cette cellule ne présente pas de comportement mémoire, c'est-

à-dire un changement réversible de la résistance. Ce résultat a motivé l'analyse de cette mémoire en utilisant d'autres conditions électriques. Les tests électriques effectués sur cette cellule ont montré que cette mémoire peut être formée en polarisation négative avec un « reset » en polarisation positive.

- Considérant ce fait, dans le chapitre 4, nous avons étudié le « forming » sous polarisation négative des CBRAMs à base de Te, également appelé « forming » inverse, pour lequel une tension négative est appliquée à l'électrode supérieure ainsi que la première étape de « reset », c'est-à-dire la première transition entre l'état de résistance faible (LRS) et l'état de résistance élevée (HRS). En résumé, on peut conclure à la fois pour les cellules à base de ZrTe / Al_2O_3 et à base de TiTe / Al_2O_3 que dans le « forming » inverse, l'électrode inférieure de Ta agit comme un getter d'oxygène créant des lacunes d'oxygène à l'interface Ti (Zr) Te / Al_2O_3. Le mouvement de l'oxygène sous la forme de O^{2-} est provoqué par le champ électrique vers l'électrode inferieure. Le processus de « forming » induit également une accumulation de Te élémentaire près de l'interface supérieure. Des ions Te^{2-} pourraient également être poussés à l'intérieur de l'alumine par le champ électrique. Lors du processus de « reset », il y a une recombinaison partielle des ions oxygène avec les lacunes d'oxygène près de l'interface Ti (Zr) Te / Al_2O_3 avec une perte de Te. Ces résultats suggèrent fortement que les mécanismes de migration typiques des CBRAMs (transport de Te) et des OxRRAMs (lacunes d'oxygène) coexistent dans ces cellules mémoire.
  En outre, nos résultats ont montré une augmentation de la tension de « forming » sous polarisation négative (-3.7 V) en comparaison avec la tension de « forming » mesurée en polarisation positive (3.0 V) pour les cellules à base de ZrTe / Al_2O_3. Ceci peut s'expliquer par le fait que la formation de ZrO_2 induite par la migration de l'oxygène vers l'électrode supérieure en polarisation positive est thermodynamiquement plus favorable par rapport à la formation d'Al_2O_3. D'autre part, pendant le « forming » inverse la réduction de l'Al_2O_3 est lié à l'oxydation moins favorable de l'électrode inférieure en Ta et donc plus difficile à induire. Ces résultats ont montré qu'un « forming » positif est plus adapté aux cellules ZrTe / Al_2O_3 compte tenu de la tendance actuelle à diminuer la consommation d'énergie au cours de cette étape.
  Les résultats présentés dans les chapitres 3 et 4 ont fourni des preuves que l'oxygène est fortement impliqué dans le mécanisme de formation des CBRAMs à base de Te. Par conséquent, lors d'une commutation résistive dans de tels dispositifs, nous ne pouvons pas exclure un éventuel impact de l'air ambiant sur le mécanisme de changement de résistivité.

- C'est pourquoi, dans le chapitre 5, l'étude du processus de « forming » a été effectuée in situ, i. e. sous ultra vide, pour mettre en évidence le rôle de l'oxydation de la surface et des interfaces sur le mécanisme de commutation résistive des structures TiN/ZrTe/ Al_2O_3/Ta. L'étude a montré qu'un processus de

« forming » sous air ambiant semble augmenter l'oxydation du TiN par insertion d'oxygène de l'air. Ce phénomène peut être réduit en effectuant un « forming » sous ultra vide, comme le montrent les mesures XPS in situ. En diminuant l'insertion d'oxygène de l'air dans la couche de protection, le mécanisme de « forming » basé sur le piégeage de l'oxygène de l'Al_2O_3 par l'électrode ZrTe est favorisé. Ce pompage d'oxygène est amélioré sous ultra vide comme le montre la profilométrie XPS. Ceci est cohérent avec une tension de « forming » inférieure et une fenêtre de résistance plus élevée sous ultra vide.

Cette thèse a montré le potentiel de la combinaison de la spectroscopie de photoélectrons par rayons X et du ToF-SIMS pour l'étude des CBRAMs. Avec ces techniques, il a été possible d'étudier les phénomènes de diffusion et les processus d'oxydoréduction qui se sont produits pendant la commutation résistive et de mettre en évidence le rôle de l'oxygène dans le mécanisme d'une cellule CBRAM. Les tests in situ ont montré que le choix d'une bonne couche de protection est crucial pour contrôler la commutation résistive de ces dispositifs. Un contrôle précis de la commutation résistive des CBRAMs à base de Te est nécessaire pour leur intégration dans les futurs dispositifs mémoire.

Bibliography

[1] R. Waser, R. Dittmann, G. Staikov, K. Szot, Redox-Based Resistive Switching Memories - Nanoionic Mechanisms, Prospects, and Challenges, Adv. Mater. 21 (2009) 2632–2663.

[2] L. Chua, Resistance switching memories are memristors, Appl. Phys. A. 102 (2011) 765–783.

[3] D.S. Jeong, R. Thomas, R.S. Katiyar, J.F. Scott, H. Kohlstedt, A. Petraru, C.S. Hwang, Emerging memories: resistive switching mechanisms and current status, Rep. Prog. Phys. 75 (2012) 076502.

[4] I. Valov, R. Waser, J.R. Jameson, M.N. Kozicki, Electrochemical metallization memories--fundamentals, applications, prospects, Nanotechnology. 22 (2011) 254003.

[5] J.S. Meena, S.M. Sze, U. Chand, T.-Y. Tseng, Overview of emerging nonvolatile memory technologies, Nanoscale Res. Lett. 9 (2014) 526.

[6] A. Chen, A review of emerging non-volatile memory (NVM) technologies and applications, Solid-State Electron. 125 (2016) 25–38.

[7] R. Landauer, Electrical resistance of disordered one-dimensional lattices, Philos. Mag. J. Theor. Exp. Appl. Phys. 21 (1970) 863–867.

[8] J.R. Jameson, D. Kamalanathan, Subquantum conductive-bridge memory, Appl. Phys. Lett. 108 (2016) 053505.

[9] M.K. Mendes, E. Martinez, A. Marty, M. Veillerot, Y. Yamashita, R. Gassilloud, M. Bernard, O. Renault, N. Barrett, Forming mechanism of Te-based conductive-bridge memories, Appl. Surf. Sci. 432 (2018) 34–40.

[10] C.S. Fadley, Hard X-ray Photoemission: An Overview and Future Perspective, in: Hard X-Ray Photoelectron Spectrosc. HAXPES, Springer, Cham, 2016: pp. 1–34.

[11] J.E. deVries, Surface characterization methods— XPS,ToF-SIMS, and SAM a complimentary ensemble of tools, J. Mater. Eng. Perform. 7 (1998) 303–311.

[12] H. Jeon, J. Park, W. Jang, H. Kim, C. Kang, H. Song, H. Kim, H. Seo, H. Jeon, Stabilized resistive switching behaviors of a Pt/TaOx/TiN RRAM under different oxygen contents, Phys. Status Solidi A. 211 (2014) 2189–2194.

[13] T.-M. Ding, Y.-J. Chen, J.-S. Jeng, J.-S. Chen, Influences of top electrode reduction potential and operation ambient on the switching characteristics of tantalum oxide resistive switching memories, AIP Adv. 7 (2017) 125313.

[14] L. Goux, P. Czarnecki, Y.Y. Chen, L. Pantisano, X. Wang, R. Degraeve, B. Govoreanu, M. Jurczak, D. Wouters, L. Altimime, Evidences of Oxygen-Mediated Resistive-Switching Mechanism in TiN\HfO2\Pt Cells, Appl. Phys. Lett. 97 (2011) 243509–243509.

[15] A. K. Sharma, Advanced Semiconductor Memories: Architectures, Designs, and Applications, (2003).

[16] E.R. Hnatek, Semiconductor memories: A review, Microprocessors. 1 (1976) 85–98.

[17] P. Cappelletti, A. Modelli, Flash Memory Reliability, in: Flash Mem., Springer, Boston, MA, 1999: pp. 399–441.

[18] S. Yu, P.Y. Chen, Emerging Memory Technologies: Recent Trends and Prospects, IEEE Solid-State Circuits Mag. 8 (2016) 43–56.

[19] Yole, Yole Développement, market research, consulting, “More than Moore”, - Emerging non volatile memory, http://www.yole.fr/Emerging_NVM_Market.aspx (accessed December 11, 2017).

[20] J.R. Jameson, P. Blanchard, C. Cheng, J. Dinh, A. Gallo, V. Gopalakrishnan, C. Gopalan, B. Guichet, S. Hsu, D. Kamalanathan, D. Kim, F. Koushan, M. Kwan, K. Law, D. Lewis, Y. Ma, V. McCaffrey, S. Park, S. Puthenthermadam, E. Runnion, J. Sanchez, J. Shields, K. Tsai, A. Tysdal, D. Wang, R. Williams, M.N. Kozicki, J. Wang, V. Gopinath, S. Hollmer, M.V. Buskirk, Conductive-bridge memory (CBRAM) with excellent high-temperature retention, in: 2013 IEEE Int. Electron Devices Meet., 2013: pp. 30.1.1–30.1.4.

[21] L. Goux, K. Opsomer, R. Schuitema, R. Degraeve, R. Muller, C. Detavernier, D.J. Wouters, M. Jurczak, L. Altimime, J.A. Kittl, Self-Limited Filament Formation and Low-Power Resistive Switching in Cu_xTe_{1-x}/Al_2O_3/Si CBRAM Cell, in: 2011 3rd IEEE Int. Mem. Workshop IMW, 2011: pp. 1–4.

[22] S. Clima, K. Sankaran, Y.Y. Chen, A. Fantini, U. Celano, A. Belmonte, L. Zhang, L. Goux, B. Govoreanu, R. Degraeve, D.J. Wouters, M. Jurczak, W. Vandervorst, S.D. Gendt, G. Pourtois, RRAMs based on anionic and cationic switching: a short overview, Phys. Status Solidi RRL – Rapid Res. Lett. 8 (2014) 501–511.

[23] A. Sawa, Resistive switching in transition metal oxides, Mater. Today. 11 (2008) 28–36.

[24] J.J. Yang, F. Miao, M.D. Pickett, D.A.A. Ohlberg, D.R. Stewart, C.N. Lau, R.S. Williams, The mechanism of electroforming of metal oxide memristive switches, Nanotechnology. 20 (2009) 215201.

[25] C. Xu, X. Dong, N.P. Jouppi, Y. Xie, Design implications of memristor-based RRAM cross-point structures, in: 2011 Des. Autom. Test Eur., 2011: pp. 1–6.

[26] C. Cagli, G. Molas, M. Harrand, S. Bernasconi, C. Charpin, K.E. Hajjam, J.F. Nodin, G. Reimbold, Study of the Energy Consumption Optimization on RRAM Memory Array for SCM Applications, in: 2017 IEEE Int. Mem. Workshop IMW, 2017: pp. 1–4.

[27] Z. Wei, Y. Kanzawa, K. Arita, Y. Katoh, K. Kawai, S. Muraoka, S. Mitani, S. Fujii, K. Katayama, M. Iijima, T. Mikawa, T. Ninomiya, R. Miyanaga, Y. Kawashima, K. Tsuji, A. Himeno, T. Okada, R. Azuma, K. Shimakawa, H. Sugaya, T. Takagi, R. Yasuhara, K. Horiba, H. Kumigashira, M. Oshima, Highly reliable TaOx ReRAM and direct evidence of redox reaction mechanism, in: 2008 IEEE Int. Electron Devices Meet., 2008: pp. 1–4.

[28] R. Waser, M. Aono, Nanoionics-based resistive switching memories, Nat. Mater. 6 (2007) 833–840.

[29] U. Russo, D. Ielmini, C. Cagli, A.L. Lacaita, S. Spiga, C. Wiemer, M. Perego, M. Fanciulli, Conductive-filament switching analysis and self-accelerated thermal dissolution model for reset in NiO-based RRAM, in: 2007 IEEE Int. Electron Devices Meet., 2007: pp. 775–778.

[30] T.-C. Chang, K.-C. Chang, T.-M. Tsai, T.-J. Chu, S.M. Sze, Resistance random access memory, Mater. Today. 19 (2016) 254–264.

[31] S. Chae, J. Lee, S. Kim, S. Lee, S.H. Chang, C. Liu, B. Kahng, H. Shin, D.-W. Kim, C.U. Jung, S. Seo, M.-J. Lee, T. Won Noh, Random Circuit Breaker Network Model for Unipolar Resistance Switching, Adv. Mater. 20 (2008) 1154–1159.

[32] D. Lee, D. Seong, I. Jo, F. Xiang, R. Dong, S. Oh, H. Hwang, Resistance switching of copper doped MoO_x films for nonvolatile memory applications, Appl. Phys. Lett. 90 (2007) 122104.

[33] D.-H. Kwon, K.M. Kim, J.H. Jang, J.M. Jeon, M.H. Lee, G.H. Kim, X.-S. Li, G.-S. Park, B. Lee, S. Han, M. Kim, C.S. Hwang, Atomic structure of conducting nanofilaments in TiO_2 resistive switching memory, Nat. Nanotechnol. 5 (2010) 148–153.

[34] N. Xu, L.F. Liu, X. Sun, C. Chen, Y. Wang, D.D. Han, X.Y. Liu, R.Q. Han, J.F. Kang, B. Yu, Bipolar switching behavior in TiN/ZnO/Pt resistive nonvolatile memory with fast switching and long retention, Semicond. Sci. Technol. 23 (2008) 075019.

[35] S. Yu, B. Lee, H.-S.P. Wong, Metal Oxide Resistive Switching Memory, in: Funct. Met. Oxide Nanostructures, Springer, New York, NY, 2012: pp. 303–335.

[36] T.J. Chu, T.C. Chang, T.M. Tsai, H.H. Wu, J.H. Chen, K.C. Chang, T.F. Young, K.H. Chen, Y.E. Syu, G.W. Chang, Y.F. Chang, M.C. Chen, J.H. Lou, J.H. Pan, J.Y. Chen, Y.H. Tai, C. Ye, H. Wang, S.M. Sze, Charge Quantity Influence on Resistance Switching Characteristic During Forming Process, IEEE Electron Device Lett. 34 (2013) 502–504.

[37] M.-J. Lee, C.B. Lee, D. Lee, S.R. Lee, M. Chang, J.H. Hur, Y.-B. Kim, C.-J. Kim, D.H. Seo, S. Seo, U.-I. Chung, I.-K. Yoo, K. Kim, A fast, high-endurance and scalable non-volatile memory device made from asymmetric $Ta_2O_{(5-x)}/TaO_{(2-x)}$ bilayer structures, Nat. Mater. 10 (2011) 625–630.

[38] Y. Wua, S. Yu, B. Lee, P. Wongb, Low-power TiN/Al_2O_3/Pt resistive switching device with sub-20 μA switching current and gradual resistance modulation: Journal of Applied Physics: Vol 110, No 9 (2011).

[39] P. Zhou, M. Yin, H.J. Wan, H. Lv, T. Tang, Y. Lin, Role of TaON interface for CuO resistive switching memory based on a combined model, Appl. Phys. Lett. 94 (2009) 053510–053510.

[40] F. De Stefano, M. Houssa, J.A. Kittl, M. Jurczak, V.V. Afanas'ev, A. Stesmans, Semiconducting-like filament formation in TiN/HfO_2/TiN resistive switching random access memories, Appl. Phys. Lett. 100 (2012) 142102.

[41] X. Guan, S. Yu, H.S.P. Wong, On the Switching Parameter Variation of Metal-Oxide RRAM, Part I: Physical Modeling and Simulation Methodology, IEEE Trans. Electron Devices. 59 (2012) 1172–1182.

[42] E. Vianello, G. Molas, F. Longnos, P. Blaise, E. Souchier, C. Cagli, G. Palma, J. Guy, M. Bernard, M. Reyboz, G. Rodriguez, A. Roule, C. Carabasse, V. Delaye, V. Jousseaume, S. Maitrejean, G. Reimbold, B. De Salvo, F. Dahmani, P. Verrier, D. Bretegnier, J. Liebault, Sb-doped GeS2 as performance and reliability booster in Conductive Bridge RAM, in: IEEE, 2012: pp. 31.5.1–31.5.4.

[43] N. Banno, T. Sakamoto, N. Iguchi, H. Sunamura, K. Terabe, T. Hasegawa, M. Aono, Diffusivity of Cu Ions in Solid Electrolyte and Its Effect on the Performance of Nanometer-Scale Switch, IEEE Trans. Electron Devices. 55 (2008) 3283–3287.

[44] K. Terabe, T. Hasegawa, T. Nakayama, M. Aono, Quantized conductance atomic switch, Nature. 433 (2005) 47–50.

[45] S. Maikap, S.Z. Rahaman, T.Y. Wu, F. Chen, M.-J. Kao, M.-J. Tsai, Low current (5 pA) resistive switching memory using high-κ Ta_2O_5 solid electrolyte, in: IEEE, (2009) pp. 217–220.

[46] C. Schindler, S.C.P. Thermadam, R. Waser, M.N. Kozicki, Bipolar and Unipolar Resistive Switching in Cu-Doped SiO_2, IEEE Trans. Electron Devices. 54 (2007) 2762–2768.

[47] L. Goux, K. Opsomer, R. Degraeve, R. Müller, C. Detavernier, D.J. Wouters, M. Jurczak, L. Altimime, J.A. Kittl, Influence of the Cu-Te composition and microstructure on the resistive switching of Cu-Te/Al_2O_3/Si cells, Appl. Phys. Lett. 99 (2011) 053502

[48] K. Sankaran, L. Goux, S. Clima, M. Mees, J.A. Kittl, M. Jurczak, L. Altimime, G.-M. Rignanese, G. Pourtois, Modeling of Copper Diffusion in Amorphous Aluminum Oxide in CBRAM Memory Stack, ECS Trans. 45 (2012) 317–330.

[49] D. Jana, S. Roy, R. Panja, M. Dutta, S.Z. Rahaman, R. Mahapatra, S. Maikap, Conductive-bridging random access memory: challenges and opportunity for 3D architecture, Nanoscale Res. Lett. 10 (2015).

[50] M.N. Kozicki, H.J. Barnaby, Conductive bridging random access memory—materials, devices and applications, Semicond. Sci. Technol. 31 (2016) 113001.

[51] M. Saadi, P. Gonon, C. Vallée, C. Mannequin, H. Grampeix, E. Jalaguier, F. Jomni, A. Bsiesy, On the mechanisms of cation injection in conducting bridge memories: The case of HfO_2 in contact with noble metal anodes (Au, Cu, Ag), J. Appl. Phys. 119 (2016) 114501.

[52] U. Celano, Filamentary-Based Resistive Switching, in: 2016: pp. 11–45.

[53] C.Y. Chen, L. Goux, A. Fantini, A. Redolfi, S. Clima, R. Degraeve, Y.Y. Chen, G. Groeseneken, M. Jurczak, Understanding the impact of programming pulses and electrode materials on the endurance properties of scaled Ta_2O_5 RRAM cells, in: 2014 IEEE Int. Electron Devices Meet., 2014: pp. 14.2.1–14.2.4.

[54] S. Toyoda, T. Shinohara, H. Kumigashira, M. Oshima, Y. Kato, Significant increase in conduction band discontinuity due to solid phase epitaxy of Al_2O_3 gate insulator films on GaN semiconductor, Appl. Phys. Lett. 101 (2012) 231607.

[55] E. Filatova, A. Konashuk, Interpretation of the Changing the Band Gap of Al_2O_3 Depending on Its Crystalline Form: Connection with Different Local Symmetries, J. Phys. Chem. C. 119 (2015).

[56] H.C. Lin, P.D. Ye, G.D. Wilk, Leakage current and breakdown electric-field studies on ultrathin atomic-layer-deposited Al_2O_3 on GaAs, Appl. Phys. Lett. 87 (2005) 182904.

[57] R. Panja, S. Roy, D. Jana, S. Maikap, Impact of device size and thickness of Al_2O_3 film on the Cu pillar and resistive switching characteristics for 3D cross-point memory application, Nanoscale Res. Lett. 9 (2014).

[58] J.A. Dawson, J. Robertson, Nature of Cu Interstitials in Al_2O_3 and the Implications for Filament Formation in Conductive Bridge Random Access Memory Devices, J. Phys. Chem. C. 120 (2016) 14474–14483.

[59] Y. Hirose, H. Hirose, Polarity-dependent memory switching and behavior of Ag dendrite in Ag-photodoped amorphous As_2S_3 films, J. Appl. Phys. 47 (1976) 2767–2772.
[60] S.-J. Choi, G.-S. Park, K.-H. Kim, S. Cho, W.-Y. Yang, X.-S. Li, J.-H. Moon, K.-J. Lee, K. Kim, In Situ Observation of Voltage-Induced Multilevel Resistive Switching in Solid Electrolyte Memory, Adv. Mater. 23 (2011) 3272–3277.
[61] Q. Liu, J. Sun, H. Lv, S. Long, K. Yin, N. Wan, Y. Li, L. Sun, M. Liu, Real-Time Observation on Dynamic Growth/Dissolution of Conductive Filaments in Oxide-Electrolyte-Based ReRAM, Adv. Mater. 24 (2012) 1844–1849.
[62] U. Celano, L. Goux, A. Belmonte, A. Schulze, K. Opsomer, C. Detavernier, O. Richard, H. Bender, M. Jurczak, W. Vandervorst, Conductive-AFM tomography for 3D filament observation in resistive switching devices, in: 2013 IEEE Int. Electron Devices Meet., 2013: pp. 21.6.1–21.6.4.
[63] W. Devulder, K. Opsomer, F. Seidel, A. Belmonte, R. Muller, B. De Schutter, H. Bender, W. Vandervorst, S. Van Elshocht, M. Jurczak, L. Goux, C. Detavernier, Influence of Carbon Alloying on the Thermal Stability and Resistive Switching Behavior of Copper-Telluride Based CBRAM Cells, ACS Appl. Mater. Interfaces. 5 (2013) 6984–6989.
[64] S. Tappertzhofen, I. Valov, T. Tsuruoka, T. Hasegawa, R. Waser, M. Aono, Generic Relevance of Counter Charges for Cation-Based Nanoscale Resistive Switching Memories, ACS Nano. 7 (2013) 6396–6402.
[65] I. Valov, I. Sapezanskaia, A. Nayak, T. Tsuruoka, T. Bredow, T. Hasegawa, G. Staikov, M. Aono, R. Waser, Atomically controlled electrochemical nucleation at superionic solid electrolyte surfaces, Nat. Mater. 11 (2012) 530–535.
[66] T. Yamamoto, T. Mizoguchi, The influence of neighboring vacancies and their charge state on the atomic migration of $LaAlO_3$, Appl. Phys. Lett. 102 (2013) 211910.
[67] G. Molas, E. Vianello, F. Dahmani, M. Barci, P. Blaise, J. Guy, A. Toffoli, M. Bernard, A. Roule, F. Pierre, C. Licitra, B.D. Salvo, L. Perniola, Controlling oxygen vacancies in doped oxide based CBRAM for improved memory performances, in: 2014 IEEE Int. Electron Devices Meet., 2014: pp. 6.1.1–6.1.4.
[68] Y.-L. Chung, W.-H. Cheng, J.-S. Jeng, W.-C. Chen, S.-A. Jhan, J.-S. Chen, Joint contributions of Ag ions and oxygen vacancies to conducting filament evolution of Ag/TaO_x/Pt memory device, J. Appl. Phys. 116 (2014) 164502.
[69] H. Jeon, J. Park, W. Jang, H. Kim, H. Song, H. Kim, H. Seo, H. Jeon, Resistive switching behaviors of Cu/TaO_x/TiN device with combined oxygen vacancy/copper conductive filaments, Curr. Appl. Phys. 15 (2015) 1005–1009.
[70] S. Liu, X. Zhao, Q. Li, N. Li, W. Wang, Q. Liu, H. Xu, Analysis of the Negative-SET Behaviors in Cu/ZrO_2/Pt Devices, Nanoscale Res. Lett. 11 (2016) 542.
[71] T. Liu, M. Verma, Y. Kang, M.K. Orlowski, Coexistence of Bipolar and Unipolar Switching of Cu and Oxygen Vacancy Nanofilaments in Cu/TaO_x/Pt Resistive Devices, ECS Solid State Lett. 1 (2012) Q11–Q13.
[72] J.R. Jameson, P. Blanchard, J. Dinh, N. Gonzales, V. Gopalakrishnan, B. Guichet, S. Hollmer, S. Hsu, G. Intrater, D. Kamalanathan, D. Kim, F. Koushan, M. Kwan, D. Lewis, B. Pedersen, M. Ramsbey, E. Runnion, J. Shields, K. Tsai, A. Tysdal, D. Wang, V. Gopinath, (Invited) Conductive Bridging RAM (CBRAM): Then, Now, and Tomorrow, ECS Trans. 75 (2016) 41–54.
[73] D.M. Mattox, Knovel (Firm), Handbook of physical vapor deposition (PVD) processing : film formation, adhesion, surface preparation and contamination control, Westwood, N.J. : Noyes Publications, 1998.
[74] M. Ohring, Materials science of thin films : deposition and structure, Academic Press, San Diego, CA, 2002.
[75] H. Hertz, Ueber einen Einfluss des ultravioletten Lichtes auf die electrische Entladung, Ann. Phys. 267 (1887) 983–1000.
[76] A. Einstein, Über einen die Erzeugung und Verwandlung des Lichtes betreffenden heuristischen Gesichtspunkt, Ann. Phys. 322 (1905) 132–148.
[77] S. Hüfner, Introduction, in: Photoelectron Spectrosc., Springer, Berlin, Heidelberg, 1996: pp. 1–26.
[78] D. Briggs, M.P. Seah, Practical surface analysis: by auger and x-ray photo-electron spectroscopy, Wiley, 1983.

[79] R.T. Lewis, M.A. Kelly, Binding-energy reference in X-ray photoelectron spectroscopy of insulators, J. Electron Spectrosc. Relat. Phenom. 20 (1980) 105–115.
[80] S. Hofmann, Auger- and X-Ray Photoelectron Spectroscopy in Materials Science: A User-Oriented Guide, Springer Science & Business Media, 2012.
[81] J.B. Pendry, Theory of photoemission, Surf. Sci. 57 (1976) 679–705.
[82] I. Adawi, Theory of the Surface Photoelectric Effect for One and Two Photons, Phys. Rev. 134 (1964) A788–A798.
[83] F. Reinert, S. Hüfner, Photoemission spectroscopy - From early days to recent applications, New J. Phys. 7 (2005) 97.
[84] D. Briggs, M.P. Seah, eds., Practical Surface Analysis, Auger and X-ray Photoelectron Spectroscopy, Volume 1 edition, Wiley, Chichester; New York, 1996.
[85] W.F. Egelhoff, Core-level binding-energy shifts at surfaces and in solids, Surf. Sci. Rep. 6 (1987) 253–415.
[86] C.S. Fadley, S.B. Hagström, J.M. Hollander, M.P. Klein, D.A. Shirley, Chemical bonding information from photoelectron spectroscopy, Science. 157 (1967) 1571–1573.
[87] E. Sokolowski, C. Nordling, K. Siegbahn, Chemical Shift Effect in Inner Electronic Levels of Cu Due to Oxidation, Phys. Rev. 110 (1958) 776–776.
[88] K. Kobayashi, Hard X-ray photoemission spectroscopy, Nucl. Instrum. Methods Phys. Res. Sect. Accel. Spectrometers Detect. Assoc. Equip. 601 (2009) 32–47.
[89] M.B. Trzhaskovskaya, V.I. Nefedov, V.G. Yarzhemsky, Photoelectron angular distribution parameters for elements z=1 to z=54 in the photoelectron energy range 100–5000 ev, At. Data Nucl. Data Tables. 77 (2001) 97–159
[90] M.B. Trzhaskovskaya, V.I. Nefedov, V.G. Yarzhemsky, Photoelectron angular distribution parameters for elements z=55 to z=100 in the photoelectron energy range 100–5000 ev, At. Data Nucl. Data Tables. 82 (2002) 257–311.
[91] J.H. Scofield, Theoretical photoionization cross sections from 1 to 1500 keV., CALIFORNIA UNIV., LIVERMORE. LAWRENCE LIVERMORE LAB., 1973.
[92] M.P. Seah, W.A. Dench, Quantitative electron spectroscopy of surfaces: A standard data base for electron inelastic mean free paths in solids, Surf. Interface Anal. 1 (1979) 2–11.
[93] C.R. Brundle, Elucidation of surface structure and bonding by photoelectron spectroscopy?, Surf. Sci. 48 (1975) 99–136.
[94] S. Tanuma, C.J. Powell, D.R. Penn, Calculations of electron inelastic mean free paths (IMFPS). IV. Evaluation of calculated IMFPs and of the predictive IMFP formula TPP-2 for electron energies between 50 and 2000 eV, Surf. Interface Anal. 20 (1993) 77–89.
[95] J.H. Lambert, E. (Ernst) Anding, Photometrie. Photometria, sive De mensura et gradibus luminis, colorum et umbrae (1760), Leipzig, W. Engelmann, 1892.
[96] Modern X Ray Tube Diagram, http://www.diagram-of-xray-tube.html/modern-x-ray-tube-diagram-of (accessed July 26, 2018).
[97] Focus 500 Monochromator, http://www.specs.de/cms/front_content.php?idcat=119 (accessed July 17, 2018).
[98] P.E. Larson, M.A. Kelly, Surface charge neutralization of insulating samples in x-ray photoemission spectroscopy, J. Vac. Sci. Technol. A. 16 (1998) 3483–3489.
[99] Resources / Synchrotron Radiation, https://www.nsrrc.org.tw/english/lightsource.aspx (accessed June 15, 2018).
[100] A. Balerna, S. Mobilio, Introduction to Synchrotron Radiation, in: Synchrotron Radiat., Springer, Berlin, Heidelberg, 2015: pp. 3–28.
[101] G. Aquilanti, L. Vaccari, J.R. Plaisier, A. Goldoni, Instrumentation at Synchrotron Radiation Beamlines, in: Synchrotron Radiat., Springer, Berlin, Heidelberg, 2015: pp. 65–104.
[102] C. Kunz, Synchrotron Radiation: Techniques and Applications, Springer Science & Business Media, 2013.

[103] J. Als-Nielsen, D. McMorrow, Elements of Modern X-ray Physics: Als-Nielsen/Elements, John Wiley & Sons, Inc., Hoboken, NJ, USA, 2011.
[104] Paul Scherrer Institut (PSI), https://www.psi.ch/ (accessed July 26, 2018).
[105] How does a synchrotron radiation source work, http://photon-science.desy.de/research/students__teaching/primers/synchrotron_radiation/index_eng.html (accessed July 26, 2018).
[106] S. Ueda, Y. Katsuya, M. Tanaka, H. Yoshikawa, Y. Yamashita, S. Ishimaru, Y. Matsushita, K. Kobayashi, Present Status of the NIMS Contract Beamline BL15XU at SPring-8, in: 2010: pp. 403–406.
[107] J.-P. Rueff, J.M. Ablett, D. Céolin, D. Prieur, T. Moreno, V. Balédent, B. Lassalle-Kaiser, J.E. Rault, M. Simon, A. Shukla, The GALAXIES beamline at the SOLEIL synchrotron: inelastic X-ray scattering and photoelectron spectroscopy in the hard X-ray range, J. Synchrotron Radiat. 22 (2015) 175–179.
[108] J.A. Coln Santana, The elements of photoemission spectroscopy, in: Morgan & Claypool Publishers, 2014.
[109] P. Willmott, An Introduction to Synchrotron Radiation: Techniques and Applications, (2011) 341–352.
[110] B. Philippe, R. Dedryvère, J. Allouche, F. Lindgren, M. Gorgoi, H. Rensmo, D. Gonbeau, K. Edström, Nanosilicon Electrodes for Lithium-Ion Batteries: Interfacial Mechanisms Studied by Hard and Soft X-ray Photoelectron Spectroscopy, Chem. Mater. 24 (2012) 1107–1115.
[111] Y. Takata, Y. Kayanuma, M. Yabashi, K. Tamasaku, Y. Nishino, D. Miwa, Y. Harada, K. Horiba, S. Shin, S. Tanaka, E. Ikenaga, K. Kobayashi, Y. Senba, H. Ohashi, T. Ishikawa, Recoil effects of photoelectrons in a solid, Phys. Rev. B. 75 (2007) 233404.
[112] C.P. Flynn, Phonon Broadening of Deep Excitations in Metals, Phys. Rev. Lett. 37 (1976) 1445–1448.
[113] D. Céolin, J.M. Ablett, D. Prieur, T. Moreno, J.-P. Rueff, T. Marchenko, L. Journel, R. Guillemin, B. Pilette, T. Marin, M. Simon, Hard X-ray photoelectron spectroscopy on the GALAXIES beamline at the SOLEIL synchrotron, J. Electron Spectrosc. Relat. Phenom. 190 (2013) 188–192.
[114] M. Nastasi, J. Mayer, J.K. Hirvonen, Ion-Solid Interactions: Fundamentals and Applications, Cambridge University Press, 1996.
[115] L.A. Giannuzzi, B.I. Prenitzer, B.W. Kempshall, Ion - Solid Interactions, in: Introd. Focus. Ion Beams, Springer, Boston, MA, 2005: pp. 13–52.
[116] I. Yamada, J. Matsuo, N. Toyoda, A. Kirkpatrick, Materials processing by gas cluster ion beams, Mater. Sci. Eng. R Rep. 34 (2001) 231–295.
[117] N. Toyoda, I. Yamada, Gas Cluster Ion Beam Equipment and Applications for Surface Processing, IEEE Trans. Plasma Sci. 36 (2008) 1471–1488.
[118] J.C. Vickerman, D. Briggs, ToF-SIMS: Materials Analysis by Mass Spectrometry, IM Publications, 2013.
[119] T. Grehl, R. Möllers, E. Niehuis, Low energy dual beam depth profiling: influence of sputter and analysis beam parameters on profile performance using TOF-SIMS, Appl. Surf. Sci. 203-204 (2003) 277–280.
[120] B. Berghmans, B. Van Daele, L. Geenen, T. Conard, A. Franquet, W. Vandervorst, Cesium near-surface concentration in low energy, negative mode dynamic SIMS, Appl. Surf. Sci. 255 (2008) 1316–1319.
[121] A. Benninghoven, F.G. Rudenauer, H.W. Werner, Secondary Ion Mass Spectrometry: Basic Concepts, Instrumental Aspects, Applications and Trends, 1987.
[122] SIMS Theory Tutorial, https://www.eag.com/resources/tutorials/sims-tutorial-theory/ (accessed July 17, 2018).
[123] K. Wittmaack, Mechanism of MCs + formation in Cs based secondary ion mass spectrometry, Surf. Sci. - Surf. SCI. 606 (2012).
[124] Secondary Ion Mass Spectrometry Instrumentation Tutorial, http://pprco.tripod.com/SIMS/Instrumentation.htm (accessed July 17, 2018).
[125] J. McPherson, J.-Y. Kim, A. Shanware, H. Mogul, Thermochemical description of dielectric breakdown in high dielectric constant materials, Appl. Phys. Lett. 82 (2003) 2121.
[126] D. Ielmini, Resistive switching memories based on metal oxides: mechanisms, reliability and scaling, Semicond. Sci. Technol. 31 (2016) 063002.
[127] S. Doniach, M. Sunjic, Many-electron singularity in X-ray photoemission and X-ray line spectra from metals, J. Phys. C Solid State Phys. 3 (1970) 285.

[128] W. Huschka, D. Ross, M. Maier, E. Umbach, Calibrated binding energies of some core levels in the energy range between 1.5–4 keV, J. Electron Spectrosc. Relat. Phenom. 46 (1988) 273–276.
[129] D.D. Sarma, C.N.R. Rao, XPES studies of oxides of second- and third-row transition metals including rare earths, J. Electron Spectrosc. Relat. Phenom. 20 (1980) 25–45.
[130] M.K. Bahl, R.L. Watson, K.J. Irgolic, X-ray photoemission studies of tellurium and some of its compounds, J. Chem. Phys. 66 (1977) 5526–5535.
[131] H. Neumann, M. Mast, J. Enderlein, R.D. Tomlinson, M.V. Yakushev, XPS Analysis of Bridgman-grown CuInTe2 and of its Native Oxide, Cryst. Res. Technol. 31 (1996) 75–85.
[132] Greenwood, N.N. and Earnshaw, A. Chemistry of the Elements. 2nd Edition, Butterworth-Heinemann, Oxford- Scientific Research Publishing, (1997).
[133] A. Walsh, C.R.A. Catlow, A.G.H. Smith, A.A. Sokol, S.M. Woodley, Strontium migration assisted by oxygen vacancies in SrTiO${}_{3}$ from classical and quantum mechanical simulations, Phys. Rev. B. 83 (2011) 220301.
[134] N. Barrett, O. Renault, J.-F. Damlencourt, F. Martin, Thermal stability of the HfO_2/SiO_2 interface for sub-0.1μm complementary metal-oxide-semiconductor gate oxide stacks: A valence band and quantitative core-level study by soft x-ray photoelectron spectroscopy, J. Appl. Phys. 96 (2004) 6362–6369.
[135] A. Jablonski, J. Zemek, Overlayer thickness determination by XPS using the multiline approach, Surf. Interface Anal. 41 (2009) 193–204.
[136] R. Kaufmann, H. Klewe-Nebenius, H. Moers, G. Pfennig, H. Jenett, H.J. Ache, XPS studies of the thermal behaviour of passivated Zircaloy-4 surfaces, Surf. Interface Anal. 11 (n.d.) 502–509.
[137] Y.-J. Huang, S.-C. Chao, D.-H. Lien, C.-Y. Wen, J.-H. He, S.-C. Lee, Dual-functional Memory and Threshold Resistive Switching Based on the Push-Pull Mechanism of Oxygen Ions, Sci. Rep. 6 (2016).
[138] O. Renault, E. Martinez, C. Zborowski, J. Mann, R. Inoue, J. Newman, K. Watanabe, Analysis of buried interfaces in multilayer device structures with hard XPS (HAXPES) using a CrKα source, Surf. Interface Anal. 0 (n.d.).
[139] P. Risterucci, O. Renault, C. Zborowski, D. Bertrand, A. Torres, J.-P. Rueff, D. Ceolin, G. Grenet, S. Tougaard, Effective inelastic scattering cross-sections for background analysis in HAXPES of deeply buried layers, Appl. Surf. Sci. 402 (2017) 78–85.
[140] T. Bertaud, C. Walczyk, D. Walczyk, M. Sowinska, D. Wolansky, B. Tillack, G. Schoof, C. Wenger, S. Thiess, T. Schroeder, HfO_2-based RRAM for Embedded Nonvolatile Memory: From Materials Science to Integrated 1T1R RRAM Arrays, Meet. Abstr. MA2012-02 (2012) 2577–2577.
[141] M.K. Mendes, E. Martinez, A. Marty, M. Veillerot, Y. Yamashita, R. Gassilloud, M. Bernard, O. Renault, N. Barrett, Forming mechanism of Te-based conductive-bridge memories, Appl. Surf. Sci. 432 (2018) 34–40.
[142] N.C. Saha, H.G. Tompkins, Titanium nitride oxidation chemistry: An x-ray photoelectron spectroscopy study, J. Appl. Phys. 72 (1992) 3072–3079.
[143] A.F. Carley, P.R. Chalker, J.C. Riviere, M.W. Roberts, The identification and characterisation of mixed oxidation states at oxidised titanium surfaces by analysis of X-ray photoelectron spectra, J. Chem. Soc. Faraday Trans. 1 Phys. Chem. Condens. Phases. 83 (1987) 351–370.
[144] P.M. Kumar, S. Badrinarayanan, M. Sastry, Nanocrystalline TiO_2 Studied by Optical, FTIR and X-ray Photoelectron Spectroscopy: Correlation to Presence of Surface States, Thin Solid Films. 358 (2000) 122–130.
[145] J.F. Moulder, W.F. Stickle, P.E. Sobol, K.D. Bomben, Handbook of X Ray Photoelectron Spectroscopy: A Reference Book of Standard Spectra for Identification and Interpretation of Xps Data, Physical Electronics, 1995.
[146] T. Dewolf, V. Delaye, N. Bernier, D. Cooper, N. Chevalier, H. Grampeix, C. Charpin, E. Jalaguier, M. Kogelschatz, S. Schamm-Chardon, G. Audoit, Nano-characterization of switching mechanism in HfO_2-based oxide resistive memories by TEM-EELS-EDS, in: Eur. Microsc. Congr. 2016, 2016: pp. 598–599.

université PARIS-SACLAY
ÉCOLE DOCTORALE
Physique en île-de-France (EDPIF)

Titre : Etudes par spectroscopie photoélectronique par rayons X de la commutation résistive dans les CBRAMs à base de Te

Mots clés : CBRAM, RRAM, spectroscopie de photoélectrons, chimie de l'interface, HAXPES

Résumé : Les mémoires à pont conducteur (CBRAM) sont une option actuellement étudiée pour la prochaine génération de mémoires non volatiles. Le stockage des données est basé sur la commutation de la résistivité entre les états de résistance élevée (HRS) et faible (LRS). Sous polarisation électrique, on suppose qu'un trajet conducteur est créé par la diffusion des ions de l'électrode active dans l'électrolyte solide. Récemment, une attention particulière a été portée sur les dispositifs contenant un élément semi-conducteur tel que le tellure, fonctionnant avec des courants réduits et présentant moins de défaillances de rétention. Dans ces « subquantum CBRAMs », le filament est censé contenir du tellure, ce qui donne une conductance de 1 atome (G_{1atom}) significativement réduite par rapport aux CBRAMs standard et permettant ainsi un fonctionnement à faible puissance. Dans cette thèse, nous utilisons la spectroscopie de photoélectrons par rayons X (XPS) pour étudier les réactions électrochimiques impliquées dans le mécanisme de commutation des CBRAMs à base de Al2O3 avec des alliages ZrTe et TiTe comme électrode active. Deux méthodes sont utilisées: i) spectroscopie de photoélectrons par rayons X de haute énergie non destructive (HAXPES) pour étudier les interfaces critiques entre l'électrolyte (Al_2O_3) et les électrodes supérieure et inférieure et ii) les faisceaux d'ions à agrégats gazeux (GCIB), une technique de pulvérisation qui conduit à une dégradation plus faible de la structure, avec un profilage en profondeur XPS pour évaluer les distributions des éléments en profondeur. Des mesures ToF-SIMS sont également effectuées pour obtenir des informations complémentaires sur la répartition en profondeur des éléments. Le but de cette thèse est de clarifier le mécanisme de changement de résistance et de comprendre les changements chimiques aux deux interfaces impliquées dans le processus de « forming » sous polarisation positive et négative ainsi que le mécanisme de « reset ». Pour cela, nous avons effectué une comparaison entre le dispositif vierge avec un état formé, i.e. l'échantillon après la première transition entre HRS et LRS et un état reset, i.e. l'échantillon après la première transition entre LRS et HRS. L'analyse du « forming » positif pour les dispositifs ZrTe / Al_2O_3 a montré une libération de Te liée à l'oxydation de Zr due au piégeage de l'oxygène de l'Al_2O_3 sous l'effet du champ électrique. D'autre part, pour les dispositifs TiTe / Al_2O_3, la présence d'une couche importante d'oxyde de titane à l'interface avec l'électrolyte a provoqué une dégradation permanente de la cellule en polarisation positive. Pour le « forming » négatif, nos résultats montrent un mécanisme hybride, à savoir une combinaison de formation de lacunes d'oxygène dans l'oxyde provoquée par la migration de O^{2-} entraîné par le champ électrique vers l'électrode inférieure et la libération de tellure pour former des filaments conducteurs. De plus, les résultats obtenus par profilométrie XPS et ToF-SIMS ont indiqué une possible diffusion de Te dans la couche d'Al_2O_3. Lors du « reset », il y a une recombinaison partielle des ions oxygène avec les lacunes d'oxygène près de l'interface TiTe / Al_2O_3 avec une perte de Te. Un mécanisme hybride a également été observé sur les dispositifs ZrTe / Al_2O_3 pendant le « forming » négatif. En tenant compte du rôle important de la migration d'oxygène dans la formation / dissolution des filaments, nous discutons également des résultats obtenus par XPS avec polarisation électrique in- situ (sous ultravide) pour mieux comprendre le rôle de l'oxydation de surface et des interfaces dans la commutation résistive.

Université Paris-Saclay
Espace Technologique / Immeuble Discovery
Route de l'Orme aux Merisiers RD 128 / 91190 Saint-Aubin, France

université PARIS-SACLAY
ÉCOLE DOCTORALE
Physique en île-de-France (EDPIF)

Title : X-ray photoelectron spectroscopy investigations of resistive switching in Te-based CBRAMs

Keywords : CBRAM, RRAM, photoelectron spectroscopy, Interface chemistry, HAXPES

Conducting bridging resistive random access memories (CBRAMs) are one option currently investigated for the next generation of non-volatile memories. Data storage is based on switching the resistivity between high (HRS) and low (LRS) resistance states. Under electrical bias, a conductive path is assumed to be created by ions diffusion from the active electrode into the solid electrolyte. Recently, special attention has been drawn to devices containing an elemental semiconductor such as tellurium, operating with reduced currents and less retention failures. In these subquantum CBRAM cells, the filament is thought to contain tellurium , yielding a 1-atom conductance (G_{1atom}) significantly reduced compared to standard CBRAMs and thus allowing low power operation. In this thesis, we use X-ray photoelectron spectroscopy (XPS) to learn about electrochemical reactions involved in the switching mechanism of Al_2O_3 based CBRAMs with ZrTe and TiTe alloys as active electrode. Two methods are used: i) non-destructive Hard X-ray photoelectron spectroscopy (HAXPES) to investigate the critical interfaces between the electrolyte (Al_2O_3) and the top and bottom electrodes and ii) Gas Cluster Ion Beams (GCIB), a sputtering technique that leads to lower structure degradation, combined with XPS depth profiling to evaluate chemical depth distributions. ToF-SIMS measurements are also performed to get complementary in-depth chemical information. The aim of this thesis is to clarify the driving mechanism and understand the chemical changes at both interfaces involved in the forming process under positive and negative polarization as well as the mechanism of the reset operation. For that, we performed a comparison between as-grown state, i.e. the pristine device with a formed state, i.e. the sample after the first transition between HRS and LRS, and reset state, i.e. the sample after the first transition between LRS and HRS.

Conducting bridging resistive random access memories (CBRAMs) are one option currently investigated for the next generation of non-volatile memories. Data storage is based on switching the resistivity between high (HRS) and low (LRS) resistance states. Under electrical bias, a conductive path is assumed to be created by ions diffusion from the active electrode into the solid electrolyte. Recently, special attention has been drawn to devices containing an elemental semiconductor such as tellurium, operating with reduced currents and less retention failures. In these subquantum CBRAM cells, the filament is thought to contain tellurium , yielding a 1-atom conductance (G1atom) significantly reduced compared to standard CBRAMs and thus allowing low power operation. In this thesis, we use X-ray photoelectron spectroscopy (XPS) to learn about electrochemical reactions involved in the switching mechanism of Al_2O_3 based CBRAMs with ZrTe and TiTe alloys as active electrode. Two methods are used: i) non-destructive Hard X-ray photoelectron spectroscopy (HAXPES) to investigate the critical interfaces between the electrolyte (Al_2O_3) and the top and bottom electrodes and ii) Gas Cluster Ion Beams (GCIB), a sputtering technique that leads to lower structure degradation, combined with XPS depth profiling to evaluate chemical depth distributions. ToF-SIMS measurements are also performed to get complementary in-depth chemical information. The aim of this thesis is to clarify the driving mechanism and understand the chemical changes at both interfaces involved in the forming process under positive and negative polarization as well as the mechanism of the reset operation. For that, we performed a comparison between as-grown state, i.e. the pristine device with a formed state, i.e. the sample after the first transition between HRS and LRS, and reset state, i.e. the sample after the first transition between LRS and HRS.

Université Paris-Saclay
Espace Technologique / Immeuble Discovery
Route de l'Orme aux Merisiers RD 128 / 91190 Saint-Aubin, France